

Title	Development of inversion-mode and junctionless Indium-Gallium-Arsenide MOSFETs
Authors	Djara, Vladimir
Publication date	2013
Original Citation	Djara, V. 2013. Development of inversion-mode and junctionless Indium-Gallium-Arsenide MOSFETs. PhD Thesis, University College Cork.
Type of publication	Doctoral thesis
Rights	© 2013, Vladimir Djara - http://creativecommons.org/licenses/by-nc-nd/3.0/
Download date	2025-07-04 06:39:39
Item downloaded from	https://hdl.handle.net/10468/1706



UCC

University College Cork, Ireland
Coláiste na hOllscoile Corcaigh

**DEVELOPMENT OF INVERSION-MODE AND
JUNCTIONLESS INDIUM-GALLIUM-ARSENIDE
MOSFETs**

Vladimir Djara

Thesis Submitted for the degree of Doctor of Philosophy

Department of Physics
University College Cork
National University of Ireland
Cork

Supervisors: Dr. Paul K. Hurley and Dr. Karim Cherkaoui
Head of Department: Prof. John McInerney

December 2013

Declaration

I declare that the entire content of this thesis is my own work, unless otherwise stated, and that this thesis has not been submitted for another degree, either at University College Cork or elsewhere.

Vladimir Djara

Contents

List of Figures	vi
List of Tables	xviii
List of Acronyms	xix
List of Symbols	xxii
Abstract	xxvii
Acknowledgments	xxx
1 Introduction	1
1.1 Extending Moore’s Law	1
1.1.1 Classic Scaling Rules	1
1.1.2 Technology Boosters	3
1.2 Challenges for High- k /III-V MOSFETs	6
1.2.1 Low Defect Densities in High- k /III-V Gate Stacks	6
1.2.2 Low Resistance Source and Drain Contacts	16
1.2.3 Integration of III-V Channel Materials on a Si Platform	18
1.3 Objectives and Organization of the Thesis	18
Bibliography	21
2 Source/Drain Activation and Impact on Gate Stack	38
2.1 Introduction	38
2.2 Samples Preparation	39
2.3 Doehlert Design of Experiment	40
2.4 Results and Discussion	41
2.4.1 Analysis of Doehlert Design of Experiment	41
2.4.2 Impact of Activation Anneal on Gate Stack Performance	45

2.4.3	Issues With First Fabricated MOSFETs	48
2.5	Conclusion	48
	Bibliography	51
3	Impact of Forming Gas Annealing on MOSFET Performance	55
3.1	Introduction	55
3.2	Samples preparation	56
3.3	Results and Discussion	57
3.3.1	Transmission Electron Microscopy Analysis of Gate Stack and Implanted Regions	57
3.3.2	Fixed Oxide Charge Passivation, Threshold Voltage Shift and OFF-State Leakage Reduction	58
3.3.3	MOSCAPs Behaviour and Density of Interface Traps	60
3.3.4	Transconductance, Drive Current and Effective Mobility Improvement . .	63
3.3.5	Junction Leakage Reduction	65
3.4	Conclusion	66
	Bibliography	68
4	Analysis of MOS Gate Stack Defects	74
4.1	Introduction	74
4.2	Full Gate Capacitance Measurement	76
4.3	Maserjian Y-Function	76
4.4	Results and Discussion	78
4.4.1	Integrated Fixed Oxide Charge and Integrated Interface Trap Density . .	78
4.4.2	Band Bending and Trap Density Profile	80
4.4.3	Comparison with Conventional Methods	84
4.5	Conclusion	86
	Bibliography	87
5	Investigation of Border Traps and Mobility	91
5.1	Introduction	91
5.2	Experimental Details	91
5.2.1	Surface-channel Al ₂ O ₃ /In _{0.53} Ga _{0.47} As MOSFETs	91
5.2.2	Inversion-Charge Pumping Method	92
5.3	Results and Discussion	94
5.3.1	Inversion-Charge Pumping Measurements	94
5.3.2	I_d - V_g Measurements	107

5.3.3	Comparison of the Effective Mobility Extracted from the Inversion-Charge Pumping, Multi-frequency Inversion-Charge Pumping and Low Temperature Split C - V Methods	109
5.3.4	Modeling of Effective Mobility	110
5.3.5	Analysis of the Surface Roughness of the Channel	111
5.4	Conclusion	114
	Bibliography	115
6	Impact of Channel Thickness on Junctionless MOSFET Performance	120
6.1	Introduction	120
6.2	Channel Thinning by Digital Etching	125
6.3	Fabrication of Planar Gate-enclosed Junctionless MOSFETs	128
6.4	Analysis of Planar Gate-enclosed Junctionless MOSFETs	130
6.4.1	Impact of Channel Thickness on Device Performance	130
6.4.2	Density of Interface Traps	133
6.4.3	Surface Carrier Concentration, Substrate Doping and Dark Space	136
6.4.4	Series Resistance	138
6.4.5	Effective Mobility	140
6.5	Conclusion	142
	Bibliography	143
7	Conclusions and Suggestions for Further Research	148
7.1	Conclusions	148
7.2	Suggestions for Further Research	150
A	Doehlert Design of Experiment	152
A.1	Implementation	152
A.2	Statistical Analysis	154
A.3	Process Optimization	154
	Bibliography	155
B	Masks	156
C	Process Flow for Junctionless MOSFETs with Raised Source and Drain	157
D	List of Achievements	159

List of Figures

1.1	Schematic illustration of the transistor scaling, where α is the scaling parameter [2].	2
1.2	Cross-section TEM images of strained silicon transistors (90-nm node) including (a) <i>n</i> -MOSFET with tensile strain induced by Si ₃ N ₄ cap film and (b) <i>p</i> -MOSFET with compressive strain induced by SiGe S/D heteroepitaxial regrowth. The gate lengths of the <i>n</i> -MOSFET and <i>p</i> -MOSFET are 45 nm and 50 nm, respectively [11, 12].	3
1.3	TEM images of <i>p</i> -MOSFETs of the (a) 65-nm node featuring a SiO ₂ /poly-Si gate stack and (b) 45-nm node featuring a high- <i>k</i> /metal gate stack. The gate lengths of the devices in (a) and (b) are 35 nm [12, 13].	4
1.4	TEM of fin, TEM of gate, and tilted SEM of 22-nm node non-planar 3-D transistors featuring thin gate for logic application (top) and thick gate for high-voltage application (bottom) [18].	6
1.5	(a) Interface traps [38–40], (b) border traps [41–43] and (c) fixed oxide charges [44] in an Al ₂ O ₃ /In _{0.53} Ga _{0.47} As MOS device.	8
1.6	Multi-frequency (M-F) capacitance-voltage (C-V) characteristics obtained on Al ₂ O ₃ / <i>n</i> -In _{0.53} Ga _{0.47} As MOSCAPs without (a) and with (b) the optimized (NH ₄) ₂ S surface passivation reported in [49]. The M-F C-V characteristics were measured by Éamon O’Connor. (c) Impact of the same surface passivation on the effective mobility (μ_{eff}) vs carrier density (N_s) extracted on flatband-mode MOSFETs [50]. The surface passivation was performed at the Tyndall National Institute and the design, fabrication and characterization of the flatband-mode Al ₂ O ₃ /In _{0.53} Ga _{0.47} As MOSFETs were performed at the University of Glasgow.	9
1.7	D_{it} values reported in the literature since 2008 for In _{0.53} Ga _{0.53} As MOS structures with LaAlO ₃ [53], ZrO ₂ [54], HfO ₂ [55–60], Al ₂ O ₃ [42, 49, 60–69], Si ₃ N ₄ [70] and SiO ₂ [71] gate oxides. The <i>k</i> -values of these gate oxides are reported in [14].	10
1.8	Comparison of the D_{it} values reported for (a) HfO ₂ /In _{0.53} Ga _{0.53} As MOS structures [55–60] and (b) Al ₂ O ₃ /In _{0.53} Ga _{0.53} As MOS structures [42, 49, 60–69].	11

1.9	D_{it} values extracted on similar <i>ex-situ</i> deposited ALD Al_2O_3 films on sulphur passivated $\text{In}_{0.53}\text{Ga}_{0.53}\text{As}$ using the conductance method [49, 57, 61, 63, 64, 66], a method based on the fitting of a measured quasi-static (Q-S) C-V [62], the high-low frequency capacitance method [49] and the charge pumping method [42].	12
1.10	Normalized C-V characteristics measured on $\text{Al}_2\text{O}_3/n\text{-In}_{0.53}\text{Ga}_{0.53}\text{As}$ MOSCAPs at a frequency (f) of 1 MHz and a temperature (T) of -50°C (a) before and (b) after FGA [99]. The oxide thickness (t_{ox}) ranges from 11.5 nm to 20 nm. The insets show the evolution of the flat-band voltage (V_{fb}) as a function of t_{ox} . N_{bulk} and N_{int} represent the bulk and the interface fixed charge densities, respectively. The beige shaded area indicates the uncertainty on the theoretical flat-band voltage (V_{fb}^{theo}).	15
1.11	Transfer length (L_t) vs specific contact resistivity (ρ_C) curve calculated for $n\text{-In}_{0.53}\text{Ga}_{0.53}\text{As}$ epitaxially doped to $\sim 3.5 \times 10^{19} / \text{cm}^3$ featuring a sheet resistance (R_{sheet}) of $17 \Omega/\square$ [103]. In this configuration, the contact length (L_C) of 7 nm targeted for the 12-nm node is much lower than L_t .	16
1.12	Percentage loss in drain current in saturation ($I_{D,sat}$) vs specific contact resistivity (ρ_C) curve calculated for a 12-nm node device using the method reported in [106].	17
1.13	Logic flow chart of research work presented in this thesis.	19
2.1	(a) Time vs temperature anneal process window showing the seven activation anneal conditions of the DOE along with activation anneal conditions reported in the literature [12–18]. The lowest thermal budget limit, where InP etch pitting starts, is also indicated [19]. (b) Optical image of a fabricated TLM structure. The width (W) of the Si-implanted TLM bar is $30 \mu\text{m}$ and the metal contact separations (d) are 5, 10, 15, 25, 40 and $60 \mu\text{m}$.	41
2.2	(a) Current-voltage (I-V) measurements of the sample annealed in run 2, where 5 to 60 indicate the contacts separations (d) in μm . (b) Resistances (R) vs d , where 1 to 7 are the run numbers. Inset: Linear extrapolation of R vs d (run 5). The slope is R_{sheet}/W , the y -intercept is $R = 2 \times R_C$ and the x -intercept is $d = -2 \times L_t$.	42
2.3	R_{sheet} response surface and contour plot as a function of annealing temperature and time. The correlation coefficient R of the model is 0.99986. The Lagrange criterion applied to the model revealed an optimized process condition of 715°C for 32 s, leading to a minimum R_{sheet} of $(195.6 \pm 3.4) \Omega/\square$.	44

2.4	(a) SRIM simulation and SIMS measurements (before and after 675°C for 30 s annealing) of the two-stage Si implantation (1×10^{14} /cm ² at 80 keV and 1×10^{14} /cm ² at 30 keV) into the HfO ₂ (10 nm)/ <i>p</i> -In _{0.53} Ga _{0.47} As (160 nm)/ <i>p</i> -InP (80 nm)/SI-InP structure. Inset: Contour plot of the HfO ₂ film thickness measured by SE across a 2-in wafer. TEM images of (b) a non-annealed sample and (c) a 675°C for 30 s annealed sample. The SIMS measurements were conducted at INTEL Ireland and the TEM analysis was performed by S. B. Newcomb (Glebe Scientific).	46
2.5	TEM images of the Si-implanted (1×10^{14} /cm ² at 80 keV and 1×10^{14} /cm ² at 30 keV) HfO ₂ (10 nm)/ <i>p</i> -In _{0.53} Ga _{0.47} As (160 nm)/ <i>p</i> -InP (80 nm)/SI-InP structure (a) before and (b) after 675°C for 30 s annealing. The TEM analysis was performed by S. B. Newcomb (Glebe Scientific).	47
2.6	Capacitance-voltage (C-V) characteristics of the Pd/HfO ₂ (8 nm)/Al ₂ O ₃ (2 nm)/ <i>p</i> -In _{0.53} Ga _{0.47} As/ <i>p</i> -InP/SI-InP structures annealed for 30 s in N ₂ at (a) 675°C and (b) 725°C. The unexpected <i>n</i> -type C-V behavior could result from a possible diffusion of unintentional <i>n</i> -type dopants from the substrate/epitaxial interface, in agreement with [28]. (c) Conductance-voltage (G-V) and C-V characteristics measured at a frequency of 100 kHz on Pd/HfO ₂ (8 nm)/Al ₂ O ₃ (2 nm)/ <i>p</i> -In _{0.53} Ga _{0.47} As/ <i>p</i> -InP/SI-InP structures annealed at 675°C, 700°C and 725°C for 30 s in N ₂	49
2.7	(a) Picture of a fabricated In _{0.53} Ga _{0.47} As MOSFET obtained with the “high- <i>k</i> first + metal-gate last” process. G, S,D and B indicate the gate, source, drain and body contacts, respectively. (b) Drain current (I_d) vs drain-source voltage (V_{ds}) for a 5- μ m gate length Pd/HfO ₂ /In _{0.53} Ga _{0.47} As MOSFET for a gate voltage (V_g) varied from -2 V to 2 V with a step of 0.5V.	50
3.1	Schematic cross-sectional diagram of a surface-channel In _{0.53} Ga _{0.47} As MOSFET with a 10-nm-thick ALD Al ₂ O ₃ dielectric and a Pd gate. The nominal gate (L) is 1, 2, 3, 5, 10, 20 or 40 μ m and the width (W) is 50 μ m. The overlap of the Pd gate over the Si-implanted n^+ regions is 1.5 μ m and the separation between the Pd gate contact and the source (S) or drain (D) contact is 4 μ m.	56
3.2	TEM images (a) through the gate stack region of the MOSFET confirming the 10-nm Al ₂ O ₃ gate oxide thickness and (b) through the gate overlap region, showing the implant defects in the Si-implanted n^+ region. The TEM analysis was performed by M. Schmidt. (Tyndall National Institute)	57

3.3	<i>I_d-V_{gs}</i> obtained on 20- μ m-gate-length and 50- μ m-gate-width MOSFETs at $V_{ds} = 50$ mV before and after FGA. The MOSFETs feature a V_T of -0.63 and 0.43 V before and after FGA, respectively. (b) Q-S C-V simulation of the Pd/Al ₂ O ₃ / <i>p</i> -In _{0.53} Ga _{0.47} As gate stack obtained using a Poisson-Schrödinger simulator [20]. The ideal V_T of 0.7 V was obtained based on a Pd work function of 4.7 eV [21], a 10-nm-thick Al ₂ O ₃ film with a k -value of 8.6, and a <i>p</i> -In _{0.53} Ga _{0.47} As doping level of 4×10^{17} /cm ³	58
3.4	Comparison of the 20°C and -50°C log <i>I_d-V_{gs}</i> measured at $V_{ds} = 50$ mV on 20- μ m-gate-length and 50- μ m-gate-width MOSFETs (a) before and (b) after FGA. The log <i>I_d-V_{gs}</i> values are shown with matched gate overdrive ($V_{gs}-V_T$).	60
3.5	Multi-frequency (M-F) capacitance-voltage (C-V) characteristics of Pd/Al ₂ O ₃ / <i>p</i> -In _{0.53} Ga _{0.47} As MOSCAPs measured from 100 Hz to 100 kHz (a) before and (b) after FGA. The V_T of the corresponding MOSFETs is highlighted on the C-V characteristics.	61
3.6	Normalized parallel conductance (G_p/ω) <i>vs</i> frequency (f) obtained with the conductance method [27, 28] for a 10-nm-thick Al ₂ O ₃ film with a k -value of 8.6. The D_{it} extraction at $V_g = -1.9$ V before FGA and at $V_g = -0.8$ V after FGA yielded the same value of $\sim 4.0 \times 10^{12}$ /cm ² .eV.	62
3.7	(a) Transconductance (g_m) versus gate overdrive ($V_{gs}-V_T$) and (b) <i>I_d-V_{ds}</i> characteristics obtained on 20- μ m-gate-length and 50- μ m-gatewidth MOSFETs before and after FGA. After FGA, the peak g_m and drive current increase by 29% and 25%, respectively.	63
3.8	Effective mobility (μ_{eff}) versus inversion charge density (N_{inv}) before and after FGA. The peak μ_{eff} increases by 15% after FGA. (Inset) 2-MHz gate-to-channel C_{gc} split C-V characteristics before and after FGA.	64
3.9	Extracted peak effective mobility (μ_{eff}) <i>vs</i> In _{0.53} Ga _{0.47} As channel doping (N_a) compared to literature values obtained in [5, 29, 31–34]. GGO stands for gallium gadolinium oxide.	65
3.10	a) I-V characteristics of the n^+/p In _{0.53} Ga _{0.47} As junction measured on a MOSFET at 293 K before and after FGA. (b) Arrhenius plot from 223 to 293 K for reverse bias going from 0.1 to 0.5 V applied to implanted n^+/p junctions before and after FGA. The area of the n^+/p junction diodes is 10^4 μ m ² . The activation energy (E_a) values are 0.37 eV and 0.40 eV before and after FGA, respectively.	66

-
- 4.1 Full gate capacitance (C_g) vs gate voltage (V_g) measurement setup, where the gate contact (G) of the MOSFET is connected to the “high” of the impedance meter and the source (S), drain (D) and substrate contacts are shorted together and connected to the “low”. 75
- 4.2 Example of theoretical (ideal) p -type C_g - V_g characteristic (a) and corresponding Maserjian Y -function (b). The threshold voltage (V_T) and flat-band voltage (V_{fb}) are obtained from the peak of the Maserjian Y -function and Equation 4.3, respectively. V_T and V_{fb} delimitate the accumulation (acc.), depletion and inversion (inv.) regions. Knowing V_{fb} allows to extract the flat-band capacitance (C_{fb}). The grey shaded areas represent the $\text{In}_{0.53}\text{Ga}_{0.47}\text{As}$ bandgap. 77
- 4.3 Comparison of the experimental and theoretical (ideal) high-frequency (H-F) C_g - V_g characteristics. The theoretical threshold voltage (V_T^{theo}), experimental threshold voltage (V_T^{exp}), theoretical flat-band voltage (V_{fb}^{theo}), experimental flat-band voltage (V_{fb}^{exp}) and $\Delta V_T = V_T^{theo} - V_T^{exp}$ are indicated on the graph. The calculation of the theoretical C_g - V_g characteristic was performed by T. P. O’Regan (Tyndall). 78
- 4.4 Illustrating the four steps in the fitting of the experimental C_g - V_g (a, c, e, g) and corresponding Maserjian Y -function (b, d, f, h). (a-b) theoretical (ideal) high-frequency (H-F) model, (c-d) H-F model with fixed oxide charge (N^+), (e-f) H-F model with N^+ and trap energy profile [$D_{trap}(E)$], and (g-h) spliced H-F model in depletion with quasi-static (Q-S) model in inversion, including N^+ and $D_{trap}(E)$. V_{fb} and V_T indicate the experimental flat-band and threshold voltages, respectively. The fitting was performed by T. P. O’Regan (Tyndall). 81
- 4.5 Gate-to-channel capacitance (C_{gc}) vs gate voltage (V_g) measured over a range of frequency (f) going 1 kHz to 1 MHz for a fixed temperature (T) of 292 K and at a f of 1 MHz and a T of 78 K. Low capacitance dispersion with f and T is observed in inversion ($V_g > 0.5$ V). 82
- 4.6 (a) Comparison of the band bending $E-E_V$ vs V_g profile obtained with the fitting of the C_g - V_g characteristic and Maserjian Y -function to the profile obtained for a theoretical (ideal) device. (b) Trap density vs energy profile obtained from the fitting of the Maserjian Y -function and C_g - V_g characteristic. The blue solid line and the red short dash line represent donor-type (+/0) and acceptor-type (0/-) trap density profiles, respectively. The donor-type trap density profile suggests the presence of two components, which are highlighted as two Gaussian distributions (blue short dot lines). The grey shaded areas represent the $\text{In}_{0.53}\text{Ga}_{0.47}\text{As}$ bandgap. 83

4.7	(a) Comparison of the band bending $E-E_V$ vs V_g profile obtained with the fitting of the C_g-V_g characteristic and Maserjian Y -function to the profile obtained with the Terman method [29] and Berglund integral [28]. (b) Comparison of the trap density vs energy profile obtained with the fitting method to the profiles extracted from the Terman (the short dash curve shows the intrappolation of the Terman data), high-low [30] and full conductance [8] methods. C_{ox}/q is indicated to highlight the limitation of the full conductance method. The grey shaded areas represent the $\text{In}_{0.53}\text{Ga}_{0.47}\text{As}$ bandgap.	85
5.1	Schematics of the Inversion-Charge Pumping (ICP) setup used to extract the inversion charge density (N_{inv}) in long channel ($L > 20 \mu\text{m}$) $\text{Al}_2\text{O}_3/\text{In}_{0.53}\text{Ga}_{0.47}\text{As}$ MOSFETs through the measurements of (a) N_{CP_SD} , (b) N_{CP_S} and (c) N_{CP_D} . V_{base} , V_{peak} , N_S and N_D represent the base voltage, peak voltage, loss to the source and loss to the drain, respectively. N_{inv} is obtained using the relationship: $N_{inv} = N_{CP_S} + N_{CP_D} - N_{CP_SD}$	93
5.2	Density of interface traps (D_{it}) vs gate voltage (V_g) profile obtained using the high-low and full-conductance methods. The high-low was performed at a temperature (T) of 292 K while that of the full-conductance method was varied from 292 K to 78 K in order to access interface traps located in different parts of the $\text{In}_{0.53}\text{Ga}_{0.47}\text{As}$ bandgap [12]. The relatively large D_{it} values (greater than C_{ox}/q) obtained with the high-low method for $V_g < -0.75$ V preclude the use of a conductance-based method in that V_g range [13]. The threshold voltage (V_T) of 0.2 V, obtained at $T = 292$ K, is used to locate the $\text{In}_{0.53}\text{Ga}_{0.47}\text{As}$ conduction band edge.	95
5.3	Energy band diagrams of a p -type metal-oxide-semiconductor (MOS) structure showing (a) the SiO_2/Si interface case, where the density of interface trap (D_{it}) distributed across the semiconductor bandgap is negligible ($< 10^{10} / \text{cm}^2.\text{eV}$), allowing to perform the ICP measurement with $V_{base} = V_{fb}$, and (b) the high- $k/\text{In}_{0.53}\text{Ga}_{0.47}\text{As}$ interface case, where the D_{it} is large, requiring $V_{fb} \ll V_{base} < V_T$ in order to maintain constant occupancy of most of the interface traps during the ICP measurement. It is noted that as V_{base} is raised from V_{fb} towards V_T , the structure is moved from a flat-band condition to a depletion condition, which involves the formation of a space charge region (SCR) energy barrier impeding the recombination of the inversion charge during the ICP measurement. In the diagrams, E_{fm} is the metal Fermi level while E_C , E_V and E_{fp} are the semiconductor conduction band edge, valence band edge and Fermi level, respectively.	96

5.4	(a) Total pumped charge density (N_{CP}) vs peak voltage (V_{peak}) obtained for a base voltage (V_{base}) ranging from -0.3 V to -0.9 V. The ICP measurements were performed on a 40- μm -channel-length device with a frequency (f) of 1 MHz, a duty cycle (D) of 50 % and pulse rise time (t_r) and fall time (t_f) of 10 ns. The density of interface traps (D_{it}) contribution to total pumped charge density (N_{CP}) reduces as base voltage (V_{base}) is raised from -0.9 V to -0.3 V. The experimental curves are non-linear and their slopes deviate from the theoretical $C_{inv} \cdot (\text{gate voltage } (V_g) - \text{threshold voltage } (V_T)) / \text{charge of an electron}$ curve, where C_{inv} is the capacitance in inversion measured by split C-V at a temperature (T) of 35 K and q is the charge of an electron. (b) Total charge density (N_{CV}) vs V_g obtained by split C-V at $f = 1$ MHz over a range of T going from 440 K to 35 K. The D_{it} contribution to N_{CV} reduces as T is reduced.	97
5.5	Loss to S/D ($1-\alpha$) vs peak voltage (V_{peak}) obtained for a base voltage (V_{base}) ranging from -0.3 V to -0.9 V. The space charge region (SCR) barrier height increases as V_{base} is raised from -0.9 V to -0.3 V.	98
5.6	Example of energy band diagrams of a p -type metal-oxide-semiconductor (MOS) structure with a density of border traps (D_{bt}) assumed to be uniformly distributed across energy. (a) Case of an ICP measurement where the base voltage (V_{base}) is set to -0.3 V and the peak voltage (V_{peak}) is set to a value above the threshold voltage (V_T), respectively. (b) Case of a split C-V measurement where the gate voltage (V_g) $>$ V_T . In an ICP measurement, the energy range (ΔE) swept by the Fermi level increases with V_{peak} , while in a split C-V measurement, ΔE depends on the amplitude of the AC signal (typically set to 25 mV) and not on V_g . Consequently, the $D_{bt} \cdot t_{ox} \cdot \Delta E$ contribution in an ICP measurement at large V_{peak} is much higher than that of a split C-V measurement performed at a V_g matching V_{peak} . In the diagrams, E_C , and E_{fp} are the semiconductor conduction band edge, and Fermi level, respectively.	100
5.7	Single pulse and DC I_d - V_g hysteresis performed on a 1- μm -channel-length device at a drain-to-source voltage (V_{ds}) of 50 mV. The rise time (t_r) and fall time (t_f) of the single pulse measurement were set to 500 ns.	101
5.8	(a) Impact of duty cycle (D) on total pumped charge density (N_{CP}) obtained from ICP performed at a frequency (f) of 1 MHz and a rise time (t_r) and fall time (t_f) of 10 ns. The curve obtained at $D = 5\%$ nearly matches the theoretical $C_{inv} \cdot (V_g - V_T) / q$ curve, consistent with a reduction of the D_{bt} contribution to N_{CP} at low D	102

5.9	Total pumped charge density (N_{CP}) plotted against frequency (f) on the top x -axis and against charging time (t_{charge}), which is equal to $1/(2f)$, on the bottom x -axis. The symbols show the experimental data obtained from the measurements performed on a 40- μm -channel-length device with the pulse rise time (t_r) and fall time (t_f) set to 10 ns, a base voltage (V_{base}) of -0.3 V and a duty cycle (D) of 50%. The peak voltage (V_{peak}) was varied from 0 V to 2 V. The lines represent the fitting of the data with the proposed charge trapping model.	103
5.10	Comparison of the total pumped-charged density (N_{CP}) obtained from inversion-charge pumping (ICP) at a frequency (f) of 1 MHz and duty cycle (D) of 5%, and multi-frequency ICP. In both measurements the base voltage (V_{base}) was -0.3 V and the rise time (t_r) and fall time (t_f) were 10 ns.	106
5.11	Comparison of the pulse and DC I_d - V_g characteristics performed on a 1- μm -channel-length device at a drain-to-source voltage (V_{ds}) of 50 mV. The rise time (t_r) and fall time (t_f) of the pulse measurement were set to 10 ns. Inset: R_{total} ($= V_{ds}/I_d$) vs channel length (L) at a gate voltage (V_g) of 2.5 V. The intercept on the y -axis yields the source and drain series resistance (R_{SD}).	108
5.12	DC I_d - V_g characteristics measured over a range of temperature (T) going from 4 K to 292 K on a 10- μm -channel-length device at a drain-to-source voltage (V_{ds}) of 50 mV. A zero-temperature coefficient (ZTC) point is observed. Inset: Source and drain series resistance (R_{SD}) as a function of temperature (T).	108
5.13	Effective mobility (μ_{eff}) vs inversion charge (N_{inv}) extracted using ICP at a frequency (f) of 1 MHz and a duty cycle (D) ranging from 50% to 5% and multi-frequency ICP. Excellent agreement is obtained between the μ_{eff} extracted from Split C - V ($f = 1$ MHz, $T = 292$ K) and that extracted by ICP ($f = 1$ MHz, $D = 50\%$). The experimental μ_{eff} values (symbols) were fitted with the empirical model reported in [37].	109
5.14	Effective mobility (μ_{eff}) vs inversion charge (N_{inv}) extracted using split C - V at a frequency (f) of 1 MHz for a range of temperature (T) going ranging from 292 K to 35 K. The experimental μ_{eff} values (symbols) were fitted with the empirical model reported in [37].	110
5.15	Scattering components obtained from the fitting of the effective mobility (μ_{eff}) vs inversion charge (N_{inv}) curves extracted from ICP ($f = 1$ MHz, $D = 50\%$) and multi-frequency (M-F) ICP. The phonon scattering mobility, the surface roughness scattering mobility, the Coulomb scattering mobility and the total mobility are noted μ_{ph} , μ_{sr} , μ_C , and μ_{tot} , respectively. While the same μ_{ph} and μ_{sr} were used to fit both curves, μ_C was adjusted to account for the removal of the border trap contribution to the total pumped-charged density (N_{CP}).	112

5.16	AFM topography data of (a) the unpassivated p -In _{0.53} Ga _{0.47} As surface and (b) the p -In _{0.53} Ga _{0.47} As surface after 10% (NH ₄) ₂ S passivation for 20 min, 10 nm Al ₂ O ₃ deposition by ALD, implant activation at 600°C for 15 s and finally Al ₂ O ₃ etch using dilute HF. Both measurements were taken over a 1 μm × 1 μm area. The AFM measurements were performed by M. Burke (Tyndall).	113
6.1	In _{0.53} Ga _{0.47} As channel thickness (t_{InGaAs}) vs In _{0.53} Ga _{0.47} As channel doping (N_d). The calculated maximum depletion width (W_d^{max}) yields the boundary between the fully depleted and non-fully depleted device structure. The 20 nm t_{InGaAs} limit, where severe effective electron mobility (μ_{eff}) degradation is reported [10], and the set of t_{InGaAs} (32, 24, 20, 16 and 12 nm) vs N_d (9×10^{17} /cm ³) parameters corresponding to the fabricated devices are also indicated.	121
6.2	Quasi-static capacitance-voltage (C - V) characteristics obtained for Pd/Al ₂ O ₃ / n -In _{0.53} Ga _{0.47} As/ p -In _{0.52} Al _{0.48} As/ p -InP structures using a self-consistent Poisson-Schrödinger solver. The structures featured In _{0.53} Ga _{0.47} As channel thicknesses (t_{InGaAs}) of 32, 24 and 16 nm and an In _{0.53} Ga _{0.47} As channel doping (N_d) of 9×10^{17} /cm ³ . A flat-band capacitance (C_{fb}) of 0.52 μF/cm ² and flat-band voltage (V_{fb}) of 0.2 V were obtained. It is noted that the dotted line inversion response of the quasi-static C - V curves will not be typically observed experimentally in a multi-frequency C - V	122
6.3	Conduction band diagrams of Pd/Al ₂ O ₃ / n -In _{0.53} Ga _{0.47} As/ p -In _{0.52} Al _{0.48} As/ p -InP structures obtained from self-consistent Poisson-Schrödinger calculations. Diagrams of a 32-nm-thick In _{0.53} Ga _{0.47} As channel device showing (a) the flat-band and (b) the fully depleted conditions. The Fermi level needs to move 0.07 eV above the conduction band edge (E_C) to reach flat-band and 0.54 eV below E_C to reach full depletion. Diagrams of a 24-nm-thick In _{0.53} Ga _{0.47} As channel device showing (c) the flat-band and (d) the fully depleted conditions. The Fermi level needs to move 0.07 eV above E_C to reach flat-band and 0.31 eV below E_C to reach full depletion.	123
6.4	(a) Energy range required to move from flat-band to full depletion as a function of In _{0.53} Ga _{0.47} As channel thickness (t_{InGaAs}). The values were obtained from self-consistent Poisson-Schrödinger calculations. (b) Comparison of the D_{it} values reported for Al ₂ O ₃ /In _{0.53} Ga _{0.47} As MOS structures [15–26].	124
6.5	Diagram and cross-section transmission electron microscopy (TEM) image of the MOVPE grown n -In _{0.53} Ga _{0.47} As (32 nm)/ p -In _{0.52} Al _{0.48} As (500 nm)/ p^+ -InP wafer structure used for the digital etch (DE) process characterization and for the device fabrication.	126

-
- 6.6 In_{0.53}Ga_{0.47}As channel thinning using a H₂O₂/HCl digital etch (DE) process [27]. Excellent agreement between spectroscopic ellipsometry (SE) and TEM (Figure 6.5) measurements was obtained prior to DE. An etch rate of 0.8 nm/cycle was extracted from the linear fit. The $R^2 = 0.999$ of the linear fit confirms the excellent control of the In_{0.53}Ga_{0.47}As etch rate. 126
- 6.7 Atomic force microscopy (AFM) topography data of *n*-In_{0.53}Ga_{0.47}As (a) before digital etch (DE) and after (b) a 10-cycle, (c) a 15-cycle and (d) a 20-cycle DE. The measurements were taken over 1 $\mu\text{m} \times 1 \mu\text{m}$ scan areas. The AFM measurements were performed by M. Burke (Tyndall). 127
- 6.8 Fabrication process flow of planar Gate-enclosed Junctionless In_{0.53}Ga_{0.47}As MOSFETs including (a) 10% (NH₄)₂S for 30 min passivation [16, 21] prior to ALD Al₂O₃, (8.5 nm), (b) Pd (200 nm) gate lift-off, (c) Al₂O₃ etch in dilute HF for S/D contact opening and (d) 10% NH₄OH for 20 sec surface treatment followed by Au (14 nm)/Ge (14 nm)/Au (14 nm)/Ni (11 nm)/Au (200 nm) [29] S/D contact lift-off. (e) Cross-section diagram of a gate-enclosed junctionless MOSFET architecture. The drain radius (r_d), gate inner radius (r_g^{in}), gate outer radius (r_g^{out}) and source radius (r_s) are 35, 45, 105 and 135 μm , respectively. 129
- 6.9 I_d - V_{ds} output characteristic of a planar gate-enclosed junctionless In_{0.53}Ga_{0.47}As MOSFET featuring a 24-nm-thick In_{0.53}Ga_{0.47}As channel. A $(W/L)_{eff}$ of 7.41 was used for the W/L normalization of I_d 130
- 6.10 I_d - V_g transfer characteristics measured at $V_{ds} = 50$ mV on planar gate-enclosed junctionless In_{0.53}Ga_{0.47}As MOSFETs with $t_{InGaAs} = 32, 24, 20, 16$ and 12 nm. A $(W/L)_{eff}$ of 7.41 was used for the W/L normalization of I_d 131
- 6.11 (a) I_{ON}/I_{OFF} vs t_{InGaAs} . The best I_{ON}/I_{OFF} value of 1.5×10^5 was obtained with $t_{InGaAs} = 20$ nm. For $t_{InGaAs} > 20$ nm, I_{ON}/I_{OFF} is degraded due to an increase in I_{OFF} . For $t_{InGaAs} < 20$ nm, the I_{ON}/I_{OFF} is degraded due to a decrease in I_{ON} . (b) Subthreshold swing (SS) vs t_{InGaAs} . SS scaling with t_{InGaAs} observed for t_{InGaAs} reducing from 24 nm to 16 nm. The lowest SS (115 mV/dec.) was obtained with $t_{InGaAs} = 16$ nm. 132
- 6.12 I - V characteristic of a *n*-In_{0.53}Ga_{0.47}As/*p*-In_{0.52}Al_{0.48}As heterojunction diode fabricated on the wafer structure shown in Figure 6.5. More than 7 orders of magnitude between the forward and reverse current is observed, indicating excellent junction isolation 133

-
- 6.13 (a) C_{gc} - V_g characteristics measured at a frequency of 1 MHz on planar gate-enclosed junctionless $\text{In}_{0.53}\text{Ga}_{0.47}\text{As}$ MOSFETs with $t_{\text{InGaAs}} = 32$ nm. Inset: Calculated minimum capacitance (C_{min}) vs $\text{In}_{0.53}\text{Ga}_{0.47}\text{As}$ doping (N_d). A measured C_{min} of $\sim 0.2 \mu\text{F}/\text{cm}^2$ at $V_g = -2$ V suggests a $N_d < 1.1 \times 10^{18} /\text{cm}^3$. (b) Fermi level position at the $\text{Al}_2\text{O}_3/\text{In}_{0.53}\text{Ga}_{0.47}\text{As}$ interface in an ideal and in the fabricated devices. In the fabricated device, the Fermi level is pinned above $E_F - E_C = -0.54$ eV [Figure 6.3(b)], preventing the full depletion of the 32-nm-thick $\text{In}_{0.53}\text{Ga}_{0.47}\text{As}$ channel. 134
- 6.14 (a) Multi-frequency C_{gc} - V_g characteristic of a 24-nm-thick $\text{In}_{0.53}\text{Ga}_{0.47}\text{As}$ channel device showing low frequency dispersion near accumulation. The low C_{min} of ~ 40 nF/cm² suggests full depletion at $V_g < -1$ V. Inset: Evolution of the conductance peak normalized to angular frequency (G/ω). (b) Comparison of the conductance and high-low methods for the extraction of the density of interface traps (D_{it}). Inset: Fermi level position at the $\text{Al}_2\text{O}_3/\text{In}_{0.53}\text{Ga}_{0.47}\text{As}$ interface in an ideal and in the fabricated devices. In the fabricated device, the Fermi level reaches $E_F - E_C = -0.3$ eV at $V_g = -1$ V, demonstrating the full depletion of the 24-nm-thick $\text{In}_{0.53}\text{Ga}_{0.47}\text{As}$ channel. 135
- 6.15 (a) 100-kHz C_{gc} - V_g characteristics measured on 24, 20 and 16-nm-thick $\text{In}_{0.53}\text{Ga}_{0.47}\text{As}$ -channel devices. The theoretical flat-band capacitance (C_{fb}) obtained from calculations is reported on the curves to extract a flat-band voltage (V_{fb}) of 0 V. (b) Plot of the surface carrier density (N_s) at flat-band vs t_{InGaAs} . The total charge density (N_{tot}) was obtained by integrating C_{gc} . N_s was obtained by correcting N_{tot} for the density of interface trap (D_{it}) integrated across the energy range of operation of the corresponding device. The N_s at flat-band vs t_{InGaAs} curves were calculated for ideal devices with $N_d = 1.1 \times 10^{18}$, 9×10^{17} and $7 \times 10^{17} /\text{cm}^3$. The x -intercepts obtained by extrapolation of the curves yielded the total dark space thickness values (accounting for the top and bottom interfaces). The case of a SiO_2/Si -on-insulator (SOI) structure with a channel N_d of $9 \times 10^{17} /\text{cm}^3$ is shown for comparison. 137

6.16 (a) Circuit equivalent model of the device. $R_{c,D}$ and $R_{c,S}$ are the resistances of the contacts to the drain and source areas, respectively. R_D , R_S , R_{D-to-G} and R_{G-to-S} are the resistances associated with the sheet resistance of the drain, source, drain-to-source and gate-to-source areas, respectively. R_{ch} is the resistance of the channel. (b) Simplified circuit equivalent model assuming a specific contact resistance (ρ_c) of $5 \times 10^{-6} \Omega \cdot \text{cm}^2$, a transfer length (L_t) of $0.5 \mu\text{m}$ and a mobility in the $n\text{-In}_{0.53}\text{Ga}_{0.47}\text{As}$ ($N_d = 9 \times 10^{17} / \text{cm}^3$) layer of $2000 \text{ cm}^2/\text{V}\cdot\text{s}$. (c) Comparison of the series resistance (R_{series}) vs t_{InGaAs} extracted from the $I_d\text{-}V_g$ curves shown in Figure 6.10 and calculated from the simplified equivalent circuit model shown in (b) with estimated and/or extracted surface carrier density [noted $n.t$ in Equation 6.4] and carrier mobility (μ) parameters. 139

6.17 Effective electron mobility (μ_{eff}) vs N_s . Values of μ_{eff} at flat-band of 2130, 1975 and $310 \text{ cm}^2/\text{V}\cdot\text{s}$ were obtained for planar gate-enclosed junctionless $\text{In}_{0.53}\text{Ga}_{0.47}\text{As}$ MOSFETs featuring t_{InGaAs} of 24, 20 and 16 nm, respectively. The abrupt drop in μ_{eff} observed for $t_{InGaAs} = 16 \text{ nm}$ is consistent with [10]. The μ_{eff} of an inversion-mode $\text{Pd}/\text{Al}_2\text{O}_3/\text{In}_{0.53}\text{Ga}_{0.47}\text{As}$ MOSFET with implanted S/D measured at a temperature (T) of 35 K (see 5) is shown for comparison. The μ_{eff} data of the junctionless devices are corrected for R_{series} and D_{it} . The μ_{eff} data of the inversion-mode device is only corrected for R_{series} but the reduced T acts as a D_{it} correction [35]. 141

List of Tables

1.1	Scaling rules. α is the scaling parameter [4].	2
1.2	Performance of state-of-the-art III-V, SOI and bulk Si n -MOSFETs.	5
2.1	TLM structure, pre-metal annealed MOSCAP and “high- k first + metal-gate last” n -channel MOSFET process flows.	39
2.2	Experimental R_{sheet} , R_C , L_t and ρ_C obtained for each run of the Doehlert DOE. F_1 and F_2 are the anneal temperature factor and the anneal time factor, respectively.	43
2.3	Student’s t -test applied to each coefficient of the R_{sheet} model.	43
2.4	ANOVA applied to the entire model.	44
5.1	Model parameters fitted for a range of peak voltage (V_{peak}) values going from 0 V to 2 V. N_{bt}^0 is the border trap density in the Al_2O_3 integrated across energy and thickness, τ is the capture time constant, β is the distribution factor of capture time constant and N_{inv} is the inversion-charge density.	104
5.2	RMS surface roughness extracted from AFM measurements. The quoted value represents the mean from at least three measurements at separate locations (each on a $1\ \mu\text{m} \times 1\ \mu\text{m}$ scan area) and the uncertainty is given by the standard deviation.	113
6.1	Root mean square (RMS) surface roughness data from AFM measurements taken on $n\text{-In}_{0.53}\text{Ga}_{0.47}\text{As}$ before digital etch (DE) and after a 10-cycle, 15-cycle and 20-cycle (DE) (Figure 6.7). The quoted values represent the mean, maximum and minimum from four measurements at separate locations (each on a $1\ \mu\text{m} \times 1\ \mu\text{m}$ scan area). The uncertainties on the mean values are given by the standard deviation.	127

List of Acronyms

3-D	3-dimension
ac	alternative current
AFM	atomic force microscopy
ALD	atomic layer deposition
ANOVA	analysis of variance
C-V	capacitance-voltage
CMOS	complementary metal-oxide-semiconductor
CP	charge pumping
CVD	chemical vapor deposition
DC	direct current
DE	digital etch
DIBL	drain-induced barrier lowering
DOE	design of experiment
EOT	equivalent oxide thickness
FDSOI	fully-depleted silicon on insulator
FET	field effect transistor
FGA	forming gas (H ₂ /N ₂) anneal
G-V	conductance-voltage
GAA	gate-all-around
GGO	gallium gadolinium oxide
H-F	high-frequency

HP	high performance
I-V	current-voltage
ICP	inversion-charge pumping
ITRS	international technology roadmap for semiconductor
LP	low power
M-F	multi-frequency
MAD	molecular atomic deposition
MBD	molecular beam deposition
MBE	molecular beam epitaxy
MOS	metal-oxide-semiconductor
MOSCAP	metal-oxide-semiconductor capacitor
MOSFET	metal-oxide-semiconductor field-effect transistor
MOVPE	metal-organic vapor phase epitaxy
OI	on insulator
PVD	physical vapor deposition
Q-S	quasi-static
RMS	root mean square
RTA	rapid thermal anneal
S/D	source and drain
SBH	Schottky barrier height
SCR	space charge region
SE	spectroscopic ellipsometry
SEM	scanning electron microscopy
SIMS	secondary ion mass spectrometry
SOI	silicon on insulator
SP	standard power
SRH	Shockley-Read-Hall
SRIM	stopping and range of ions in matter
SS	subthreshold swing

List of Acronyms

TEM	transmission electron microscopy
TLM	transfer length method
TMA	trimethyl-aluminum [Al(CH ₃) ₃]
ZTC	zero-temperature coefficient

List of Symbols

α	scaling parameter	
β_0	offset coefficient	
β_{12}	interaction coefficient	
β_{11}, β_{22}	first-order coefficients	
β_1, β_2	first-order coefficients	
C	capacitance	[F/m ²]
C_{fb}	flat-band capacitance	[F/m ²]
C_g	full-gate capacitance	[F/m ²]
C_{gc}	gate-to-channel capacitance	[F/m ²]
C_{inv}	inversion capacitance	[F/m ²]
C_{min}	minimum capacitance	[F/m ²]
C_{ox}	oxide capacitance	[F/m ²]
D	duty cycle	[%]
d	contact separation	[m]
D_{bt}	density of border traps	[/m ³ .eV]
ΔV_T	threshold voltage shift	[V]
D_{it}	density of interface traps	[/m ² .eV]
D_{trap}	surface-equivalent density of interface and border trap	[/m ² .eV]
E	energy	[eV]
E_a	activation energy	[eV]
E_C	conduction band edge	[eV]
E_f	Fermi energy	[eV]
E_g	bandgap	[eV]
ϵ_s	semiconductor dielectric constant	[F/m]

List of Symbols

E_V	valence band edge	[eV]
f	frequency	[Hz]
F_1, F_2	factors	
G	conductance	[S]
g_m	transconductance	[S/m]
G_p	parallel conductance	[S/m ²]
I	current	[A]
I_d	drain current	[A/m]
$I_{D,sat}$	drain current in saturation	[A/m]
I_{junc}	junction current	[A]
I_{OFF}	OFF-state current	[A/m]
I_{ON}	ON-state current	[A/m]
I_{ON}/I_{OFF}	ON-state-to-OFF-state current ratio	[A/m]
k	relative dielectric constant	
k_B	Boltzmann constant	[J/K]
L	length	[m]
λ	attenuation coefficient	[m]
L_C	contact length	[m]
L_t	transfer length	[m]
μ_C	coulomb scattering mobility	[m ² /V.s]
μ_{eff}	effective mobility	[m ² /V.s]
μ_{ph}	phonon scattering mobility	[m ² /V.s]
μ_{sr}	surface roughness scattering mobility	[m ² /V.s]
μ_{tot}	total mobility	[m ² /V.s]
N_a	<i>p</i> -type dopant density	[/m ³]
N_{bt}^0	density of border traps integrated across energy and oxide thickness	[/m ²]
N_{bulk}	bulk fixed charge density	[/m ³]
N_{CP}	total pumped charge density	[/m ²]
N_{CV}	total charge density (N_{CV}) obtained from split C-V	[/m ²]
N_D	density of charge lost to the drain	[/m ²]

N_d	n -type dopant density	$[/m^3]$
n_i	intrinsic carrier density	$[/m^3]$
N_{int}	interface fixed charge density	$[/m^2]$
N_{inv}	inversion-charge density	$[/m^2]$
N^+	surface-equivalent density of fixed positive oxide charge	$[/m^2]$
N_S	density of charge lost to the source	$[/m^2]$
N_s	carrier density	$[/m^2]$
N_{tot}	total charge density	$[/m^2]$
ω	angular frequency	$[\text{rad/s}]$
P	P -value	
q	charge of an electron	$[C]$
Q_{fixed}	fixed oxide charge	$[C/m^2]$
R	resistance	$[\Omega]$
R	correlation coefficient	
R^2	determinant coefficient	
R_C	contact resistance	$[\Omega]$
$R_{c,D}$	contact resistance of the drain	$[\Omega]$
R_{ch}	channel resistance	$[\Omega]$
$R_{c,S}$	contact resistance of the source	$[\Omega]$
R_D	resistance associated to the sheet resistance of the drain	$[\Omega]$
r_d	drain radius	$[m]$
R_{D-to-G}	resistance associated to the sheet resistance of the drain-to-gate area	$[\Omega]$
r_g^{in}	gate inner radius	$[m]$
r_g^{out}	gate outer radius	$[m]$
r^{in}	disk inner radius	$[m]$
r^{out}	disk outer radius	$[m]$
R_{G-to-S}	resistance associated to the sheet resistance of the gate-to-source area	$[\Omega]$
ρ_C	specific contact resistance	$[\Omega.m^2]$
R_{ring}	resistance of a ring	$[\Omega]$
R_S	resistance associated to the sheet resistance of the source	$[\Omega]$
r_s	source radius	$[m]$
R_{SD}	source and drain series resistance	$[\Omega], [\Omega/m]$
R_{series}	series resistance	$[\Omega], [\Omega/m]$

List of Symbols

R_{sheet}	sheet resistance	$[\Omega/\square]$
R_{total}	total resistance	$[\Omega]$
σ	capture cross section	$[\text{m}^2]$
T	temperature	$[\text{K}], [^\circ\text{C}]$
τ	capture time constant	$[\text{s}]$
τ_e	electron lifetime	$[\text{s}]$
t_{bar}	thickness of the bar	$[\text{m}]$
t_{bt}	oxide thickness over which the border traps are probed	$[\text{m}]$
t_{charge}	charge time	$[\text{s}]$
t_{dark}	dark space thickness	$[\text{m}]$
$t_{discharge}$	discharge time	$[\text{s}]$
t_f	fall time	$[\text{s}]$
t_{InGaAs}	$\text{In}_{0.53}\text{Ga}_{0.47}\text{As}$ channel thickness	$[\text{m}]$
t_{ox}	oxide thickness	$[\text{m}]$
t_r	rise time	$[\text{s}]$
t_t	tunneling time	$[\text{s}]$
V	voltage	$[\text{V}]$
V_{base}	base voltage	$[\text{V}]$
V_d	drain voltage	$[\text{V}]$
V_{DD}	supply voltage	$[\text{V}]$
V_{ds}	drain-to-source voltage	$[\text{V}]$
V_{fb}	flat-band voltage	$[\text{V}]$
V_{fb}^{exp}	experimental flat-band voltage	$[\text{V}]$
V_{fb}^{theo}	theoretical flat-band voltage	$[\text{V}]$
V_g	gate voltage	$[\text{V}]$
V_{gs}	gate-to-source voltage	$[\text{V}]$
V_{junc}	voltage across the junction	$[\text{V}]$
V_{peak}	peak voltage	$[\text{V}]$
V_T	threshold voltage	$[\text{V}]$
V_T^{exp}	experimental threshold voltage	$[\text{V}]$
V_T^{theo}	theoretical threshold voltage	$[\text{V}]$
v_{th}	thermal velocity	$[\text{m/s}]$
W	width	$[\text{m}]$

W_d^{max}	maximum depletion width	[m]
W_f	metal work function	[eV]
W_{fin}	fin width	[m]
x	distance	[m]
X_1, X_2	normalized variables	
\hat{Y}	estimated response	

Abstract

This PhD covers the design, fabrication and characterization of planar inversion-mode and junctionless $\text{In}_{0.53}\text{Ga}_{0.47}\text{As}$ metal-oxide-semiconductor field-effect transistors (MOSFETs). The objectives of this work were to (1) use the fabricated devices as test vehicles for further studies of the defects present in the $\text{Al}_2\text{O}_3/\text{In}_{0.53}\text{Ga}_{0.47}\text{As}$ gate stack through the development of alternative electrical characterization techniques, (2) identify and understand the impact of the MOSFET fabrication process steps on the gate stack defects and (3) explore defect passivation techniques and alternative device architectures to reduce gate stack defects.

An implant activation anneal process was first developed for the formation of the source and drain (S/D) terminals of the inversion-mode device. Test structures based on the transfer length method (TLM) were fabricated and used as part of a Doehlert design of experiment (DOE) to investigate a process window covering annealing temperatures of 625°C to 725°C and annealing times of 15 s to 45 s. The optimized process was 715°C for 32 s, leading to a minimum sheet resistance (R_{sheet}) of $(195.6 \pm 3.4) \Omega/\square$. Non-alloyed Au/Ge/Au/Ni/Au contacts, on the sample annealed at 675°C for 30 s (centre point of the experimental domain), exhibited a low specific contact resistance (ρ_C) of $(7.4 \pm 4.5) \times 10^{-7} \Omega.\text{cm}^2$.

The sample annealed at 675°C for 30 s was further investigated using secondary ion mass spectrometry (secondary ion mass spectrometry (SIMS)) and cross-sectional transmission electron microscopy (TEM) analyses. SIMS revealed that Si ions did not diffuse with annealing, while TEM showed the formation of characteristic loop defects potentially responsible for the R_{sheet} and ρ_C degradation. The impact of the activation anneal on the performance of the metal-oxide-semiconductor (MOS) gate stack was also studied. Large density of interface traps (D_{it}) values of 2.0, 2.3 and $2.7 \times 10^{13} / \text{cm}^2.\text{eV}$ were estimated using the conductance method on $\text{In}_{0.53}\text{Ga}_{0.47}\text{As}$ metal-oxide-semiconductor capacitors (MOSCAPs) annealed at 675°C , 700°C and 725°C , respectively. The results indicated that, in the 675°C to 725°C range, an increase of 25°C increased D_{it} by $\sim 16\%$.

Fabricated inversion-mode $\text{Al}_2\text{O}_3/\text{In}_{0.53}\text{Ga}_{0.47}\text{As}$ MOSFETs were used to investigate the impact of a 300°C for 30 min forming gas (H_2/N_2) anneal (FGA) process on their electrical performance. *The FGA was found to effectively remove or passivate the fixed positive oxide charge*

present in the Al_2O_3 gate dielectric, as a reduction in surface-equivalent density of fixed positive oxide charge (N^+) from $6.3 \times 10^{12} /cm^2$ to $1.3 \times 10^{12} /cm^2$ was observed following FGA. The reduction in N^+ yielded an increase in ON-state-to-OFF-state current ratio (I_{ON}/I_{OFF}) ratio of three orders of magnitude due to the removal of an inversion layer, located at the periphery of the devices, responsible for a large OFF-state current (I_{OFF}). Moreover, the FGA significantly improved the source or drain-to-substrate junction isolation, with a reduction of two orders of magnitude in the reverse bias leakage exhibited by the Si-implanted $In_{0.53}Ga_{0.47}As$ n^+/p junctions, consistent with a passivation of mid-gap defects in the implanted $In_{0.53}Ga_{0.47}As$ areas. Following FGA, the devices exhibited a subthreshold swing (SS) of 150 mV/decade, an I_{ON}/I_{OFF} of $\sim 10^4$ and the transconductance, drive current and peak effective mobility increased by 29% [to 1.1 mS/mm for a gate length (L) of 20 μm and a drain-to-source voltage (V_{ds}) of 50 mV], 25% [to 19 mV/mm for a L of 20 μm , a V_{ds} of 1.5 V and a gate overdrive of 2 V] and 15% (to 750 $cm^2/V.s$), respectively.

An alternative technique, based on the fitting of the measured full-gate capacitance (C_g) vs gate voltage (V_g) and corresponding Maserjian Y -function using a self-consistent Poisson-Schrödinger solver, was developed to further investigate gate stack defects. *The proposed techniques provides more information than the conventional Terman, high-low and conductance methods. Indeed, this technique can yield (1) the band bending efficiency of the gate stack, (2) the surface-equivalent density of interface and border trap (D_{trap}) vs energy (E) profile across the full $In_{0.53}Ga_{0.47}As$ bandgap and extending in the $In_{0.53}Ga_{0.47}As$ conduction band and (3) the donor and acceptor nature of the traps. The obtained $D_{trap}(E)$ featured a peak of donor-like interface traps with a density of $1.5 \times 10^{13} /cm^2.eV$ located at ~ 0.36 eV above the $In_{0.53}Ga_{0.47}As$ valence band edge (E_V) and a high density of donor-like traps increasing towards E_V . The analysis also indicated acceptor-like traps located in the $In_{0.53}Ga_{0.47}As$ conduction band, with a density of $\sim 2.5 \times 10^{13} /cm^2.eV$ at 0.3 eV above the $In_{0.53}Ga_{0.47}As$ conduction band edge (E_C).*

The inversion-charge pumping (ICP) method was investigated for the extraction of the inversion-charge density (N_{inv}) and effective mobility (μ_{eff}). The initial method was modified to minimize the overestimation of N_{inv} due to charge trapping mechanisms involving traps located at energy levels lying in the $In_{0.53}Ga_{0.47}As$ bandgap and $In_{0.53}Ga_{0.47}As$ conduction band. *The method was further developed and a multi-frequency (M-F) ICP approach was proposed to (1) study the traps located at energy levels aligned with the $In_{0.53}Ga_{0.47}As$ conduction band and (2) effectively separate the charge trapping contribution from N_{inv} . A discrete trap capture cross section (σ) of $\sim 4.5 \times 10^{-21} cm^2$ was obtained, suggesting a very narrow spatial distribution of border traps located at a distance of $\sim 1.5 \text{ \AA}$ from the interface. The analysis also revealed a μ_{eff} peaking at $\sim 2850 cm^2/V.s$ at a low N_{inv} of $7 \times 10^{11} cm^2/V.s$ and rapidly decreasing to $\sim 600 cm^2/V.s$ at $N_{inv} = 1 \times 10^{13} /cm^2$. Gate-to-channel capacitance (C_{gc}) split capacitance-voltage (C-V) measurements performed over a range of temperature going from 292 K to 35 K*

indicated that surface roughness scattering was the main factor limiting the mobility. Atomic force microscopy (AFM) measurements confirmed a large surface roughness of 1.95 ± 0.28 nm on the $\text{In}_{0.53}\text{Ga}_{0.47}\text{As}$ channel caused by the S/D implant activation anneal process.

In order to circumvent the issue relative to the S/D implant activation, a planar junctionless MOSFET based on an $\text{Al}_2\text{O}_3/n\text{-In}_{0.53}\text{Ga}_{0.47}\text{As}/p\text{-In}_{0.52}\text{Al}_{0.48}\text{As}$ structure was designed and fabricated. *One significant advantage of this device architecture is that the thermal budget is set by the Al_2O_3 deposition process by atomic layer deposition (ALD). A digital etch (DE) process was used to thin the $\text{In}_{0.53}\text{Ga}_{0.47}\text{As}$ channel in order to investigate the impact of the $\text{In}_{0.53}\text{Ga}_{0.47}\text{As}$ channel thickness (t_{InGaAs}) on the device operation and performance. The DE process characterization using spectroscopic ellipsometry (SE) and AFM revealed an etch rate of 0.8 nm/cycle and a root mean square (RMS) surface roughness of 0.28 nm (after 20 cycles), respectively. Values of D_{it} near the conduction band in the low- 10^{12} / cm^2 .eV were also extracted, suggesting that the DE process did not significantly degrade the $\text{Al}_2\text{O}_3/\text{In}_{0.53}\text{Ga}_{0.47}\text{As}$ interface properties. The reduction of t_{InGaAs} offers the advantage of reducing the energy range swept by the Fermi level when switching the device from ON-state to OFF-state. This was used to maintain the device operation within the upper part of the $\text{In}_{0.53}\text{Ga}_{0.47}\text{As}$ bandgap, where D_{it} is the lowest, in order to achieve lower SS. Scaling of the SS with t_{InGaAs} was successfully demonstrated for t_{InGaAs} going from 24 to 16 nm, with a minimum SS of 115 mV/dec. for $t_{\text{InGaAs}} = 16$ nm. Flat-band μ_{eff} values of 2130 and 1975 $\text{cm}^2/\text{V.s}$ were also extracted on devices with t_{InGaAs} values of 24 and 20 nm, respectively.*

Acknowledgments

After five years of excitement, ups and downs and also hard work, it is a great pleasure to look back, remember and thank everyone who helped me along the way.

First of all, I would like to thank my supervisor Dr Paul Hurley for giving me the opportunity to join his group and work on such an exciting project. Paul's expertise, guidance and enthusiasm have been invaluable to me. I would also like to say a huge "merci" to my second PhD supervisor Dr Karim Cherkaoui, for his continuous help and great support.

I am extremely grateful to my former CFF managers Brendan O'Neill and John Pike for making it possible for me to enroll in a part-time PhD program while still working as a Process Engineer in the Fab.

I would like to thank my examiners Prof Iain Thayne, Prof Greg Hughes and Prof Jim Greer for accepting to take part in my PhD evaluation.

I also wish to say a warm thanks to my dear colleagues of the CFF Carmel and Dan for their training, help with processing and more generally for making my time with the CFF highly enjoyable.

A big thanks to Paul's group, and especially to Terrance, Eamon, Adi, Scott and Brendan, for their fruitful collaborations and friendliness. I also thank Eamon and Rathnait, whose early work on $\text{Al}_2\text{O}_3/\text{In}_{0.53}\text{Ga}_{0.47}\text{As}$ effectively prepared the way for me to develop the MOSFETs.

I also want to acknowledge Ian Povey, Martyn Pemble, Micheal Burke, John MacHale, Aidan Quinn, Roger Nagle, Ray Duffy, Richard Murphy, Thomas Lopez, Micheal Schmidt, Simon Newcomb, Kevin Thomas, Emanuele Pelucchi, James O'Callaghan, John Justice, Liam Floyd, Alan Blake and Aileen O'Mahony for their direct contribution to this work and/or for helping me out at some stage.

A special thanks to the maintenance group, and especially to Pat, Richie, Alan and Feargal, for taking in charge the crucial task of keeping the III-V Fab up and running every day.

Last but not least, I want to thank my friends and family, and particularly Anne-Laure and Arthur, for their patience, love and constant support, which have given me the strength and energy to achieve something I am really proud of.

Chapter 1

Introduction

1.1 Extending Moore's Law

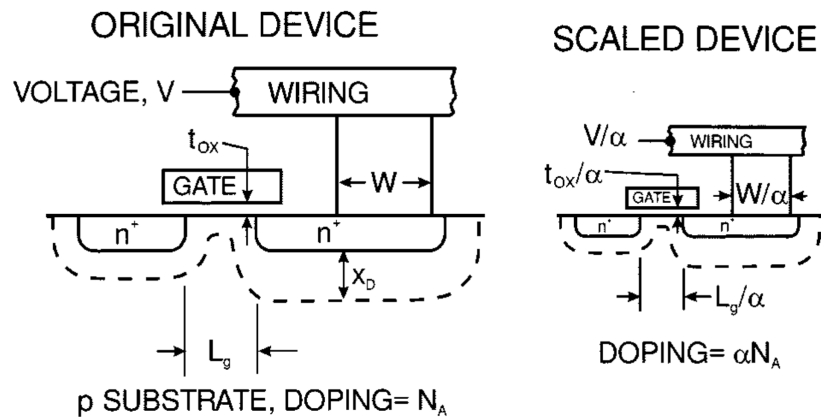
1.1.1 Classic Scaling Rules

In 1965, Gordon Moore predicted that the density of transistors on a chip would double approximately every 18 months [1]. Even though this empirical prediction was only based on data collected over a 6-year period (1959 - 1965), the so-called Moore's law has held remarkably well over the past 48 years, due to the continuous efforts from the semiconductor industry to push the limits of technology. While it is clear that increasing the density of transistors enables to add more circuit functionalities to a chip of a given size, many other advantages arise from reducing the size of the transistors.

In 1974, Dennard and co-workers first introduced the principles of transistor scaling (Figure 1.1), where the dimensions of a transistor are reduced by a scaling factor α to produce a smaller transistor with enhanced performance [2, 3]. As the dimensions and voltages are reduced by α and the doping is increased by α , the electric field configuration in the smaller transistor remains the same as that in the original one. As a result, the switching speed of the smaller transistor increases by α and the power dissipation reduces by α^2 .

Table 1.1 shows the scaling rules of the main physical parameters. It is worth noting that these scaling rules imply that the threshold voltage (V_T) should also reduce by α [4]. This cannot be achieved in a conventional metal-oxide-semiconductor field-effect transistor (MOSFET) due to the impossibility to scale the subthreshold swing (SS) below the 60 mV/dec. limit [at a temperature (T) of 292 K], which is known as the Boltzmann limit [5, 6].

The "classic" Dennard's scaling rules were followed by the semiconductor industry until 2001 (130-nm node) [7], when geometrical scaling was still sufficient to deliver performance improvement. In all subsequent technology nodes (i.e.: < 100 nm), "short-channel effects", arising from the very small distance separating the source from the drain, involved performance degradation.

Figure 1.1: Schematic illustration of the transistor scaling, where α is the scaling parameter [2].Table 1.1: Scaling rules. α is the scaling parameter [4].

Physical Parameter	Scaling Factor
Channel Length and Width	$1/\alpha$
Wiring Width	$1/\alpha$
Gate Oxide Thickness	$1/\alpha$
Electric Field in Device	1
Voltage	$1/\alpha$
On-current per Device	$1/\alpha$
Doping	α
Area	$1/\alpha^2$
Capacitance	$1/\alpha$
Gate Delay	$1/\alpha$
Power Dissipation	$1/\alpha^2$
Power Density	1

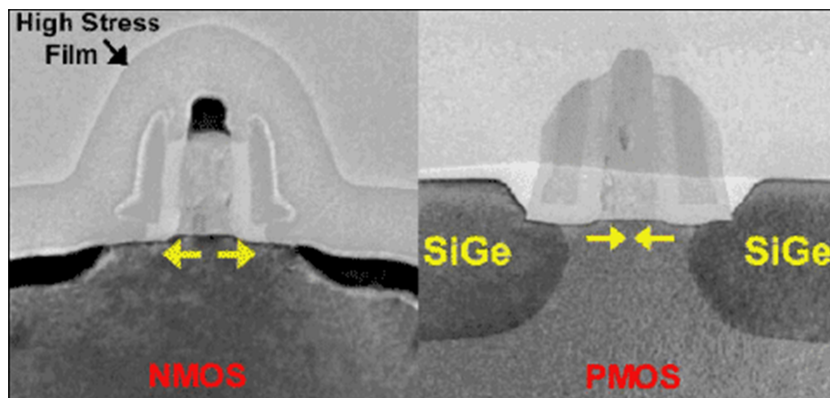


Figure 1.2: Cross-section TEM images of strained silicon transistors (90-nm node) including (a) n -MOSFET with tensile strain induced by Si_3N_4 cap film and (b) p -MOSFET with compressive strain induced by SiGe S/D heteroepitaxial regrowth. The gate lengths of the n -MOSFET and p -MOSFET are 45 nm and 50 nm, respectively [11, 12].

Indeed, as the channel length reduces, drain-induced electrostatic effects lower the energy barrier between the source and the drain, which degrades the V_T [V_T roll-off, drain-induced barrier lowering (DIBL) and SS] [8]. Various techniques including the use of ultra-thin gate dielectrics, shallow source/drain junctions and high channel doping can be used to reduce short-channel effects and improve devices performance [9]. However, most of these approaches directly conflict with the goal of obtaining high carrier mobility, low SS, low source and drain series resistance (R_{SD}), and therefore large ON-state current (I_{ON}) and low OFF-state current (I_{OFF}) at low supply voltage.

1.1.2 Technology Boosters

So far, to delay the end of Moore’s law, imaginative “technology boosters” have been progressively introduced [7]. Since 2003 (90-nm node), tensile and compressive local strain across the Si channel have been used for the mobility enhancement of holes and electrons, respectively. Tensile strain on the channel of n -MOSFETs is induced by a Si_3N_4 cap film deposited above the gate stack [Figure 1.2(a)], while compressive strain on the channel of p -MOSFETs is implemented by SiGe heteroepitaxial regrowth of the source and drain (S/D) [Figure 1.2(b)] [10]. Unfortunately, the scaling of the transistor dimensions decreases the volume/quantity of the stressor materials for both n and p -MOSFETs, thus decreasing mobility and drive current. As a result, performance was gained in the following technology nodes owing to the integration of even more challenging processes.

From 2003 to 2007 (90-nm and 65-nm nodes), the scaling of the SiO_2 gate dielectric slowed as

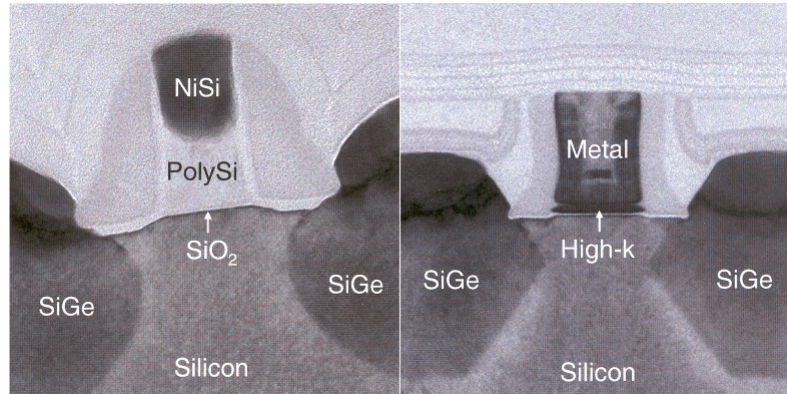


Figure 1.3: TEM images of *p*-MOSFETs of the (a) 65-nm node featuring a SiO₂/poly-Si gate stack and (b) 45-nm node featuring a high-*k*/metal gate stack. The gate lengths of the devices in (a) and (b) are 35 nm [12, 13].

a result of the power limitations arising from an increase in gate leakage. Indeed, as the thickness of the SiO₂ gate dielectric reduced to < 2 nm [Figure 1.3(a)], the gate leakage current due to direct tunneling of electrons through the SiO₂ increased to unacceptable levels [14]. In order to overcome this issue, the “high-*k*/metal gate” stack, [Figure 1.3(b)], was introduced in 2008 (45 nm node) [15]. The high dielectric constant (high-*k*) oxide enabled a gate leakage reduction by a factor > 25 while scaling the equivalent oxide thickness (EOT) by a factor 0.7 [13]. The metal gate also replaced the doped polysilicon gate in order to resolve issues of drive current degradation due to polysilicon depletion [16] and V_T variations due to Fermi level pinning at the high-*k*/polysilicon interface [17].

In 2011 (22-nm node), a non-planar 3-dimension (3-D) device architecture was introduced in order to further reduce short-channel effects (Figure 1.4). In this device architecture, the gate is wrapped around the top and the sidewalls of a Si fin, creating a tri-gate with an improved electrostatic control over the channel [18]. However, the tri-gate device architecture brings further process complexity when compared to the conventional planar device architecture. For instance, obtaining a uniform S/D doping of the fin surfaces using implantation has been found difficult due to the shadowing effect of adjacent fins [19], suggesting that an alternative technique, such as plasma doping may be required to achieve sidewall “conformal” doping [20]. Furthermore, significant challenges remain to maintain a high level of mobility enhancement from stress in fin structures with numerous free surfaces [7]. Maintaining the scaling roadmap will, therefore, require further improvement in channel mobility.

The monolithic integration of high-mobility III-V (and Ge) materials on a Si platform represents a potential long-term option for future sub-22-nm technology nodes [28]. Although III-V

Table 1.2: Performance of state-of-the-art III-V, SOI and bulk Si n -MOSFETs.

Device [Ref.]	Dimensions		Performance			
	length (L) (nm)	W_{fin} (nm)	I_{ON} ($\mu\text{A}/\mu\text{m}$)	I_{OFF} (nA/ μm)	DIBL (mV/V)	SS (mV/dec.)
InAs-OI Planar FET 6 nm Al_2O_3 [21]	55	–	278 $V_{ds} = 0.5$ V $V_g - V_T = 0.5$ V	~ 20 $V_{ds} = 0.5$ V $V_g - V_T = -0.35$ V	84	105
$\text{In}_{0.62}\text{GaAl}_{0.35}\text{As}$ GAA FET 4 nm LaAlO_3 / 0.5 nm Al_2O_3 [22]	80	20	~ 510 $V_{ds} = 0.5$ V $V_g - V_T = 0.5$ V	~ 40 $V_{ds} = 0.5$ V $V_g - V_T = -0.3$ V	23	63 $V_{ds} = 0.5$ V
$\text{In}_{0.53}\text{GaAl}_{0.47}\text{As}$ Planar FET 6.5 nm HfO_2 / 0.5 nm Al_2O_3 [23]	140	–	~ 200 $V_{ds} = 0.5$ V $V_g - V_T = 0.5$ V	~ 20 $V_{ds} = 0.5$ V $V_g - V_T = -0.35$ V	110	100 $V_{ds} = 0.5$ V
$\text{In}_{0.53}\text{GaAl}_{0.47}\text{As}$ GAA FET 7 nm Al_2O_3 / 1 nm InP [24]	140	40	~ 200 $V_{ds} = 0.5$ V $V_g - V_T = 0.5$ V	~ 4 $V_{ds} = 0.5$ V $V_g - V_T = -0.35$ V	20	90 $V_{ds} = 0.5$ V
$\text{In}_{0.53}\text{GaAl}_{0.47}\text{As}$ Tri-gate FET high- k [25]	60	40	~ 500 $V_{ds} = 0.5$ V $V_g - V_T = 0.5$ V	~ 100 $V_{ds} = 0.5$ V $V_g - V_T = -0.2$ V	65	95 $V_{ds} = 0.5$ V
FDSOI Planar FET [26]	24	–	1070 $V_{ds} = 1$ V	16 $V_{ds} = 1$ V	< 100	< 85 $V_{ds} = 0.5$ V
SOI Junctionless FET HfSiON [27]	13	22	455 $V_{ds} = 0.9$ V $V_g - V_T = 0.65$ V	5 $V_{ds} = 0.9$ V $V_g - V_T = -0.25$ V	130	70 $V_{ds} = 0.9$ V
Bulk Si Tri-gate FET (LP) (SP) (HP) [18]	34 34 30	– – –	410 710 1080 $V_{ds} = 0.75$ V	30×10^{-3} 1 100 $V_{ds} = 0.75$ V	30 30 30	64 66 71 $V_{ds} = 0.75$ V

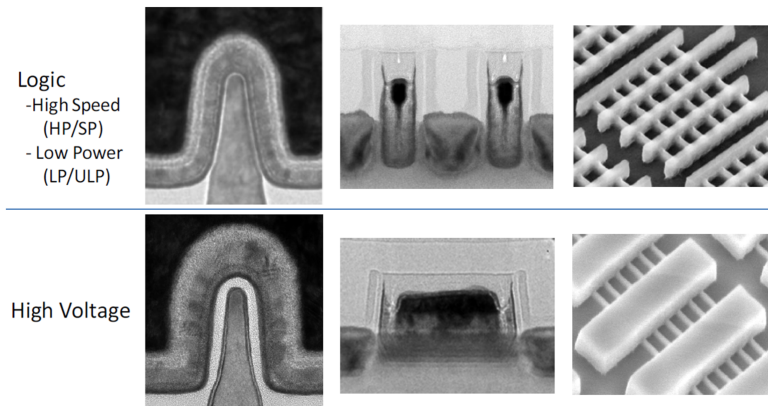


Figure 1.4: TEM of fin, TEM of gate, and tilted SEM of 22-nm node non-planar 3-D transistors featuring thin gate for logic application (top) and thick gate for high-voltage application (bottom) [18].

MOSFETs with a deeply-scaled channel in planar and non-planar 3-D architectures have already been reported to have performance approaching that of state-of-the-art and silicon on insulator (SOI) and bulk Si n -MOSFETs (Table 1.2), many issues still need to be addressed for this option to become viable from an industry standpoint. First, high- k /III-V gate stacks with sufficiently low defect densities will have to be obtained in order to demonstrate III-V MOSFETs with performance significantly exceeding that of the best Si and SOI MOSFETs. In addition, S/D regions with extremely low contact resistance will have to be demonstrated in order to meet the scaling targets of the 12-nm node. Finally, the III-V materials will have to be integrated on large Si platforms in order to enable mass production and large economy of scale.

1.2 Challenges for High- k /III-V MOSFETs

1.2.1 Low Defect Densities in High- k /III-V Gate Stacks

Achieving low defect densities in high- k /III-V gate stacks represents a considerable challenge as, unlike their Si counterpart, III-V semiconductors do not have a high quality native oxide. As a result, a high density of electrically active defects is observed not only at the high- k /III-V interface but also within the high- k dielectric.

The terminology used to define these defects is in line with the standardized terminology developed for the SiO₂/Si system by the Deal committee in 1979 [29] and updated by Fleetwood in 1992 [30]. The high- k /III-V defect terminology is presented using the case of the Al₂O₃/In_{0.53}Ga_{0.53}As system, which is the most widely studied high- k /III-V system.

The Al₂O₃ and In_{0.53}Ga_{0.53}As materials combine interesting electrical properties with good

growth process control, making the $\text{Al}_2\text{O}_3/\text{In}_{0.53}\text{Ga}_{0.53}\text{As}$ system highly attractive for metal-oxide-semiconductor (MOS) studies. Al_2O_3 offers a high bandgap (~ 9 eV), a high breakdown electric field (5 - 30 MV/cm), a reasonably high dielectric constant (8.6 - 10) along with a high thermal stability ($> 1000^\circ\text{C}$) [31], while $\text{In}_{0.53}\text{Ga}_{0.53}\text{As}$ features a high Hall electron mobility of 4000 - 5000 $\text{cm}^2/\text{V}\cdot\text{s}$ [32], a sufficiently large bandgap of 0.74 eV [33] to avoid leakage current due to band-to-band tunneling [34] and a large intervalley separation of 0.5 eV that prevents population of the low mobility L and X valleys [35]. Moreover, from a processing point of view, the deposition of highly uniform Al_2O_3 films by atomic layer deposition (ALD) using trimethylaluminum [$\text{Al}(\text{CH}_3)_3$] (TMA) and H_2O precursors is very well controlled [36] and high quality $\text{In}_{0.53}\text{Ga}_{0.53}\text{As}$ films are routinely grown lattice matched to epi-ready InP substrates by molecular beam epitaxy (MBE) and metal-organic vapor phase epitaxy (MOVPE) [37].

Defects such as interface traps, near-interface oxide traps (referred to here as border traps^{1,2}) and fixed oxide charges are depicted separately in Figure 1.5 (a), (b) and (c), respectively. Interface traps can exchange charges with the $\text{In}_{0.53}\text{Ga}_{0.53}\text{As}$ channel through a thermally activated Shockley-Read-Hall (SRH) process [45] and the trap occupancy is set by the Fermi-Dirac statistics [46]. In the $\text{Al}_2\text{O}_3/\text{In}_{0.53}\text{Ga}_{0.53}\text{As}$ MOS system, the interface traps located at energy levels lying within the bandgap are donors (+/0), while the interface traps located within the conduction band [47] are acceptors (0/-) [Figure 1.5(a)] [38, 39].

Recent studies have also indicated the presence of border traps located within a few nanometers from the $\text{Al}_2\text{O}_3/\text{In}_{0.53}\text{Ga}_{0.53}\text{As}$ interface [41, 42] and at energy levels aligned with the $\text{In}_{0.53}\text{Ga}_{0.53}\text{As}$ conduction band [43] [Figure 1.5(b)]. Border traps are charged and discharged through a temperature-independent tunneling process [43] within timescales depending on their distances from the interface [38, 48].

Fixed oxide charges are oxide traps that do not “communicate” with the underlying channel as their energy position is either too high or too low to be reached by the Fermi level, making them always empty or always full [44] [Figure 1.5(c)]. The sign of their charge then depends on their nature (donor or acceptor) and on their energy position. As a result, a fixed positive charge is an always-empty donor (+/0) oxide trap, while a fixed negative charge is an always-full acceptor (0/-) oxide trap.

The interface traps located within the $\text{In}_{0.53}\text{Ga}_{0.53}\text{As}$ bandgap are responsible for the degradation of the switching performance (high SS). In the case of excessively large density of interface traps (D_{it}), the Fermi level can remain pinned within the $\text{In}_{0.53}\text{Ga}_{0.53}\text{As}$ bandgap, preventing the device from turning off. The interface traps located within the $\text{In}_{0.53}\text{Ga}_{0.53}\text{As}$ conduction band have been reported to pin the Fermi level within the conduction band [47], limiting the

¹The term border trap originates from an analogy with the term border state, which was used in the context of the American Civil War (1861-1865) [30].

²Fleetwood defined border traps as oxide traps located within ~ 3 nm from the interface [30]. In recent MOS gate stack technologies, the oxides are so thin that all oxide traps can be considered to be border traps.

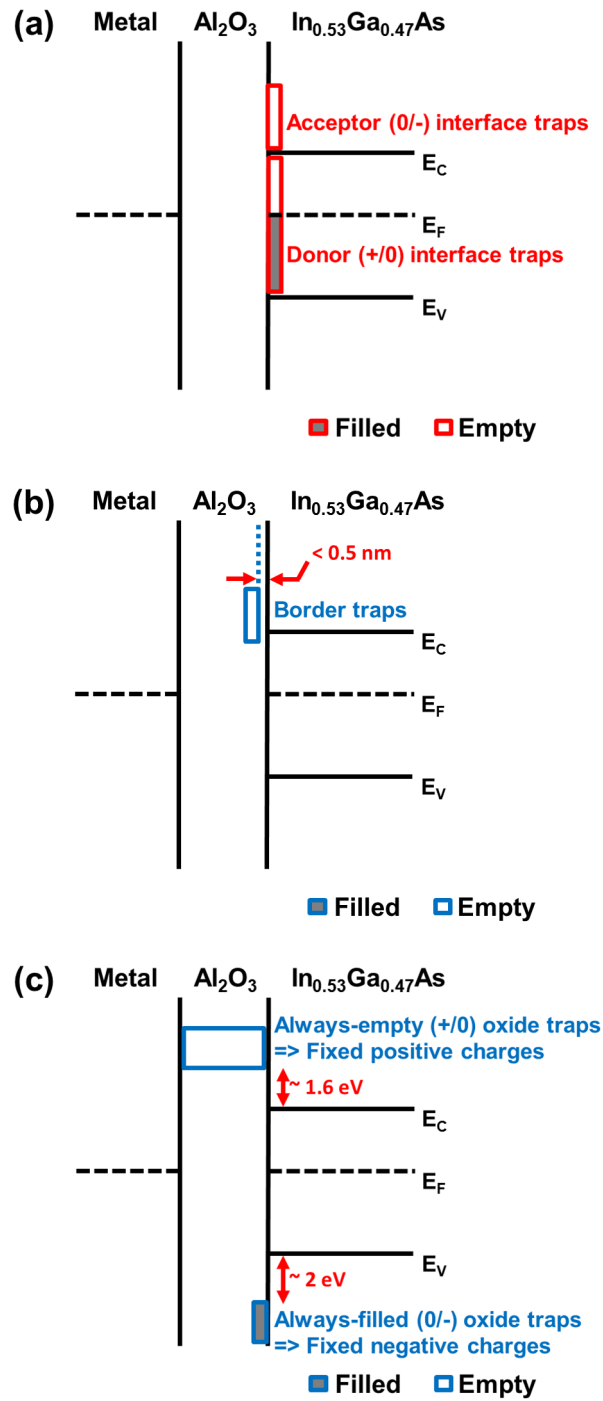


Figure 1.5: (a) Interface traps [38–40], (b) border traps [41–43] and (c) fixed oxide charges [44] in an Al₂O₃/In_{0.53}Ga_{0.47}As MOS device.

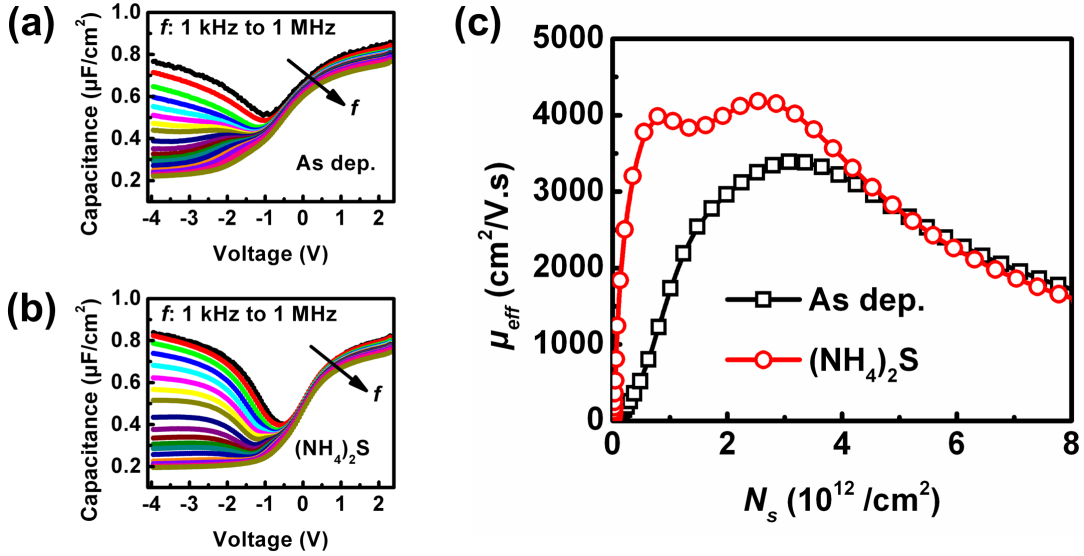


Figure 1.6: Multi-frequency (M-F) capacitance-voltage (C-V) characteristics obtained on $\text{Al}_2\text{O}_3/n\text{-In}_{0.53}\text{Ga}_{0.47}\text{As}$ MOSCAPs without (a) and with (b) the optimized $(\text{NH}_4)_2\text{S}$ surface passivation reported in [49]. The M-F C-V characteristics were measured by Éamon O'Connor. (c) Impact of the same surface passivation on the effective mobility (μ_{eff}) *vs* carrier density (N_s) extracted on flatband-mode MOSFETs [50]. The surface passivation was performed at the Tyndall National Institute and the design, fabrication and characterization of the flatband-mode $\text{Al}_2\text{O}_3/\text{In}_{0.53}\text{Ga}_{0.47}\text{As}$ MOSFETs were performed at the University of Glasgow.

electron mobility and drive current. Since the interface traps located within the $\text{In}_{0.53}\text{Ga}_{0.53}\text{As}$ conduction band are acceptors, they also have the potential to result in mobility degradation due to Coulomb scattering. The border traps are responsible for the hysteresis generally observed in the current-voltage (I-V) and capacitance-voltage (C-V) characteristics of transistors, leading to V_T instabilities. Fixed oxide charges are responsible for the V_T shift and for the mobility degradation due to Coulomb scattering.

Continuous efforts to improve defect passivation and dielectric deposition processes have resulted in significant reductions in the densities of interface traps, border traps and fixed oxide charges present in high- k /III-V gate stacks. The use of metal-oxide-semiconductor capacitors (MOSCAPs) has been particularly relevant to the optimization of high- k /III-V gate stacks. Indeed, when compared to MOSFETs, MOSCAPs offer the process simplicity needed for testing alternative passivation and deposition processes in the absence of the subsequent transistor process steps (i.e.: implantation, anneal, plasma etch), which can also affect the gate stack quality. Once optimized using a MOSCAP, the gate stack process can be integrated in a MOSFET process

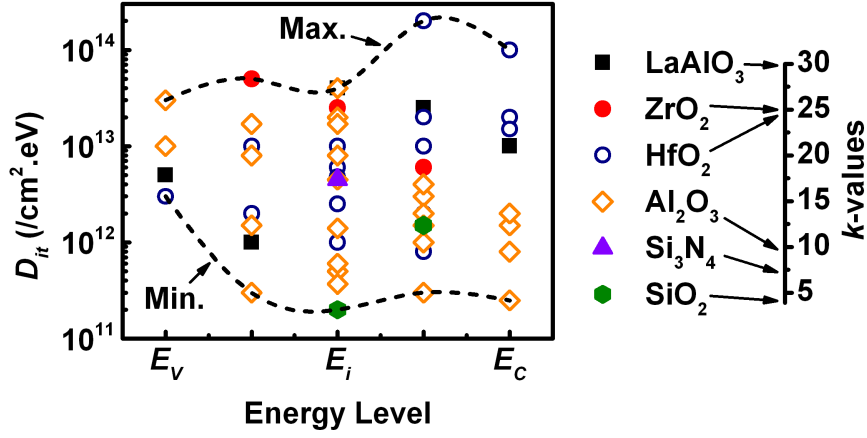


Figure 1.7: D_{it} values reported in the literature since 2008 for $\text{In}_{0.53}\text{Ga}_{0.53}\text{As}$ MOS structures with LaAlO_3 [53], ZrO_2 [54], HfO_2 [55–60], Al_2O_3 [42, 49, 60–69], Si_3N_4 [70] and SiO_2 [71] gate oxides. The k -values of these gate oxides are reported in [14].

flow. As an example, Figure 1.6(a) and (b) show the significant reduction in frequency dispersion near the accumulation region in the multi-frequency (M-F) C-V characteristics of $\text{Al}_2\text{O}_3/n\text{-In}_{0.53}\text{Ga}_{0.53}\text{As}$ MOSCAPs following the optimized $(\text{NH}_4)_2\text{S}$ surface passivation process reported in [49]. The integration of this process in an implant-free flatband-mode $\text{Al}_2\text{O}_3/\text{In}_{0.53}\text{Ga}_{0.53}\text{As}$ MOSFET process flow [51] yielded a significant increase in effective mobility (μ_{eff}) at low carrier density (N_s) [Figure 1.6(c)] [50], consistent with a reduction in Coulomb scattering [52] due to a reduction in D_{it} near the $\text{In}_{0.53}\text{Ga}_{0.53}\text{As}$ conduction band.

The main results reported on the passivation and electrical characterization of interface traps, border traps and fixed oxide charges are discussed in further detail in sub-sections 1.2.1.1, 1.2.1.2 and 1.2.1.3, respectively.

1.2.1.1 Interface Trap Passivation and Characterization

The passivation and characterization of interface traps, located at energy levels lying within the $\text{In}_{0.53}\text{Ga}_{0.53}\text{As}$ bandgap, have been the focus of intense research in recent years. Figure 1.7 compares D_{it} values reported in the literature since 2008 for $\text{In}_{0.53}\text{Ga}_{0.53}\text{As}$ MOSCAPs with LaAlO_3 [53], ZrO_2 [54], HfO_2 [55–60], Al_2O_3 [42, 49, 60–69], Si_3N_4 [70] and SiO_2 [71] gate oxides. The short-dash red lines, representing the minimum and maximum D_{it} values, show a discrepancy of more than 2 orders of magnitude, with reported D_{it} values ranging from low- 10^{11} / $\text{cm}^2.\text{eV}$ to exceeding 10^{14} / $\text{cm}^2.\text{eV}$.

Part of this discrepancy can be attributed to the variability in surface passivation and oxide

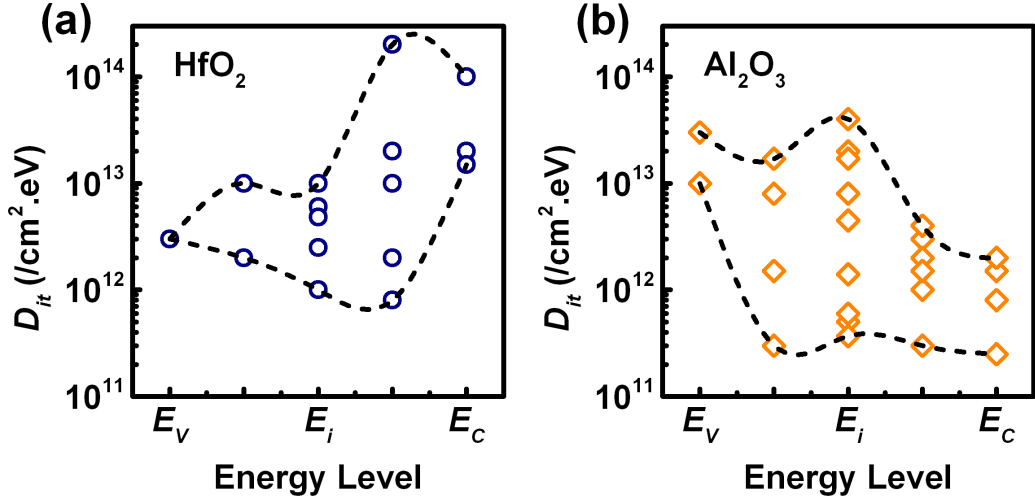


Figure 1.8: Comparison of the D_{it} values reported for (a) $\text{HfO}_2/\text{In}_{0.53}\text{Ga}_{0.53}\text{As}$ MOS structures [55–60] and (b) $\text{Al}_2\text{O}_3/\text{In}_{0.53}\text{Ga}_{0.53}\text{As}$ MOS structures [42, 49, 60–69].

deposition processes. Various passivation methods, including treatment in $(\text{NH}_4)_2\text{S}$ [49], *in-situ* H_2S exposure subsequent to MOVPE [72], *in-situ* hydrogen [73] and nitrogen [59] plasmas prior to ALD, deposition of thin Si [74, 75], and Ge interlayers [76] and forming gas (H_2/N_2) annealing [77, 78] have shown improvements over unpassivated interfaces. Moreover, chemical vapor deposition (CVD) [70], physical vapor deposition (PVD) [71], molecular atomic deposition (MAD) [65] and molecular beam deposition (MBD) [79] have been reported for the deposition of various gate dielectrics on $\text{In}_{0.53}\text{Ga}_{0.53}\text{As}$, but the ALD [36, 80] has now become mainstream, especially since the observation of the ALD “self-cleaning” effect on GaAs [81–83] and on InGaAs [84].

Part of this discrepancy can also be attributed to the high- $k/\text{In}_{0.53}\text{Ga}_{0.47}\text{As}$ interface control dependence on the composition of the gate dielectric. Figure 1.8 suggests that Al_2O_3 can offer significantly better interface properties than HfO_2 , especially in the upper part of the $\text{In}_{0.53}\text{Ga}_{0.47}\text{As}$ bandgap, which is of particular interest for n -channel MOSFETs. A number of groups have taken advantage of the good interface properties of the $\text{Al}_2\text{O}_3/\text{InGaAs}$ system to form bi-layer oxide stacks, where the Al_2O_3 is sandwiched between the InGaAs and an oxide of high- k value such as HfO_2 [59, 60, 85, 86], ZrO_2 [54] and LaAlO_3 [22].

The discrepancy in the reported D_{it} values extracted on high- $k/\text{In}_{0.53}\text{Ga}_{0.53}\text{As}$ MOSCAPs can also arise from the differences in D_{it} extraction methods [87]. This issue is illustrated in Figure 1.9, where a discrepancy of ~ 2 orders of magnitude is observed between reported mid-gap D_{it} values extracted on similar ALD Al_2O_3 films deposited *ex-situ* on sulphur passivated

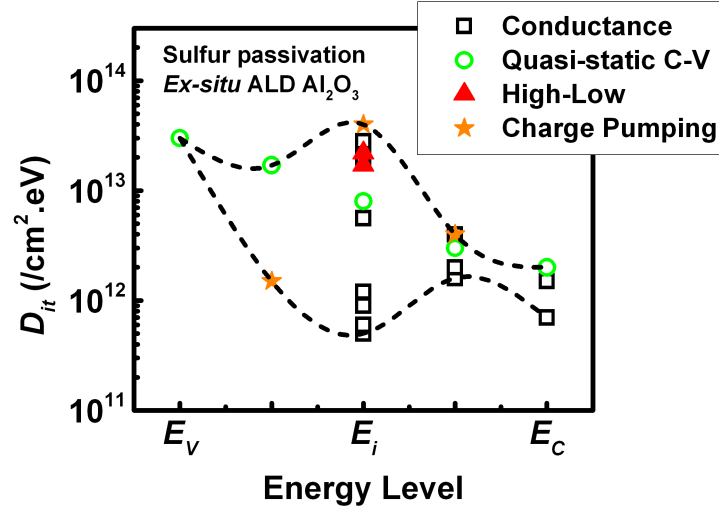


Figure 1.9: D_{it} values extracted on similar *ex-situ* deposited ALD Al₂O₃ films on sulphur passivated In_{0.53}Ga_{0.53}As using the conductance method [49, 57, 61, 63, 64, 66], a method based on the fitting of a measured quasi-static (Q-S) C-V [62], the high-low frequency capacitance method [49] and the charge pumping method [42].

In_{0.53}Ga_{0.53}As surfaces using the conductance method [49, 57, 61, 63, 64, 66], a method based on the fitting of a measured quasi-static (Q-S) C-V [62], the high-low frequency capacitance method [49] and the charge pumping method [42].

The most commonly used methods, such as the conductance method [88], the low-frequency (Berglund) method [89], the high-frequency (Terman) method [90] and the combined high-low frequency capacitance (Castagné-Vapaille) method [91], were initially established to evaluate interface trap densities in the SiO₂/Si system. Unfortunately, these methods require various assumptions/approximations to be made in order to obtain parameters such as the oxide capacitance, the doping concentration or the capture cross sections. While these assumptions/approximations enable correct D_{it} extraction in the SiO₂/Si system, blindly applying them to high- k /InGaAs systems can lead to erroneous D_{it} values [92, 93]. This is mainly due to the fact that InGaAs features a lower conduction band density of state and smaller bandgap than Si and that the D_{it} in high- k /InGaAs systems is significantly higher than that in the SiO₂/Si MOS system. Although some guidelines [92] have been reported to improve on the accuracy of the D_{it} extraction in the high- k /InGaAs MOSCAPs, several issues still remain.

The conductance method, which is the most reliable and widely used D_{it} extraction method [93], is only valid when applied in depletion [88]. This represents a significant limitation for extracting the D_{it} profile across the full InGaAs bandgap, which is generally circumvented through the measurement of both n -type and p -type MOS structures [49] under the assumption that the

Si (*n*-type) and Zn (*p*-type) dopants, and differences in InGaAs growth conditions, have similar or no impact on the quality of the high-*k*/InGaAs interface.

The availability of high-*k*/III-V MOSFETs has enabled the development of alternative D_{it} extraction methods to address the limitation of the conductance method. Martens *et al.* developed a “full conductance” method to extract the D_{it} across the full semiconductor bandgap [93, 94], Ali *et al.* modeled the M-F gate-to-channel split C-V and conductance-voltage (G-V) characteristics to extract the D_{it} near the $\text{In}_{0.53}\text{Ga}_{0.53}\text{As}$ conduction band [53] and complement the conventional conductance method [88]. The charge pumping technique [95] was also used to profile the D_{it} across the InGaAs bandgap [42, 67, 96, 97], and yielded D_{it} profiles in reasonable agreement with those obtained from the other methods. Hall measurements were recently performed on high-*k*/III-V gated Hall bars as part of mobility studies [47, 98]. Contrary to the conventional gate-to-channel split C-V technique, which only enables to extract the total charge density (sum of inversion charge and trapped charge densities), the Hall measurement technique yields the mobile (inversion) charge density. In the work reported by Taoka *et al.* in [47], the total charge density obtained from gate-to-channel split C-V measurements was compared to the mobile charge density extracted from Hall measurements in order to extract the trap density located at energy levels aligned with the conduction band. This study revealed that large trap densities $> 10^{12} / \text{cm}^2 \cdot \text{eV}$ were responsible for the Fermi level pinning inside the InGaAs conduction band, leading to a significant I_{ON} degradation. Although this issue was initially attributed to the presence of interface traps located at energy levels aligned with the InGaAs conduction band [47], it is noted that border traps could also contribute to the pinning of the Fermi level inside the InGaAs conduction band.

1.2.1.2 Border Trap Passivation and Characterization

The presence of border traps located at energy levels aligned with the InGaAs conduction band and their effective passivation using a forming gas (H_2/N_2) anneal (FGA) process was demonstrated in [43] through the analysis of the frequency dispersion in the accumulation region of the M-F C-V characteristics of $\text{Al}_2\text{O}_3/n\text{-In}_{0.53}\text{Ga}_{0.53}\text{As}$ MOSCAPs measured over a range of T before and after FGA. No significant change in frequency dispersion in accumulation was observed when varying T during measurements, suggesting the presence of a tunneling process involving border traps located at energy levels aligned with the $\text{In}_{0.53}\text{Ga}_{0.53}\text{As}$ conduction band. Moreover, a marked reduction in frequency dispersion was observed following FGA, indicating a passivation of border traps with FGA. Admittance models accounting for the spatial distribution of border traps were then developed to explain the frequency dispersion in the accumulation region of the M-F C-V characteristics of $\text{Al}_2\text{O}_3/n\text{-In}_{0.53}\text{Ga}_{0.53}\text{As}$ MOSCAPs [38, 48]. Following these studies, a more direct method based on the charge pumping technique [95] was applied

to $\text{Al}_2\text{O}_3/n\text{-In}_{0.53}\text{Ga}_{0.53}\text{As}$ MOSFETs in order to obtain the spatial distribution of border traps across the Al_2O_3 film thickness [42]. However, as the charge pumping method requires the use of a body contact, which is not always available in III-V MOSFETs, an alternative method based on high-frequency transconductance measurements was proposed by Johansson *et al.* in order to circumvent this problem [41]. This alternative method, demonstrated on planar surface-channel and vertical nanowire III-V MOSFETs, featuring a 6.5-nm-thick HfO_2 gate dielectric on a 0.5-nm-thick Al_2O_3 interface control layer, yielded border trap densities of $\sim 10^{21}$ / $\text{cm}^3\cdot\text{eV}$ near the interface (depth < 0.5 nm) and of $\sim 10^{19}$ / $\text{cm}^3\cdot\text{eV}$ deeper in the oxide (depth > 0.5 nm) [41]. These border trap density values are consistent with the values extracted from C-V [38, 43, 48] and charge pumping [42] measurements.

1.2.1.3 Fixed Oxide Charge Passivation and Characterization

The nature and density of fixed oxide charges can be extracted using a set of MOSCAPs featuring different oxide thickness (t_{ox}) [100]. This method was applied in [99] to characterize the fixed oxide charges present in the $\text{Al}_2\text{O}_3/\text{In}_{0.53}\text{Ga}_{0.53}\text{As}$ system. C-V characteristics, recorded at a frequency (f) of 1 MHz and a T of -50°C to minimize the contribution of interface and border traps to the measured capacitance [Figure 1.10(a)], were used to extract the flat-band voltage (V_{fb}) associated with each t_{ox} . As the presence of positive (negative) fixed charges manifests itself as a negative (positive) shift of the V_{fb} relative to the theoretical flat-band voltage, the negative slope and positive intercept of the linear relationship observed on the V_{fb} vs t_{ox} curve revealed a negative interface fixed charge density (N_{int}) of 10^{13} / cm^2 at the $\text{Al}_2\text{O}_3/n\text{-In}_{0.53}\text{Ga}_{0.53}\text{As}$ interface along with a positive bulk fixed charge density (N_{bulk}) of 2×10^{19} / cm^3 distributed throughout the bulk of the Al_2O_3 film [inset Figure 1.10(a)].

The effect of FGA on the fixed oxide charges present in the $\text{Al}_2\text{O}_3/\text{In}_{0.53}\text{Ga}_{0.53}\text{As}$ system has been studied in [44, 99, 101]. Comparing the pre-FGA [Figure 1.10(a)] and post-FGA [Figure 1.10(b)] C-V characteristics reported in [99], clearly shows that FGA is an efficient technique to passivate fixed charges. Indeed, after FGA, the C-V characteristics are aligned at V_{fb}^{theo} (within the error on the estimation of the metal work function) [Figure 1.10(b)] and the V_{fb} shift with t_{ox} has become negligible [inset Figure 1.10(b)]. A detailed analysis of the V_{fb} vs t_{ox} data following FGA revealed a negative fixed charge density of 7.4×10^{11} / cm^2 at the interface along with a positive fixed charge density of 5×10^{18} / cm^3 distributed throughout the bulk of the Al_2O_3 film, representing a reduction in interface fixed charge density and bulk fixed charge density of 92% and 75%, respectively.

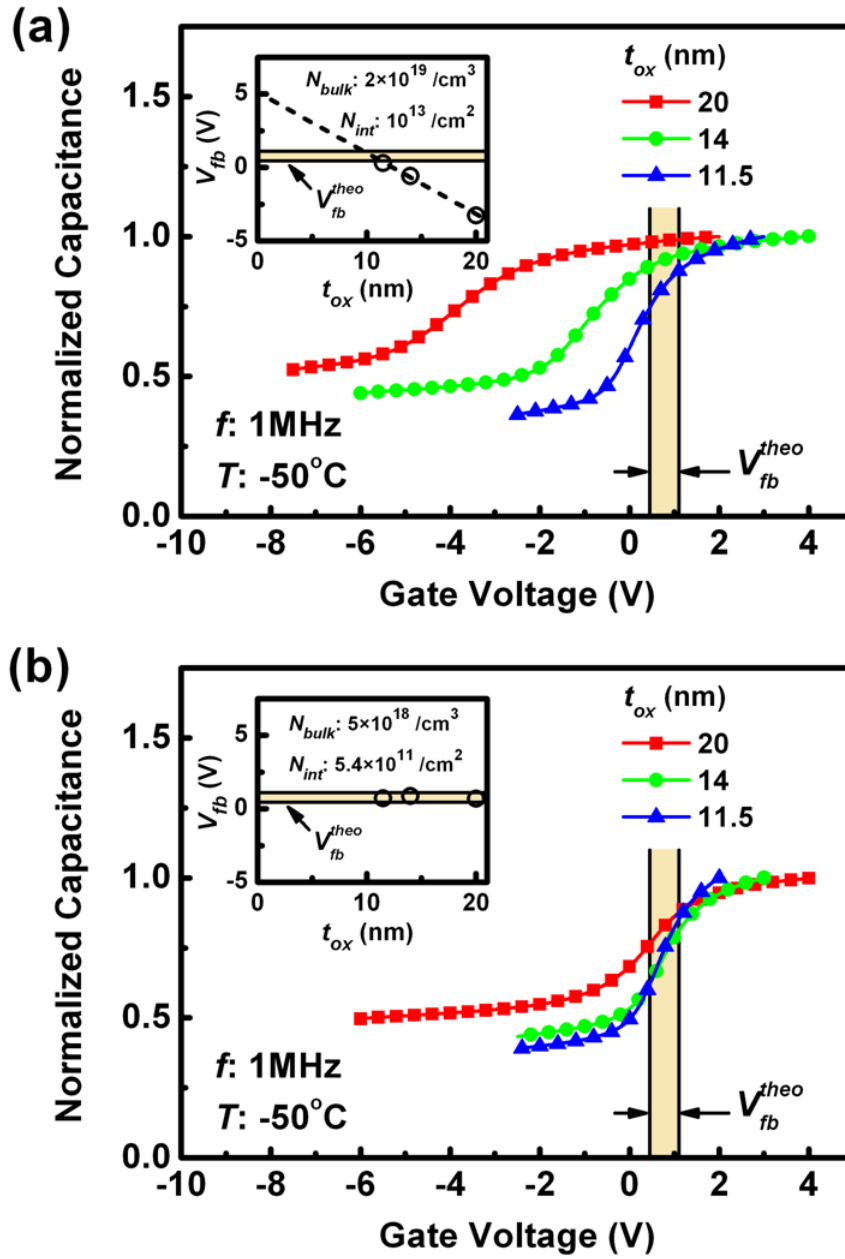


Figure 1.10: Normalized C-V characteristics measured on Al₂O₃/n-In_{0.53}Ga_{0.53}As MOSCAPs at a frequency (f) of 1 MHz and a temperature (T) of -50°C (a) before and (b) after FGA [99]. The oxide thickness (t_{ox}) ranges from 11.5 nm to 20 nm. The insets show the evolution of the flat-band voltage (V_{fb}) as a function of t_{ox} . N_{bulk} and N_{int} represent the bulk and the interface fixed charge densities, respectively. The beige shaded area indicates the uncertainty on the theoretical flat-band voltage (V_{fb}^{theo}).

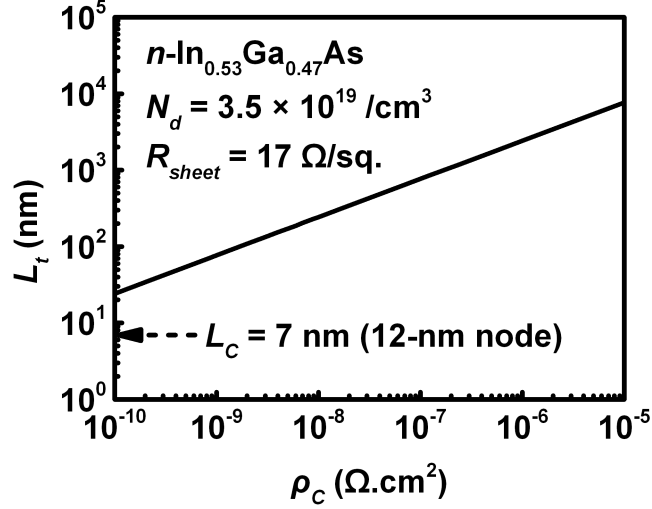


Figure 1.11: Transfer length (L_t) vs specific contact resistivity (ρ_C) curve calculated for $n\text{-In}_{0.53}\text{Ga}_{0.53}\text{As}$ epitaxially doped to $\sim 3.5 \times 10^{19} / \text{cm}^3$ featuring a sheet resistance (R_{sheet}) of $17 \Omega/\square$ [103]. In this configuration, the contact length (L_C) of 7 nm targeted for the 12-nm node is much lower than L_t .

1.2.2 Low Resistance Source and Drain Contacts

Aggressive scaling of the S/D is also urgently needed for potential insertion of III-V MOSFETs into production by 2020 (12-nm node). At this stage and according to the international technology roadmap for semiconductor (ITRS), the MOSFETs should feature a drain current in saturation ($I_{D,sat}$) of $2733 \mu\text{A}/\mu\text{m}$ at a supply voltage (V_{DD}) of 0.68 V with a S/D contact length (L_C) of 7 nm and a R_{SD} of $120 \Omega\cdot\mu\text{m}$ [102].

In order to put these values in the perspective of a future III-V MOSFET, we can assume an $\text{In}_{0.53}\text{Ga}_{0.53}\text{As}$ device meeting the 12-nm node performance/scaling targets [102] and featuring S/D made of an $n\text{-In}_{0.53}\text{Ga}_{0.53}\text{As}$ material epitaxially doped to its saturation limit ($\sim 3.5 \times 10^{19} / \text{cm}^3$). The successful MBE growth of such a material was reported in [103], where the presented transfer length method (TLM) [104] analysis was used to extract an $n\text{-In}_{0.53}\text{Ga}_{0.53}\text{As}$ sheet resistance (R_{sheet}) of $\sim 17 \Omega/\square$. The transfer length (L_t), which is the distance over which most ($1/e$) of the current flows from the semiconductor to the metal (or vice versa), can then be calculated as a function of specific contact resistance (ρ_C) for a given R_{sheet} (Figure 1.11) using:

$$L_t = \rho_C / \sqrt{R_{sheet}} \quad (1.1)$$

In such a device configuration, it is clear that the L_C of 7 nm targeted for the 12-nm node would be much lower than L_t , leading to significant current crowding and an exponential increase in ρ_C

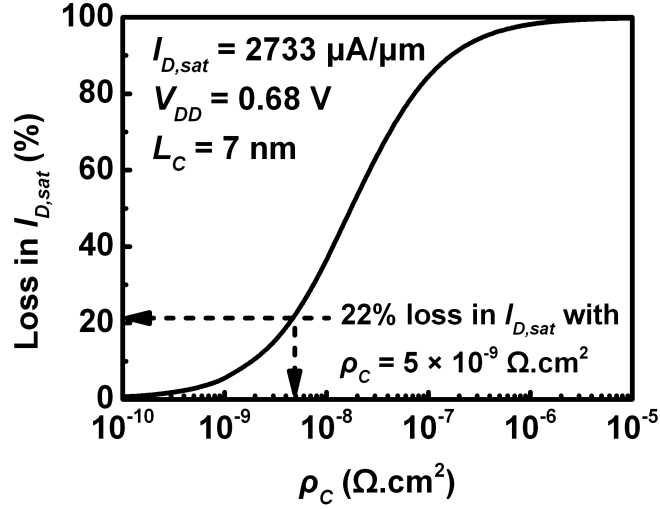


Figure 1.12: Percentage loss in drain current in saturation ($I_{D,sat}$) vs specific contact resistivity (ρ_C) curve calculated for a 12-nm node device using the method reported in [106].

[105]. Assuming a R_{SD} dominated by contact resistances, it is possible to estimate the impact of ρ_C on $I_{D,sat}$ using the method reported in [106]. From Figure 1.12, it is clear that the 12-nm node will require an ultralow ρ_C of $< 5 \times 10^{-9} \Omega\cdot\text{cm}^2$, in close agreement with [105].

In the case of experimental InGaAs MOSFETs used as test vehicles for gate stack engineering and characterization, the S/D areas are generally formed by Si implantation [39, 42, 77, 101, 107–109]. So far, maximum doping concentrations in the range of $\sim 4 \times 10^{18} /\text{cm}^3$ have been achieved using this technique [110]. Such doping levels appear to be insufficient to achieve the $\rho_C < 5 \times 10^{-9} \Omega\cdot\text{cm}^2$ target. Alternatives to implantation are currently under investigation. Values of $\rho_C < 10^{-8} \Omega\cdot\text{cm}^2$ have been successfully obtained on n -InGaAs surfaces epitaxially doped to $\sim 3.5 \times 10^{19} /\text{cm}^3$ and treated with HN_4OH prior to metal contact deposition [103]. To improve on the reproducibility, contacts deposited *in-situ* by MBE on highly doped ($> 10^{19} /\text{cm}^3$) n -InAs and n -InGaAs surfaces were investigated and revealed ultralow ρ_C values in the range of 5.0×10^{-9} to $1.5 \times 10^{-8} \Omega\cdot\text{cm}^2$ [111, 112].

However, since this technique adds significant process complexity, a different approach to form low Schottky barrier height (SBH) contacts using a “nikelide” $\text{Ni-In}_x\text{Ga}_{1-x}\text{As}$ metallic phase is now attracting significant attention [113, 114]. In [115], contacts formed by alloying a thin *ex-situ* deposited Ni film with $\text{In}_x\text{Ga}_{1-x}\text{As}$, were reported to offer a low SBH of 0.13 eV for $\text{Ni-In}_{0.53}\text{Ga}_{0.53}\text{As}/\text{In}_{0.53}\text{Ga}_{0.53}\text{As}$ and almost 0 eV for $\text{Ni-In}_x\text{Ga}_{1-x}\text{As}/\text{In}_x\text{Ga}_{1-x}\text{As}$ ($x > 0.7$). This technique, which also offers the advantage of being fully complementary metal-oxide-semiconductor (CMOS) compatible [116], was adopted by a number of groups for the S/D contact

formation of III-V MOSFETs [21, 116, 117]. Very recently, this technique was applied to undoped InAs to form a Ni-InAs phase, which yielded a record low ρ_C value of $2.7 \times 10^{-9} \Omega \cdot \text{cm}^2$ [118]. This important result not only confirms the trend reported in [115] for SBH reduction with In concentration, but also gives strong evidence that the 12-nm node ITRS target for ρ_C is achievable with InAs.

1.2.3 Integration of III-V Channel Materials on a Si Platform

Finally, the insertion of III-V MOSFETs into production will require the integration of III-V materials on large Si platforms. While various techniques including the use of III-V composite buffers [119, 120], shallow trenches in Si for aspect ratio trapping [121, 122] and wafer bonding [123, 124] have already been demonstrated, further improvements are still required in order to meet industry requirements. While it is clear that addressing this issue is of critical importance to the future of the III-V MOSFET technology, this research topic goes beyond the objectives of this thesis.

1.3 Objectives and Organization of the Thesis

This thesis covers the development and analysis of two $\text{Al}_2\text{O}_3/\text{In}_{0.53}\text{Ga}_{0.53}\text{As}$ MOSFET device architectures. The fabricated devices were used to investigate the fixed oxide charge [107], interface traps [39] and border traps in the $\text{Al}_2\text{O}_3/\text{In}_{0.53}\text{Ga}_{0.53}\text{As}$ gate stack along with the factors which limit carrier mobility in the $\text{In}_{0.53}\text{Ga}_{0.53}\text{As}$ channel [108, 125]. The first $\text{Al}_2\text{O}_3/\text{In}_{0.53}\text{Ga}_{0.53}\text{As}$ MOSFET developed was a conventional inversion-mode device, with a surface channel and Si-implanted S/D regions [126]. The second $\text{Al}_2\text{O}_3/\text{In}_{0.53}\text{Ga}_{0.53}\text{As}$ MOSFET architecture was based on the junctionless device concept, first reported by Prof. J. P. Colinge on SOI in 2010 [127]. The fabricated junctionless $\text{Al}_2\text{O}_3/\text{In}_{0.53}\text{Ga}_{0.53}\text{As}$ MOSFET featured a fully-depleted $\text{In}_{0.53}\text{Ga}_{0.53}\text{As}$ channel isolated by a wide bandgap $\text{In}_{0.52}\text{Al}_{0.48}\text{As}$ buffer [126].

Figure 1.13 shows a logic flow chart of the research work presented in this thesis. The work started with a preliminary study of the Si implant activation in $p\text{-In}_{0.53}\text{Ga}_{0.53}\text{As}$ [78], to form the S/D regions of the inversion-mode MOSFET. Test structures based on the TLM [104] were used in a Doehlert design of experiment [128] to optimize the activation anneal process, while MOSCAPs were used to investigate the impact of the activation anneal process on the MOS gate stack performance [129] (**Chapter 2**). A FGA process was used to improve the performance of the fabricated inversion-mode MOSFETs [107] and extend on the study of fixed oxide charge passivation by FGA reported by Long *et al.* in [99] (**Chapter 3**). The devices were also used as test vehicles for the investigation of electrically active defects present in the $\text{Al}_2\text{O}_3/\text{In}_{0.53}\text{Ga}_{0.53}\text{As}$ gate stack [39, 130]. An alternative technique based on a combination of full-gate capacitance

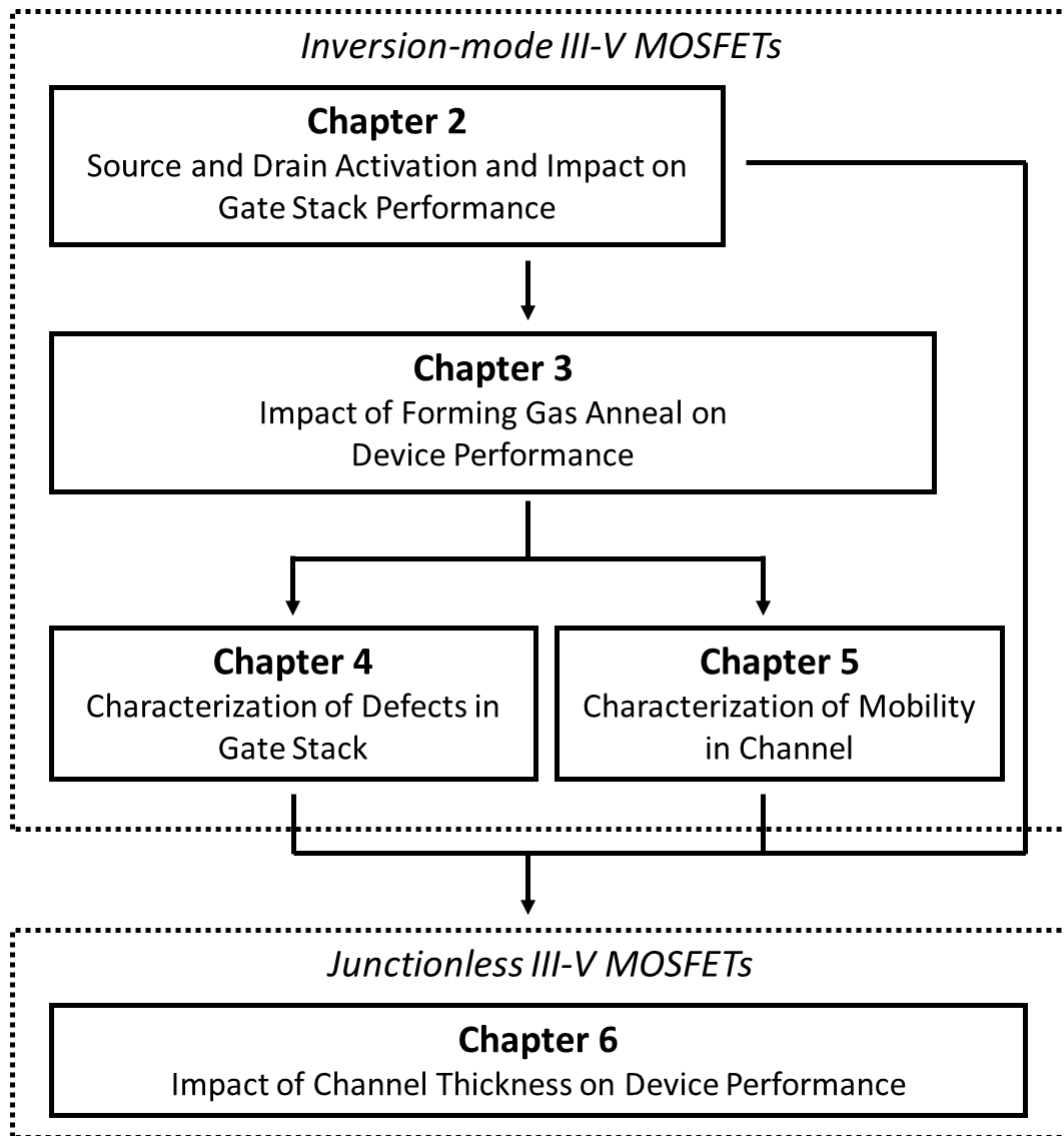


Figure 1.13: Logic flow chart of research work presented in this thesis.

measurements [131] and self-consistent Poisson-Schrödinger calculations [132, 133] was developed for this purpose (**Chapter 4**). The electron mobility in the $\text{In}_{0.53}\text{Ga}_{0.53}\text{As}$ channel was also investigated (**Chapter 5**). The application of the inversion-charge pumping (ICP) method, first proposed by Kerber *et al.* in [95, 134] for the mobility extraction of high- k /SiO₂/Si MOSFETs, was demonstrated on Al₂O₃/In_{0.53}Ga_{0.53}As MOSFETs [125] and further developed for the characterization of border traps. The obtained mobility results were also compared to low-temperature split C-V results. These detailed investigations allowed to identify a major issue arising from the S/D formation of the inversion-mode device architecture. In order to circumvent this issue, an Al₂O₃/In_{0.53}Ga_{0.53}As junctionless MOSFET was developed [126]. The impact of channel thickness on the performance of the fabricated junctionless devices was also studied (**Chapter 6**). In the last chapter (**Chapter 7**), a summary of the main results obtained in this work is presented along with some suggestions for further research.

Bibliography

- [1] G. E. Moore, "Cramming more components onto integrated circuits," *Electronics*, vol. 38, no. 8, p. 114, Apr. 1965. [Online]. Available: <http://dx.doi.org/10.1109/JPROC.1998.658762>
- [2] B. Davari, R. Dennard, and G. Shahidi, "CMOS scaling for high performance and low power-the next ten years," *Proceedings of the IEEE*, vol. 83, no. 4, p. 595, Apr. 1995. [Online]. Available: <http://dx.doi.org/10.1109/5.371968>
- [3] R. Dennard, F. Gaensslen, H.-N. Yu, V. Rideout, E. Bassous, and A. R. Leblanc, "Design Of Ion-implanted MOSFET's with Very Small Physical Dimensions," *IEEE J. Solid-St. Circ.*, vol. 9, no. 5, p. 256, Oct. 1974. [Online]. Available: <http://dx.doi.org/10.1109/JSSC.1974.1050511>
- [4] D. Frank, R. Dennard, E. Nowak, P. Solomon, Y. Taur, and H.-S. P. Wong, "Device scaling limits of Si MOSFETs and their application dependencies," *Proceedings of the IEEE*, vol. 89, no. 3, p. 259, Mar. 2001. [Online]. Available: <http://dx.doi.org/10.1109/5.915374>
- [5] S. Salahuddin and S. Datta, "Can the subthreshold swing in a classical FET be lowered below 60 mV/decade?" in *Electron Devices Meeting, 2008. IEDM 2008. IEEE International*, 2008, p. 1. [Online]. Available: <http://dx.doi.org/10.1109/IEDM.2008.4796789>
- [6] I. Ferain, C. A. Colinge, and J.-P. Colinge, "Multigate transistors as the future of classical metal-oxide-semiconductor field-effect transistors," *Nature*, vol. 479, p. 310, Nov. 2011. [Online]. Available: <http://dx.doi.org/10.1038/nature10676>
- [7] K. Kuhn, "Moore's law past 32 nm: Future challenges in device scaling," in *Structures, Structural Dynamics, and Materials Conference (SSDM)*, Oct. 2009. [Online]. Available: <http://dx.doi.org/10.1109/IWCE.2009.5091124>
- [8] M. Lundstrom, "Moore's Law Forever?" *Science*, vol. 299, no. 5604, p. 210, Jan. 2003. [Online]. Available: <http://dx.doi.org/10.1126/science.1079567>
- [9] K. C. Saraswat, D. Kim, T. Krishnamohan, and A. Peth, "Performance Limitations of Si Bulk CMOS and Alternatives for future ULSI," *ECS Transactions*, vol. 8, no. 1, p. 9, 2007. [Online]. Available: <http://dx.doi.org/10.1149/1.2767279>
- [10] C. H. Jan, P. Bai, J. Choi, G. Curello, S. Jacobs, J. Jeong, K. Johnson, D. Jones, S. Klopčič, J. Lin, N. Lindert, A. Lio, S. Natarajan, J. Neiryneck, P. Packan, J. Park, I. Post, M. Patel, S. Ramey, P. Reese, L. Rockford, A. Roskowski, G. Sacks, B. Turkot, Y. Wang, L. Wei, J. Yip, I. Young, K. Zhang, Y. Zhang, M. Bohr, and B. Holt, "A 65nm

- ultra low power logic platform technology using uni-axial strained silicon transistors,” in *Electron Devices Meeting, 2005. IEDM Technical Digest. IEEE International*, 2005, p. 60. [Online]. Available: <http://dx.doi.org/10.1109/IEDM.2005.1609266>
- [11] T. Ghani, M. Armstrong, C. Auth, M. Bost, P. Charvat, G. Glass, T. Hoffmann, K. Johnson, C. Kenyon, J. Klaus, B. McIntyre, K. Mistry, A. Murthy, J. Sandford, M. Silberstein, S. Sivakumar, P. Smith, K. Zawadzki, S. Thompson, and M. Bohr, “A 90nm high volume manufacturing logic technology featuring novel 45nm gate length strained silicon CMOS transistors,” in *Electron Devices Meeting, 2003. IEDM '03 Technical Digest. IEEE International*, 2003, pp. 11.6.1–11.6.3. [Online]. Available: <http://dx.doi.org/10.1109/IEDM.2003.1269442>
- [12] T. Ghani, in *Nikkei Presentation*, 2009. [Online]. Available: <http://www.intel.com>
- [13] C. Auth, A. Cappellani, J. S. Chun, A. Dalis, A. Davis, T. Ghani, G. Glass, T. Glassman, M. Harper, M. Hattendorf, P. Hentges, S. Jaloviar, S. Joshi, J. Klaus, K. Kuhn, D. Lavric, M. Lu, H. Mariappan, K. Mistry, B. Norris, N. Rahhal-orabi, P. Ranade, J. Sandford, L. Shifren, V. Souw, K. Tone, F. Tambwe, A. Thompson, D. Towner, T. Troeger, P. Vandervoorn, C. Wallace, J. Wiedemer, and C. Wiegand, “45nm High-k + metal gate strain-enhanced transistors,” in *VLSI Technology, 2008 Symposium on*, 2008, p. 128. [Online]. Available: <http://dx.doi.org/10.1109/VLSIT.2008.4588589>
- [14] J. Robertson, “High dielectric constant oxides,” *The European Physical Journal Applied Physics*, vol. 28, p. 265, Dec. 2004. [Online]. Available: <http://dx.doi.org/10.1051/epjap:2004206>
- [15] M. Bohr, R. Chau, T. Ghani, and K. Mistry, “The High-k Solution,” *Spectrum, IEEE*, vol. 44, no. 10, pp. 29–35, Oct. 2007. [Online]. Available: <http://dx.doi.org/10.1109/MSPEC.2007.4337663>
- [16] B. Yu, D.-H. Ju, W.-C. Lee, N. Kepler, T.-J. King, and C. Hu, “Gate engineering for deep-submicron CMOS transistors,” *Electron Devices, IEEE Transactions on*, vol. 45, no. 6, p. 1253, Jun. 1998. [Online]. Available: <http://dx.doi.org/10.1109/16.678529>
- [17] R. Chau, S. Datta, M. Doczy, B. Doyle, J. Kavalieros, and M. Metz, “High-K/metal-gate stack and its MOSFET characteristics,” *Electron Device Letters, IEEE*, vol. 25, no. 6, p. 408, Jun. 2004. [Online]. Available: <http://dx.doi.org/10.1109/LED.2004.828570>
- [18] K. Kuhn, U. Avci, A. Cappellani, M. Giles, M. Haverty, S. Kim, R. Kotlyar, S. Manipatruni, D. Nikonov, C. Pawashe, M. Radosavljevic, R. Rios, S. Shankar, R. Vedula, R. Chau, and I. Young, “The ultimate CMOS device and beyond,” in *Electron*

- Devices Meeting (IEDM), 2012 IEEE International*, 2012, p. 8.1.1. [Online]. Available: <http://dx.doi.org/10.1109/IEDM.2012.6479001>
- [19] L. A. Larson, J. M. Williams, and M. I. Current, "Ion Implantation for Semiconductor Doping and Materials Modification," *Reviews of Accelerator Science and Technology*, vol. 4, no. 1, p. 11, 2011. [Online]. Available: <http://dx.doi.org/10.1142/S1793626811000616>
- [20] Y. Sasaki, K. Okashita, K. Nakamoto, T. Kitaoka, B. Mizuno, and M. Ogura, "Conformal doping for FinFETs and precise controllable shallow doping for planar FET manufacturing by a novel B₂H₆/Helium Self-Regulatory Plasma Doping process," in *Electron Devices Meeting, 2008. IEDM 2008. IEEE International*, 2008, p. 1. [Online]. Available: <http://dx.doi.org/10.1109/IEDM.2008.4796850>
- [21] S. H. Kim, M. Yokoyama, N. Taoka, R. Nakane, T. Yasuda, O. Ichikawa, N. Fukuhara, M. Hata, M. Takenaka, and S. Takagi, "Sub-60 nm deeply-scaled channel length extremely-thin body In_xGa_{1-x}As-on-insulator MOSFETs on Si with Ni-InGaAs metal S/D and MOS interface buffer engineering," in *VLSI Technology (VLSIT), 2012 Symposium on*, 2012, p. 177. [Online]. Available: <http://dx.doi.org/10.1109/VLSIT.2012.6242519>
- [22] J. Gu, X. Wang, H. Wu, J. Shao, A. Neal, M. Manfra, R. Gordon, and P. Ye, "20-80nm Channel Length InGaAs Gate-all-around Nanowire MOSFETs with EOT=1.2nm and Lowest SS=63mV/dec," in *Electron Devices Meeting (IEDM), 2012 IEEE International*, 2012, p. 27.6.1. [Online]. Available: <http://dx.doi.org/10.1109/IEDM.2012.6479117>
- [23] M. Egard, L. Ohlsson, B. M. Borg, F. Lenrick, R. Wallenberg, L.-E. Wernersson, and E. Lind, "High transconductance self-aligned gate-last surface channel In_{0.53}Ga_{0.47}As MOSFET," in *Electron Devices Meeting (IEDM), 2011 IEEE International*, 2011, p. 13.2.1. [Online]. Available: <http://dx.doi.org/10.1109/IEDM.2011.6131544>
- [24] F. Xue, A. Jiang, Y.-T. Chen, Y. Wang, F. Zhou, Y.-F. Chang, and J. Lee, "Excellent device performance of 3D In_{0.53}Ga_{0.47}As gate-wrap-around field-effect-transistors with high-*k* gate dielectrics," in *Electron Devices Meeting (IEDM), 2012 IEEE International*, 2012, p. 27.5.1. [Online]. Available: <http://dx.doi.org/10.1109/IEDM.2012.6479116>
- [25] M. Radosavljevic, G. Dewey, D. Basu, J. Boardman, B. Chu-Kung, J. Fastenau, S. Kabehie, J. Kavalieros, V. Le, W. K. Liu, D. Lubyshev, M. Metz, K. Millard, N. Mukherjee, L. Pan, R. Pillarisetty, W. Rachmady, U. Shah, H. W. Then, and R. Chau, "Electrostatics improvement in 3-D tri-gate over ultra-thin body planar InGaAs quantum well field effect transistors with high-*K* gate dielectric and scaled gate-to-drain/gate-to-source separation," in *Electron Devices Meeting (IEDM), 2011 IEEE International*, 2011, p. 33.1.1. [Online]. Available: <http://dx.doi.org/10.1109/IEDM.2011.6131661>

-
- [26] N. Planes, O. Weber, V. Barral, S. Haendler, D. Noblet, D. Croain, M. Bocat, P. Sassoulas, X. Federspiel, A. Cros, A. Bajolet, E. Richard, B. Dumont, P. Perreau, D. Petit, D. Golanski, C. Fenouillet-Beranger, N. Guillot, M. Rafik, V. Huard, S. Puget, X. Montagner, M. A. Jaud, O. Rozeau, O. Saxod, F. Wacquant, F. Monsieur, D. Barge, L. Pinzelli, M. Mellier, F. Boeuf, F. Arnaud, and M. Haond, "28nm FDSOI technology platform for high-speed low-voltage digital applications," in *VLSI Technology (VLSIT), 2012 Symposium on*, 2012, p. 133. [Online]. Available: <http://dx.doi.org/10.1109/VLSIT.2012.6242497>
- [27] S. Barraud, M. Berthome, R. Coquand, M. Casse, T. Ernst, M. P. Samson, P. Perreau, K. Bourdelle, O. Faynot, and T. Poiroux, "Scaling of Trigate Junctionless Nanowire MOSFET With Gate Length Down to 13 nm," *Electron Device Letters, IEEE*, vol. 33, no. 9, p. 1225, Sep. 2012. [Online]. Available: <http://dx.doi.org/10.1109/LED.2012.2203091>
- [28] J. A. del Alamo, "Nanometre-scale electronics with III-V compound semiconductors," *Nature*, vol. 479, p. 317, Nov. 2011. [Online]. Available: <http://dx.doi.org/10.1038/nature10677>
- [29] B. E. Deal, "Standardized terminology for oxide charges associated with thermally oxidized silicon," *Electron Devices, IEEE Transactions on*, vol. 27, no. 3, p. 606, Mar. 1980. [Online]. Available: <http://dx.doi.org/10.1109/T-ED.1980.19908>
- [30] D. Fleetwood, "'Border traps' in MOS devices," *Nuclear Science, IEEE Transactions on*, vol. 39, no. 2, p. 269, Apr. 1992. [Online]. Available: <http://dx.doi.org/10.1109/23.277495>
- [31] Y. Q. Wu, H. C. Lin, P. D. Ye, and G. D. Wilk, "Current transport and maximum dielectric strength of atomic-layer-deposited ultrathin Al₂O₃ on GaAs," *Applied Physics Letters*, vol. 90, no. 7, p. 072105, Feb. 2007. [Online]. Available: <http://dx.doi.org/10.1063/1.2535528>
- [32] R. J. Young, L. O. Mereni, N. Petkov, G. R. Knight, V. Dimastrodonato, P. K. Hurley, G. Hughes, and E. Pelucchi, "Low-angle misorientation dependence of the optical properties of InGaAs/AlInAs quantum wells," *J. Cryst. Growth*, vol. 312, no. 9, p. 1546, Apr. 2010. [Online]. Available: <http://dx.doi.org/10.1016/j.jcrysgro.2010.01.033>
- [33] [Online]. Available: <http://www.ioffe.rssi.ru/SVA/NSM/Semicond/GaInAs>
- [34] N. L. E. S. Harmon, J. Hyland, D. B. Salzman, T. P. Ma, Y. Xuan, and P. D. Ye, "Properties of InAs metal-oxide-semiconductor structures with atomic-layer-deposited Al₂O₃ dielectric," *Applied Physics Letters*, vol. 92, no. 14, p. 143507, Apr. 2008. [Online]. Available: <http://dx.doi.org/10.1063/1.2908926>

- [35] K. Saraswat, C. O. Chui, D. Kim, T. Krishnamohan, and A. Pethe, “High Mobility Materials and Novel Device Structures for High Performance Nanoscale MOSFETs,” in *Electron Devices Meeting, 2006. IEDM '06. International*, 2006, pp. 1–4. [Online]. Available: <http://dx.doi.org/10.1109/IEDM.2006.346871>
- [36] S. M. George, “Atomic layer deposition: An overview,” *Chemical reviews*, vol. 110, no. 1, p. 111, Jan. 2010. [Online]. Available: <http://dx.doi.org/10.1021/cr900056b>
- [37] A. Overs, G. Jacob, M. P. Besland, V. Drouot, M. Gendry, G. Hollinger, M. Gauneau, D. Lecrosnier, and J. L. Benchimol, “Evaluation of InP Epi-ready wafers for epitaxial growth,” in *Indium Phosphide and Related Materials, 1993. Conference Proceedings., Fifth International Conference on*, Apr. 1993, p. 267. [Online]. Available: <http://dx.doi.org/10.1109/ICIPRM.1993.380659>
- [38] G. Brammertz, A. Alian, D.-C. Lin, M. Meuris, M. Caymax, and W. E. Wang, “A Combined Interface and Border Trap Model for High-Mobility Substrate Metal-Oxide-Semiconductor Devices Applied to In_{0.53}Ga_{0.47}As and InP Capacitors,” *Electron Devices, IEEE Transactions on*, vol. 58, no. 11, p. 3890, Nov. 2011. [Online]. Available: <http://dx.doi.org/10.1109/TED.2011.2165725>
- [39] V. Djara, T. P. O’Regan, K. Cherkaoui, M. Schmidt, S. Monaghan, É. O’Connor, I. M. Povey, D. O’Connell, M. E. Pemble, and P. K. Hurley, “Electrically active interface defects in the In_{0.53}Ga_{0.47}As MOS system,” *Microelectronic Engineering*, vol. 109, no. 0, p. 182, Sep. 2013. [Online]. Available: <http://dx.doi.org/10.1016/j.mee.2013.03.026>
- [40] P. K. Hurley, R. Long, T. O’Regan, E. O’Connor, S. Monaghan, V. Djara, M. A. Negara, A. O’Mahony, I. Povey, A. Blake, R. Nagle, D. O’Connell, M. Pemble, and K. Cherkaoui, “Equivalent Oxide Thickness Correction in the High-k/In_{0.53}Ga_{0.47}As/InP System,” *ECS Transactions*, vol. 33, no. 3, p. 433, Oct. 2010. [Online]. Available: <http://dx.doi.org/10.1149/1.3481632>
- [41] S. Johansson, M. Berg, K.-M. Persson, and E. Lind, “A High-Frequency Transconductance Method for Characterization of High-*K* Border Traps in III-V MOSFETs,” *Electron Devices, IEEE Transactions on*, vol. 60, no. 2, p. 776, Feb. 2013. [Online]. Available: <http://dx.doi.org/10.1109/TED.2012.2231867>
- [42] M. E. Ramón, T. Akyol, D. Shahrjerdi, C. D. Young, J. Cheng, L. F. Register, and S. K. Banerjee, “Fast and slow transient charging in various III-V field-effect transistors with atomic-layer-deposited-Al₂O₃ gate dielectric,” *Applied Physics Letters*, vol. 102, no. 2, p. 022104, Jan. 2013. [Online]. Available: <http://dx.doi.org/10.1063/1.4776678>

-
- [43] E. J. Kim, L. Wang, P. M. Asbeck, K. C. Saraswat, and P. C. McIntyre, "Border traps in $\text{Al}_2\text{O}_3/\text{In}_{0.53}\text{Ga}_{0.47}\text{As}$ (100) gate stacks and their passivation by hydrogen anneals," *Applied Physics Letters*, vol. 96, no. 1, p. 012906, Jan. 2010. [Online]. Available: <http://dx.doi.org/10.1063/1.3281027>
- [44] B. Shin, J. R. Weber, R. D. Long, P. K. Hurley, C. G. V. de Walle, and P. C. McIntyre, "Origin and passivation of fixed charge in atomic layer deposited aluminum oxide gate insulators on chemically treated InGaAs substrates," *Applied Physics Letters*, vol. 96, no. 15, p. 152908, Apr. 2010. [Online]. Available: <http://dx.doi.org/10.1063/1.3399776>
- [45] W. Shockley and W. T. Read, "Statistics of the Recombinations of Holes and Electrons," *Phys. Rev.*, vol. 87, p. 835, Sep. 1952. [Online]. Available: <http://dx.doi.org/10.1103/PhysRev.87.835>
- [46] G. Brammertz, K. Martens, S. Sioncke, A. Delabie, M. Caymax, M. Meuris, and M. Heyns, "Characteristic trapping lifetime and capacitance-voltage measurements of GaAs metal-oxide-semiconductor structures," *Applied Physics Letters*, vol. 91, no. 13, p. 133510, Sep. 2007. [Online]. Available: <http://dx.doi.org/10.1063/1.2790787>
- [47] N. Taoka, M. Yokoyama, S. Kim, R. Suzuki, R. Iida, S. Lee, T. Hoshii, W. Jevasuwan, T. Maeda, T. Yasuda, O. Ichikawa, N. Fukuhara, M. Hata, M. Takenaka, and S. Takagi, "Impact of Fermi level pinning inside conduction band on electron mobility of $\text{In}_x\text{Ga}_{1-x}\text{As}$ MOSFETs and mobility enhancement by pinning modulation," in *Electron Devices Meeting (IEDM), 2011 IEEE International*, 2011, p. 27.2.1. [Online]. Available: <http://dx.doi.org/10.1109/IEDM.2011.6131622>
- [48] Y. Yuan, L. Wang, B. Yu, B. Shin, J. Ahn, P. C. McIntyre, P. Asbeck, M. J. W. Rodwell, and Y. Taur, "A Distributed Model for Border Traps in $\text{Al}_2\text{O}_3\text{-InGaAs}$ MOS Devices," *Electron Device Letters, IEEE*, vol. 32, no. 4, p. 485, Apr. 2011. [Online]. Available: <http://dx.doi.org/10.1109/LED.2011.2105241>
- [49] É. O'Connor, B. Brennan, V. Djara, K. Cherkaoui, S. Monaghan, S. B. Newcomb, R. Contreras, M. Milojevic, G. Hughes, M. E. Pemble, R. M. Wallace, and P. K. Hurley, "A systematic study of $(\text{NH}_4)_2\text{S}$ passivation (22%, 10%, 5%, or 1%) on the interface properties of the $\text{Al}_2\text{O}_3/\text{In}_{0.53}\text{Ga}_{0.47}\text{As}/\text{InP}$ system for n -type and p -type $\text{In}_{0.53}\text{Ga}_{0.47}\text{As}$ epitaxial layers," *Journal of Applied Physics*, vol. 109, no. 2, p. 024101, Jan. 2011. [Online]. Available: <http://dx.doi.org/10.1063/1.3533959>
- [50] I. G. Thayne, "III-V MOSFETs: Some observations associated with scaling towards technologically relevant critical dimensions," in *IEEE Semiconductor Interface Specialists Conference (SISC), Arlington, VA*, Dec. 2011.

- [51] S. Bentley, M. Holland, X. Li, G. Paterson, H. Zhou, O. Ignatova, D. Macintyre, S. Thoms, A. Asenov, B. Shin, J. Ahn, P. C. McIntyre, and I. Thayne, "Electron Mobility in Surface- and Buried-Channel Flatband MOSFETs With ALD Gate Dielectric," *Electron Device Letters, IEEE*, vol. 32, no. 4, p. 494, Apr. 2011. [Online]. Available: <http://dx.doi.org/10.1109/LED.2011.2107876>
- [52] S. Takagi, A. Toriumi, M. Iwase, and H. Tango, "On the universality of inversion layer mobility in Si MOSFET's: Part I-effects of substrate impurity concentration," *Electron Devices, IEEE Transactions on*, vol. 41, no. 12, p. 2357, Dec. 1994. [Online]. Available: <http://dx.doi.org/10.1109/16.337449>
- [53] A. Ali, H. Madan, S. Kovesnikov, S. Oktyabrsky, R. Kambhampati, T. Heeg, D. Schlom, and S. Datta, "Small-Signal Response of Inversion Layers in High-Mobility $\text{In}_{0.53}\text{Ga}_{0.47}\text{As}$ MOSFETs Made With Thin High- K Dielectrics," *Electron Devices, IEEE Transactions on*, vol. 57, no. 4, p. 742, Apr. 2010. [Online]. Available: <http://dx.doi.org/10.1109/TED.2010.2041855>
- [54] J. Huang, N. Goel, H. Zhao, C. Y. Kang, K. Min, G. Bersuker, S. Oktyabrsky, C. K. Gaspe, M. Santos, P. Majhi, P. Kirsch, H.-H. Tseng, J. Lee, and R. Jammy, "InGaAs MOSFET performance and reliability improvement by simultaneous reduction of oxide and interface charge in ALD $(\text{La})\text{AlO}_x/\text{ZrO}_2$ gate stack," in *Electron Devices Meeting (IEDM), 2009 IEEE International*, 2009, pp. 1–4. [Online]. Available: <http://dx.doi.org/10.1109/IEDM.2009.5424357>
- [55] Y. Hwang, R. Engel-Herbert, and S. Stemmer, "Influence of trimethylaluminum on the growth and properties of $\text{HfO}_2/\text{In}_{0.53}\text{Ga}_{0.47}\text{As}$ interfaces," *Applied Physics Letters*, vol. 98, no. 5, p. 052911, Feb. 2011. [Online]. Available: <http://dx.doi.org/10.1063/1.3553275>
- [56] Y. Hwang, R. Engel-Herbert, N. G. Rudawski, and S. Stemmer, "Effect of postdeposition anneals on the Fermi level response of $\text{HfO}_2/\text{In}_{0.53}\text{Ga}_{0.47}\text{As}$ gate stacks," *Journal of Applied Physics*, vol. 108, no. 3, p. 034111, Aug. 2010. [Online]. Available: <http://dx.doi.org/10.1063/1.3465524>
- [57] H. Zhao, J. Huang, Y.-T. Chen, J. H. Yum, Y. Wang, F. Zhou, F. Xue, and J. C. Lee, "Effects of gate-first and gate-last process on interface quality of $\text{In}_{0.53}\text{Ga}_{0.47}\text{As}$ metal-oxide-semiconductor capacitors using atomic-layer-deposited Al_2O_3 and HfO_2 oxides," *Applied Physics Letters*, vol. 95, no. 25, p. 253501, Dec. 2009. [Online]. Available: <http://dx.doi.org/10.1063/1.3275001>
- [58] Y. C. Chang, M. L. Huang, K. Y. Lee, Y. J. Lee, T. D. Lin, M. Hong, J. Kwo, T. S. Lay, C. C. Liao, and K. Y. Cheng, "Atomic-layer-deposited HfO_2 on $\text{In}_{0.53}\text{Ga}_{0.47}\text{As}$:

- Passivation and energy-band parameters,” *Applied Physics Letters*, vol. 92, no. 7, p. 072901, Feb. 2008. [Online]. Available: <http://dx.doi.org/10.1063/1.2883967>
- [59] V. Chobpattana, J. Son, J. J. M. Law, R. Engel-Herbert, C.-Y. Huang, and S. Stemmer, “Nitrogen-passivated dielectric/InGaAs interfaces with sub-nm equivalent oxide thickness and low interface trap densities,” *Applied Physics Letters*, vol. 102, no. 2, p. 022907, Jan. 2013. [Online]. Available: <http://dx.doi.org/10.1063/1.4776656>
- [60] R. Suzuki, N. Taoka, M. Yokoyama, S. Lee, S. H. Kim, T. Hoshii, T. Yasuda, W. Jevasuwan, T. Maeda, O. Ichikawa, N. Fukuhara, M. Hata, M. Takenaka, and S. Takagi, “1-nm-capacitance-equivalent-thickness HfO₂/Al₂O₃/InGaAs metal-oxide-semiconductor structure with low interface trap density and low gate leakage current density,” *Applied Physics Letters*, vol. 100, no. 13, p. 132906, Mar. 2012. [Online]. Available: <http://dx.doi.org/10.1063/1.3698095>
- [61] H.-C. Lin, W.-E. Wang, G. Brammertz, M. Meuris, and M. Heyns, “Electrical study of sulfur passivated In_{0.53}Ga_{0.47}As MOS capacitor and transistor with ALD Al₂O₃ as gate insulator,” *Microelectronic Engineering*, vol. 86, no. 7-9, p. 1554, Jul.-Sep. 2009. [Online]. Available: <http://dx.doi.org/10.1016/j.mee.2009.03.112>
- [62] G. Brammertz, H.-C. Lin, M. Caymax, M. Meuris, M. Heyns, and M. Passlack, “On the interface state density at In_{0.53}Ga_{0.47}As/oxide interfaces,” *Applied Physics Letters*, vol. 95, no. 20, p. 202109, Nov. 2009. [Online]. Available: <http://dx.doi.org/10.1063/1.3267104>
- [63] H. D. Trinh, E. Y. Chang, P. W. Wu, Y. Y. Wong, C. T. Chang, Y. F. Hsieh, C. C. Yu, H. Q. Nguyen, Y. C. Lin, K. L. Lin, and M. K. Hudait, “The influences of surface treatment and gas annealing conditions on the inversion behaviors of the atomic-layer-deposition Al₂O₃/n-In_{0.53}Ga_{0.47}As metal-oxide-semiconductor capacitor,” *Applied Physics Letters*, vol. 97, no. 4, p. 042903, Jul. 2010. [Online]. Available: <http://dx.doi.org/10.1063/1.3467813>
- [64] É. O’Connor, S. Monaghan, K. Cherkaoui, I. M. Povey, and P. K. Hurley, “Analysis of the minority carrier response of n-type and p-type Au/Ni/Al₂O₃/In_{0.53}Ga_{0.47}As/InP capacitors following an optimized (NH₄)₂S treatment,” *Applied Physics Letters*, vol. 99, no. 21, p. 212901, Nov. 2011. [Online]. Available: <http://dx.doi.org/10.1063/1.3663535>
- [65] Z. Liu, S. Cui, P. Shekhter, X. Sun, L. Kornblum, J. Yang, M. Eizenberg, K. S. Chang-Liao, and T. P. Ma, “Effect of H on interface properties of Al₂O₃/In_{0.53}Ga_{0.47}As,” *Applied Physics Letters*, vol. 99, no. 22, p. 222104, Nov. 2011. [Online]. Available: <http://dx.doi.org/10.1063/1.3665395>

- [66] T. Hoshii, S. Lee, R. Suzuki, N. Taoka, M. Yokoyama, H. Yamada, M. Hata, T. Yasuda, M. Takenaka, and S. Takagi, "Reduction in interface state density of Al₂O₃/InGaAs metal-oxide-semiconductor interfaces by InGaAs surface nitridation," *Journal of Applied Physics*, vol. 112, no. 7, p. 073702, Oct. 2012. [Online]. Available: <http://dx.doi.org/10.1063/1.4755804>
- [67] H. C. Chiu, L. T. Tung, Y. H. Chang, Y. J. Lee, C. C. Chang, J. Kwo, and M. Hong, "Achieving a low interfacial density of states in atomic layer deposited Al₂O₃ on In_{0.53}Ga_{0.47}As," *Applied Physics Letters*, vol. 93, no. 20, p. 202903, Nov. 2008. [Online]. Available: <http://dx.doi.org/10.1063/1.3027476>
- [68] H.-P. Chen, Y. Yuan, B. Yu, J. Ahn, P. C. McIntyre, P. Asbeck, M. J. W. Rodwell, and Y. Taur, "Interface-State Modeling of Al₂O₃-InGaAs MOS From Depletion to Inversion," *Electron Devices, IEEE Transactions on*, vol. 59, no. 9, p. 2383, Sep. 2012. [Online]. Available: <http://dx.doi.org/10.1109/TED.2012.2205255>
- [69] Y. Xuan, Y. Wu, H. Lin, T. Shen, and P. Ye, "Submicrometer Inversion-Type Enhancement-Mode InGaAs MOSFET With Atomic-Layer-Deposited Al₂O₃ as Gate Dielectric," *Electron Device Letters, IEEE*, vol. 28, no. 11, p. 935, Nov. 2007. [Online]. Available: <http://dx.doi.org/10.1109/LED.2007.906436>
- [70] É. O'Connor, V. Djara, S. Monaghan, P. Hurley, and K. Cherkaoui, "Capacitance-Voltage and Interface State Density Characteristics of GaAs and In_{0.53}Ga_{0.47}As MOS Capacitors Incorporating a PECVD Si₃N₄ Dielectric," *ECS Transactions*, vol. 35, no. 3, p. 415, 2011. [Online]. Available: <http://dx.doi.org/10.1149/1.3569934>
- [71] T. Hoshii, M. Yokoyama, H. Yamada, M. Hata, T. Yasuda, M. Takenaka, and S. Takagi, "Impact of InGaAs surface nitridation on interface properties of InGaAs metal-oxide-semiconductor capacitors using electron cyclotron resonance plasma sputtering SiO₂," *Applied Physics Letters*, vol. 97, no. 13, p. 132102, Sep. 2010. [Online]. Available: <http://dx.doi.org/10.1063/1.3464170>
- [72] É. O'Connor, R. D. Long, K. Cherkaoui, K. K. Thomas, F. Chalvet, I. M. Povey, M. E. Pemble, P. K. Hurley, B. Brennan, G. Hughes, and S. B. Newcomb, "*In situ* h₂S passivation of In_{0.53}Ga_{0.47}As/InP metal-oxide-semiconductor capacitors with atomic-layer deposited HfO₂ gate dielectric," *Applied Physics Letters*, vol. 92, no. 2, p. 022902, Jan. 2008. [Online]. Available: <http://dx.doi.org/10.1063/1.2829586>
- [73] W. J. Carter, A. D. and Mitchell, B. J. Thibeault, J. J. M. Law, and M. J. W. Rodwell, "Al₂O₃ Growth on (100) In_{0.53}Ga_{0.47}As Initiated by Cyclic Trimethylaluminum and

- Hydrogen Plasma Exposures,” *Appl. Phys. Express*, vol. 4, no. 9, p. 091102, Aug. 2001. [Online]. Available: <http://dx.doi.org/10.1143/APEX.4.091102>
- [74] A. M. Sonnet, C. L. Hinkle, M. N. Jivani, R. A. Chapman, G. P. Pollack, R. M. Wallace, and E. M. Vogel, “Performance enhancement of n -channel inversion type $\text{In}_x\text{Ga}_{1-x}\text{As}$ metal-oxide-semiconductor field effect transistor using *ex situ* deposited thin amorphous silicon layer,” *Applied Physics Letters*, vol. 93, no. 12, p. 122109, Sep. 2008. [Online]. Available: <http://dx.doi.org/10.1063/1.2991340>
- [75] M. E. Kazzi, L. Czornomaz, C. Rossel, C. Gerl, D. Caimi, H. Siegart, J. Fompeyrine, and C. Marchiori, “Thermally stable, sub-nanometer equivalent oxide thickness gate stack for gate-first $\text{In}_{0.53}\text{Ga}_{0.47}\text{As}$ metal-oxide-semiconductor field-effect-transistors,” *Applied Physics Letters*, vol. 100, no. 6, p. 063505, Feb. 2012. [Online]. Available: <http://dx.doi.org/10.1063/1.3683472>
- [76] H.-S. Kim, I. Ok, F. Zhu, M. Zhang, S. Park, J. Yum, H. Zhao, P. Majhi, D. I. Garcia-Gutierrez, N. Goel, W. Tsai, C. K. Gaspe, M. B. Santos, and J. C. Lee, “High mobility HfO_2 -based $\text{In}_{0.53}\text{Ga}_{0.47}\text{As}$ n -channel metal-oxide-semiconductor field effect transistors using a germanium interfacial passivation layer,” *Applied Physics Letters*, vol. 93, no. 13, p. 132902, Sep. 2008. [Online]. Available: <http://dx.doi.org/10.1063/1.2990645>
- [77] M. Si, J. J. Gu, X. Wang, J. Shao, X. Li, M. J. Manfra, R. G. Gordon, and P. D. Ye, “Effects of forming gas anneal on ultrathin InGaAs nanowire metal-oxide-semiconductor field-effect transistors,” *Applied Physics Letters*, vol. 102, no. 9, p. 093505, Mar. 2013. [Online]. Available: <http://dx.doi.org/10.1063/1.4794846>
- [78] V. Djara, K. Cherkaoui, S. B. Newcomb, K. Thomas, E. Pelucchi, D. O’Connell, L. Floyd, V. Dimastrodonato, L. O. Mereni, and P. K. Hurley, “On the activation of implanted silicon ions in $p\text{-In}_{0.53}\text{Ga}_{0.47}\text{As}$,” *Semiconductor Science and Technology*, vol. 27, no. 8, p. 082001, Aug. 2012. [Online]. Available: <http://dx.doi.org/10.1088/0268-1242/27/8/082001>
- [79] N. Goel, P. Majhi, W. Tsai, M. Warusawithana, D. G. Schlom, M. B. Santos, J. S. Harris, and Y. Nishi, “High-indium-content InGaAs metal-oxide-semiconductor capacitor with amorphous LaAlO_3 gate dielectric,” *Applied Physics Letters*, vol. 91, no. 9, p. 093509, Aug. 2007. [Online]. Available: <http://dx.doi.org/10.1063/1.2776846>
- [80] R. M. Wallace, P. C. McIntyre, J. Kim, and Y. Nishi, “Atomic Layer Deposition of Dielectrics on Ge and III-V Materials for Ultrahigh Performance Transistors,” *MRS Bull.*, vol. 34, no. 7, p. 493, Jul. 2009. [Online]. Available: <http://dx.doi.org/10.1557/mrs2009.137>

- [81] P. D. Ye, G. D. Wilk, B. Yang, J. Kwo, S. N. G. Chu, S. Nakahara, H.-J. L. Gossmann, J. P. Mannaerts, M. Hong, K. K. Ng, and J. Bude, "GaAs metal-oxide-semiconductor field-effect transistor with nanometer-thin dielectric grown by atomic layer deposition," *Applied Physics Letters*, vol. 83, no. 1, p. 180, May 2003. [Online]. Available: <http://dx.doi.org/10.1063/1.1590743>
- [82] M. M. Frank, G. D. Wilk, D. Starodub, T. Gustafsson, E. Garfunkel, Y. J. Chabal, J. Grazul, and D. A. Muller, "HfO₂ and Al₂O₃ gate dielectrics on GaAs grown by atomic layer deposition," *Applied Physics Letters*, vol. 86, no. 15, p. 152904, Apr. 2005. [Online]. Available: <http://dx.doi.org/10.1063/1.1899745>
- [83] C. L. Hinkle, A. M. Sonnet, E. M. Vogel, S. McDonnell, G. J. Hughes, M. Milojevic, B. Lee, F. S. Aguirre-Tostado, K. J. Choi, H. C. Kim, J. Kim, and R. M. Wallace, "GaAs interfacial self-cleaning by atomic layer deposition," *Applied Physics Letters*, vol. 92, no. 7, p. 071901, Feb. 2008. [Online]. Available: <http://dx.doi.org/10.1063/1.2883956>
- [84] C.-H. Chang, Y.-K. Chiou, Y.-C. Chang, K.-Y. Lee, T.-D. Lin, T.-B. Wu, M. Hong, and J. Kwo, "Interfacial self-cleaning in atomic layer deposition of HfO₂ gate dielectric on In_{0.15}Ga_{0.85}As," *Applied Physics Letters*, vol. 89, no. 24, p. 242911, Dec. 2006. [Online]. Available: <http://dx.doi.org/10.1063/1.2405387>
- [85] A. O'Mahony, S. Monaghan, G. Provenzano, I. M. Povey, M. G. Nolan, É. O'Connor, K. Cherkaoui, S. B. Newcomb, F. Crupi, P. K. Hurley, and M. E. Pemble, "Structural and electrical analysis of the atomic layer deposition of HfO₂/*n*-In_{0.53}Ga_{0.47}As capacitors with and without an Al₂O₃ interface control layer," *Applied Physics Letters*, vol. 97, no. 5, p. 052904, Aug. 2010. [Online]. Available: <http://dx.doi.org/10.1063/1.3473773>
- [86] L. K. Chu, C. Merckling, A. Alian, J. Dekoster, J. Kwo, M. Hong, M. Caymax, and M. Heyns, "Low interfacial trap density and sub-nm equivalent oxide thickness in In_{0.53}Ga_{0.47}As (001) metal-oxide-semiconductor devices using molecular beam deposited HfO₂/Al₂O₃ as gate dielectrics," *Applied Physics Letters*, vol. 99, no. 4, p. 042908, Jul. 2011. [Online]. Available: <http://dx.doi.org/10.1063/1.3617436>
- [87] D. Veksler, P. Nagaiah, T. Chidambaram, R. Cammarere, V. Tokranov, M. Yakimov, Y.-T. Chen, J. Huang, N. Goel, J. Oh, G. Bersuker, C. Hobbs, P. D. Kirsch, and S. Oktyabrsky, "Quantification of interfacial state density (D_{it}) at the high-k/III-V interface based on Hall effect measurements," *Journal of Applied Physics*, vol. 112, no. 5, p. 054504, Dec. 2012. [Online]. Available: <http://dx.doi.org/10.1063/1.4749403>
- [88] E. H. Nicollian and A. Goetzberger, "The Si-SiO₂ interface: Electrical properties as determined by the metal-insulator-silicon conductance technique," *Bell Syst.*

-
- Tech. J.*, vol. XLVI, no. 6, p. 1055, Jul. 1967. [Online]. Available: <http://archive.org/details/bstj46-6-1055>
- [89] C. N. Berglund, "Surface states at steam-grown silicon-silicon dioxide interfaces," *Electron Devices, IEEE Transactions on*, vol. 13, no. 10, p. 701, Oct. 1966. [Online]. Available: <http://dx.doi.org/10.1109/T-ED.1966.15827>
- [90] L. M. Terman, "An investigation of surface states at a silicon/silicon oxide interface employing metal-oxide-silicon diodes," *Solid-State Electronics*, vol. 5, no. 5, p. 285, Sep. 1962. [Online]. Available: [http://dx.doi.org/10.1016/0038-1101\(62\)90111-9](http://dx.doi.org/10.1016/0038-1101(62)90111-9)
- [91] R. Castagné and A. Vapaille, "Description of the SiO₂/Si interface properties by means of very low frequency MOS capacitance measurements," *Surface Science*, vol. 28, no. 1, p. 157, Nov. 1971. [Online]. Available: [http://dx.doi.org/10.1016/0039-6028\(71\)90092-6](http://dx.doi.org/10.1016/0039-6028(71)90092-6)
- [92] R. Engel-Herbert, Y. Hwang, and S. Stemmer, "Comparison of methods to quantify interface trap densities at dielectric/III-V semiconductor interfaces," *Journal of Applied Physics*, vol. 108, no. 12, p. 124101, Dec. 2010. [Online]. Available: <http://dx.doi.org/10.1063/1.3520431>
- [93] K. Martens, C. O. Chui, G. Brammertz, B. De Jaeger, D. Kuzum, M. Meuris, M. M. Heyns, T. Krishnamohan, K. Saraswat, H. Maes, and G. Groeseneken, "On the Correct Extraction of Interface Trap Density of MOS Devices With High-Mobility Semiconductor Substrates," *Electron Devices, IEEE Transactions on*, vol. 55, no. 2, p. 547, Feb. 2008. [Online]. Available: <http://dx.doi.org/10.1109/TED.2007.912365>
- [94] A. Alian, C. Merckling, G. Brammertz, M. Meuris, M. Heyns, and K. D. Meyer, "InGaAs MOS Transistors Fabricated through a Digital-Etch Gate-Recess Process and the Influence of Forming Gas Anneal on Their Electrical Behavior," *ECS Journal of Solid State Science and Technology*, vol. 1, no. 6, p. P310, Oct. 2012. [Online]. Available: <http://dx.doi.org/10.1149/2.001301jss>
- [95] G. Groeseneken, "Introduction to charge pumping and its applications. Tutorial IEEE Semiconductor Interface Specialists Conference (SISC), San Diego, CA, Dec. 2008." [Online]. Available: <http://www.ieeesisc.org>
- [96] W. Wang, J. Deng, J. C. M. Hwang, Y. Xuan, Y. Wu, and P. D. Ye, "Charge-pumping characterization of interface traps in Al₂O₃/In_{0.75}Ga_{0.25}As metal-oxide-semiconductor field-effect transistors," *Applied Physics Letters*, vol. 96, no. 7, p. 072102, Feb. 2010. [Online]. Available: <http://dx.doi.org/10.1063/1.3315870>

- [97] D. Varghese, Y. Xuan, Y. Q. Wu, T. Shen, P. Ye, and M. Alam, "Multi-probe interface characterization of $\text{In}_{0.65}\text{Ga}_{0.35}\text{As}/\text{Al}_2\text{O}_3$ MOSFET," in *Electron Devices Meeting, 2008. IEDM 2008. IEEE International*, 2008, p. 1. [Online]. Available: <http://dx.doi.org/10.1109/IEDM.2008.4796699>
- [98] D. Shahrjerdi, J. Nah, B. Hekmatshoar, T. Akyol, M. Ramon, E. Tutuc, and S. K. Banerjee, "Hall mobility measurements in enhancement-mode GaAs field-effect transistors with Al_2O_3 gate dielectric," *Applied Physics Letters*, vol. 97, no. 21, p. 213506, Nov. 2010. [Online]. Available: <http://dx.doi.org/10.1063/1.3521284>
- [99] R. D. Long, B. Shin, S. Monaghan, K. Cherkaoui, J. Cagnon, S. Stemmer, P. C. McIntyre, and P. K. Hurley, "Charged Defect Quantification in $\text{Pt}/\text{Al}_2\text{O}_3/\text{In}_{0.53}\text{Ga}_{0.47}\text{As}/\text{InP}$ MOS Capacitors," *Journal of The Electrochemical Society*, vol. 158, no. 5, p. G103, Mar. 2011. [Online]. Available: <http://dx.doi.org/10.1149/1.3545799>
- [100] D. K. Schroder, *Fixed, Oxide Trapped, And Mobile Oxide Charge*, 3rd ed. Hoboken, NJ, USA: John Wiley & Sons, Inc., 2006.
- [101] J. Hu and H.-S. P. Wong, "Effect of annealing ambient and temperature on the electrical characteristics of atomic layer deposition $\text{Al}_2\text{O}_3/\text{In}_{0.53}\text{Ga}_{0.47}\text{As}$ metal-oxide-semiconductor capacitors and MOSFETs," *Journal of Applied Physics*, vol. 111, no. 4, p. 044105, Feb. 2012. [Online]. Available: <http://dx.doi.org/10.1063/1.3686628>
- [102] [Online]. Available: <http://www.itrs.net>
- [103] A. M. Crook, E. Lind, Z. Griffith, M. J. W. Rodwell, J. D. Zimmerman, A. C. Gossard, and S. R. Bank, "Low resistance, nonalloyed Ohmic contacts to InGaAs," *Applied Physics Letters*, vol. 91, no. 19, p. 192114, Nov. 2007. [Online]. Available: <http://dx.doi.org/10.1063/1.2806235>
- [104] H. H. Berger, "Contact Resistance and Contact Resistivity," *Journal of The Electrochemical Society*, vol. 119, no. 4, p. 507, Apr. 1972. [Online]. Available: <http://dx.doi.org/10.1149/1.2404240>
- [105] I. Thayne, S. Bentley, M. Holland, W. Jansen, X. Li, D. Macintyre, S. Thoms, B. Shin, J. Ahn, and P. McIntyre, "III-V nMOSFETs - Some issues associated with roadmap worthiness," *Microelectronic Engineering*, vol. 88, no. 7, p. 1070, Jul. 2011. [Online]. Available: <http://dx.doi.org/10.1016/j.mee.2011.03.100>
- [106] M. Shayesteh, C. Daunt, D. O'Connell, V. Djara, M. White, B. Long, and R. Duffy, "NiGe Contacts and Junction Architectures for P and As Doped Germanium Devices,"

-
- Electron Devices, IEEE Transactions on*, vol. 58, no. 11, p. 3801, Nov. 2011. [Online]. Available: <http://dx.doi.org/10.1109/TED.2011.2164801>
- [107] V. Djara, K. Cherkaoui, M. Schmidt, S. Monaghan, É. O'Connor, I. Povey, D. O'Connell, M. Pemble, and P. K. Hurley, "Impact of Forming Gas Annealing on the Performance of Surface-Channel $\text{In}_{0.53}\text{Ga}_{0.47}\text{As}$ MOSFETs With an ALD Al_2O_3 Gate Dielectric," *Electron Devices, IEEE Transactions on*, vol. 59, no. 4, p. 1084, Apr. 2012. [Online]. Available: <http://dx.doi.org/10.1109/TED.2012.2185242>
- [108] M. Negara, V. Djara, T. O'Regan, K. Cherkaoui, M. Burke, Y. Gomeniuk, M. Schmidt, É. O'Connor, I. Povey, A. Quinn, and P. Hurley, "Investigation of electron mobility in surface-channel $\text{Al}_2\text{O}_3/\text{In}_{0.53}\text{Ga}_{0.47}\text{As}$ MOSFETs," *Solid-State Electronics*, vol. 88, p. 37, Oct. 2013. [Online]. Available: <http://dx.doi.org/10.1016/j.sse.2013.04.014>
- [109] Y. Wang, Y.-T. Chen, F. Xue, F. Zhou, and J. C. Lee, "HfO₂ dielectrics engineering using low power SF₆ plasma on InP and $\text{In}_{0.53}\text{Ga}_{0.47}\text{As}$ metal-oxide-semiconductor field-effect-transistors," *Applied Physics Letters*, vol. 100, no. 24, p. 243508, Jun. 2012. [Online]. Available: <http://dx.doi.org/10.1063/1.4729606>
- [110] A. Alian, G. Brammertz, N. Waldron, C. Merckling, G. Hellings, H. Lin, W. Wang, M. Meuris, E. Simoen, K. D. Meyer, and M. Heyns, "Silicon and selenium implantation and activation in $\text{In}_{0.53}\text{Ga}_{0.47}\text{As}$ under low thermal budget conditions," *Microelectronic Engineering*, vol. 88, no. 2, p. 155, Feb. 2011. [Online]. Available: <http://dx.doi.org/10.1016/j.mee.2010.10.002>
- [111] U. Singiseti, M. A. Wistey, J. D. Zimmerman, B. J. Thibeault, M. J. W. Rodwell, A. C. Gossard, and S. R. Bank, "Ultralow resistance in situ Ohmic contacts to InGaAs/InP," *Applied Physics Letters*, vol. 93, no. 18, p. 183502, Nov. 2008. [Online]. Available: <http://dx.doi.org/10.1063/1.3013572>
- [112] U. Singiseti, J. D. Zimmerman, M. A. Wistey, J. Cagnon, B. J. Thibeault, M. J. W. Rodwell, A. C. Gossard, S. Stemmer, and S. R. Bank, "ErAs epitaxial Ohmic contacts to InGaAs/InP," *Applied Physics Letters*, vol. 94, no. 8, p. 083505, Feb. 2009. [Online]. Available: <http://dx.doi.org/10.1063/1.3087313>
- [113] Ivana, J. Pan, Z. Zhang, X. Zhang, H. Guo, X. Gong, and Y.-C. Yeo, "Photoelectron spectroscopy study of band alignment at interface between Ni-InGaAs and $\text{In}_{0.53}\text{Ga}_{0.47}\text{As}$," *Applied Physics Letters*, vol. 99, no. 1, p. 012105, Jul. 2011. [Online]. Available: <http://dx.doi.org/10.1063/1.3607959>

- [114] S. Mehari, A. Gavrilov, S. Cohen, P. Shekhter, M. Eizenberg, and D. Ritter, "Measurement of the Schottky barrier height between Ni-InGaAs alloy and $\text{In}_{0.53}\text{Ga}_{0.47}\text{As}$," *Applied Physics Letters*, vol. 101, no. 7, p. 072103, Aug. 2012. [Online]. Available: <http://dx.doi.org/10.1063/1.4746254>
- [115] S. H. Kim, M. Yokoyama, N. Taoka, R. Iida, S. Lee, R. Nakane, Y. Urabe, N. Miyata, T. Yasuda, H. Yamada, N. Fukuhara, M. Hata, M. Takenaka, and S. Takagi, "Self-aligned metal source/drain $\text{In}_x\text{Ga}_{1-x}\text{As}$ n-MOSFETs using Ni-InGaAs alloy," in *Electron Devices Meeting (IEDM), 2010 IEEE International*, 2010, p. 26.6.1. [Online]. Available: <http://dx.doi.org/10.1109/IEDM.2010.5703429>
- [116] L. Czornomaz, M. E. Kazzi, M. Hopstaken, D. Caimi, P. Mächler, C. Rossel, M. Bjoerk, C. Marchiori, H. Siegwart, and J. Fompeyrine, "CMOS compatible self-aligned S/D regions for implant-free InGaAs MOSFETs," *Solid-State Electronics*, vol. 74, no. 0, p. 71, Aug. 2012. [Online]. Available: <http://dx.doi.org/10.1016/j.sse.2012.04.014>
- [117] X. Zhang, Ivana, H. X. Guo, X. Gong, Q. Zhou, and Y.-C. Yeo, "A Self-Aligned Ni-InGaAs Contact Technology for InGaAs Channel n-MOSFETs," *Journal of The Electrochemical Society*, vol. 159, no. 5, p. H511, Mar. 2012. [Online]. Available: <http://dx.doi.org/10.1149/2.060205jes>
- [118] R. Oxland, S. W. Chang, X. Li, S. W. Wang, G. Radhakrishnan, W. Priyantha, M. J. H. Van Dal, C. Hsieh, G. Vellianitis, G. Doornbos, K. Bhuiwarka, B. Duriez, I. Thayne, R. Droopad, M. Passlack, C. Diaz, and Y. C. Sun, "An Ultralow-Resistance Ultrashallow Metallic Source/Drain Contact Scheme for III-V NMOS," *Electron Device Letters, IEEE*, vol. 33, no. 4, p. 501, Apr. 2012. [Online]. Available: <http://dx.doi.org/10.1109/LED.2012.2185919>
- [119] M. Radosavljevic, B. Chu-Kung, S. Corcoran, G. Dewey, M. Hudait, J. Fastenau, J. Kavalieros, W. K. Liu, D. Lubyshev, M. Metz, K. Millard, N. Mukherjee, W. Rachmady, U. Shah, and R. Chau, "Advanced high- K gate dielectric for high-performance short-channel $\text{In}_{0.7}\text{Ga}_{0.3}\text{As}$ quantum well field effect transistors on silicon substrate for low power logic applications," in *Electron Devices Meeting (IEDM), 2009 IEEE International*, 2009, p. 1. [Online]. Available: <http://dx.doi.org/10.1109/IEDM.2009.5424361>
- [120] X. Zhou, Q. Li, C. W. Tang, and K. M. Lau, "Inverted-Type InGaAs Metal-Oxide-Semiconductor High-Electron-Mobility Transistor on Si Substrate with Maximum Drain Current Exceeding 2 A/mm," *Applied Physics Express*, vol. 5, no. 10, p. 104201, Oct. 2012. [Online]. Available: <http://dx.doi.org/10.1143/APEX.5.104201>

-
- [121] M. Heyns, A. Alian, G. Brammertz, M. Caymax, Y. C. Chang, L. K. Chu, B. De Jaeger, G. Eneman, F. Gencarelli, G. Groeseneken, G. Hellings, A. Hikavy, T. Y. Hoffmann, M. Houssa, C. Huyghebaert, D. Leonelli, D. Lin, R. Loo, W. Magnus, C. Merckling, M. Meuris, J. Mitard, L. Nyns, T. Orzali, R. Rooyackers, S. Sioncke, B. Soree, X. Sun, A. Vandooren, A. Verhulst, B. Vincent, N. Waldron, G. Wang, W. E. Wang, and L. Witters, "Advancing CMOS beyond the Si roadmap with Ge and III/V devices," in *Electron Devices Meeting (IEDM), 2011 IEEE International*, 2011, p. 13.1.1. [Online]. Available: <http://dx.doi.org/10.1109/IEDM.2011.6131543>
- [122] N. Waldron, G. Wang, N. D. Nguyen, T. Orzali, C. Merckling, G. Brammertz, P. Ong, G. Winderickx, G. Hellings, G. Eneman, M. Caymax, M. Meuris, N. Horiguchi, and A. Thean, "Integration of InGaAs Channel n-MOS Devices on 200mm Si Wafers Using the Aspect-Ratio-Trapping Technique," *ECS Transactions*, vol. 45, no. 4, p. 115, 2012. [Online]. Available: <http://dx.doi.org/10.1149/1.3700460>
- [123] L. Czornomaz, N. Daix, D. Caimi, M. Sousa, R. Erni, M. Rossell, M. El-Kazzi, C. Rossel, C. Marchiori, E. Uccelli, M. Richter, H. Siegwart, and J. Fompeyrine, "An integration path for gate-first UTB III-V-on-insulator MOSFETs with silicon, using direct wafer bonding and donor wafer recycling," in *Electron Devices Meeting (IEDM), 2012 IEEE International*, 2012, p. 23.4.1. [Online]. Available: <http://dx.doi.org/10.1109/IEDM.2012.6479088>
- [124] M. Yokoyama, R. Iida, S. Kim, N. Taoka, Y. Urabe, H. Takagi, T. Yasuda, H. Yamada, N. Fukuhara, M. Hata, M. Sugiyama, Y. Nakano, M. Takenaka, and S. Takagi, "Sub-10-nm Extremely Thin Body InGaAs-on-Insulator MOSFETs on Si Wafers With Ultrathin Buried Oxide Layers," *Electron Device Letters, IEEE*, vol. 32, no. 9, p. 1218, Sep. 2011. [Online]. Available: <http://dx.doi.org/10.1109/LED.2011.2158568>
- [125] V. Djara, K. Cherkaoui, A. Negara, J. MacHale, M. Burke, E. O'Connor, I. M. Povey, D. O'Connell, M. E. Pemble, A. Quinn, and P. K. Hurley, "Inversion-Charge Pumping Method for Mobility Extraction in Surface-Channel $\text{Al}_2\text{O}_3/\text{In}_{0.53}\text{Ga}_{0.47}\text{As}$ MOSFETs," in *IEEE Semiconductor Interface Specialists Conference (SISC), San Diego, CA*, Dec. 2012.
- [126] V. Djara, K. Cherkaoui, T. Lopez, E. O'Connor, I. M. Povey, K. K. Thomas, and P. K. Hurley, "Junctionless InGaAs MOSFETs with InAlAs Barrier Isolation and Channel Thinning by Digital Wet Etching," in *IEEE Device Research Conference (DRC), 2013. Conference Digest*, 2013, p. 131.
- [127] J.-P. Colinge, C.-W. Lee, A. Afzalian, N. D. Akhavan, R. Yan, I. Ferain, P. Razavi, B. O'Neill, A. Blake, M. White, A.-M. Kelleher, B. McCarthy, and R. Murphy, "Nanowire

- transistors without junctions,” *Nature Nano.*, vol. 5, p. 225, Feb. 2010. [Online]. Available: <http://dx.doi.org/10.1038/nnano.2010.15>
- [128] D. H. Doehlert, “Uniform Shell Designs,” *Journal of the Royal Statistical Society. Series C (Applied Statistics)*, vol. 19, no. 3, pp. pp. 231–239. [Online]. Available: <http://www.jstor.org/stable/2346327>
- [129] V. Djara, K. Cherkaoui, K. Thomas, E. Pelucchi, D. O’Connell, L. Floyd, and P. K. Hurley, “Annealing investigations for high- k first n -channel $\text{In}_{0.53}\text{Ga}_{0.47}\text{As}$ MOSFET development,” in *Ultimate Integration on Silicon (ULIS), 2011 12th International Conference on*, Mar. 2011, pp. 1–4. [Online]. Available: <http://dx.doi.org/10.1109/ULIS.2011.5758001>
- [130] P. Hurley, E. O’Connor, V. Djara, S. Monaghan, I. Povey, R. Long, B. Sheehan, J. Lin, P. McIntyre, B. Brennan, R. Wallace, M. Pemble, and K. Cherkaoui, “The characterisation and passivation of fixed oxide charges and interface states in the $\text{Al}_2\text{O}_3/\text{InGaAs}$ MOS system,” *Device and Materials Reliability, IEEE Transactions on*, vol. PP, no. 99, p. 1, 2013. [Online]. Available: <http://dx.doi.org/10.1109/TDMR.2013.2282216>
- [131] G. Ghibaudo, “New characterization methods for nanomofets,” in *Nanoscale CMOS and Si-based Beyond CMOS Nanodevices, MIGAS Summer School ’08, Autrans-Grenoble, France*, 2008. [Online]. Available: <http://www.migas.inpg.fr>
- [132] T. P. O’Regan, P. K. Hurley, B. Sorée, and M. V. Fischetti, “Modeling the capacitance-voltage response of $\text{In}_{0.53}\text{Ga}_{0.47}\text{As}$ metal-oxide-semiconductor structures: Charge quantization and nonparabolic corrections,” *Applied Physics Letters*, vol. 96, no. 21, p. 213514, May 2010. [Online]. Available: <http://dx.doi.org/10.1063/1.3436645>
- [133] T. P. O’Regan and P. K. Hurley, “Calculation of the capacitance-voltage characteristic of GaAs, $\text{In}_{0.53}\text{Ga}_{0.47}\text{As}$, and InAs metal-oxide-semiconductor structures,” *Applied Physics Letters*, vol. 99, no. 16, p. 163502, Oct. 2011. [Online]. Available: <http://dx.doi.org/10.1063/1.3652699>
- [134] A. Kerber, E. Cartier, L.-A. Ragnarsson, M. Rosmeulen, L. Pantisano, R. Degraeve, Y. Kim, and G. Groeseneken, “Direct measurement of the inversion charge in MOSFETs: application to mobility extraction in alternative gate dielectrics,” in *VLSI Technology, 2003. Digest of Technical Papers. 2003 Symposium on*, 2003, p. 159. [Online]. Available: <http://dx.doi.org/10.1109/VLSIT.2003.1221134>

Chapter 2

Source/Drain Activation and Impact on Gate Stack

2.1 Introduction

As mentioned in section 1.2.1 (page 6), a significant amount of research has already been dedicated to the integration of high- k gate oxides on $\text{In}_{0.53}\text{Ga}_{0.47}\text{As}$ substrates through the use of metal-oxide-semiconductor capacitors (MOSCAPs). However, the additional process steps required to form the source and drain (S/D) of an $\text{In}_{0.53}\text{Ga}_{0.47}\text{As}$ MOSFET can significantly increase the complexity of the device fabrication process flow. As a result, the $\text{In}_{0.53}\text{Ga}_{0.47}\text{As}$ MOSFET fabrication process flow must be carefully engineered so that the formation of the S/D does not excessively degrade the electrical properties of the gate stack.

Two types of process flows are generally reported for S/D-implanted III-V metal-oxide-semiconductor field-effect transistors (MOSFETs): the gate-first process [1–3] and the gate-last process [3–5]. The gate-first process offers the advantage of being a self-aligned process. However, since the high- k /metal-gate stack is formed before the S/D implant and anneal steps, the metal, the high- k and the high- k / $\text{In}_{0.53}\text{Ga}_{0.47}\text{As}$ interface have to withstand the activation anneal process, which generally leads to performance degradation of the gate stack. In the gate-last process, which is non self-aligned, the high- k /metal-gate stack is deposited after the S/D implant and anneal steps. This adds further process complexity as a sacrificial oxide layer needs to be deposited before the S/D implant and removed after the S/D activation anneal. Although it was demonstrated in [3] that the gate-last process offers better gate stack electrical properties than the gate-first process, we speculate that the gate-last process may suffer from repeatability issues as the $\text{In}_{0.53}\text{Ga}_{0.47}\text{As}$ surface is exposed to additional processing before the high- k oxide deposition.

The “high- k first + metal-gate last” process represents an intermediate approach between the

Table 2.1: TLM structure, pre-metal annealed MOSCAP and “high- k first + metal-gate last” n -channel MOSFET process flows.

Process step	TLM	MOSCAP	MOSFET
High- k ALD (HfO ₂ or Al ₂ O ₃ /HfO ₂)	X	X	X
High- k and mesa etch	X		X
Si Implantation	X		X
Activation anneal	X	X	X
High- k etch	X	X	X
Field SiO ₂ evaporation			X
Ti/Pt/Au body contact		X	X
Pd gate contact		X	X
Au/Ge/Au/Ni/Au ohmic contacts	X		X

gate-first and gate-last processes, where the high- k oxide is deposited before the S/D implant and S/D activation anneal but the metal-gate is formed after the S/D activation anneal. This approach enables to minimize the In_{0.53}Ga_{0.47}As native oxide formation due to air exposure and the In_{0.53}Ga_{0.47}As surface degradation/contamination due to additional wet chemical treatments. It also avoids the annealing of the metal-gate during the S/D activation process. Removing these sources of gate stack degradation allows the study of the impact of the S/D activation anneal on the high- k oxide insulating properties and on the high- k /In_{0.53}Ga_{0.47}As interface.

In this work, we first optimized the S/D activation anneal process using test structures based on the transfer length method (TLM) [6] as part of a Doehlert design of experiment (DOE) [7]. We also investigated the impact of the S/D activation anneal process on the gate stack performance of “pre-metal annealed” In_{0.53}Ga_{0.47}As MOSCAPs and fabricated “high- k first + metal-gate-last” In_{0.53}Ga_{0.47}As n -MOSFETs.

2.2 Samples Preparation

TLM structures, pre-metal annealed MOSCAPs (MOSCAPs exposed to S/D activation anneal prior to gate metal deposition) and “high- k first + metal-gate last” n -channel MOSFETs, were fabricated on p -In_{0.53}Ga_{0.47}As (80 nm, 5×10^{16} /cm³)/ p -InP buffer (80 nm, 5×10^{16} /cm³)/Semi-Insulating (SI)-InP wafers grown by metal-organic vapor phase epitaxy (MOVPE). The growth was performed at low pressure (80 mbar) in a commercial horizontal MOVPE reactor using standard metalorganic precursors: trimethylindium (TMIn), trimethylgallium (TMGa), and Diethylzinc (DEZn), purified hydride precursors: arsine (AsH₃) and phosphine (PH₃) in purified N₂ carrier gas. The growth temperature was 760°C (thermocouple) and the growth rate was 1 μ m/h throughout. The V/III ratio during the In_{0.53}Ga_{0.47}As layer growth was 140. Low temperature photoluminescence (10 K) linewidths below 1 meV (unpublished data) were system-

atically obtained on $\text{In}_{0.53}\text{Ga}_{0.47}\text{As}$ quantum wells in GaAs barriers, confirming state of the art MOVPE quality [8]. The InP buffer layer and the $\text{In}_{0.53}\text{Ga}_{0.47}\text{As}$ layer were both Zn doped to $5 \times 10^{16} / \text{cm}^3$. The Zn doping level was extracted by electrochemical capacitance-voltage profile.

The process flows of the fabricated TLM structures, pre-metal annealed MOSCAPs and MOSFETs are shown in Table 2.1. Details on the lithography mask sets designed for the fabrication of the devices are given in Appendix B. The high- k oxide (10 nm HfO_2 or 2 nm Al_2O_3 followed by 8 nm HfO_2) films were deposited by atomic layer deposition (ALD) at 250°C without any $\text{In}_{0.53}\text{Ga}_{0.47}\text{As}$ surface passivation process. The ALD films were characterized by spectroscopic ellipsometry (SE). The implantation was performed at a 7° angle with a Si dose of $1 \times 10^{14} \text{ cm}^{-2}$ at 80 keV and $1 \times 10^{14} \text{ cm}^{-2}$ at 30 keV (similar to [9]). It is noted that the implant parameters were selected to obtain an implant profile extending all the way through the $p\text{-In}_{0.53}\text{Ga}_{0.47}\text{As}/p\text{-InP}$ layers to the Si-InP substrate [Figure 2.4(a)], preventing any parasitic leakage from an underlying p -type layer.

The high- k oxide was etched in a BCl_3 plasma and the mesa were formed using a CH_4/H_2 plasma etch process (etch depth ~ 200 nm). The implant activation anneal was performed in a N_2 ambient using a calibrated rapid thermal anneal (RTA) system. The field SiO_2 , the Pd gate and the Au (14 nm)/Ge (14 nm)/Au (14 nm)/Ni (11 nm)/Au (200 nm)¹ S/D contacts [11] were defined by lift-off lithography and deposited via electron-beam evaporation.

A review of the activation anneal processes reported in the literature [12–18] clearly indicated that a wide part of the experimental domain remained unexplored [Figure 2.1(a)]. This was partly explained by our preliminary tests (data not shown), which revealed that the $\text{In}_{0.53}\text{Ga}_{0.47}\text{As}/\text{InP}$ system was subject to surface etch pits when exposed to thermal budgets greater 700°C for 20 s, in agreement with [19]. With this in mind, we selected and designed a Doehlert DOE to cover most of the remaining experimental domain. Figure 2.1(b) shows an optical image of a fabricated TLM structure used as part of the DOE. The width (W) of the Si-implanted TLM bar is $30 \mu\text{m}$ and the metal contact separation (d) are 5, 10, 15, 25, 40 and $60 \mu\text{m}$.

2.3 Doehlert Design of Experiment

Doehlert DOEs are second-order uniform-shell designs [7], which offer significant advantages over second-order counterparts such as central composite and Box-Behnken designs. They need fewer experimental runs per number of model coefficients and are, therefore, more efficient [20]. The methods of implementation, statistical analysis and process optimization used in this study are presented in Appendix A (page 152). Further details can be obtained in reference [21]. Briefly,

¹The Au/Ge/Au stack forms an eutectic that melts at 360°C . The Ge diffuses in the $\text{In}_{0.53}\text{Ga}_{0.47}\text{As}$ and acts as a n -type dopant. The Ni enhances the Ge diffusion process and also prevents the contact from “balling-up”. The 200-nm-thick Au overcoat is used to reduce the sheet resistance of the metal stack [10].

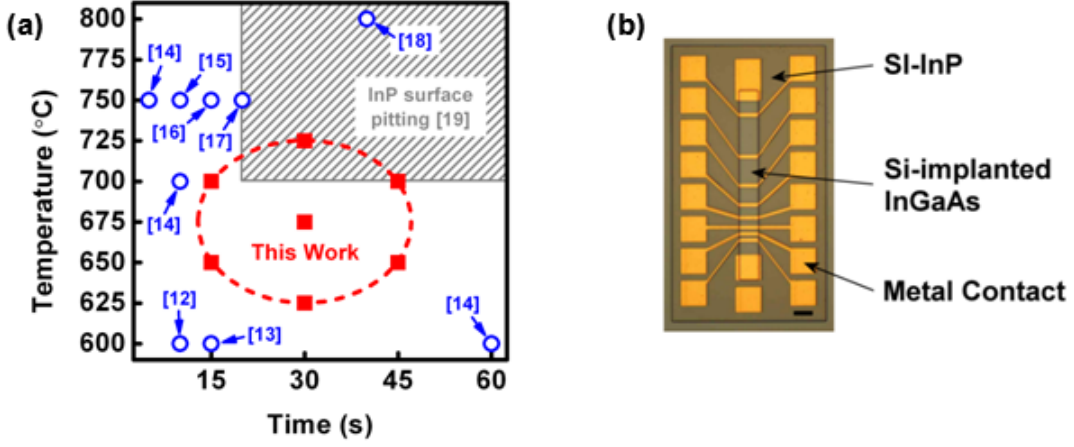


Figure 2.1: (a) Time *vs* temperature anneal process window showing the seven activation anneal conditions of the DOE along with activation anneal conditions reported in the literature [12–18]. The lowest thermal budget limit, where InP etch pitting starts, is also indicated [19]. (b) Optical image of a fabricated TLM structure. The width (W) of the Si-implanted TLM bar is $30 \mu\text{m}$ and the metal contact separations (d) are 5, 10, 15, 25, 40 and $60 \mu\text{m}$.

a two-factor Doehlert DOE relies on the following mathematical model:

$$\hat{Y} = \beta_0 + \beta_1 X_1 + \beta_2 X_2 + \beta_{11} X_1^2 + \beta_{22} X_2^2 + \beta_{12} X_1 X_2 \quad (2.1)$$

where \hat{Y} is the estimated response, X_1 and X_2 are the normalized variables representing the two factors, β_0 is the offset coefficient, β_1 and β_2 are the first-order coefficients, β_{11} and β_{22} are the second-order coefficients and β_{12} is the interaction coefficient. Seven experimental runs are required to obtain the six coefficients of the model. The statistical significance of the coefficients is assessed with a Student's *t*-test and the statistical significance of the model is checked with an analysis of variance (ANOVA). The process optimization is performed using the Lagrange criterion.

2.4 Results and Discussion

2.4.1 Analysis of Doehlert Design of Experiment

The current-voltage (I-V) characteristics obtained on all the TLM samples showed ohmic behavior [Figure 2.2(a)]. The measured resistances of the seven samples plotted against their corresponding measured contact separation are shown in Figure 2.2(b). The contact separations were measured using a calibrated optical microscope. The results obtained for each run were

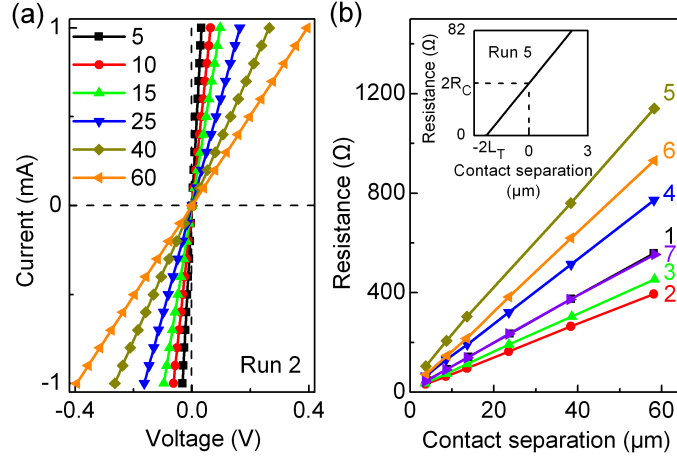


Figure 2.2: (a) Current-voltage (I-V) measurements of the sample annealed in run 2, where 5 to 60 indicate the contacts separations (d) in μm . (b) Resistances (R) vs d , where 1 to 7 are the run numbers. Inset: Linear extrapolation of R vs d (run 5). The slope is R_{sheet}/W , the y -intercept is $R = 2 \times R_C$ and the x -intercept is $d = -2 \times L_t$.

fitted with a linear model in order to extract the sheet resistance (R_{sheet}) values. The correlation coefficient (R) of each individual fit was found to be greater than 0.99991, indicating excellent fitting of the linear models to the experimental data. Values of contact resistance (R_C) and transfer length (L_t) were obtained by extrapolating the linear fits [inset of Figure 2.2(b)] and their corresponding specific contact resistance (ρ_C) values were calculated from $\rho_C = R_{sheet} \times L_t^2$. Table 2.2 shows the obtained R_{sheet} , R_C , L_t and ρ_C values. The R_{sheet} values were used as part of the Doehlert DOE to obtain the following model:

$$\hat{Y} = 265.0 - 167.6 \times X_1 - 35.8 \times X_2 + 102.9 \times X_1^2 + 47.9 \times X_2^2 + 25.9 \times X_1 X_2 \quad (2.2)$$

where \hat{Y} is the estimated R_{sheet} , X_1 is the normalized anneal temperature and X_2 is the normalized anneal time. The Student's t -test [P -value (P) < 0.05] showed that all the coefficients are statistically significant (Table 2.3). The effect of the anneal temperature on R_{sheet} is more important than the effect of anneal time since $\beta_1 > \beta_2$ and $\beta_{11} > \beta_{22}$. The ANOVA (P < 0.05) revealed that the model is statistically significant (Table 2.4). A determinant coefficient (R^2) of 0.99972 was obtained, indicating that less than 0.1% of the experimental response is not explained by the model. Moreover, the corresponding R of 0.99986 indicates an excellent fit of the model to the experimental response. Figure 2.3 shows the evolution of R_{sheet} within the experimental domain. R_{sheet} reduces dramatically with anneal temperature and an anneal time slightly above 30 s gives the lowest R_{sheet} achievable with any given anneal temperature of the experimental domain. The Lagrange criterion applied to the model revealed an optimized

Table 2.2: Experimental R_{sheet} , R_C , L_t and ρ_C obtained for each run of the Doehlert DOE. F_1 and F_2 are the anneal temperature factor and the anneal time factor, respectively.

Run	F_1 ($^{\circ}\text{C}$)	F_2 (s)	R_{sheet} (Ω/\square)	R_C (Ω)	L_t (nm)	ρ_C ($\Omega.\text{cm}^2$)
1 (mean)	675	30	265.0	5.0	5.3×10^2	7.4×10^{-7} ^a
2	725	30	199.1	3.5	5.2×10^2	5.5×10^{-7}
3	700	45	224.2	4.8	6.3×10^2	8.9×10^{-7}
4	650	45	367.0	8.2	6.3×10^2	1.5×10^{-6}
5	625	30	536.8	20.4	1.1×10^3	6.3×10^{-6}
6	650	15	451.5	3.6	2.3×10^2	2.3×10^{-7}
7	700	15	263.9	5.7	6.1×10^2	9.8×10^{-7}

^a Mean of: 1.1×10^{-6} , 5.1×10^{-8} , 6.6×10^{-7} , 6.8×10^{-7} , 1.2×10^{-6} .

Table 2.3: Student's t -test applied to each coefficient of the R_{sheet} model.

Term	Coefficient	Estimate	Standard error	t -value	P -value
Constant	β_0	265.0	3.0	87.1	3.8×10^{-9} ^a
Temperature	β_1	-167.6	1.8	-95.5	2.4×10^{-9} ^a
Time	β_2	-35.8	1.8	-20.4	5.1×10^{-6} ^a
Temperature \times Time	β_{12}	25.9	3.5	7.4	7.3×10^{-4} ^a
Temperature \times Temperature	β_{11}	102.9	3.7	27.6	1.2×10^{-6} ^a
Time \times Time	β_{22}	47.9	3.7	12.9	5.2×10^{-5} ^a

^a Significant at a 5% level ($P < 0.05$).

process condition of 715°C for 32 s, leading to a minimum R_{sheet} of $(195.6 \pm 3.4) \Omega/\square$.

Since the range of values obtained for ρ_C in run 1 was comparable to the range of ρ_C values of the entire study (Table 2.2), we could not obtain a reliable Doehlert model for ρ_C and no definite conclusions could be drawn in relation to the variation of ρ_C with activation anneal temperature and time. This can be explained by the fact that the R_C values are much lower than the R_{sheet} values, making the extraction of the ρ_C values very sensitive to errors in the measurements of the TLM resistances and dimensions. In this case, the approach used in [22], where TLM structures with a range of sub-micron spacing between the contacts are used, should provide a significantly lower error in the extracted ρ_C values and yield a statistically significant ρ_C model. A ρ_C value of $(7.4 \pm 4.5) \times 10^{-7} \Omega.\text{cm}^2$ was obtained by applying the error analysis reported in [23] to the set of ρ_C values of run 1. Although this value, obtained with a non-alloyed Au/Ge/Au/Ni/Au contact and no surface preparation, is comparable to the $\rho_C = 4.3 \times 10^{-7} \Omega.\text{cm}^2$ reported in [24] for annealed Pd/Si-based contacts on a $1 \times 10^{19} /\text{cm}^3$ Si-doped $\text{In}_{0.5}\text{Ga}_{0.5}\text{As}$ epitaxial layer, a significant ρ_C improvement is still required for S/D-implanted III-V MOSFETs to be considered as a viable alternative to standard Si MOSFETs. Considering the international technology roadmap for semiconductor (ITRS) timescales for potential III-V

Table 2.4: ANOVA applied to the entire model.

Source of variation	Sum of squares	Degree of freedom	Mean square	<i>F</i> -value	<i>P</i> -value
Model	106447.1	5	21289.4	2314.1	2.1×10^{-8} ^a
Residuals	46.0	5	9.2		
Lack of fit	8.6	1	8.6	0.9	0.4
Pure error	37.4	4	9.3		
Total	106476.8	10	10647.7		

$R^2 = 0.99972$, $R = 0.99986$. ^a Significant at a 5% level ($P < 0.05$).

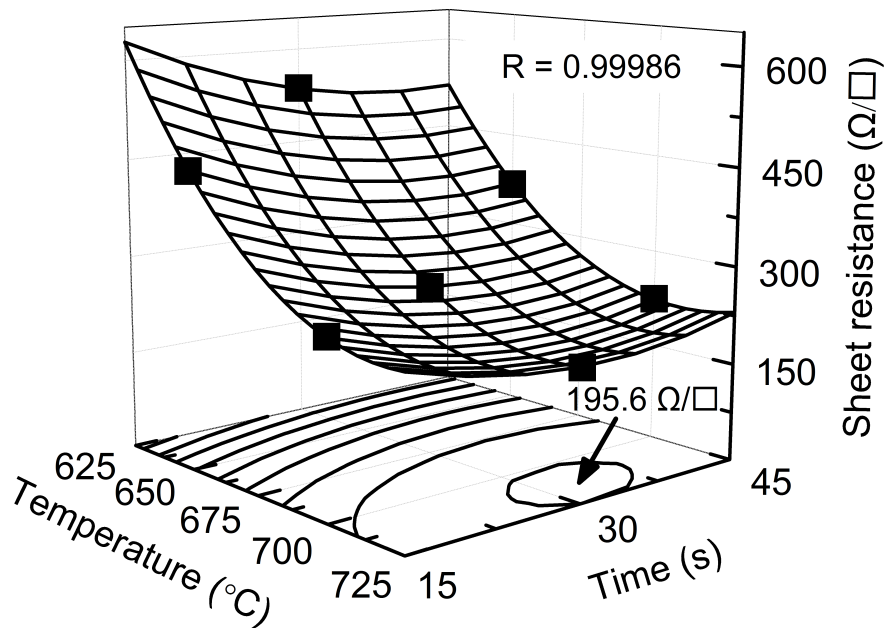


Figure 2.3: R_{sheet} response surface and contour plot as a function of annealing temperature and time. The correlation coefficient R of the model is 0.99986. The Lagrange criterion applied to the model revealed an optimized process condition of 715 $^{\circ}\text{C}$ for 32 s, leading to a minimum R_{sheet} of $(195.6 \pm 3.4) \Omega/\square$.

MOSFETs insertion into production, ρ_C values below $5 \times 10^{-9} \Omega \cdot \text{cm}^2$ will have to be achieved [25]. Although our results suggest that such low ρ_C values might not be achievable with ion implantation, the issue of S/D formation might not represent a showstopper for III-V MOSFETs as a ρ_C of $2.7 \times 10^{-9} \Omega \cdot \text{cm}^2$ was recently achieved with an alternative technique to form a metallic Ni-InAs contact on InAs [22] (see also section 1.2.2 page 16).

We performed secondary ion mass spectrometry (SIMS) measurements and cross-sectional transmission electron microscopy (TEM) analysis on the sample annealed in run 1 (at 675°C for 30 s) as it represents the centre point of the experimental domain used for the DOE. The comparison of the SIMS Si ion profiles before and after activation annealing shown in Figure 2.4(a) clearly indicates that the Si ions did not diffuse during activation annealing, in agreement with [26] and ruling out the degradation of R_{sheet} and ρ_C due to a loss of Si ions. The SIMS profiles show reasonably good agreement with the stopping and range of ions in matter (SRIM) simulation [27]. It is noted that a HfO_2 thickness of (10.1 ± 0.1) nm across a 2-in wafer was measured by SE [inset of Figure 2.4(a)] and used in the simulation. The SIMS and simulated profiles show a high Si ion concentration ($> 2 \times 10^{19} / \text{cm}^3$) within the first 40 nm of the $p\text{-In}_{0.53}\text{Ga}_{0.47}\text{As}$ along with a ~ 100 nm/dec. tail roll-off. Figure 2.4(b) reveals that the location of the ion implantation defects follows the trend of the Si ion concentration of the SIMS profile. Extended defects are observed in the $p\text{-In}_{0.53}\text{Ga}_{0.47}\text{As}$ to a depth of ~ 75 nm, while coarser agglomerates can be seen to a depth of ~ 40 nm, where the Si ion concentration in the SIMS profile is highest [Figure 2.5(a)]. Figure 2.4(c) shows that the 675°C for 30 s anneal process did not eliminate the implantation defects, consistent with [26], while Figure 2.5(b) indicates that the anneal leads to the formation of characteristic loop defects that have a peak depth of ~ 50 nm. We speculate that these defects could be responsible for the degradation of R_{sheet} and ρ_C .

2.4.2 Impact of Activation Anneal on Gate Stack Performance

Pre-metal annealed MOSCAPs featuring bi-layer oxide films, composed of 2 nm of Al_2O_3 and 8 nm of HfO_2 , were characterized in terms of leakage and capacitance to study the impact of the S/D activation anneal process on the gate stack performance. Low leakage current densities below $2.1 \times 10^{-8} \text{ A/cm}^2$ at electrical fields below $\sim 3 \text{ MV/cm}$ were obtained. Although the $\text{Al}_2\text{O}_3/\text{HfO}_2$ films were deposited on a p -doped $\text{In}_{0.53}\text{Ga}_{0.47}\text{As}$ material, the capacitance-voltage (C-V) characteristics revealed n -type behaviour [Figure 2.6(a) and (b)]. This is an unexpected result, which could indicate possible diffusion effects of unintentional n -type dopants arising from the substrate/epitaxial interface during the MOVPE growth and/or the activation anneal process, consistent with a recent report from Ostinelli *et al.* [28]. Increasing the anneal temperature from 675°C [Figure 2.6(a)] to 725°C range [Figure 2.6(b)], did not increase the dispersion of capacitance per decade of frequency in accumulation, which remained at a low value

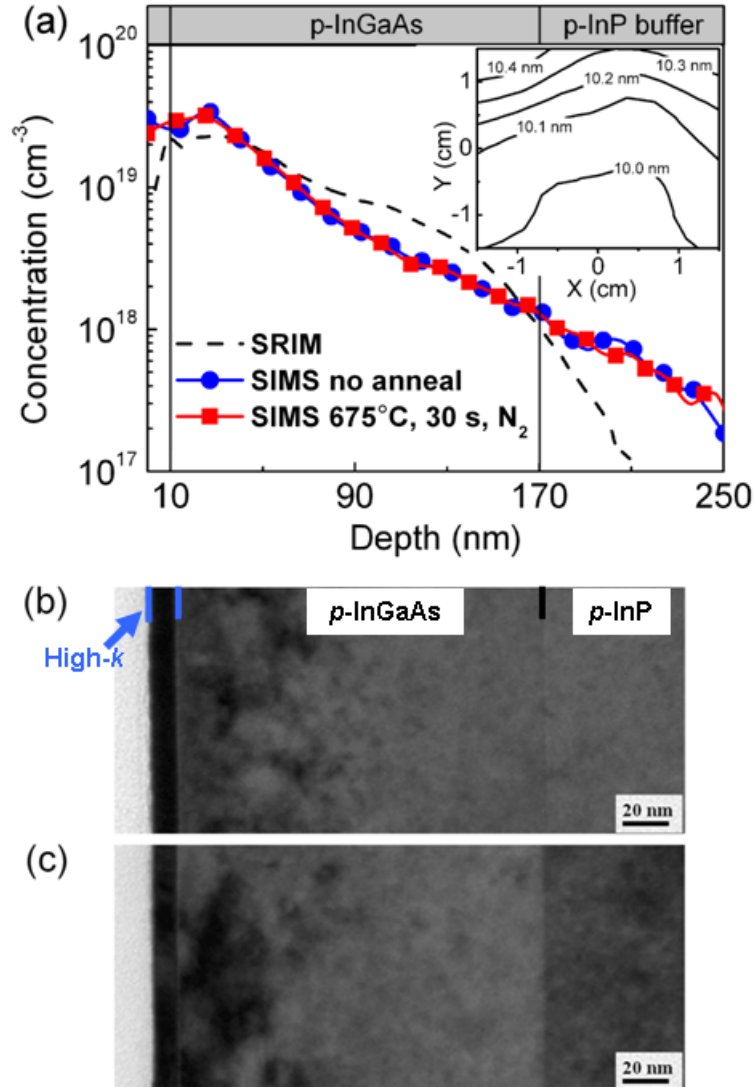


Figure 2.4: (a) SRIM simulation and SIMS measurements (before and after 675°C for 30 s annealing) of the two-stage Si implantation ($1 \times 10^{14} / \text{cm}^2$ at 80 keV and $1 \times 10^{14} / \text{cm}^2$ at 30 keV) into the HfO₂ (10 nm)/*p*-In_{0.53}Ga_{0.47}As (160 nm)/*p*-InP (80 nm)/SI-InP structure. Inset: Contour plot of the HfO₂ film thickness measured by SE across a 2-in wafer. TEM images of (b) a non-annealed sample and (c) a 675°C for 30 s annealed sample. The SIMS measurements were conducted at INTEL Ireland and the TEM analysis was performed by S. B. Newcomb (Glebe Scientific).

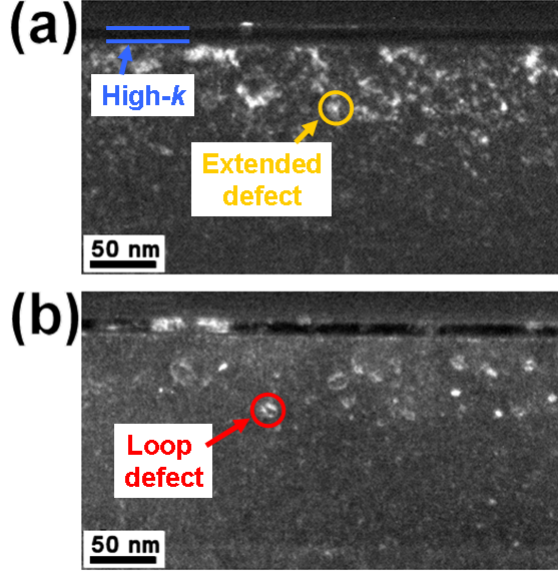


Figure 2.5: TEM images of the Si-implanted ($1 \times 10^{14} / \text{cm}^2$ at 80 keV and $1 \times 10^{14} / \text{cm}^2$ at 30 keV) HfO_2 (10 nm)/ $p\text{-In}_{0.53}\text{Ga}_{0.47}\text{As}$ (160 nm)/ $p\text{-InP}$ (80 nm)/SI-InP structure (a) before and (b) after 675°C for 30 s annealing. The TEM analysis was performed by S. B. Newcomb (Glebe Scientific).

of 1.7%, suggesting that the annealing did not involve the creation of a significant amount of oxide traps. However, a significantly larger distortion of the C-V characteristics was observed on the sample annealed at 725°C. This is consistent with an increase in density of interface traps (D_{it}) in the $\text{In}_{0.53}\text{Ga}_{0.47}\text{As}$ bandgap with anneal temperature. Figure 2.6(c) shows the 100 kHz conductance-voltage (G-V) and C-V characteristics of samples annealed at 675°C, 700°C and 725°C. The impact of the increasing conductance peak with temperature is clearly visible on the C-V characteristics, where it manifests as an increase in stretch out. D_{it} estimates for each anneal temperature were obtained using the conductance method [29]. Although D_{it} calculations using the 100-kHz conductance peaks underestimate the actual D_{it} values, it is interesting to consider the D_{it} trend with anneal temperature. Large D_{it} values of 2.0, 2.3 and $2.7 \times 10^{13} / \text{cm}^2 \cdot \text{eV}$ were obtained for the samples annealed at 675°C, 700°C and 725°C, respectively. This indicates that, in the 675°C to 725°C range, an increase of 25°C increases D_{it} by $\sim 16\%$. Considering the following relationship between the MOSFET subthreshold swing (SS) and D_{it} [30, 31]:

$$SS \approx \left(\frac{k_B T \ln(10)}{q} \right) \left(1 + \frac{q D_{it}}{C_{ox}} \right) \quad (2.3)$$

where k_B is the Boltzmann constant, T is the temperature and C_{ox} is the oxide capacitance, it is clear that this issue is of critical importance for the fabrication of future high-performance $\text{In}_{0.53}\text{Ga}_{0.47}\text{As}$ MOSFETs.

2.4.3 Issues With First Fabricated MOSFETs

Figure 2.7(a) shows a picture of an $\text{In}_{0.53}\text{Ga}_{0.47}\text{As}$ MOSFET fabricated with the “high- k -first + metal-gate last” process. The S/D activation anneal was performed at 650°C for 30 sec in N_2 . We used a lower activation anneal temperature than that of the optimum point predicted by the DOE in order to maintain reasonable D_{it} in the $\text{In}_{0.53}\text{Ga}_{0.47}\text{As}$ bandgap. Figure 2.7(b) shows the drain current (I_d) vs drain-to-source voltage (V_{ds}) characteristics of a $5\text{-}\mu\text{m}$ -gate-length device featuring a 10-nm-thick HfO_2 gate oxide. Although a maximum I_d of 180 mA/mm was achieved at a gate voltage (V_g) of 2 V and a V_{ds} of 2.5 V, a large OFF-state current (I_{OFF}) was observed, even at a V_g of -2 V. This large I_{OFF} is consistent with the unexpected n -type behaviour of the C-V characteristics. Indeed, since the devices are not isolated, any $n\text{-In}_{0.53}\text{Ga}_{0.47}\text{As}$ linking the source and drain terminals outside of the gate area could potentially contribute to the I_{OFF} . Another possibility that should not be ruled out is that the Fermi level could be pinned inside the $\text{In}_{0.53}\text{Ga}_{0.47}\text{As}$ bandgap due to the presence of a large D_{it} arising from the high temperature activation anneal process.

2.5 Conclusion

We studied the effect of the implant activation anneal process on the S/D sheet resistance and gate oxide capacitance as part of the development of a “high- k first + metal-gate last” $\text{In}_{0.53}\text{Ga}_{0.47}\text{As}$ MOSFET. TLM structures were fabricated as part of a Doehlert DOE to investigate an experimental domain of 625°C to 725°C and 15 s to 45 s. While the R_{sheet} model presented a minimum at 715°C for 32 s leading to a minimum R_{sheet} value of $(195.6 \pm 3.4) \Omega/\square$, the ρ_C model was not found to be statistically significant due to a large error in the ρ_C extraction. It is noted that TLM structures with a range of sub-micron spacing between the contacts would significantly reduce the error in the ρ_C extraction and could yield a statistically significant ρ_C model.

Physical analysis was also performed on the sample annealed at 675°C for 30 s (centre point of the experimental domain). The SIMS analysis showed that the activation anneal process did not involve Si ion diffusion within the $p\text{-In}_{0.53}\text{Ga}_{0.47}\text{As}$, while the TEM revealed the formation of characteristic loop defects that have a peak depth of approximately 50 nm. We speculate that these defects could have a significant effect on R_{sheet} and ρ_C . Further investigations to correlate loop defect densities with the R_{sheet} and ρ_C degradation are required.

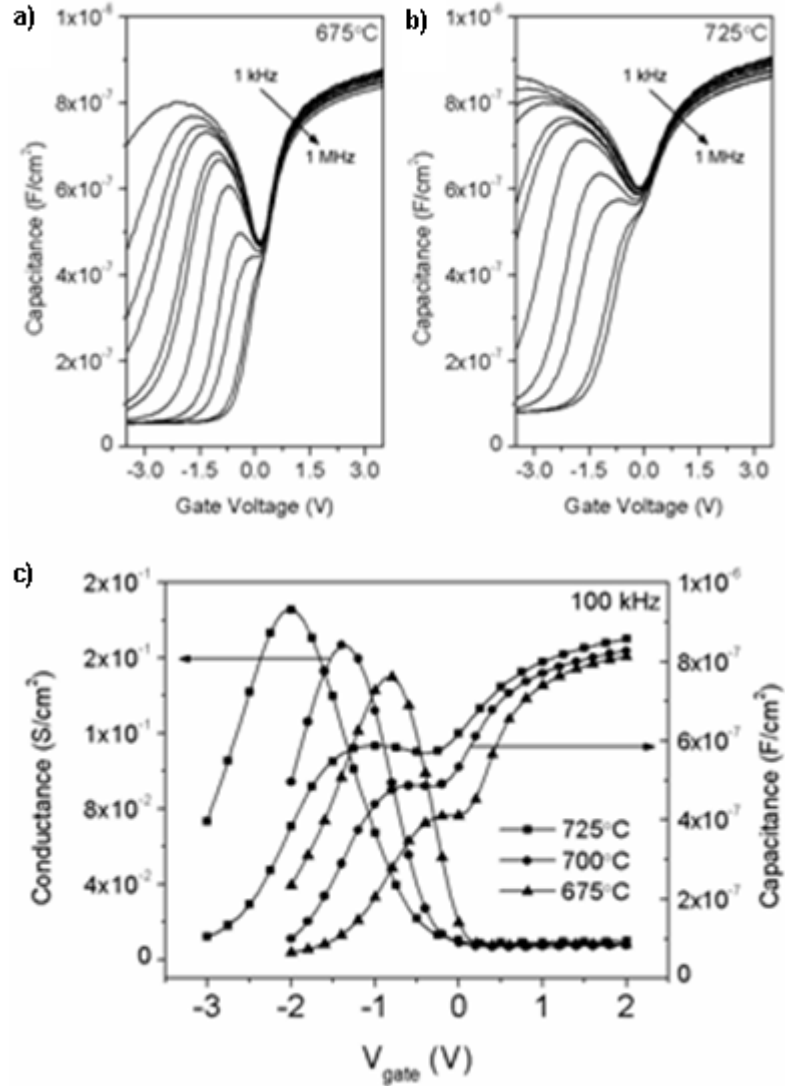


Figure 2.6: Capacitance-voltage (C-V) characteristics of the Pd/HfO₂ (8 nm)/Al₂O₃ (2 nm)/p-In_{0.53}Ga_{0.47}As/p-InP/SI-InP structures annealed for 30 s in N₂ at (a) 675°C and (b) 725°C. The unexpected *n*-type C-V behavior could result from a possible diffusion of unintentional *n*-type dopants from the substrate/epitaxial interface, in agreement with [28]. (c) Conductance-voltage (G-V) and C-V characteristics measured at a frequency of 100 kHz on Pd/HfO₂ (8 nm)/Al₂O₃ (2 nm)/p-In_{0.53}Ga_{0.47}As/p-InP/SI-InP structures annealed at 675°C, 700°C and 725°C for 30 s in N₂.

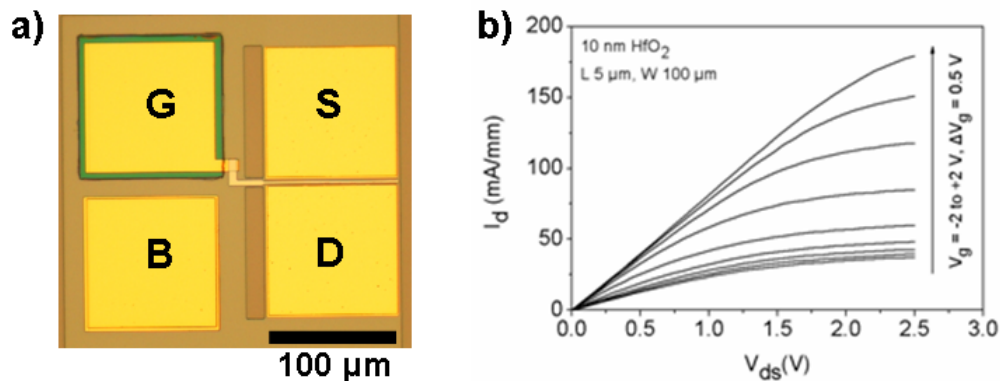


Figure 2.7: (a) Picture of a fabricated $\text{In}_{0.53}\text{Ga}_{0.47}\text{As}$ MOSFET obtained with the “high- k first + metal-gate last” process. G, S, D and B indicate the gate, source, drain and body contacts, respectively. (b) Drain current (I_d) vs drain-source voltage (V_{ds}) for a 5- μm gate length Pd/HfO₂/In_{0.53}Ga_{0.47}As MOSFET for a gate voltage (V_g) varied from -2 V to 2 V with a step of 0.5 V.

The Pd/HfO₂/Al₂O₃/ p -In_{0.53}Ga_{0.47}As/ p -InP/SI-InP MOSCAPs subjected to activation annealing of 675°C to 725°C for 30 s presented reasonable leakage currents below 2.1×10^{-8} A/cm² for electric fields of ~ 3 MV/cm. However, the C-V measurements (performed on p -type MOSCAPs) revealed an unexpected n -type C-V behavior, suggesting a possible diffusion of unintentional n -type dopants arising from the substrate/epitaxial interface. The dispersion of capacitance per decade of frequency in accumulation remained at a low value of 1.7% over the same temperature range, indicating that annealing did not involve the creation of a significant amount of oxide traps. However, the degradation of the C-V characteristics with increasing anneal temperature revealed a $\sim 16\%$ increase in D_{it} for every 25°C increase within the studied temperature range of 675°C to 725°C.

A “high- k first + metal-gate last” In_{0.53}Ga_{0.47}As MOSFET was demonstrated. Although the 5- μm -channel-length device featured a reasonable maximum I_d of 180 mA/mm at a V_g of 2 V and a V_{ds} of 2.5 V, a large I_{OFF} was observed. This large I_{OFF} could originate from (1) the possible diffusion of unintentional n -type dopants in the In_{0.53}Ga_{0.47}As/InP epitaxial layers during the MOVPE growth and/or during the S/D activation anneal process, leading to leakage paths between the source and drain terminals or (2) a high D_{it} caused by the S/D activation anneal process and responsible for the pinning of the Fermi level inside the In_{0.53}Ga_{0.47}As bandgap, preventing the device from switching off.

Bibliography

- [1] T. D. Lin, H. C. Chiu, P. Chang, L. T. Tung, C. P. Chen, M. Hong, J. Kwo, W. Tsai, and Y. C. Wang, "High-performance self-aligned inversion-channel $\text{In}_{0.53}\text{Ga}_{0.47}\text{As}$ metal-oxide-semiconductor field-effect-transistor with $\text{Al}_2\text{O}_3/\text{Ga}_2\text{O}_3(\text{Gd}_2\text{O}_3)$ as gate dielectrics," *Applied Physics Letters*, vol. 93, no. 3, p. 033516, Jul. 2008. [Online]. Available: <http://dx.doi.org/10.1063/1.2956393>
- [2] I. Ok, H. Kim, M. Zhang, T. Lee, F. Zhu, L. Yu, S. Koveshnikov, W. Tsai, V. Tokranov, M. Yakimov, S. Oktyabrsky, and J. C. Lee, "Self-Aligned n- and p-channel GaAs MOSFETs on Undoped and P-type Substrates Using HfO_2 and Silicon Interface Passivation Layer," in *Electron Devices Meeting, 2006. IEDM '06. International*, 2006, p. 1. [Online]. Available: <http://dx.doi.org/10.1109/IEDM.2006.346742>
- [3] H. Zhao, J. Huang, Y.-T. Chen, J. H. Yum, Y. Wang, F. Zhou, F. Xue, and J. C. Lee, "Effects of gate-first and gate-last process on interface quality of $\text{In}_{0.53}\text{Ga}_{0.47}\text{As}$ metal-oxide-semiconductor capacitors using atomic-layer-deposited Al_2O_3 and HfO_2 oxides," *Applied Physics Letters*, vol. 95, no. 25, p. 253501, Dec. 2009. [Online]. Available: <http://dx.doi.org/10.1063/1.3275001>
- [4] F. Ren, J. Kuo, M. Hong, W. Hobson, J. Lothian, J. Lin, H. Tsai, J. Mannaerts, J. Kwo, S.-N. Chu, Y. K. Chen, and A. Cho, " $\text{Ga}_2\text{O}_3(\text{Gd}_2\text{O}_3)/\text{InGaAs}$ enhancement-mode n-channel MOSFETs," *Electron Device Letters, IEEE*, vol. 19, no. 8, p. 309, Aug. 1998. [Online]. Available: <http://dx.doi.org/10.1109/55.704409>
- [5] Y. Xuan, Y. Wu, T. Shen, T. Yang, and P. Ye, "High performance submicron inversion-type enhancement-mode InGaAs MOSFETs with ALD Al_2O_3 , HfO_2 and HfAlO as gate dielectrics," in *Electron Devices Meeting, 2007. IEDM 2007. IEEE International*, 2007, p. 637. [Online]. Available: <http://dx.doi.org/10.1109/IEDM.2007.4419020>
- [6] H. H. Berger, "Contact Resistance and Contact Resistivity," *Journal of The Electrochemical Society*, vol. 119, no. 4, p. 507, Apr. 1972. [Online]. Available: <http://dx.doi.org/10.1149/1.2404240>
- [7] D. H. Doehlert, "Uniform Shell Designs," *Journal of the Royal Statistical Society. Series C (Applied Statistics)*, vol. 19, no. 3, pp. pp. 231–239. [Online]. Available: <http://www.jstor.org/stable/2346327>
- [8] R. J. Young, L. O. Mereni, N. Petkov, G. R. Knight, V. Dimastrodonato, P. K. Hurley, G. Hughes, and E. Pelucchi, "Low-angle misorientation dependence of the optical properties

- of InGaAs/AlInAs quantum wells,” *J. Cryst. Growth*, vol. 312, no. 9, p. 1546, Apr. 2010. [Online]. Available: <http://dx.doi.org/10.1016/j.jcrysgro.2010.01.033>
- [9] Y. Xuan, Y. Wu, H. Lin, T. Shen, and P. Ye, “Submicrometer Inversion-Type Enhancement-Mode InGaAs MOSFET With Atomic-Layer-Deposited Al₂O₃ as Gate Dielectric,” *Electron Device Letters, IEEE*, vol. 28, no. 11, p. 935, Nov. 2007. [Online]. Available: <http://dx.doi.org/10.1109/LED.2007.906436>
- [10] R. Williams, *Modern GaAs Processing Methods*. Artech House Publishers, 1990.
- [11] P. A. F. Herbert, L. P. Floyd, J. I. Braddell, E. M. Baldwin, and W. M. Kelly, “The application of ohmic contacts to nanometric structures,” *Microelectronic Engineering*, vol. 17, no. 1-4, p. 541, Mar. 1992. [Online]. Available: [http://dx.doi.org/10.1016/0167-9317\(92\)90111-4](http://dx.doi.org/10.1016/0167-9317(92)90111-4)
- [12] B. S. Ong, K. L. Pey, C. Y. Ong, C. S. Tan, D. A. Antoniadis, and E. A. Fitzgerald, “Comparison between chemical vapor deposited and physical vapor deposited WSi₂ metal gate for InGaAs n-metal-oxide-semiconductor field-effect transistors,” *Applied Physics Letters*, vol. 98, no. 18, p. 182102, May 2011. [Online]. Available: <http://dx.doi.org/10.1063/1.3584024>
- [13] M. Si, J. J. Gu, X. Wang, J. Shao, X. Li, M. J. Manfra, R. G. Gordon, and P. D. Ye, “Effects of forming gas anneal on ultrathin InGaAs nanowire metal-oxide-semiconductor field-effect transistors,” *Applied Physics Letters*, vol. 102, no. 9, p. 093505, Mar. 2013. [Online]. Available: <http://dx.doi.org/10.1063/1.4794846>
- [14] H. Oh, J. Lin, S. Suleiman, G.-Q. Lo, D. L. Kwong, D. Chi, and S. Lee, “Thermally robust phosphorous nitride interface passivation for ingaas self-aligned gate-first n-mosfet integrated with high-k dielectric,” in *Electron Devices Meeting (IEDM), 2009 IEEE International*, 2009, p. 339. [Online]. Available: <http://dx.doi.org/10.1109/IEDM.2009.5424354>
- [15] Y. Xuan, Y. Wu, and P. Ye, “High-Performance Inversion-Type Enhancement-Mode InGaAs MOSFET With Maximum Drain Current Exceeding 1 A/mm,” *Electron Device Letters, IEEE*, vol. 29, no. 4, pp. 294–296, Apr. 2008. [Online]. Available: <http://dx.doi.org/10.1109/LED.2008.917817>
- [16] Y. Wang, Y.-T. Chen, H. Zhao, F. Xue, F. Zhou, and J. C. Lee, “Impact of SF₆ plasma treatment on performance of TaN-HfO₂-InP metal-oxide-semiconductor field-effect transistor,” *Applied Physics Letters*, vol. 98, no. 4, p. 043506, Jan. 2011. [Online]. Available: <http://dx.doi.org/10.1063/1.3549197>

- [17] H. Zhao, D. Shahrjerdi, F. Zhu, M. Zhang, H.-S. Kim, I. OK, J. H. Yum, S. I. Park, S. K. Banerjee, and J. C. Lee, "Gate-first inversion-type InP metal-oxide-semiconductor field-effect transistors with atomic-layer-deposited Al₂O₃ gate dielectric," *Applied Physics Letters*, vol. 92, no. 23, p. 233508, Jun. 2008. [Online]. Available: <http://dx.doi.org/10.1063/1.2937117>
- [18] A. M. Sonnet, C. L. Hinkle, M. N. Jivani, R. A. Chapman, G. P. Pollack, R. M. Wallace, and E. M. Vogel, "Performance enhancement of *n*-channel inversion type In_xGa_{1-x}As metal-oxide-semiconductor field effect transistor using *ex situ* deposited thin amorphous silicon layer," *Applied Physics Letters*, vol. 93, no. 12, p. 122109, Sep. 2008. [Online]. Available: <http://dx.doi.org/10.1063/1.2991340>
- [19] J. Wan, D. Thompson, and J. Simmons, "Ion implantation induced compositional intermixing in the InGaAs/InP MQW system for wavelength shifted waveguides," *Nuclear Instruments and Methods in Physics Research Section B: Beam Interactions with Materials and Atoms*, vol. 106, no. 1-4, pp. 461 – 465, Dec. 1995. [Online]. Available: [http://dx.doi.org/10.1016/0168-583X\(95\)00753-9](http://dx.doi.org/10.1016/0168-583X(95)00753-9)
- [20] S. L. Ferreira, W. N. dos Santos, C. M. Quintella, B. B. Neto, and J. M. Bosque-Sendra, "Doehlert matrix: a chemometric tool for analytical chemistry-review ," *Talanta*, vol. 63, no. 4, p. 1061, Jul. 2004. [Online]. Available: <http://dx.doi.org/10.1016/j.talanta.2004.01.015>
- [21] M. A. Bezerra, R. E. Santelli, E. P. Oliveira, L. S. Villar, and L. A. Escalera, "Response surface methodology (RSM) as a tool for optimization in analytical chemistry," *Talanta*, vol. 76, no. 5, p. 965, Sep. 2008. [Online]. Available: <http://dx.doi.org/10.1016/j.talanta.2008.05.019>
- [22] R. Oxland, S. W. Chang, X. Li, S. W. Wang, G. Radhakrishnan, W. Priyantha, M. J. H. Van Dal, C. Hsieh, G. Vellianitis, G. Doornbos, K. Bhuiwala, B. Duriez, I. Thayne, R. Droopad, M. Passlack, C. Diaz, and Y. C. Sun, "An Ultralow-Resistance Ultrashallow Metallic Source/Drain Contact Scheme for III-V NMOS," *Electron Device Letters, IEEE*, vol. 33, no. 4, p. 501, Apr. 2012. [Online]. Available: <http://dx.doi.org/10.1109/LED.2012.2185919>
- [23] H.-J. Ueng, D. Janes, and K. Webb, "Error analysis leading to design criteria for transmission line model characterization of ohmic contacts," *Electron Devices, IEEE Transactions on*, vol. 48, no. 4, p. 758, Apr. 2001. [Online]. Available: <http://dx.doi.org/10.1109/16.915721>

-
- [24] I.-H. Kim, "Pd/Si-based ohmic contacts to n-type InGaAs for AlGaAs/GaAs HBTs," *Materials Letters*, vol. 58, no. 6, p. 1107, Feb. 2004. [Online]. Available: <http://dx.doi.org/10.1016/j.matlet.2003.09.001>
- [25] I. Thayne, S. Bentley, M. Holland, W. Jansen, X. Li, D. Macintyre, S. Thoms, B. Shin, J. Ahn, and P. McIntyre, "III-V nMOSFETs - Some issues associated with roadmap worthiness," *Microelectronic Engineering*, vol. 88, no. 7, p. 1070, Jul. 2011. [Online]. Available: <http://dx.doi.org/10.1016/j.mee.2011.03.100>
- [26] A. Alian, G. Brammertz, N. Waldron, C. Merckling, G. Hellings, H. Lin, W. Wang, M. Meuris, E. Simoen, K. D. Meyer, and M. Heyns, "Silicon and selenium implantation and activation in In_{0.53}Ga_{0.47}As under low thermal budget conditions," *Microelectronic Engineering*, vol. 88, no. 2, p. 155, Feb. 2011. [Online]. Available: <http://dx.doi.org/10.1016/j.mee.2010.10.002>
- [27] J. F. Ziegler, "SRIM-2003," *Nuclear Instruments and Methods in Physics Research Section B: Beam Interactions with Materials and Atoms*, vol. 219-220, p. 1027, Jun. 2004. [Online]. Available: <http://dx.doi.org/10.1016/j.nimb.2004.01.208>
- [28] O. Ostinelli, A. R. Alt, R. Lovblom, and C. R. Bolognesi, "Growth and characterization of iron-doped semi-insulating InP buffer layers for Al-free GaInP/GaInAs high electron mobility transistors," *Journal of Applied Physics*, vol. 108, no. 11, p. 114502, Dec. 2010. [Online]. Available: <http://dx.doi.org/10.1063/1.3516490>
- [29] E. H. Nicollian and A. Goetzberger, "The Si-SiO₂ interface: Electrical properties as determined by the metal-insulator-silicon conductance technique," *Bell Syst. Tech. J.*, vol. XLVI, no. 6, p. 1055, Jul. 1967. [Online]. Available: <http://archive.org/details/bstj46-6-1055>
- [30] I. Ferain, C. A. Colinge, and J.-P. Colinge, "Multigate transistors as the future of classical metal-oxide-semiconductor field-effect transistors," *Nature*, vol. 479, p. 310, Nov. 2011. [Online]. Available: <http://dx.doi.org/10.1038/nature10676>
- [31] J. Gu, X. Wang, H. Wu, R. Gordon, and P. Ye, "Variability Improvement by Interface Passivation and EOT Scaling of InGaAs Nanowire MOSFETs," *Electron Device Letters, IEEE*, vol. 34, no. 5, p. 608, May 2013. [Online]. Available: <http://dx.doi.org/.1109/LED.2013.2248114>

Chapter 3

Impact of Forming Gas Annealing on MOSFET Performance

3.1 Introduction

A major obstacle to the development of surface-channel $\text{In}_{0.53}\text{Ga}_{47}\text{As}$ metal-oxide-semiconductor field-effect transistors (MOSFETs) is the integration of high- k gate oxides on the $\text{In}_{0.53}\text{Ga}_{47}\text{As}$ surface with a sufficiently low density of interface traps, border traps and fixed oxide charges, as seen in section 1.2.1 (page 6). Various methods such as $(\text{NH}_4)_2\text{S}$ passivation [1–4], silicon inter-layer [5, 6], interface control layer [7, 8] and InP capping [9], have been explored to reduce defects in high- $k/\text{In}_{0.53}\text{Ga}_{47}\text{As}$ structures. The use of a forming gas (H_2/N_2) anneal (FGA), which is well known for passivating P_b -like defects in SiO_2/Si and high- $k/\text{SiO}_x/\text{Si}$ systems [10, 11], represents an alternative or complimentary approach for reducing defects in high- $k/\text{In}_{0.53}\text{Ga}_{0.47}\text{As}$ structures subsequent to the gate oxide deposition.

Recent studies using metal-oxide-semiconductor capacitors (MOSCAPs) have shown that a FGA can reduce the fixed charge density in $\text{Al}_2\text{O}_3/\text{In}_{0.53}\text{Ga}_{47}\text{As}$ systems [12, 13] and reduce the density of interface traps (D_{it}) near the $\text{In}_{0.53}\text{Ga}_{47}\text{As}$ conduction band in $\text{HfO}_2/n\text{-In}_{0.53}\text{Ga}_{47}\text{As}$ MOSCAPs [14]. However, results reported to date do not indicate any significant influence of FGA on the prominent donor-like defects near mid-gap [1].

In this chapter, we extend on the work reported to date on the effect of FGA on $\text{In}_{0.53}\text{Ga}_{47}\text{As}$ MOSCAPs [12, 13] to investigate the impact of FGA on the performance of surface-channel $\text{In}_{0.53}\text{Ga}_{47}\text{As}$ MOSFETs.

Since our preliminary $\text{In}_{0.53}\text{Ga}_{47}\text{As}$ MOSFET indicated a large OFF-state current (I_{OFF}) (section 2.4, page 41) resulting from a possible diffusion of unintentional n -type dopants from the SI-InP substrate to the $\text{In}_{0.53}\text{Ga}_{47}\text{As}$ channel during the metal-organic vapor phase epitaxy (MOVPE) growth and/or during the source and drain (S/D) activation anneal, we modified our

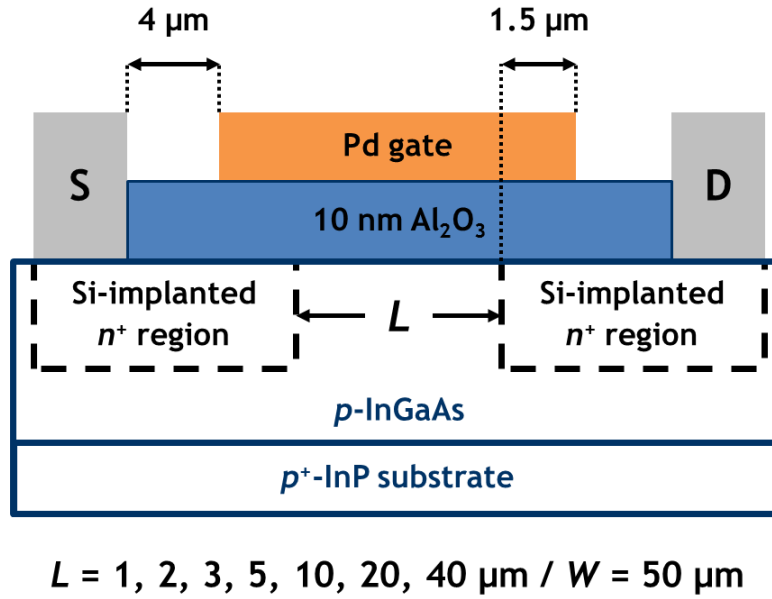


Figure 3.1: Schematic cross-sectional diagram of a surface-channel $\text{In}_{0.53}\text{Ga}_{0.47}\text{As}$ MOSFET with a 10-nm-thick ALD Al_2O_3 dielectric and a Pd gate. The nominal gate (L) is 1, 2, 3, 5, 10, 20 or 40 μm and the width (W) is 50 μm . The overlap of the Pd gate over the Si-implanted n^+ regions is 1.5 μm and the separation between the Pd gate contact and the source (S) or drain (D) contact is 4 μm .

device wafer structure and fabrication process flow in order to mitigate this issue. We used a much thicker (2 μm) $\text{In}_{0.53}\text{Ga}_{0.47}\text{As}$ layer, replaced the SI-InP substrate by a p^+ InP substrate and further reduced the thermal budget of the S/D activation anneal process.

3.2 Samples preparation

Surface-channel MOSFETs (Figure 3.1) and MOSCAP were fabricated on a 2- μm -thick Zn-doped ($4 \times 10^{17} / \text{cm}^3$) $p\text{-In}_{0.53}\text{Ga}_{0.47}\text{As}$ layer grown on a 2-inch p^+ InP wafer by MOVPE. A dedicated lithography mask set was designed for the fabrication of the devices (Appendix B). The $\text{In}_{0.53}\text{Ga}_{0.47}\text{As}$ surface passivation prior to gate oxide deposition was an immersion in 10% $(\text{NH}_4)_2\text{S}$ at room temperature for 20 min, which was found to be an optimum in terms of interface state reduction and for the suppression of native oxide formation [1, 2]. The transfer time to the atomic layer deposition (ALD) reactor after surface passivation was 3 to 5 min. A 10-nm-thick Al_2O_3 gate oxide film was formed by ALD using alternating pulses of trimethyl-aluminum $[\text{Al}(\text{CH}_3)_3]$ (TMA) and H_2O precursors at 250°C. The S/D regions were selectively implanted

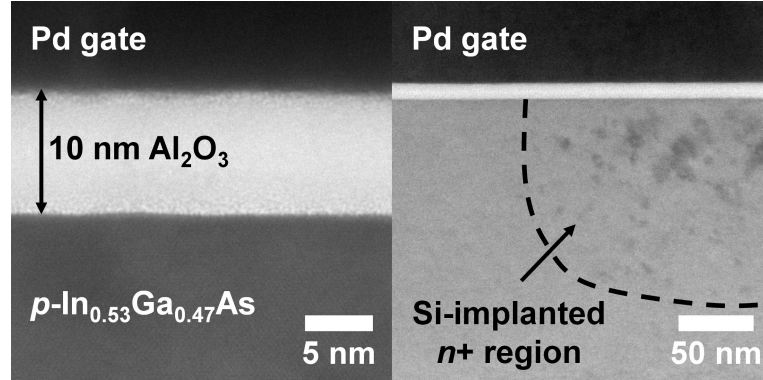


Figure 3.2: TEM images (a) through the gate stack region of the MOSFET confirming the 10-nm Al_2O_3 gate oxide thickness and (b) through the gate overlap region, showing the implant defects in the Si-implanted n^+ region. The TEM analysis was performed by M. Schmidt. (Tyndall National Institute)

with a Si dose of $1 \times 10^{14} / \text{cm}^2$ at 80 keV and $1 \times 10^{14} / \text{cm}^2$ at 30 keV. Based on the results obtained in Chapter 2, a rapid thermal anneal (RTA) process of 600°C for 15 s in a N_2 atmosphere was selected for the activation of the implant. A 140-nm-thick SiO_2 field oxide was formed by electron beam evaporation and liftoff to minimize the gate pad capacitance. Non-self-aligned ohmic contacts were defined by lithography, selective wet etching of the Al_2O_3 in dilute HF and electron beam evaporation of a Au (14 nm)/Ge (14 nm)/Au (14 nm)/Ni (11 nm)/Au (200 nm) metal stack [15]. A 200-nm-thick Pd gate was defined by electron beam evaporation and liftoff. Tests confirmed the absence of delamination of the Pd metal following FGA. A 300°C for 30 min FGA was carried out in an open tube furnace.

The finished devices had a nominal gate length (L) of 1, 2, 3, 5, 10, 20, 40 μm with a 1.5 μm gate metal overlap over the Si-implanted S/D regions, 4- μm gate contact to source or drain contact separation and a 50- μm gate width (Figure 3.1). Relatively long channel length devices were intentionally selected for the study to allow the effect of the FGA process on the electrical properties of the $\text{In}_{0.53}\text{Ga}_{0.47}\text{As}$ MOSFETs to be examined in the absence of short channel effects.

3.3 Results and Discussion

3.3.1 Transmission Electron Microscopy Analysis of Gate Stack and Implanted Regions

Cross-sectional transmission electron microscopy (TEM) images through the gate oxide region and through the implanted area at the end of device fabrication are shown in Figure 3.2(a) and (b), respectively. Figure 3.2(a) confirms the 10 nm Al_2O_3 film thickness, which corresponds to

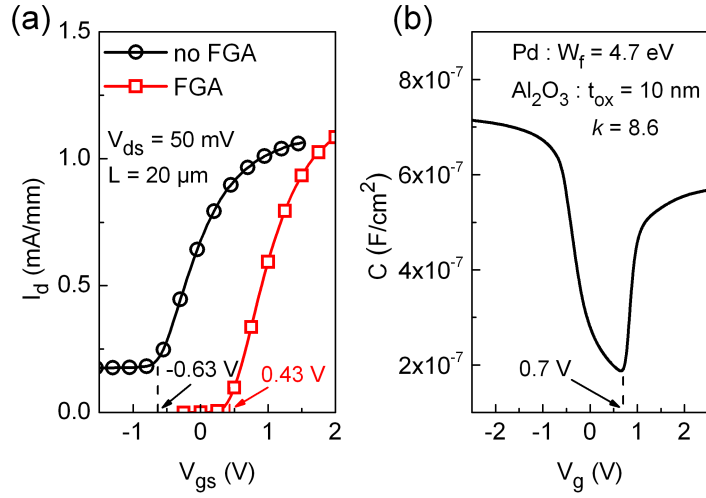


Figure 3.3: I_d - V_{gs} obtained on 20- μm -gate-length and 50- μm -gate-width MOSFETs at $V_{ds} = 50 \text{ mV}$ before and after FGA. The MOSFETs feature a V_T of -0.63 and 0.43 V before and after FGA, respectively. (b) Q-S C-V simulation of the Pd/Al₂O₃/ p -In_{0.53}Ga_{0.47}As gate stack obtained using a Poisson-Schrödinger simulator [20]. The ideal V_T of 0.7 V was obtained based on a Pd work function of 4.7 eV [21], a 10-nm-thick Al₂O₃ film with a k -value of 8.6 , and a p -In_{0.53}Ga_{0.47}As doping level of $4 \times 10^{17} / \text{cm}^3$.

the nominal value from the ALD process and a growth rate per cycle of $1 \text{ \AA}/\text{cycle}$. There is no evidence of an interface oxide between the In_{0.53}Ga_{0.47}As surface and the Al₂O₃ layer, consistent with previous reports for the optimised (NH₄)₂S process and subsequent ALD Al₂O₃ formation [1], and with the reported “self-cleaning” effect of ALD on GaAs [16–18] and on InGaAs [19] surfaces. Figure 3.2(b) shows the remaining implant defects in the gate overlap region after activation anneal and FGA, indicating that these two anneals are not sufficient to fully remove the defects caused by the Si implantation process.

3.3.2 Fixed Oxide Charge Passivation, Threshold Voltage Shift and OFF-State Leakage Reduction

Figure 3.3(a) shows the drain current (I_d) vs gate-to-source voltage (V_{gs}) characteristics at a drain-to-source voltage (V_{ds}) = 50 mV obtained on a 20- μm -gate-length and 50- μm -gate-width device before and after FGA. The threshold voltage (V_T)¹ shifts from -0.63 V before FGA to 0.43 V after FGA. The negative V_T before FGA indicates the presence of fixed positive charges within the Al₂O₃. Figure 3.3(b) shows a quasi-static (Q-S) capacitance-voltage (C-V) of the Pd/Al₂O₃/ p -In_{0.53}Ga_{0.47}As gate stack obtained using a self consistent Poisson-Schrödinger

¹The V_T is extracted using the linear extrapolation method.

simulator [20]. The asymmetric shape of the simulated Q-S C-V response, due to the very low density of states of the $\text{In}_{0.53}\text{Ga}_{0.47}\text{As}$ conduction band, is not experimentally observed. This absence of asymmetry has been attributed to the presence of additional traps located at energy levels aligned with the $\text{In}_{0.53}\text{Ga}_{0.47}\text{As}$ conduction band [22]. In the simulation, the metal work function (W_f) of Pd on Al_2O_3 , the Al_2O_3 oxide thickness (t_{ox}) and k -value and the $\text{In}_{0.53}\text{Ga}_{0.47}\text{As}$ p -type dopant density (N_a) were set to 4.7 eV [21], 10 nm, 8.6^2 [23] and $4 \times 10^{17} / \text{cm}^3$, respectively. Considering an ideal V_T of 0.7 V [Figure 3.3(b)] and an oxide capacitance (C_{ox}) of $7.6 \times 10^{-7} \text{ F/cm}^2$, we calculated an equivalent density of fixed positive oxide charge at the $\text{Al}_2\text{O}_3/p\text{-In}_{0.53}\text{Ga}_{0.47}\text{As}$ interface before and after FGA of $6.3 \times 10^{12} / \text{cm}^2$ and $1.3 \times 10^{12} / \text{cm}^2$, respectively. Recent studies of $\text{Al}_2\text{O}_3/\text{In}_{0.53}\text{Ga}_{0.47}\text{As}$ MOSCAPs over n - and p -type $\text{In}_{0.53}\text{Ga}_{0.47}\text{As}$ prior to FGA reported fixed positive oxide charge densities of $\sim 1 \times 10^{19} / \text{cm}^3$ distributed throughout the Al_2O_3 layer [12]. A density of $\sim 1 \times 10^{19} / \text{cm}^3$ throughout a 10-nm-thick Al_2O_3 film corresponds to an equivalent surface density at the $\text{Al}_2\text{O}_3/\text{In}_{0.53}\text{Ga}_{0.47}\text{As}$ interface of $\sim 1 \times 10^{13} / \text{cm}^2$, which is consistent with our pre-FGA value of $6.3 \times 10^{12} / \text{cm}^2$. The reduction in the fixed positive oxide charge after the FGA is also in agreement with [12, 13].

The origin of the fixed positive charge has been assigned to Al dangling bonds based on theoretical modelling [13], and its reduction following the FGA process is consistent with hydrogen passivation of the dangling bond sites in the Al_2O_3 .

The fixed charge within the Al_2O_3 gate oxide can have a significant impact on the MOSFET behaviour. We calculated that, for an $\text{In}_{0.53}\text{Ga}_{0.47}\text{As}$ N_a of $4 \times 10^{17} / \text{cm}^3$, fixed positive charge densities in excess of $2 \times 10^{12} / \text{cm}^2$ are sufficient to create an inversion layer at the $\text{Al}_2\text{O}_3/p\text{-In}_{0.53}\text{Ga}_{0.47}\text{As}$ interface.³ This indicates that the fixed positive oxide charge density of $6.3 \times 10^{12} / \text{cm}^2$ before FGA is sufficient to invert the $p\text{-In}_{0.53}\text{Ga}_{0.47}\text{As}$ surface, while the fixed positive oxide charge density of $1.3 \times 10^{12} / \text{cm}^2$ after FGA is not. The strong inversion layer before FGA can be modulated in the region under the Pd gate. However, this inversion charge is also present in the region outside the area defined by the gate, and is subsequently referred to as the “peripheral inversion region”. We suggest that the high I_{OFF} and poor subthreshold swing (SS) of the MOSFET before FGA [Figure 3.4(a)] are due to the presence of a peripheral inversion region that cannot be controlled by the gate voltage. The $\log I_d\text{-}V_{gs}$ characteristics measured at 20°C and -50°C before FGA [Figure 3.4(a)] reveals that the I_{OFF} (I_d at $V_{gs}\text{-}V_T < 0$) is only weakly temperature dependent, which further indicates that the I_{OFF} before FGA is due to the

²The k -value of 8.6 for Al_2O_3 was obtained from the slope of the capacitance equivalent thickness in accumulation *vs* t_{ox} for $\text{Al}_2\text{O}_3/\text{In}_{0.53}\text{Ga}_{0.47}\text{As}$ metal-oxide-semiconductor (MOS) structures with t_{ox} ranging from 5 to 20 nm. These measurements were performed by Y. Y. Gomeniuk (Lashkaryov Institute of Semiconductor Physics, Kiev, Ukraine).

³For an $\text{In}_{0.53}\text{Ga}_{0.47}\text{As}$ N_a of $4 \times 10^{17} / \text{cm}^3$, the maximum depletion width is 50 nm (where the intrinsic carrier density (n_i) for $\text{In}_{0.53}\text{Ga}_{0.47}\text{As}$ is taken as $6.3 \times 10^{11} / \text{cm}^3$ [24]). Hence, the total density of charge resulting from the ionized acceptor at the onset of inversion is $2 \times 10^{12} / \text{cm}^2$. Positive oxide charge densities in Al_2O_3 in excess of $2 \times 10^{12} / \text{cm}^2$ will result in inversion of the $p\text{-In}_{0.53}\text{Ga}_{0.47}\text{As}$ surface.

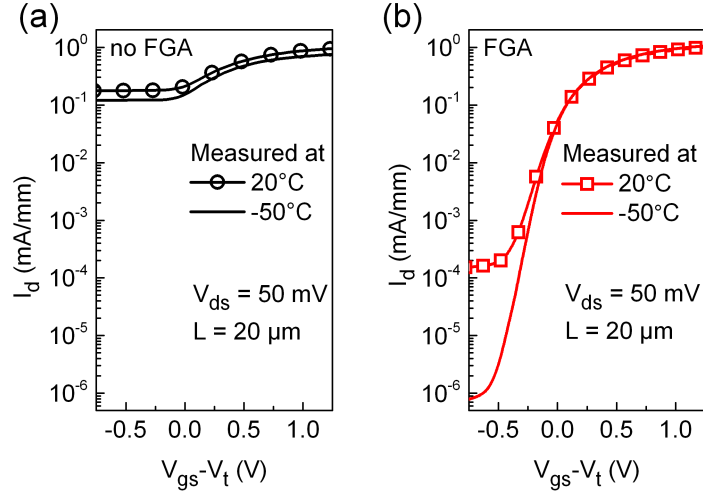


Figure 3.4: Comparison of the 20°C and -50°C $\log I_d-V_{gs}$ measured at $V_{ds} = 50$ mV on 20- μm -gate-length and 50- μm -gate-width MOSFETs (a) before and (b) after FGA. The $\log I_d-V_{gs}$ values are shown with matched gate overdrive ($V_{gs}-V_T$).

peripheral inversion region. It is noted that the formation of a peripheral inversion depends on the substrate doping concentration, the oxide capacitance, and the density and sign of the fixed oxide charge. Moreover, a high leakage current due to a peripheral inversion region will not be observed on a “ring-gate” MOSFET, where the gate encircles the drain and obviates the need for isolation [25]. Figure 3.4(b) shows a I_{OFF} reduction of three orders of magnitude (ON-state-to-OFF-state current ratio $(I_{ON}/I_{OFF})^4 \sim 10^4$) due to the removal of the peripheral inversion region following the FGA process. The temperature dependence of the I_{OFF} after FGA is evident and the I_{ON}/I_{OFF} at -50°C is $\sim 10^6$.

Following the FGA process, we obtained a SS of 150 mV/dec. This SS yielded a D_{it} value in the upper part of the $\text{In}_{0.53}\text{Ga}_{47}\text{As}$ bandgap of $\sim 5.8 \times 10^{12} / \text{cm}^2 \cdot \text{eV}$, in line with the literature values reported for the $\text{Al}_2\text{O}_3/\text{In}_{0.53}\text{Ga}_{47}\text{As}$ system [Figure 1.8(b), page 11)]. It is noted that for the pre-FGA case, the SS is dominated by the peripheral leakage current and cannot be used for interface state density determination.

3.3.3 MOSCAPs Behaviour and Density of Interface Traps

Figure 3.5(a) and (b) show the multi-frequency (M-F) C-V characteristics of Pd/ Al_2O_3 / p - $\text{In}_{0.53}\text{Ga}_{47}\text{As}$ MOSCAPs before and after the FGA. These MOSCAPs are adjacent to the MOS-

⁴ I_{ON}/I_{OFF} is defined here as the ratio between the maximum and minimum drain currents, irrespective of the gate voltage swing.

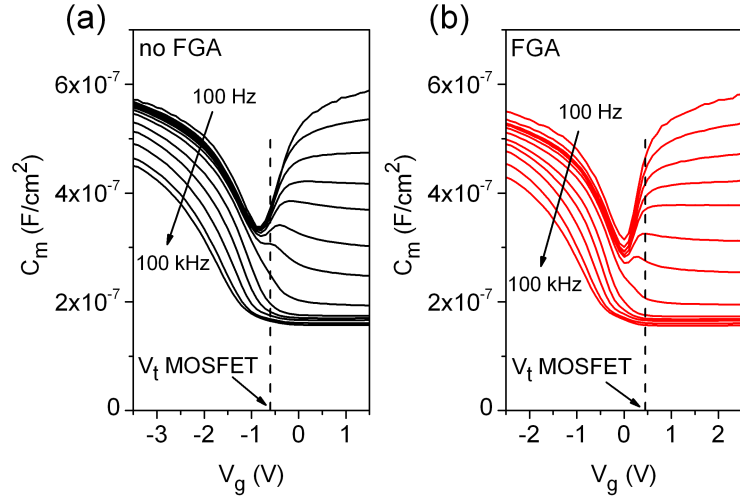


Figure 3.5: Multi-frequency (M-F) capacitance-voltage (C-V) characteristics of Pd/Al₂O₃/p-In_{0.53}Ga_{0.47}As MOSCAPs measured from 100 Hz to 100 kHz (a) before and (b) after FGA. The V_T of the corresponding MOSFETs is highlighted on the C-V characteristics.

FETs on the same wafer. The passivation of fixed positive charges within the Al₂O₃ after FGA results in a C-V shift consistent with the shift observed on the I_d - V_{gs} characteristics shown in Figure 3.3(a). The V_T of the corresponding MOSFETs is highlighted in Figure 3.5(a) and (b). The comparison of the 100-Hz C-V responses at the on-set of inversion shows a steeper slope after FGA, indicating a reduction in D_{it} near the p-In_{0.53}Ga_{0.47}As conduction band, consistent with [14].

There has been debate over the expected M-F C-V response of In_{0.53}Ga_{0.47}As MOSCAPs in inversion and the method to identify genuine surface inversion [26]. The availability of the MOSCAPs and adjacent MOSFETs on the same wafer allows the V_T , obtained from the MOSFETs, to be identified on the M-F C-V response of the Pd/Al₂O₃/p-In_{0.53}Ga_{0.47}As MOSCAPs. In addition, the M-F C-V response for gate voltage (V_g) > V_T illustrates the behaviour of a Pd/Al₂O₃/p-In_{0.53}Ga_{0.47}As MOSCAP beyond inversion. Figure 3.5(a) and (b) show that, beyond inversion, the capacitance as a function of applied voltage increases and then acquires an approximately constant value. The value of the capacitance in inversion increases with decreasing frequency up to a maximum value set by the oxide capacitance. This frequency dependent C-V behaviour has also been obtained following an optimized (NH₄)₂S treatment of *n*- and p-In_{0.53}Ga_{0.47}As prior to ALD Al₂O₃ deposition [3].

Figure 3.6 shows the parallel conductance (G_p) normalized to angular frequency (ω) plotted as a function of frequency (f) for a selected V_g . A clear G_p/ω peak was observed for $V_g = -1.9$ V before FGA and $V_g = -0.8$ V after FGA. Considering the V_T shift induced by the FGA and

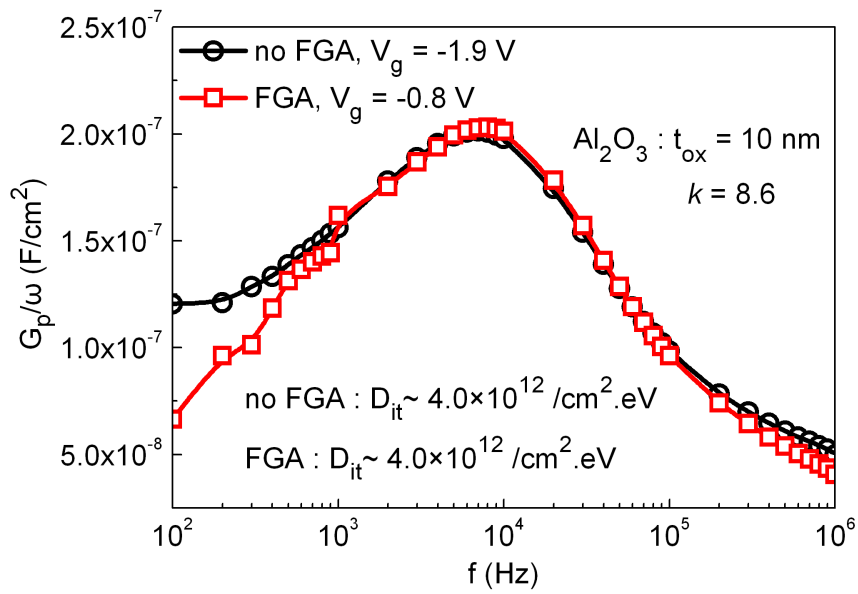


Figure 3.6: Normalized parallel conductance (G_p/ω) vs frequency (f) obtained with the conductance method [27, 28] for a 10-nm-thick Al_2O_3 film with a k -value of 8.6. The D_{it} extraction at $V_g = -1.9 \text{ V}$ before FGA and at $V_g = -0.8 \text{ V}$ after FGA yielded the same value of $\sim 4.0 \times 10^{12} / \text{cm}^2 \cdot \text{eV}$.

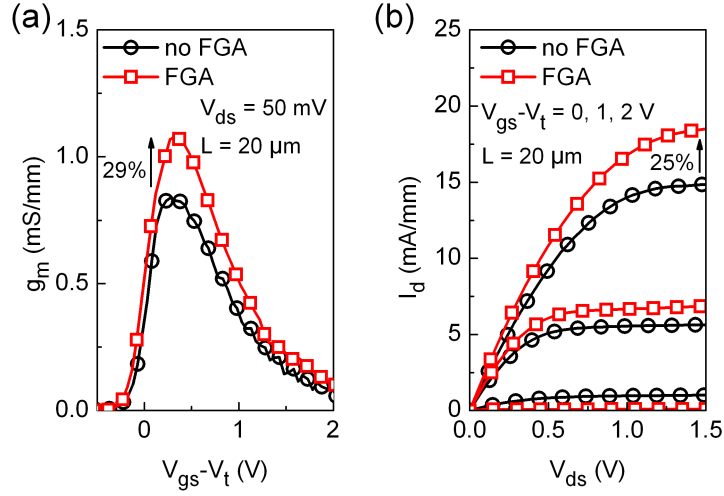


Figure 3.7: (a) Transconductance (g_m) versus gate overdrive ($V_{gs} - V_T$) and (b) $I_d - V_{ds}$ characteristics obtained on 20- μm -gate-length and 50- μm -gate-width MOSFETs before and after FGA. After FGA, the peak g_m and drive current increase by 29% and 25%, respectively.

that both V_g values corresponded to the same $V_g - V_T$ of ~ -1.25 V, we assumed that the Fermi level in both cases was at the same energy position. The values of D_{it} and trap capture time constant (τ) were obtained using the conductance method [27, 28]. The FGA did not reduce the D_{it} as values of $\sim 4.0 \times 10^{12} / \text{cm}^2 \cdot \text{eV}$ were extracted before and after FGA. These D_{it} values are in reasonable agreement with the D_{it} of $\sim 5.8 \times 10^{12} / \text{cm}^2 \cdot \text{eV}$ extracted from the SS of the MOSFETs post FGA. The FGA did not have a significant impact on τ as values of ~ 48.5 μs and ~ 43.8 μs were obtained before and after FGA, respectively.

3.3.4 Transconductance, Drive Current and Effective Mobility Improvement

Figure 3.7(a) compares the transconductance (g_m) vs gate overdrive ($V_{gs} - V_T$) obtained on 20- μm -gate-length and 50- μm -gate-width MOSFETs before and after FGA. Whereas the peak g_m increases by 29% after FGA, the higher field values of g_m only slightly improve with FGA.

Figure 3.7(b) shows the drain current versus drain voltage ($I_d - V_{ds}$) output characteristics obtained for an $\text{In}_{0.53}\text{Ga}_{0.47}\text{As}$ MOSFET with a gate length of 20 μm and a gate width of 50 μm before and after FGA. The device exhibits well behaved output characteristics with drain current saturation for $V_{ds} > V_{gs} - V_T$. The drive current at a 2-V gate overdrive was 14.8 mA/mm before FGA and 18.5 mA/mm after FGA, representing a 25% improvement with FGA. These drive current values are comparable to, or slightly higher, than other published values for surface channel $\text{In}_{0.53}\text{Ga}_{0.47}\text{As}$ MOSFETs [5, 29], assuming drive current scaling with $1/L$.

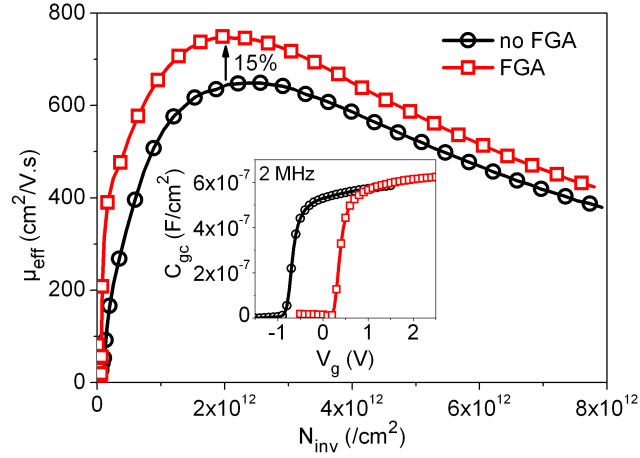


Figure 3.8: Effective mobility (μ_{eff}) versus inversion charge density (N_{inv}) before and after FGA. The peak μ_{eff} increases by 15% after FGA. (Inset) 2-MHz gate-to-channel C_{gc} split C-V characteristics before and after FGA.

Figure 6.17 shows the effective mobility (μ_{eff}) as a function of the inversion-charge density (N_{inv}), extracted using the I_d - V_{gs} characteristics (Figure 3.3(a)) and the 2-MHz gate-to-channel split C-V characteristics (inset Figure 6.17). The parasitic overlap capacitances were removed from the measured gate-to-channel capacitance (C_{gc}) using the method reported in [30]. Devices with L ranging from 1 μm to 40 μm were used to extract the source and drain series resistance (R_{SD}) values used in the μ_{eff} . R_{SD} values were evaluated at $V_{ds} = 50$ mV to ensure devices operation in the linear region. The devices featured a R_{SD} of 235 Ω and 103 Ω before and after FGA, respectively. The peak μ_{eff} increased from 650 $\text{cm}^2/\text{V.s}$ to 750 $\text{cm}^2/\text{V.s}$ with FGA. This 15% improvement in the peak μ_{eff} after FGA is consistent with a reduction in the positive oxide charge, which reduces the coulomb scattering component. A reduction in the D_{it} near the $\text{In}_{0.53}\text{Ga}_{47}\text{As}$ conduction band, as suggested by the C-V characteristics before and after FGA (Figure 3.5(a) and (b)) and consistent with [14], could also contribute to the increase in peak μ_{eff} .

Figure 3.9 shows that the extracted peak μ_{eff} after FGA is comparable to other published values for surface-channel $\text{In}_{0.53}\text{Ga}_{47}\text{As}$ MOSFETs [5, 29, 31–34]. It is noted that the $\text{In}_{0.53}\text{Ga}_{47}\text{As}$ channel N_a of $4 \times 10^{17} / \text{cm}^3$ used in this study is four to twenty times higher than the values used in the comparative publications. The published experimental values for the peak μ_{eff} in surface-channel $\text{In}_{0.53}\text{Ga}_{47}\text{As}$ MOSFETs remain well below the theoretical values expected for reasonable values of fixed oxide charge, interface traps and surface roughness, where peak values of $\sim 4000 \text{ cm}^2/\text{V.s}$ are calculated [35]. This discrepancy could relate to the approach typically

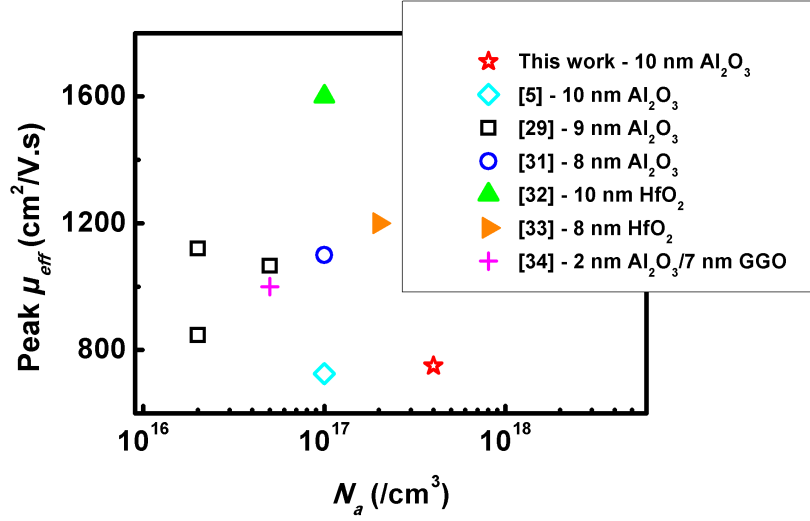


Figure 3.9: Extracted peak effective mobility (μ_{eff}) vs $\text{In}_{0.53}\text{Ga}_{0.47}\text{As}$ channel doping (N_a) compared to literature values obtained in [5, 29, 31–34]. GGO stands for gallium gadolinium oxide.

employed to determine μ_{eff} . Indeed, for the calculation of N_{inv} on the x -axis of Figure 6.17, it is assumed that the integral of C_{gc} for $V_g > V_T$ yields N_{inv} , and is unaffected by trapped charges in interface and oxide traps. However, a number of recent publications have reported the presence of interface traps [22, 36, 37] and oxide traps [37–40] located at energy levels aligned with the $\text{In}_{0.53}\text{Ga}_{0.47}\text{As}$ conduction band. In this case, the integral of C_{gc} will contain contributions from both free charge and trapped charge, which will result in an overestimation of N_{inv} and a corresponding underestimation of μ_{eff} . No corrections for the effect of bulk oxide charge trapping have been applied in this work in order to allow a fair comparison with the μ_{eff} values reported in [5, 29, 31]. However, a detailed study of this issue will be presented in Chapter 4 and Chapter 5.

3.3.5 Junction Leakage Reduction

The FGA also improves the current-voltage behaviour of the source or drain-to-substrate n^+/p junctions. Figure 3.10(a) shows the current-voltage (I-V) characteristics for the n^+/p junctions before and after FGA. The saturation current in reverse bias is reduced by more than two orders of magnitude as a result of the FGA. The measurement temperature (223 K to 293 K) and applied bias (0.1 V to 0.5 V) dependence of the n^+/p junction characteristics before and after the FGA is shown in Figure 3.10(b). The activation energy (E_a) extrapolated to zero bias from Figure 3.10(b) yields values of 0.37 eV and 0.40 eV before and after the FGA, respectively. The

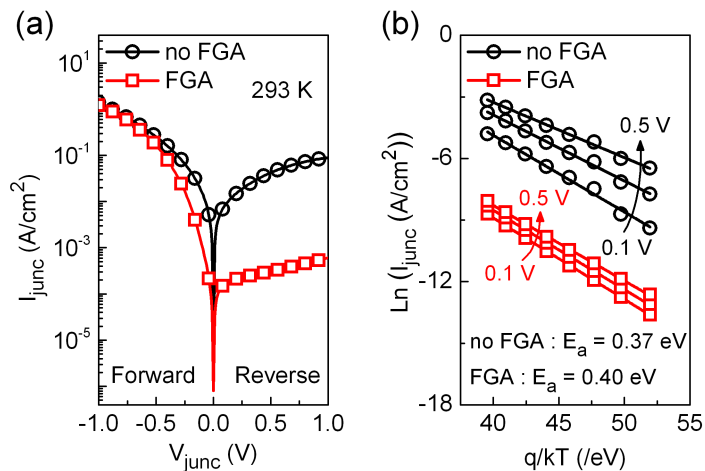


Figure 3.10: a) I-V characteristics of the n^+/p $\text{In}_{0.53}\text{Ga}_{0.47}\text{As}$ junction measured on a MOSFET at 293 K before and after FGA. (b) Arrhenius plot from 223 to 293 K for reverse bias going from 0.1 to 0.5 V applied to implanted n^+/p junctions before and after FGA. The area of the n^+/p junction diodes is $10^4 \mu\text{m}^2$. The activation energy (E_a) values are 0.37 eV and 0.40 eV before and after FGA, respectively.

extracted E_a indicates thermal generation of electron-hole pairs through mid-gap states in the $\text{In}_{0.53}\text{Ga}_{0.47}\text{As}$ depletion region as the mechanism of the reverse bias leakage both before and after FGA. The reduction of leakage current density is consistent with passivation of the mid-gap states by the FGA. Both before and after FGA, the E_a decreases with increasing reverse bias, which is characteristic of a field-enhanced (Poole-Frenkel)-type emission process [41].

3.4 Conclusion

We demonstrated that a 300°C , 30 min FGA dramatically improved the performance of surface-channel $\text{In}_{0.53}\text{Ga}_{0.47}\text{As}$ MOSFETs with Al_2O_3 as gate dielectric. The FGA process reduced the density of fixed positive charges in the Al_2O_3 , which removed a parasitic peripheral inversion region, and resulted in an increase in I_{ON}/I_{OFF} by three orders of magnitude. The FGA improved the g_m , drive current and peak μ_{eff} by 29%, 25% and 15%, respectively. C-V measurements of MOSCAPs revealed that the FGA reduced D_{it} near the $\text{In}_{0.53}\text{Ga}_{0.47}\text{As}$ conduction band but did not reduce the mid-gap D_{it} . A reduction of two orders of magnitude was also observed in the reverse bias leakage current density in the Si-implanted $\text{In}_{0.53}\text{Ga}_{0.47}\text{As}$ n^+/p junctions in the S/D regions of the MOSFETs, consistent with the passivation of mid-gap states in the $\text{In}_{0.53}\text{Ga}_{0.47}\text{As}$ by the FGA.

The fabricated devices featured sufficient electrical performance to be used as test vehicles for the development of alternative electrical characterization techniques, which will be presented in Chapter 4 and Chapter 5.

Bibliography

- [1] É. O'Connor, B. Brennan, V. Djara, K. Cherkaoui, S. Monaghan, S. B. Newcomb, R. Contreras, M. Milojevic, G. Hughes, M. E. Pemble, R. M. Wallace, and P. K. Hurley, "A systematic study of $(\text{NH}_4)_2\text{S}$ passivation (22%, 10%, 5%, or 1%) on the interface properties of the $\text{Al}_2\text{O}_3/\text{In}_{0.53}\text{Ga}_{0.47}\text{As}/\text{InP}$ system for n -type and p -type $\text{In}_{0.53}\text{Ga}_{0.47}\text{As}$ epitaxial layers," *Journal of Applied Physics*, vol. 109, no. 2, p. 024101, Jan. 2011. [Online]. Available: <http://dx.doi.org/10.1063/1.3533959>
- [2] B. Brennan, M. Milojevic, C. Hinkle, F. Aguirre-Tostado, G. Hughes, and R. Wallace, "Optimisation of the ammonium sulphide $(\text{NH}_4)_2\text{S}$ passivation process on $\text{In}_{0.53}\text{Ga}_{0.47}\text{As}$," *Applied Surface Science*, vol. 257, no. 9, p. 4082, Feb. 2011. [Online]. Available: <http://dx.doi.org/10.1016/j.apsusc.2010.11.179>
- [3] É. O'Connor, S. Monaghan, K. Cherkaoui, I. M. Povey, and P. K. Hurley, "Analysis of the minority carrier response of n -type and p -type $\text{Au}/\text{Ni}/\text{Al}_2\text{O}_3/\text{In}_{0.53}\text{Ga}_{0.47}\text{As}/\text{InP}$ capacitors following an optimized $(\text{NH}_4)_2\text{S}$ treatment," *Applied Physics Letters*, vol. 99, no. 21, p. 212901, Nov. 2011. [Online]. Available: <http://dx.doi.org/10.1063/1.3663535>
- [4] J. J. Gu, A. T. Neal, and P. D. Ye, "Effects of $(\text{NH}_4)_2\text{S}$ passivation on the off-state performance of 3-dimensional InGaAs metal-oxide-semiconductor field-effect transistors," *Applied Physics Letters*, vol. 99, no. 15, p. 152113, Oct. 2011. [Online]. Available: <http://dx.doi.org/10.1063/1.3651754>
- [5] A. M. Sonnet, C. L. Hinkle, M. N. Jivani, R. A. Chapman, G. P. Pollack, R. M. Wallace, and E. M. Vogel, "Performance enhancement of n -channel inversion type $\text{In}_x\text{Ga}_{1-x}\text{As}$ metal-oxide-semiconductor field effect transistor using *ex situ* deposited thin amorphous silicon layer," *Applied Physics Letters*, vol. 93, no. 12, p. 122109, Sep. 2008. [Online]. Available: <http://dx.doi.org/10.1063/1.2991340>
- [6] F. Zhu, H. Zhao, I. Ok, H. S. Kim, J. Yum, J. C. Lee, N. Goel, W. Tsai, C. K. Gaspe, and M. B. Santos, "Effects of Anneal and Silicon Interface Passivation Layer Thickness on Device Characteristics of $\text{In}_{0.53}\text{Ga}_{0.47}\text{As}$ Metal-Oxide-Semiconductor Field-Effect Transistors," *Electrochemical and Solid-State Letters*, vol. 12, no. 4, p. H131, Jan. 2009. [Online]. Available: <http://dx.doi.org/10.1149/1.3074298>
- [7] A. O'Mahony, S. Monaghan, G. Provenzano, I. M. Povey, M. G. Nolan, É. O'Connor, K. Cherkaoui, S. B. Newcomb, F. Crupi, P. K. Hurley, and M. E. Pemble, "Structural and electrical analysis of the atomic layer deposition of $\text{HfO}_2/n\text{-In}_{0.53}\text{Ga}_{0.47}\text{As}$ capacitors with and without an Al_2O_3 interface control layer," *Applied Physics Letters*, vol. 97, no. 5, p. 052904, Aug. 2010. [Online]. Available: <http://dx.doi.org/10.1063/1.3473773>

- [8] S. Monaghan, A. O'Mahony, K. Cherkaoui, E. O'Connor, I. M. Povey, M. G. Nolan, D. O'Connell, M. E. Pemble, P. K. Hurley, G. Provenzano, F. Crupi, and S. B. Newcomb, "Electrical analysis of three-stage passivated $\text{In}_{0.53}\text{Ga}_{0.47}\text{As}$ capacitors with varying HfO_2 thicknesses and incorporating an Al_2O_3 interface control layer," vol. 29, no. 1. AVS, Jan. 2011, p. 01A807. [Online]. Available: <http://dx.doi.org/10.1116/1.3532826>
- [9] M. Radosavljevic, B. Chu-Kung, S. Corcoran, G. Dewey, M. Hudait, J. Fastenau, J. Kavalieros, W. K. Liu, D. Lubyshev, M. Metz, K. Millard, N. Mukherjee, W. Rachmady, U. Shah, and R. Chau, "Advanced high- K gate dielectric for high-performance short-channel $\text{In}_{0.7}\text{Ga}_{0.3}\text{As}$ quantum well field effect transistors on silicon substrate for low power logic applications," in *Electron Devices Meeting (IEDM), 2009 IEEE International*, 2009, p. 1. [Online]. Available: <http://dx.doi.org/10.1109/IEDM.2009.5424361>
- [10] A. Stesmans and V. V. Afanas'ev, "Si dangling-bond-type defects at the interface of (100)Si with ultrathin layers of SiO_x , Al_2O_3 , and ZrO_2 ," *Applied Physics Letters*, vol. 80, no. 11, p. 1957, Mar. 2002. [Online]. Available: <http://dx.doi.org/10.1063/1.1448169>
- [11] R. J. Carter, E. Cartier, A. Kerber, L. Pantisano, T. Schram, S. D. Gendt, and M. Heyns, "Passivation and interface state density of $\text{SiO}_2/\text{HfO}_2$ -based/polycrystalline-Si gate stacks," *Applied Physics Letters*, vol. 83, no. 3, p. 533, Jul. 2003. [Online]. Available: dx.doi.org/10.1063/1.1592639
- [12] R. D. Long, B. Shin, S. Monaghan, K. Cherkaoui, J. Cagnon, S. Stemmer, P. C. McIntyre, and P. K. Hurley, "Charged Defect Quantification in $\text{Pt}/\text{Al}_2\text{O}_3/\text{In}_{0.53}\text{Ga}_{0.47}\text{As}/\text{InP}$ MOS Capacitors," *Journal of The Electrochemical Society*, vol. 158, no. 5, p. G103, Mar. 2011. [Online]. Available: <http://dx.doi.org/10.1149/1.3545799>
- [13] B. Shin, J. R. Weber, R. D. Long, P. K. Hurley, C. G. V. de Walle, and P. C. McIntyre, "Origin and passivation of fixed charge in atomic layer deposited aluminum oxide gate insulators on chemically treated InGaAs substrates," *Applied Physics Letters*, vol. 96, no. 15, p. 152908, Apr. 2010. [Online]. Available: <http://dx.doi.org/10.1063/1.3399776>
- [14] E. O'Connor, S. Monaghan, R. D. Long, A. O'Mahony, I. M. Povey, K. Cherkaoui, M. E. Pemble, G. Brammertz, M. Heyns, S. B. Newcomb, V. V. Afanas'ev, and P. K. Hurley, "Temperature and frequency dependent electrical characterization of $\text{HfO}_2/\text{In}_x\text{Ga}_{1-x}\text{As}$ interfaces using capacitance-voltage and conductance methods," *Applied Physics Letters*, vol. 94, no. 10, p. 102902, Mar. 2009. [Online]. Available: dx.doi.org/10.1063/1.3089688
- [15] P. A. F. Herbert, L. P. Floyd, J. I. Braddell, E. M. Baldwin, and W. M. Kelly, "The application of ohmic contacts to nanometric structures," *Microelectronic*

-
- Engineering*, vol. 17, no. 1-4, p. 541, Mar. 1992. [Online]. Available: [http://dx.doi.org/10.1016/0167-9317\(92\)90111-4](http://dx.doi.org/10.1016/0167-9317(92)90111-4)
- [16] P. D. Ye, G. D. Wilk, B. Yang, J. Kwo, S. N. G. Chu, S. Nakahara, H.-J. L. Gossmann, J. P. Mannaerts, M. Hong, K. K. Ng, and J. Bude, "GaAs metal-oxide-semiconductor field-effect transistor with nanometer-thin dielectric grown by atomic layer deposition," *Applied Physics Letters*, vol. 83, no. 1, p. 180, May 2003. [Online]. Available: <http://dx.doi.org/10.1063/1.1590743>
- [17] M. M. Frank, G. D. Wilk, D. Starodub, T. Gustafsson, E. Garfunkel, Y. J. Chabal, J. Grazul, and D. A. Muller, "HfO₂ and Al₂O₃ gate dielectrics on GaAs grown by atomic layer deposition," *Applied Physics Letters*, vol. 86, no. 15, p. 152904, Apr. 2005. [Online]. Available: <http://dx.doi.org/10.1063/1.1899745>
- [18] C. L. Hinkle, A. M. Sonnet, E. M. Vogel, S. McDonnell, G. J. Hughes, M. Milojevic, B. Lee, F. S. Aguirre-Tostado, K. J. Choi, H. C. Kim, J. Kim, and R. M. Wallace, "GaAs interfacial self-cleaning by atomic layer deposition," *Applied Physics Letters*, vol. 92, no. 7, p. 071901, Feb. 2008. [Online]. Available: <http://dx.doi.org/10.1063/1.2883956>
- [19] C.-H. Chang, Y.-K. Chiou, Y.-C. Chang, K.-Y. Lee, T.-D. Lin, T.-B. Wu, M. Hong, and J. Kwo, "Interfacial self-cleaning in atomic layer deposition of HfO₂ gate dielectric on In_{0.15}Ga_{0.85}As," *Applied Physics Letters*, vol. 89, no. 24, p. 242911, Dec. 2006. [Online]. Available: <http://dx.doi.org/10.1063/1.2405387>
- [20] [Online]. Available: <http://www.nd.edu/~gsnider/>
- [21] A. Diligenti and M. Stagi, "Tunnelling in aluminium/aluminium-oxide/palladium junctions: hydrogen-induced variations," *Electronics Letters*, vol. 19, no. 18, p. 717, Jul. 1983. [Online]. Available: <http://dx.doi.org/10.1049/el:19830488>
- [22] G. Brammertz, H.-C. Lin, M. Caymax, M. Meuris, M. Heyns, and M. Passlack, "On the interface state density at In_{0.53}Ga_{0.47}As/oxide interfaces," *Applied Physics Letters*, vol. 95, no. 20, p. 202109, Nov. 2009. [Online]. Available: <http://dx.doi.org/10.1063/1.3267104>
- [23] V. Djara, K. Cherkaoui, M. Schmidt, Y. Y. Gomeniuk, E. O'Connor, I. Povey, D. O'Connell, S. Monaghan, M. E. Pemble, and P. Hurley, "Study of interface and oxide defects in high-*k*/In_{0.53}Ga_{0.47}As *n*-MOSFETs," in *Ultimate Integration on Silicon (ULIS), 2012 13th International Conference on*, Mar. 2012, p. 29. [Online]. Available: <http://dx.doi.org/10.1109/ULIS.2012.6193349>
- [24] [Online]. Available: <http://www.ioffe.rssi.ru/SVA/NSM/Semicond/GaInAs>

- [25] F. Zhu, H. Zhao, I. Ok, H. S. Kim, J. Yum, J. C. Lee, N. Goel, W. Tsai, C. K. Gaspe, and M. B. Santos, "A high performance $\text{In}_{0.53}\text{Ga}_{0.47}\text{As}$ metal-oxide-semiconductor field effect transistor with silicon interface passivation layer," *Applied Physics Letters*, vol. 94, no. 1, p. 013511, Jan. 2009. [Online]. Available: <http://dx.doi.org/10.1063/1.3068752>
- [26] R. Engel-Herbert, Y. Hwang, and S. Stemmer, "Comparison of methods to quantify interface trap densities at dielectric/III-V semiconductor interfaces," *Journal of Applied Physics*, vol. 108, no. 12, p. 124101, Dec. 2010. [Online]. Available: <http://dx.doi.org/10.1063/1.3520431>
- [27] E. H. Nicollian and A. Goetzberger, "The Si-SiO₂ interface: Electrical properties as determined by the metal-insulator-silicon conductance technique," *Bell Syst. Tech. J.*, vol. XLVI, no. 6, p. 1055, Jul. 1967. [Online]. Available: <http://archive.org/details/bstj46-6-1055>
- [28] E. H. Nicollian and J. R. Brews, *MOS Physics and Technology*. New York: Wiley, 1982.
- [29] H. Zhao, F. Zhu, Y.-T. Chen, J. H. Yum, Y. Wang, and J. C. Lee, "Effect of channel doping concentration and thickness on device performance for $\text{In}_{0.53}\text{Ga}_{0.47}\text{As}$ metal-oxide-semiconductor transistors with atomic-layer-deposited Al_2O_3 dielectrics," *Applied Physics Letters*, vol. 94, no. 9, p. 093505, Mar. 2009. [Online]. Available: <http://dx.doi.org/10.1063/1.3093442>
- [30] K. Romanjek, F. Andrieu, T. Ernst, and G. Ghibaudo, "Improved split C-V method for effective mobility extraction in sub-0.1- μm Si MOSFETs," *Electron Device Letters, IEEE*, vol. 25, no. 8, p. 583, Aug. 2004. [Online]. Available: <http://dx.doi.org/10.1109/LED.2004.832786>
- [31] Y. Xuan, Y. Wu, H. Lin, T. Shen, and P. Ye, "Submicrometer Inversion-Type Enhancement-Mode InGaAs MOSFET With Atomic-Layer-Deposited Al_2O_3 as Gate Dielectric," *Electron Device Letters, IEEE*, vol. 28, no. 11, p. 935, Nov. 2007. [Online]. Available: <http://dx.doi.org/10.1109/LED.2007.906436>
- [32] J. Lin, S. Lee, H.-J. Oh, W. Yang, G. Q. Lo, D. L. Kwong, and D. Chi, "Plasma PH_3 -passivated high mobility inversion InGaAs MOSFET fabricated with self-aligned gate-first process and HfO_2/TaN gate stack," in *Electron Devices Meeting, 2008. IEDM 2008. IEEE International*, 2008, pp. 1–4.
- [33] Y. Xuan, Y. Wu, T. Shen, T. Yang, and P. Ye, "High performance submicron inversion-type enhancement-mode InGaAs MOSFETs with ALD Al_2O_3 , HfO_2 and HfAlO as gate dielectrics," in *Electron Devices Meeting, 2007. IEDM 2007. IEEE International*, 2007, p. 637. [Online]. Available: <http://dx.doi.org/10.1109/IEDM.2007.4419020>

- [34] T. Lin, C. Chen, H. Chiu, P. Chang, C. A. Lin, M. Hong, J. Kwo, and W. Tsai, "Self-aligned inversion-channel and D-mode InGaAs MOSFET using $\text{Al}_2\text{O}_3/\text{Ga}_2\text{O}_3(\text{Gd}_2\text{O}_3)$ as gate dielectrics," in *Device Research Conference, 2008*, 2008, pp. 39–40. [Online]. Available: <http://dx.doi.org/10.1109/DRC.2008.4800726>
- [35] T. P. O'Regan, M. V. Fischetti, B. Sorée, S. Jin, W. Magnus, and M. Meuris, "Calculation of the electron mobility in III-V inversion layers with high- K dielectrics," *Journal of Applied Physics*, vol. 108, no. 10, p. 103705, Nov. 2010. [Online]. Available: <http://dx.doi.org/10.1063/1.3500553>
- [36] N. Taoka, M. Yokoyama, S. Kim, R. Suzuki, R. Iida, S. Lee, T. Hoshii, W. Jevasuwan, T. Maeda, T. Yasuda, O. Ichikawa, N. Fukuhara, M. Hata, M. Takenaka, and S. Takagi, "Impact of Fermi level pinning inside conduction band on electron mobility of $\text{In}_x\text{Ga}_{1-x}\text{As}$ MOSFETs and mobility enhancement by pinning modulation," in *Electron Devices Meeting (IEDM), 2011 IEEE International*, 2011, p. 27.2.1. [Online]. Available: <http://dx.doi.org/10.1109/IEDM.2011.6131622>
- [37] G. Brammertz, A. Alian, D.-C. Lin, M. Meuris, M. Caymax, and W. E. Wang, "A Combined Interface and Border Trap Model for High-Mobility Substrate Metal-Oxide-Semiconductor Devices Applied to $\text{In}_{0.53}\text{Ga}_{0.47}\text{As}$ and InP Capacitors," *Electron Devices, IEEE Transactions on*, vol. 58, no. 11, p. 3890, Nov. 2011. [Online]. Available: <http://dx.doi.org/10.1109/TED.2011.2165725>
- [38] S. Johansson, M. Berg, K.-M. Persson, and E. Lind, "A High-Frequency Transconductance Method for Characterization of High- K Border Traps in III-V MOSFETs," *Electron Devices, IEEE Transactions on*, vol. 60, no. 2, p. 776, Feb. 2013. [Online]. Available: <http://dx.doi.org/10.1109/TED.2012.2231867>
- [39] Y. Yuan, L. Wang, B. Yu, B. Shin, J. Ahn, P. C. McIntyre, P. Asbeck, M. J. W. Rodwell, and Y. Taur, "A Distributed Model for Border Traps in Al_2O_3 -InGaAs MOS Devices," *Electron Device Letters, IEEE*, vol. 32, no. 4, p. 485, Apr. 2011. [Online]. Available: <http://dx.doi.org/10.1109/LED.2011.2105241>
- [40] D. Lin, A. Alian, S. Gupta, B. Yang, E. Bury, S. Sioncke, R. Degraeve, M. Toledano, R. Krom, P. Favia, H. Bender, M. Caymax, K. Saraswat, N. Collaert, and A. Thean, "Beyond interface: The impact of oxide border traps on InGaAs and Ge n-MOSFETs," in *Electron Devices Meeting (IEDM), 2012 IEEE International*, 2012, p. 28.3.1.
- [41] S. D. Ganichev, E. Ziemann, W. Prettl, I. N. Yassievich, A. A. Istratov, and E. R. Weber, "Distinction between the Poole-Frenkel and tunneling models of electric-field-stimulated

carrier emission from deep levels in semiconductors," *Phys. Rev. B*, vol. 61, p. 10361, Apr. 2000. [Online]. Available: <http://dx.doi.org/10.1103/PhysRevB.61.10361>

Chapter 4

Analysis of MOS Gate Stack Defects

4.1 Introduction

Although InGaAs metal-oxide-semiconductor field-effect transistors (MOSFETs) with performance approaching that of state-of-the-art Si devices have already been demonstrated (see Table 1.2, page 5), further performance improvements are still required for potential introduction of InGaAs devices into production. Considering the case of the high- k /In_{0.53}Ga_{0.47}As metal-oxide-semiconductor (MOS) system, the density of interface traps (D_{it}), located in the middle of the In_{0.53}Ga_{0.47}As bandgap, is typically reported to be in the range of low- 10^{11} to mid- 10^{13} /cm².eV (see Figure 1.7, page 10). Moreover, recent reports have also indicated the presence of both interface traps [1–3] and border traps [1, 4, 5] aligned with the conduction band.

A better understanding and control of interface and border traps could enable to significantly improve device performance. The study of the traps located throughout the full energy range swept by the Fermi level during device operation, might enable to achieve this goal. Moreover, knowledge of the energy distribution of interface and border traps is important as any specific features of the extracted surface-equivalent density of interface and border trap (D_{trap}) *vs* energy (E) profile can be compared to theoretical models of defect energies in order to identify the physical origin of the traps [6].

One approach to obtain the $D_{trap}(E)$ profile of a high- k /In_{0.53}Ga_{0.47}As system is to compare the quasi-static (Q-S) capacitance-voltage (C-V) response measured on a metal-oxide-semiconductor capacitor (MOSCAP) to a theoretical Q-S C-V response [2]. An alternative approach is to use n and p -type In_{0.53}Ga_{0.47}As MOSCAPs to examine the D_{trap} profile in the upper and lower portions of the In_{0.53}Ga_{0.47}As bandgap, respectively [7].

The availability of surface-channel high- k /In_{0.53}Ga_{0.47}As MOSFETs opens up new possibilities for investigating interface and border traps when compared to high- k /In_{0.53}Ga_{0.47}As MOSCAPs. Martens *et al.* developed a “full conductance” method for surface-channel III-V

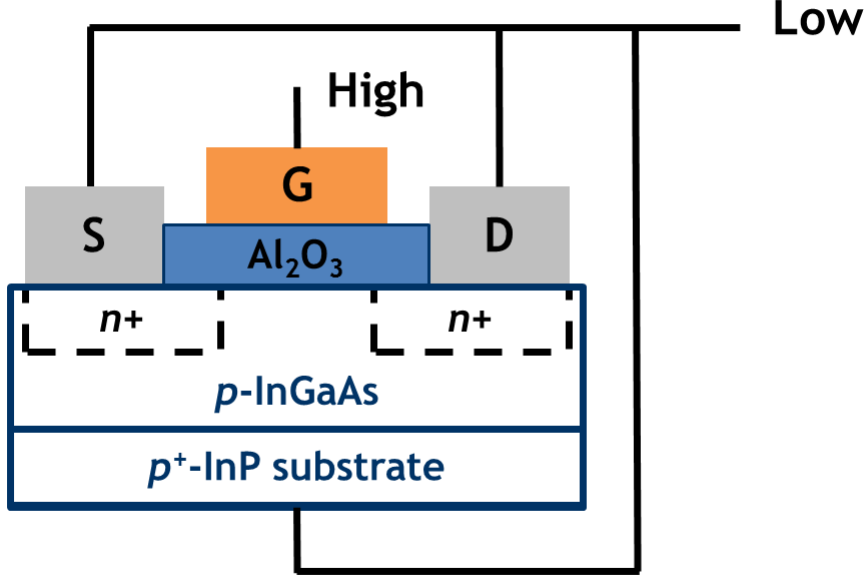


Figure 4.1: Full gate capacitance (C_g) vs gate voltage (V_g) measurement setup, where the gate contact (G) of the MOSFET is connected to the “high” of the impedance meter and the source (S), drain (D) and substrate contacts are shorted together and connected to the “low”.

(and Ge) MOSFETs to extract the $D_{trap}(E)$ across the full semiconductor bandgap [8, 9]. Ali *et al.* modelled the multi-frequency (M-F) gate-to-channel split C-V/conductance-voltage (G-V) characteristics of a surface-channel $\text{LaAlO}_3/\text{In}_{0.53}\text{Ga}_{0.47}\text{As}$ MOSFET to extract the $D_{trap}(E)$ near the $\text{In}_{0.53}\text{Ga}_{0.53}\text{As}$ conduction band [10] and complement the conventional conductance method [11, 12].

First, we will compare a measured full-gate capacitance (C_g) vs gate voltage (V_g) characteristic to a theoretical (ideal) high-frequency (H-F) C-V characteristic calculated with a self-consistent Poisson-Schrödinger solver [13] in order to extract a surface-equivalent density of fixed positive oxide charge (N^+) along with a D_{trap} integrated across the $\text{In}_{0.53}\text{Ga}_{0.47}\text{As}$ bandgap. Then, we will demonstrate an alternative $D_{trap}(E)$ extraction method based on the fitting of the measured C_g - V_g characteristic and its corresponding Maserjian Y-function [14, 15] by introducing a $D_{trap}(E)$ into the self-consistent Poisson-Schrödinger calculations.

4.2 Full Gate Capacitance Measurement

The C_g - V_g characteristic of the $\text{Al}_2\text{O}_3/\text{In}_{0.53}\text{Ga}_{0.47}\text{As}$ MOSFET was obtained using a measurement configuration where the gate contact is connected to the “high” of the impedance meter and the source, drain and substrate contacts are shorted together and connected to the “low” (Figure 4.1). The advantage of this measurement, when compared to the C-V measurement of a MOSCAP, is that for the condition of strong inversion the source and drain areas supply the inversion charge at the $\text{Al}_2\text{O}_3/p\text{-In}_{0.53}\text{Ga}_{0.47}\text{As}$ interface,¹ allowing a full C_g - V_g response to be obtained.

A frequency (f) of 1 MHz and a temperature (T) of -50°C were selected in order to minimize the capacitance response associated with the presence of interface traps and border traps and obtain the approximation of the true H-F C_g - V_g response required for the fitting. Values of f higher than 1 MHz were avoided to prevent distortion of the inversion part of the C_g - V_g characteristic due to parasitic channel resistance effects [10]. A T of -50°C was selected as it represented the lowest T available on the probe station².

The experimental C_g - V_g characteristic was corrected for the parasitic capacitances associated with the gate overlap (Figure 3.1) and gate pad using the method reported in [17].

4.3 Maserjian Y -Function

The Maserjian Y -function applied to a C_g - V_g characteristic is expressed as follows [14]:

$$Y = \frac{1}{C_g^3} \frac{dC_g}{dV_g} \quad (4.1)$$

Figure 4.2a) and (b) show a theoretical (ideal) p -type C_g - V_g characteristic and its corresponding Maserjian Y -function, respectively. The Maserjian Y -function is generally used to extract key MOS parameters such as the threshold voltage (V_T), the p -type dopant density (N_a) and the flat-band voltage (V_{fb}) without prior knowledge of the oxide capacitance (C_{ox}) [14, 15]. This is particularly useful in the analysis of high- k /III-V MOS systems as the low density of states in the conduction band [18] together with issues of traps with energies aligned with the conduction band [1–3], make the extraction of C_{ox} particularly difficult.

First, the Maserjian Y -function features a sharp peak at V_T [Figure 4.2b)]. Then, the Y_{min} plateau observed in depletion can be used to extract N_a and V_{fb} using Equations 4.2 and 4.3, respectively:

¹The same process is involved in a conventional gate-to-channel capacitance (C_{gc}) split C-V measurement [16].

²It is noted that lower temperature measurements at 77 K or below may be required to obtain the true H-F C_g - V_g response.

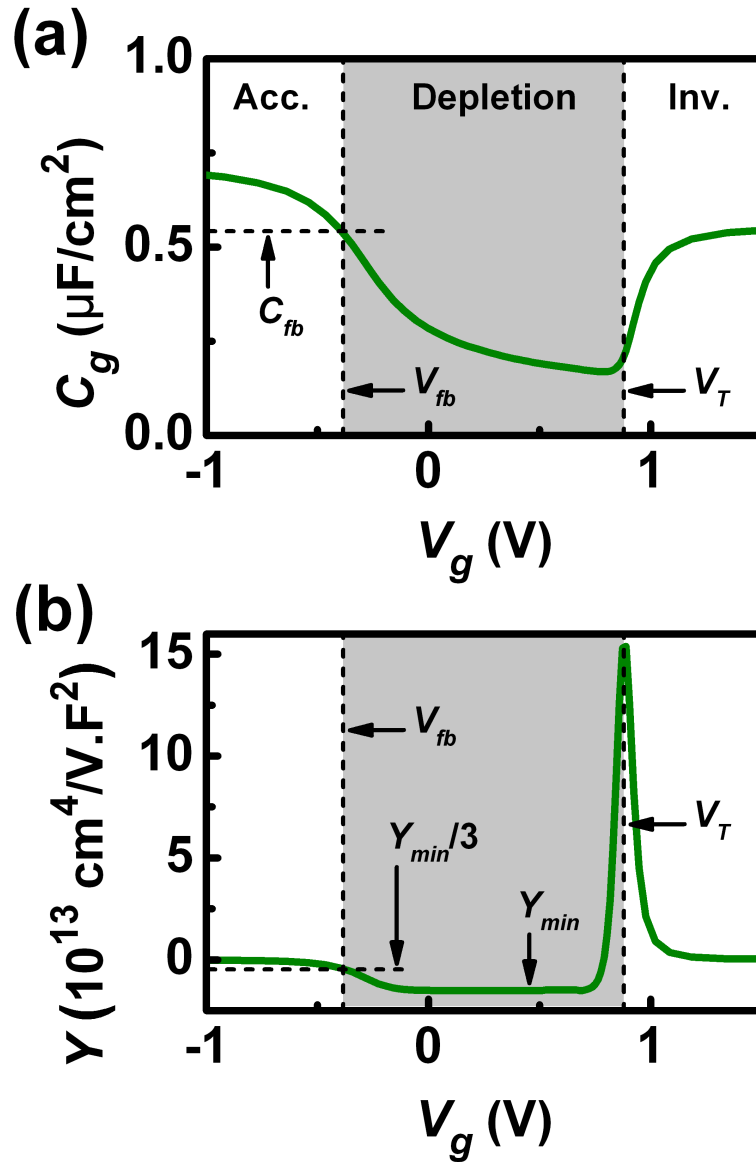


Figure 4.2: Example of theoretical (ideal) p -type C_g - V_g characteristic (a) and corresponding Maserjian Y -function (b). The threshold voltage (V_T) and flat-band voltage (V_{fb}) are obtained from the peak of the Maserjian Y -function and Equation 4.3, respectively. V_T and V_{fb} delimitate the accumulation (acc.), depletion and inversion (inv.) regions. Knowing V_{fb} allows to extract the flat-band capacitance (C_{fb}). The grey shaded areas represent the $\text{In}_{0.53}\text{Ga}_{0.47}\text{As}$ bandgap.

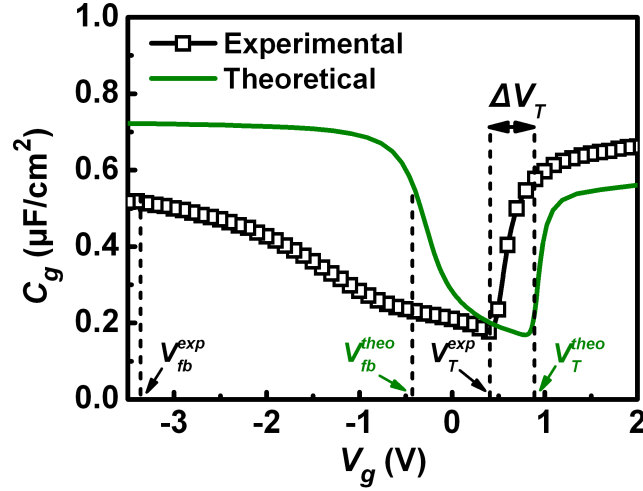


Figure 4.3: Comparison of the experimental and theoretical (ideal) high-frequency (H-F) C_g - V_g characteristics. The theoretical threshold voltage (V_T^{theo}), experimental threshold voltage (V_T^{exp}), theoretical flat-band voltage (V_{fb}^{theo}), experimental flat-band voltage (V_{fb}^{exp}) and $\Delta V_T = V_T^{theo} - V_T^{exp}$ are indicated on the graph. The calculation of the theoretical C_g - V_g characteristic was performed by T. P. O'Regan (Tyndall).

$$Y_{min} = -(q \epsilon_s N_a)^{-1} \quad (4.2)$$

$$Y(V_{fb}) = Y_{min}/3 \quad (4.3)$$

where q is the charge of an electron, ϵ_s is the semiconductor dielectric constant.

4.4 Results and Discussion

4.4.1 Integrated Fixed Oxide Charge and Integrated Interface Trap Density

The C_g - V_g characteristic measured at $f = 1$ MHz and $T = -50^\circ\text{C}$ is shown in Figure 4.3. Considering the Shockley-Read-Hall (SRH) statistics [19] and assuming an interface trap capture cross section (σ) of $\sim 1 \times 10^{-15}$ cm² [20], the T of -50°C and f of 1 MHz should remove the interface defect capacitance response over an energy range relative to the $\text{In}_{0.53}\text{Ga}_{0.47}\text{As}$ valence band edge (E_V) going from $E - E_V = 0.17$ eV to 0.63 eV. Also plotted in Figure 4.3 is the theoretical (ideal) H-F C_g - V_g response for the case of no interface/border traps, or fixed oxide charges. The theoretical C_g - V_g response was obtained by solving the Poisson equation in depletion [21] and by

self-consistently solving the Poisson-Schrödinger equations in inversion, including quantization in all valleys [22]. In the theoretical calculations, the metal work function (W_f) for Pd on Al_2O_3 , the Al_2O_3 film thickness and k -value, and the p - $\text{In}_{0.53}\text{Ga}_{0.47}\text{As}$ doping were set to 4.7 eV [23], 10 nm (see cross-sectional transmission electron microscopy (TEM) image shown in Figure 3.2(a), page 57), 8.6 [24] and $3.3 \times 10^{17} / \text{cm}^3$ (obtained from measured minimum capacitance), respectively. The measured C_g - V_g can then be compared to the theoretical (ideal) C_g - V_g to highlight the impact of fixed oxide charges and interface/border traps.

Firstly, it is clear from Figure 4.3 that the experimental threshold voltage (V_T^{exp}) is shifted in the negative direction relative to the theoretical threshold voltage (V_T^{theo}), indicating the presence of positive fixed charge in the Al_2O_3 . The magnitude of the difference between the V_T^{theo} and the V_T^{exp} (ΔV_T) yields a N^+ , which is given by:

$$N^+ = C_{ox} \times \frac{\Delta V_T}{q} \quad (4.4)$$

where, $\Delta V_T = V_T^{theo} - V_T^{exp}$. Based on the ΔV_T obtained from Figure 4.3, a N^+ of $1.2 \times 10^{12} / \text{cm}^2$ is obtained, in close agreement with the results presented in Sub-section 3.3.2 (page 58) and consistent with previous reports [25, 26]. As already mentioned in Sub-section 1.2.1.3 (page 14), the $\text{Al}_2\text{O}_3/\text{In}_{0.53}\text{Ga}_{0.47}\text{As}$ system features a negative fixed charge located at the $\text{Al}_2\text{O}_3/\text{In}_{0.53}\text{Ga}_{0.47}\text{As}$ interface along with a positive fixed charge distributed throughout the thickness of the Al_2O_3 film. It is therefore important to point out that the N^+ calculated in Equation 4.4 is a surface-equivalent density of fixed oxide charge in units [$/\text{cm}^2$] as it represents the net fixed charge integrated across the interface and oxide thickness.

Secondly, the experimental characteristic is stretched out from V_T^{exp} towards the experimental flat-band voltage (V_{fb}^{exp}) in comparison to the theoretical response [Figure 4.3]. This stretch out is attributed to the presence of interface traps (and possibly border traps) located within the $\text{In}_{0.53}\text{Ga}_{0.47}\text{As}$ bandgap. The experimental and theoretical values of V_T and V_{fb} , as identified in Figure 4.3, can be used to estimate the integrated D_{trap} across the $\text{In}_{0.53}\text{Ga}_{0.47}\text{As}$ bandgap in units [$/\text{cm}^2$]. For $\text{In}_{0.53}\text{Ga}_{0.47}\text{As}$ with a bandgap (E_g) of ~ 0.75 eV and a N_a of $3.3 \times 10^{17} / \text{cm}^3$, the conditions of flat band and inversion correspond to Fermi energy (E_f) positions at the $\text{Al}_2\text{O}_3/\text{In}_{0.53}\text{Ga}_{0.47}\text{As}$ interface of $E_f - E_V = 0.04$ eV and $E_f - E_V = 0.71$ eV, respectively. This indicates that the majority of the $\text{In}_{0.53}\text{Ga}_{0.47}\text{As}$ bandgap is swept as V_g goes from V_T^{exp} to V_{fb}^{exp} . The approach presented here expands on the method reported in [26], where the experimental flat band conditions in n - and p -doped $\text{Al}_2\text{O}_3/\text{In}_{0.53}\text{Ga}_{0.47}\text{As}$ MOS structures were used to evaluate the integrated D_{trap} across the $\text{In}_{0.53}\text{Ga}_{0.47}\text{As}$ bandgap. The availability of a four terminal transistor allows the evaluation of the integrated D_{trap} value with a single device structure. The additional gate voltage required to sweep from V_T^{exp} to V_{fb}^{exp} in the experimental curve compared to the theoretical curve is directly related to the integrated D_{trap} across the

In_{0.53}Ga_{0.47}As bandgap, as:

$$D_{trap} = C_{ox} \times \frac{(V_{fb}^{exp} - V_{fb}^{theo}) - (V_T^{exp} - V_T^{theo})}{q} \quad (4.5)$$

where V_{fb}^{theo} is the theoretical flat-band voltage. From Figure 4.3, this yields a value of $D_{trap} = 1.2 \times 10^{13}$ /cm², which represents the integrated $D_{trap}(E)$ from the flat band condition ($E_f - E_V = 0.04$ eV) to the onset of inversion ($E_f - E_V = 0.71$ eV).

4.4.2 Band Bending and Trap Density Profile

Our approach to obtaining the $D_{trap}(E)$ is based on the fitting of the experimental $C_g - V_g$ characteristic using a self-consistent Poisson-Schrödinger solver accounting for fixed oxide charge and interface/border traps. To assist with the fitting process, we used the Maserjian Y -function. Figure 4.4 illustrates the four steps required to obtain a good fit.

Starting with a theoretical (ideal) H-F $C_g - V_g$ characteristic [Figure 4.4(a)] and corresponding Maserjian Y -function [Figure 4.4(b)], the N^+ of 1.2×10^{12} /cm² obtained in Section 4.4.1 is introduced in the H-F model in order to align the V_T^{theo} to the V_T^{exp} [Figure 4.4(c) and (d)]. It is clear from Figure 4.4(c) that the experimental $C_g - V_g$ characteristic is significantly stretched out over the 0.5 V to -3.5 V gate bias range compare to the calculated $C_g - V_g$ characteristic. This stretch out is attributed to the effect of traps located in the In_{0.53}Ga_{0.47}As bandgap. In Figures 4.4(e) and (f), a $D_{trap}(E)$ is introduced in the H-F model in order to account for the stretch out of the experimental $C_g - V_g$ characteristic³. It is noted that the Maserjian Y -function was found very useful at this stage to match the stretched out over the 0.5 V to -3.5 V gate bias range [inset Figure 4.4(f)] and fine tune the $D_{trap}(E)$ across the In_{0.53}Ga_{0.47}As bandgap. Figure 4.4(e) shows that the the experimental capacitance in inversion exceeds the theoretical maximum value. This observation is consistent with the presence of interface traps [1–3] and/or border traps [1, 4, 5] at energy levels aligned with the In_{0.53}Ga_{0.47}As conduction band, providing an additional capacitance in parallel with the inversion capacitance. The $C_{gc} - V_g$ characteristics shown in Figure 4.5 indicate that very little dispersion in capacitance in inversion is observed over a range of f going from 1 kHz to 1 MHz at $T = 292$ K and for T going from 292 K to 78 K at $f = 1$ MHz⁴. This suggests that it is not possible to “freeze-out” the effect of traps at a $f = 1$ MHz and $T = -50^\circ\text{C}$ in the inversion region of the $C_g - V_g$ characteristic. This results is consistent with the inversion capacitance exceeding the theoretical maximum value and indicates that the inversion region of the $C_g - V_g$ characteristic cannot not be fitted with the H-F model,

³In the H-F model, the introduction of a $D_{trap}(E)$ induces a stretch out of the $C_g - V_g$ characteristic along the x -axis but no stretch out along the y -axis (no trap capacitance is added).

⁴These measurements were performed on devices obtained with the same fabrication process flow but from a different batch. Although the devices featured slightly different electrical performance, the point made relative to the lack of dispersion in capacitance in strong inversion with f and T remains valid.

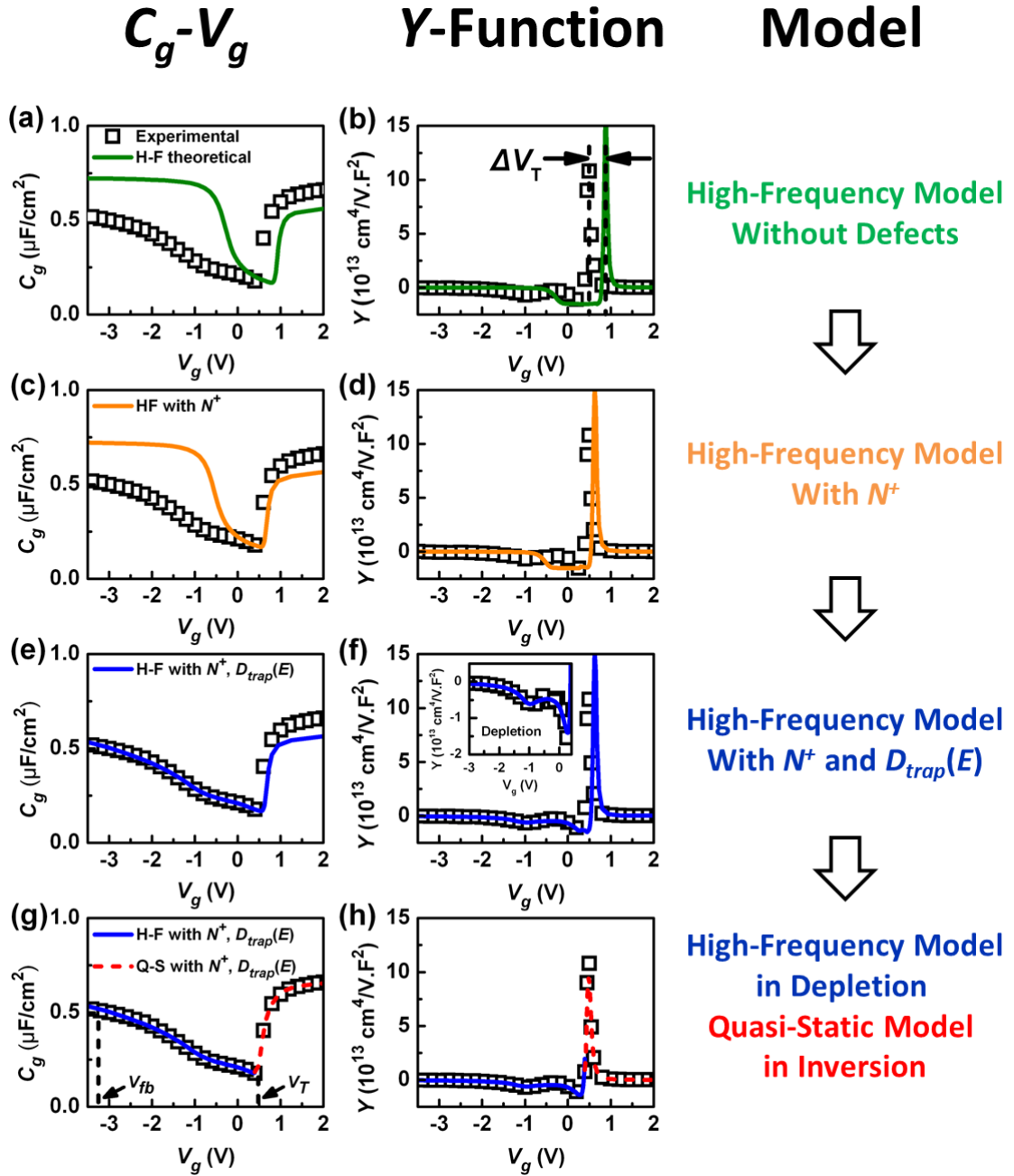


Figure 4.4: Illustrating the four steps in the fitting of the experimental C_g-V_g (a, c, e, g) and corresponding Maserjian Y-function (b, d, f, h). (a-b) theoretical (ideal) high-frequency (H-F) model, (c-d) H-F model with fixed oxide charge (N^+), (e-f) H-F model with N^+ and trap energy profile [$D_{trap}(E)$], and (g-h) spliced H-F model in depletion with quasi-static (Q-S) model in inversion, including N^+ and $D_{trap}(E)$. V_{fb} and V_T indicate the experimental flat-band and threshold voltages, respectively. The fitting was performed by T. P. O'Regan (Tyndall).

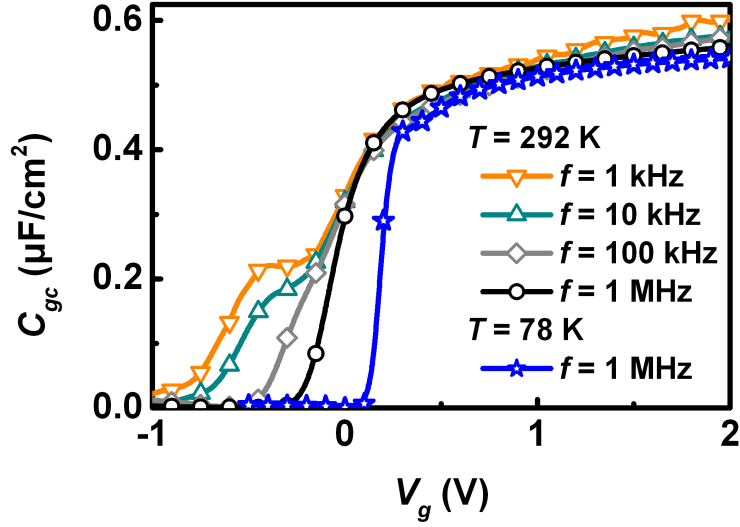


Figure 4.5: Gate-to-channel capacitance (C_{gc}) vs gate voltage (V_g) measured over a range of frequency (f) going 1 kHz to 1 MHz for a fixed temperature (T) of 292 K and at a f of 1 MHz and a T of 78 K. Low capacitance dispersion with f and T is observed in inversion ($V_g > 0.5$ V).

even with the introduction of a $D_{trap}(E)$ extending into the $\text{In}_{0.53}\text{Ga}_{0.47}\text{As}$ conduction band. As a consequence, the inversion part of the curve is fitted with the Q-S self-consistent Poisson-Schrödinger model including a D_{trap} profile extending into the $\text{In}_{0.53}\text{Ga}_{0.47}\text{As}$ conduction band. The resulting experimental and theoretical C_g - V_g responses and the corresponding Maserjian Y -functions are shown in Figure 4.4(g) and (h), respectively.

Figure 4.6(a) shows the extracted experimental band bending $E-E_V$ vs V_g profile along with the profile of a theoretical (ideal) device. A marked degradation of the band bending efficiency is observed in the lower part of the $\text{In}_{0.53}\text{Ga}_{0.47}\text{As}$ bandgap as well as in the $\text{In}_{0.53}\text{Ga}_{0.47}\text{As}$ conduction band. The corresponding $D_{trap}(E)$ profile presents three main features [Figure 4.6(b)]:

1. A large density of donor (+/0) traps extending from the $\text{In}_{0.53}\text{Ga}_{0.47}\text{As}$ valence band into the lower part of the $\text{In}_{0.53}\text{Ga}_{0.47}\text{As}$ bandgap is observed. While our method can reveal the electrical nature of the traps (i.e.: donor or acceptor), further analysis is required to state about the physical nature of the traps (i.e.: interface traps or border traps).
2. A distribution of donor (+/0) traps peaking at $1.5 \times 10^{13} / \text{cm}^2 \cdot \text{eV}$ and centred at 0.36 eV above the $\text{In}_{0.53}\text{Ga}_{0.47}\text{As}$ valence band edge (mid-gap) is also observed. This peak, associated with the presence of interface traps in [7, 10], is not always reported. Indeed, the $D_{trap}(E)$ profiles reported in [2, 27] show a monotonic increase from the $\text{In}_{0.53}\text{Ga}_{0.47}\text{As}$ conduction band towards the valence band edge. It is possible that, in these works, a broader

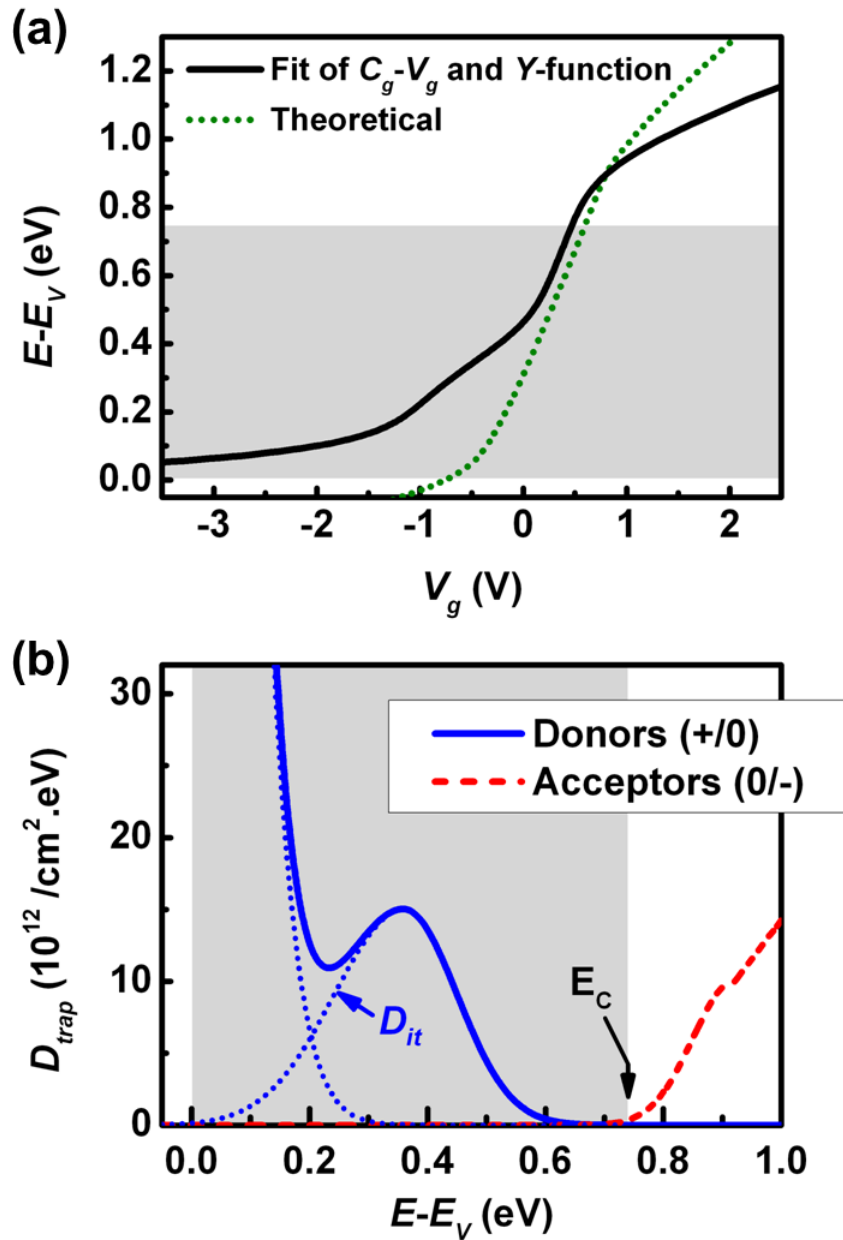


Figure 4.6: (a) Comparison of the band bending $E-E_V$ vs V_g profile obtained with the fitting of the C_g-V_g characteristic and Maserjian Y-function to the profile obtained for a theoretical (ideal) device. (b) Trap density vs energy profile obtained from the fitting of the Maserjian Y-function and C_g-V_g characteristic. The blue solid line and the red short dash line represent donor-type (+/0) and acceptor-type (0/-) trap density profiles, respectively. The donor-type trap density profile suggests the presence of two components, which are highlighted as two Gaussian distributions (blue short dot lines). The grey shaded areas represent the $\text{In}_{0.53}\text{Ga}_{0.47}\text{As}$ bandgap.

feature extending from the valence band into the bandgap could prevent the observation of a clear peak around the mid-gap.

3. A broad feature extending into the $\text{In}_{0.53}\text{Ga}_{0.47}\text{As}$ conduction band, acquiring a density of $\sim 2.5 \times 10^{13} / \text{cm}^2 \cdot \text{eV}$ at 0.3 eV above the $\text{In}_{0.53}\text{Ga}_{0.47}\text{As}$ conduction band edge (E_C). This density value is in very close agreement with $\text{Al}_2\text{O}_3/\text{In}_{0.53}\text{Ga}_{0.47}\text{As}$ MOS structures reported in [2] and the case of the $\text{Al}_2\text{O}_3/\text{In}_{0.53}\text{Ga}_{0.47}\text{As}$ MOS with an $(\text{NH}_4)_2\text{S}$ surface preparation reported in [3].

4.4.3 Comparison with Conventional Methods

In this subsection, the data obtained using the fitting of the C_g - V_g characteristic and Maserjian Y-function (Figure 4.6) is compared to the results obtained with conventional methods such as the Berglund integral [28], the Terman method [29], the high-low method [30] and the full conductance method [8]. *It is important to note here that these methods were only applied after the data extraction based on the fitting the C_g - V_g and Maserjian Y-function was performed, indicating that the extraction process was not biased by any preliminary analysis.*

Figure 4.7(a) compares the band bending *vs* V_g obtained using the fitting of the C_g - V_g and Maserjian Y-function, the Terman method [29] and the Berglund integral [28]. While the data used with the Terman method is the same as that used for the fitting (i.e.: C_g - V_g measured at $f = 1$ MHz and $T = -50^\circ\text{C}$), the data used in the calculation of the Berglund integral is a C_g - V_g characteristic measured at $f = 200$ Hz and $T = 25^\circ\text{C}$ (not shown)⁵. Excellent agreement is obtained between the fitting method and the Terman method. However, a significant discrepancy between the Berglund integral and the other methods is observed. For V_g going from 0.4 V to -0.4 V, the Berglund integral indicates a less efficient band bending than the other methods. This could be attributed to the fact that the D_{trap} response near the band edges could not be “frozen out” at $f = 1$ MHz and $T = -50^\circ\text{C}$, leading to an overestimation of the band bending efficiency near the band edges with the methods relying on an estimate of the H-F C_g - V_g response (i.e.: fitting method and Terman method), consistent with [31]. For $V_g > -0.4$ V, the Berglund integral severely overestimates the band bending efficiency, suggesting that the f of 200 Hz is not sufficiently low to obtain a full response of the interface traps located near the middle of the $\text{In}_{0.53}\text{Ga}_{0.47}\text{As}$ bandgap. This is in agreement with [7], where the use of a f as low as 40 Hz is recommended to maximize the D_{trap} response.

Figure 4.7(b) compares the $D_{trap}(E)$ profile obtained with the fitting method to the profiles extracted with the Terman, high-low and full conductance methods. The excellent agreement

⁵The C_g - V_g characteristic is corrected for parasitic capacitance using the method reported in [17]. This method requires the measurement of a device with a long gate length and a device with a short gate length. The small gate area of the short gate-length device, the lowest f giving acceptable noise level was 200 Hz.

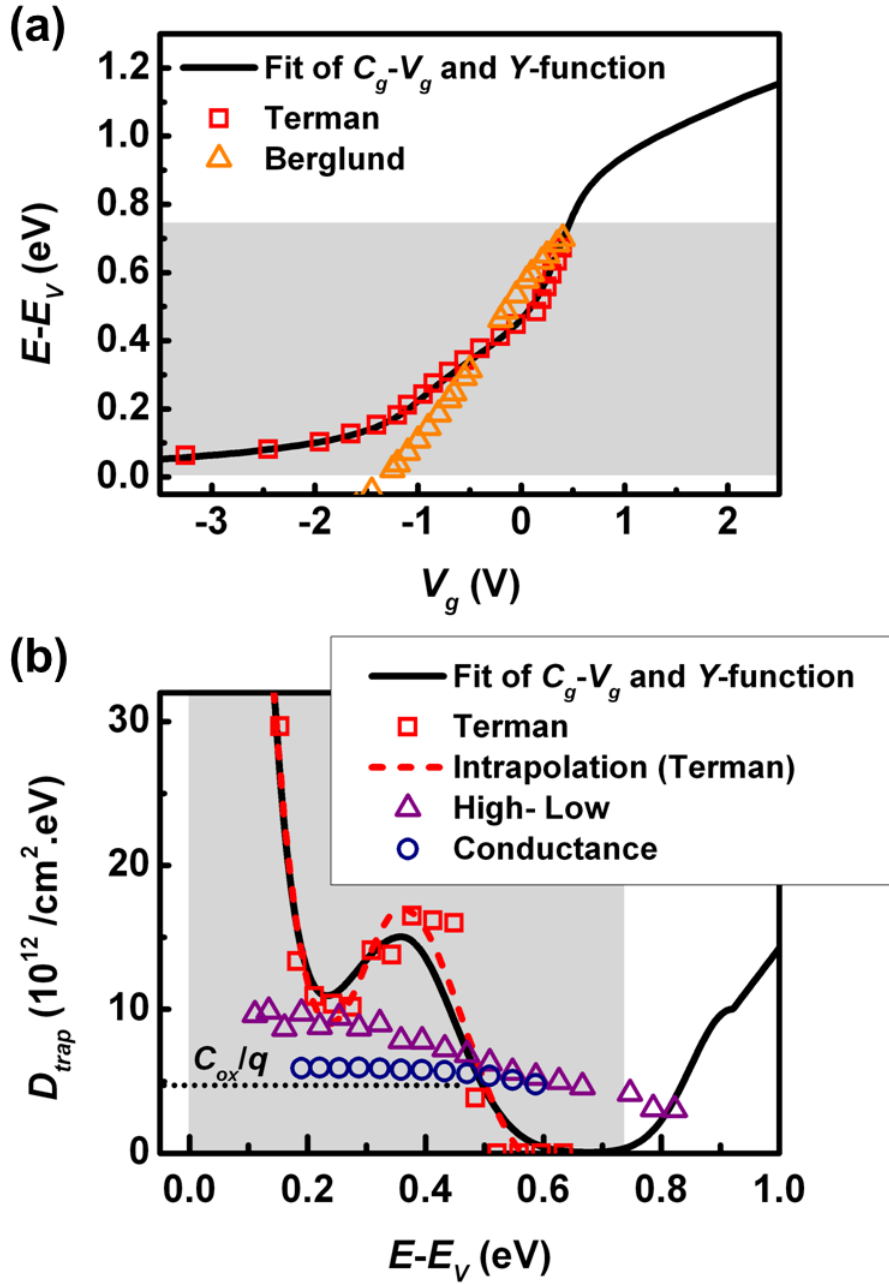


Figure 4.7: (a) Comparison of the band bending $E-E_V$ vs V_g profile obtained with the fitting of the C_g-V_g characteristic and Maserjian Y-function to the profile obtained with the Terman method [29] and Berglund integral [28]. (b) Comparison of the trap density vs energy profile obtained with the fitting method to the profiles extracted from the Terman (the short dash curve shows the intrappolation of the Terman data), high-low [30] and full conductance [8] methods. C_{ox}/q is indicated to highlight the limitation of the full conductance method. The grey shaded areas represent the $\text{In}_{0.53}\text{Ga}_{0.47}\text{As}$ bandgap.

between the fitting method and the Terman method is consistent with the analysis of the band bending shown in Figure 4.7(a). For $E-E_V$ going from 0.5 eV to 0.73 eV, it is clear that the fitting method and the Terman method underestimate D_{trap} . The high-low and the conductance methods, however, show reasonable agreement in this energy range, where D_{trap} decreases from $5.8 \times 10^{12} / \text{cm}^2 \cdot \text{eV}$ to $4.2 \times 10^{12} / \text{cm}^2 \cdot \text{eV}$. For $E-E_V < 0.5$ eV, the high-low method underestimates D_{trap} as it suffers from the same limitation as that observed in the analysis of the Berglund integral [Figure 4.7(a)]. The conductance method also underestimates D_{trap} in this energy range. This underestimation is consistent with recent works [8, 31] reporting D_{it} underestimation with the conductance method in the case of D_{it} values exceeding C_{ox}/q . This is the case in our devices since $C_{ox}/q = 4.75 \times 10^{12} / \text{cm}^2 \cdot \text{eV}$ and the fitting method indicates a mid-gap D_{it} feature peaking at $1.5 \times 10^{13} / \text{cm}^2 \cdot \text{eV}$.

4.5 Conclusion

The fixed oxide charges and interface/border traps present in the $\text{Al}_2\text{O}_3/\text{In}_{0.53}\text{Ga}_{0.47}\text{As}$ MOSFETs presented in Chapter 3 were examined through the study of the full gate capacitance C_g-V_g characteristic. The C_g-V_g characteristic was measured at a f of 1 MHz and a T of -50°C in order to approximate a true H-F response. The comparison of the measured C_g-V_g characteristic with a theoretical (ideal) H-F characteristic yielded a N^+ of $1.2 \times 10^{12} / \text{cm}^2$ along with an integrated D_{trap} across the $\text{In}_{0.53}\text{Ga}_{0.47}\text{As}$ bandgap of $1.2 \times 10^{13} / \text{cm}^2$.

The fitting of the C_g-V_g characteristic and corresponding Maserjian Y -function yielded a $D_{trap}(E)$ across the $\text{In}_{0.53}\text{Ga}_{0.47}\text{As}$ energy gap and extending into the $\text{In}_{0.53}\text{Ga}_{0.47}\text{As}$ conduction band. This analysis revealed donor-like (+/0) traps within the $\text{In}_{0.53}\text{Ga}_{0.47}\text{As}$ bandgap, with a peak density of $\sim 1.5 \times 10^{13} / \text{cm}^2 \cdot \text{eV}$ and centered at 0.36 eV above the $\text{In}_{0.53}\text{Ga}_{0.47}\text{As}$ E_V . A sharp increase in donor-like (+/0) trap density in the energy range of 0.1 eV to 0.2 eV above the $\text{In}_{0.53}\text{Ga}_{0.47}\text{As}$ E_V was also observed. The analysis also indicated acceptor-like (0/-) traps located at energy levels aligned with the $\text{In}_{0.53}\text{Ga}_{0.47}\text{As}$ conduction band, with a density of $\sim 2.5 \times 10^{13} / \text{cm}^2 \cdot \text{eV}$ at 0.3 eV above the $\text{In}_{0.53}\text{Ga}_{0.47}\text{As}$ E_C . Although the fitting could reveal whether the observed traps were donors or acceptors, this method could not discern whether these traps were interface traps, border traps, or a combination of both.

Finally, excellent agreement with the conventional Terman method was obtained. However, the comparison with the high-low and conductance methods highlighted a D_{trap} underestimation near the $\text{In}_{0.53}\text{Ga}_{0.47}\text{As}$ band edges. This issue may be addressed through the measurement and fitting of a C_g-V_g characteristic obtained at a T of 77 K or lower.

Bibliography

- [1] G. Brammertz, A. Alian, D.-C. Lin, M. Meuris, M. Caymax, and W. E. Wang, "A Combined Interface and Border Trap Model for High-Mobility Substrate Metal-Oxide-Semiconductor Devices Applied to $\text{In}_{0.53}\text{Ga}_{0.47}\text{As}$ and InP Capacitors," *Electron Devices, IEEE Transactions on*, vol. 58, no. 11, p. 3890, Nov. 2011. [Online]. Available: <http://dx.doi.org/10.1109/TED.2011.2165725>
- [2] G. Brammertz, H.-C. Lin, M. Caymax, M. Meuris, M. Heyns, and M. Passlack, "On the interface state density at $\text{In}_{0.53}\text{Ga}_{0.47}\text{As}$ /oxide interfaces," *Applied Physics Letters*, vol. 95, no. 20, p. 202109, Nov. 2009. [Online]. Available: <http://dx.doi.org/10.1063/1.3267104>
- [3] N. Taoka, M. Yokoyama, S. Kim, R. Suzuki, R. Iida, S. Lee, T. Hoshii, W. Jevasuwan, T. Maeda, T. Yasuda, O. Ichikawa, N. Fukuhara, M. Hata, M. Takenaka, and S. Takagi, "Impact of Fermi level pinning inside conduction band on electron mobility of $\text{In}_x\text{Ga}_{1-x}\text{As}$ MOSFETs and mobility enhancement by pinning modulation," in *Electron Devices Meeting (IEDM), 2011 IEEE International*, 2011, p. 27.2.1. [Online]. Available: <http://dx.doi.org/10.1109/IEDM.2011.6131622>
- [4] E. J. Kim, L. Wang, P. M. Asbeck, K. C. Saraswat, and P. C. McIntyre, "Border traps in $\text{Al}_2\text{O}_3/\text{In}_{0.53}\text{Ga}_{0.47}\text{As}$ (100) gate stacks and their passivation by hydrogen anneals," *Applied Physics Letters*, vol. 96, no. 1, p. 012906, Jan. 2010. [Online]. Available: <http://dx.doi.org/10.1063/1.3281027>
- [5] Y. Yuan, L. Wang, B. Yu, B. Shin, J. Ahn, P. C. McIntyre, P. Asbeck, M. J. W. Rodwell, and Y. Taur, "A Distributed Model for Border Traps in Al_2O_3 -InGaAs MOS Devices," *Electron Device Letters, IEEE*, vol. 32, no. 4, p. 485, Apr. 2011. [Online]. Available: <http://dx.doi.org/10.1109/LED.2011.2105241>
- [6] H.-P. Komsa and A. Pasquarello, "Identification of defect levels at As/oxide interfaces through hybrid functionals," *Microelectronic Engineering*, vol. 88, no. 7, p. 1436, Jul. 2011. [Online]. Available: <http://dx.doi.org/10.1016/j.mee.2011.03.081>
- [7] É. O'Connor, B. Brennan, V. Djara, K. Cherkaoui, S. Monaghan, S. B. Newcomb, R. Contreras, M. Milojevic, G. Hughes, M. E. Pemble, R. M. Wallace, and P. K. Hurley, "A systematic study of $(\text{NH}_4)_2\text{S}$ passivation (22%, 10%, 5%, or 1%) on the interface properties of the $\text{Al}_2\text{O}_3/\text{In}_{0.53}\text{Ga}_{0.47}\text{As}/\text{InP}$ system for n -type and p -type $\text{In}_{0.53}\text{Ga}_{0.47}\text{As}$ epitaxial layers," *Journal of Applied Physics*, vol. 109, no. 2, p. 024101, Jan. 2011. [Online]. Available: <http://dx.doi.org/10.1063/1.3533959>

-
- [8] K. Martens, C. O. Chui, G. Brammertz, B. De Jaeger, D. Kuzum, M. Meuris, M. M. Heyns, T. Krishnamohan, K. Saraswat, H. Maes, and G. Groeseneken, "On the Correct Extraction of Interface Trap Density of MOS Devices With High-Mobility Semiconductor Substrates," *Electron Devices, IEEE Transactions on*, vol. 55, no. 2, p. 547, Feb. 2008. [Online]. Available: <http://dx.doi.org/10.1109/TED.2007.912365>
- [9] A. Alian, C. Merckling, G. Brammertz, M. Meuris, M. Heyns, and K. D. Meyer, "InGaAs MOS Transistors Fabricated through a Digital-Etch Gate-Recess Process and the Influence of Forming Gas Anneal on Their Electrical Behavior," *ECS Journal of Solid State Science and Technology*, vol. 1, no. 6, p. P310, Oct. 2012. [Online]. Available: <http://dx.doi.org/10.1149/2.001301jss>
- [10] A. Ali, H. Madan, S. Kovesnikov, S. Oktyabrsky, R. Kambhampati, T. Heeg, D. Schlom, and S. Datta, "Small-Signal Response of Inversion Layers in High-Mobility In_{0.53}Ga_{0.47}As MOSFETs Made With Thin High-K Dielectrics," *Electron Devices, IEEE Transactions on*, vol. 57, no. 4, p. 742, Apr. 2010. [Online]. Available: <http://dx.doi.org/10.1109/TED.2010.2041855>
- [11] E. H. Nicollian and J. R. Brews, *MOS Physics and Technology*. New York: Wiley, 1982.
- [12] E. H. Nicollian and A. Goetzberger, "The Si-SiO₂ interface: Electrical properties as determined by the metal-insulator-silicon conductance technique," *Bell Syst. Tech. J.*, vol. XLVI, no. 6, p. 1055, Jul. 1967. [Online]. Available: <http://archive.org/details/bstj46-6-1055>
- [13] [Online]. Available: <http://www.nd.edu/~gsnider/>
- [14] J. Maserjian, G. Petersson, and C. Svensson, "Saturation capacitance of thin oxide MOS structures and the effective surface density of states of silicon," *Solid-State Electronics*, vol. 17, no. 4, p. 335, Apr. 1974. [Online]. Available: [http://dx.doi.org/10.1016/0038-1101\(74\)90125-7](http://dx.doi.org/10.1016/0038-1101(74)90125-7)
- [15] G. Ghibaudo, S. Bruyere, T. Devoivre, B. DeSalvo, and E. Vincent, "Improved method for the oxide thickness extraction in MOS structures with ultrathin gate dielectrics," *Semiconductor Manufacturing, IEEE Transactions on*, vol. 13, no. 2, p. 152, May 2000. [Online]. Available: <http://dx.doi.org/10.1109/66.843630>
- [16] F. Lime, K. Oshima, M. Cassé, G. Ghibaudo, S. Cristoloveanu, B. Guillaumot, and H. Iwai, "Carrier mobility in advanced CMOS devices with metal gate and HfO₂ gate dielectric," *Solid-State Electronics*, vol. 47, no. 10, p. 1617, Oct. 2003. [Online]. Available: [http://dx.doi.org/10.1016/S0038-1101\(03\)00176-X](http://dx.doi.org/10.1016/S0038-1101(03)00176-X)

- [17] K. Romanjek, F. Andrieu, T. Ernst, and G. Ghibaudo, "Improved split C-V method for effective mobility extraction in sub-0.1- μm Si MOSFETs," *Electron Device Letters, IEEE*, vol. 25, no. 8, p. 583, Aug. 2004. [Online]. Available: <http://dx.doi.org/10.1109/LED.2004.832786>
- [18] [Online]. Available: <http://www.ioffe.rssi.ru/SVA/NSM/Semicond/GaInAs>
- [19] W. Shockley and W. T. Read, "Statistics of the Recombinations of Holes and Electrons," *Phys. Rev.*, vol. 87, p. 835, Sep. 1952. [Online]. Available: <http://dx.doi.org/10.1103/PhysRev.87.835>
- [20] G. Brammertz, K. Martens, S. Sioncke, A. Delabie, M. Caymax, M. Meuris, and M. Heyns, "Characteristic trapping lifetime and capacitance-voltage measurements of GaAs metal-oxide-semiconductor structures," *Applied Physics Letters*, vol. 91, no. 13, p. 133510, Sep. 2007. [Online]. Available: <http://dx.doi.org/10.1063/1.2790787>
- [21] T. P. O'Regan and P. K. Hurley, "Calculation of the capacitance-voltage characteristic of GaAs, $\text{In}_{0.53}\text{Ga}_{0.47}\text{As}$, and InAs metal-oxide-semiconductor structures," *Applied Physics Letters*, vol. 99, no. 16, p. 163502, Oct. 2011. [Online]. Available: <http://dx.doi.org/10.1063/1.3652699>
- [22] T. P. O'Regan, P. K. Hurley, B. Sorée, and M. V. Fischetti, "Modeling the capacitance-voltage response of $\text{In}_{0.53}\text{Ga}_{0.47}\text{As}$ metal-oxide-semiconductor structures: Charge quantization and nonparabolic corrections," *Applied Physics Letters*, vol. 96, no. 21, p. 213514, May 2010. [Online]. Available: <http://dx.doi.org/10.1063/1.3436645>
- [23] A. Diligenti and M. Stagi, "Tunnelling in aluminium/aluminium-oxide/palladium junctions: hydrogen-induced variations," *Electronics Letters*, vol. 19, no. 18, p. 717, Jul. 1983. [Online]. Available: <http://dx.doi.org/10.1049/el:19830488>
- [24] V. Djara, K. Cherkaoui, M. Schmidt, Y. Y. Gomeniuk, E. O'Connor, I. Povey, D. O'Connell, S. Monaghan, M. E. Pemble, and P. Hurley, "Study of interface and oxide defects in high- k / $\text{In}_{0.53}\text{Ga}_{0.47}\text{As}$ n -MOSFETs," in *Ultimate Integration on Silicon (ULIS), 2012 13th International Conference on*, Mar. 2012, p. 29. [Online]. Available: <http://dx.doi.org/10.1109/ULIS.2012.6193349>
- [25] B. Shin, J. R. Weber, R. D. Long, P. K. Hurley, C. G. V. de Walle, and P. C. McIntyre, "Origin and passivation of fixed charge in atomic layer deposited aluminum oxide gate insulators on chemically treated InGaAs substrates," *Applied Physics Letters*, vol. 96, no. 15, p. 152908, Apr. 2010. [Online]. Available: <http://dx.doi.org/10.1063/1.3399776>

-
- [26] R. D. Long, B. Shin, S. Monaghan, K. Cherkaoui, J. Cagnon, S. Stemmer, P. C. McIntyre, and P. K. Hurley, "Charged Defect Quantification in Pt/Al₂O₃/In_{0.53}Ga_{0.47}As/InP MOS Capacitors," *Journal of The Electrochemical Society*, vol. 158, no. 5, p. G103, Mar. 2011. [Online]. Available: <http://dx.doi.org/10.1149/1.3545799>
- [27] D. Varghese, Y. Xuan, Y. Q. Wu, T. Shen, P. Ye, and M. Alam, "Multi-probe interface characterization of In_{0.65}Ga_{0.35}As/Al₂O₃ MOSFET," in *Electron Devices Meeting, 2008. IEDM 2008. IEEE International*, 2008, p. 1. [Online]. Available: <http://dx.doi.org/10.1109/IEDM.2008.4796699>
- [28] C. N. Berglund, "Surface states at steam-grown silicon-silicon dioxide interfaces," *Electron Devices, IEEE Transactions on*, vol. 13, no. 10, p. 701, Oct. 1966. [Online]. Available: <http://dx.doi.org/10.1109/T-ED.1966.15827>
- [29] L. M. Terman, "An investigation of surface states at a silicon/silicon oxide interface employing metal-oxide-silicon diodes," *Solid-State Electronics*, vol. 5, no. 5, p. 285, Sep. 1962. [Online]. Available: [http://dx.doi.org/10.1016/0038-1101\(62\)90111-9](http://dx.doi.org/10.1016/0038-1101(62)90111-9)
- [30] R. Castagné and A. Vapaille, "Description of the SiO₂/Si interface properties by means of very low frequency MOS capacitance measurements," *Surface Science*, vol. 28, no. 1, p. 157, Nov. 1971. [Online]. Available: [http://dx.doi.org/10.1016/0039-6028\(71\)90092-6](http://dx.doi.org/10.1016/0039-6028(71)90092-6)
- [31] R. Engel-Herbert, Y. Hwang, and S. Stemmer, "Comparison of methods to quantify interface trap densities at dielectric/III-V semiconductor interfaces," *Journal of Applied Physics*, vol. 108, no. 12, p. 124101, Dec. 2010. [Online]. Available: <http://dx.doi.org/10.1063/1.3520431>

Chapter 5

Investigation of Border Traps and Mobility

5.1 Introduction

InGaAs and related compound semiconductors have become serious candidates for replacing strained Si in future complementary metal-oxide-semiconductor (CMOS) device applications due to their remarkable electron mobility [1]. The “standard” method for extracting the effective mobility (μ_{eff}) in a metal-oxide-semiconductor field-effect transistor (MOSFET) relies on a gate-to-channel split capacitance-voltage (C-V) measurement combined with a measurement of the drain current (I_d) vs gate voltage (V_g) characteristic in direct current (DC) [2]. While this method enables highly accurate μ_{eff} extraction on SiO₂/Si MOSFETs, its accuracy when applied to emerging high- k /InGaAs devices, with relatively high density of interface traps (D_{it}) and density of border traps (D_{bt}), becomes questionable. In an attempt to address this issue, we investigated the use of an alternative method based on the inversion-charge pumping (ICP) and pulsed I_d - V_g measurements, first proposed by Kerber *et al.* for Si based MOSFETs in [3], for the μ_{eff} extraction of surface-channel Al₂O₃/In_{0.53}Ga_{0.47}As MOSFETs.

5.2 Experimental Details

5.2.1 Surface-channel Al₂O₃/In_{0.53}Ga_{0.47}As MOSFETs

The In_{0.53}Ga_{0.47}As MOSFETs used in this study were fabricated using the fabrication process flow presented in Chapter 3. Briefly, the devices featured a p -In_{0.53}Ga_{0.47}As channel nominally doped to 4×10^{17} /cm³. An optimized (NH₄)₂S surface passivation [4, 5] was performed before the formation of a 10-nm-thick Al₂O₃ gate dielectric by atomic layer deposition (ALD). The

source and drain (S/D) areas were implanted with Si ions and subsequently activated at 600°C for 30 sec in N₂. The Pd gate and the Au/Ge/Au/Ni/Au S/D metal contacts were formed by electron-beam evaporation and lift-off. It is noted that, although the fabrication process remained the same, the devices examined in this Chapter were processed approximately a year after those presented in Chapter 3 and, consequently, exhibited slightly different DC performance at room temperature. Indeed, while the subthreshold swing (SS) remained at ~ 150 mV/dec., a threshold voltage (V_T) of 0.2 V was obtained, indicating the presence of a higher fixed positive charge in the Al₂O₃ compared to the devices presented in Chapter 3.

5.2.2 Inversion-Charge Pumping Method

The ICP measurement setup shown in Figure 5.1 is similar to that of an amplitude sweep charge pumping (CP) method [6, 7]. The S/D contacts are shorted and connected to the ground, a square pulse train of variable amplitude going from base voltage (V_{base}) \approx flat-band voltage (V_{fb}) to peak voltage (V_{peak}) is applied to the gate contact and the total pumped charge density (N_{CP}) is measured on the substrate contact. The geometrical and trapped charge components of N_{CP} are respectively expressed as the first and second terms in the brackets of equation 5.1 [6, 8]:

$$N_{CP} = \alpha \cdot C_{ox} \cdot (V_g - V_T) / q + (D_{it} + D_{bt} \cdot t_{bt}) \cdot \Delta E \quad (5.1)$$

where α is the fraction of inversion-charge density (N_{inv}) recombining in the substrate, C_{ox} is the gate oxide capacitance, q is the charge of an electron, t_{bt} is the oxide thickness over which the border traps are probed and ΔE is the energy interval swept by the Fermi level going from $V_g = V_{base}$ to V_{peak} . The ICP method applied to devices featuring low D_{it} and D_{bt} , such as SiO₂/Si MOSFETs, enables direct extraction of N_{inv} by simply maximizing the geometrical component, [9], through the use of devices with channel length (L) > 20 μm in combination with fast (10 ns) pulse rise time (t_r) and fall time (t_f) [3, 7]. Under such conditions, most of N_{inv} is forced to recombine in the substrate and contributes to N_{CP} . A correction for the fraction ($1 - \alpha$) of N_{inv} lost by diffusion to the S/D, representing the sum of the density of charge lost to the source (N_S) and the density of charge lost to the drain (N_D), is applied through the measurements of N_{CP_S} [Figure 5.1(b)] and N_{CP_D} [Figure 5.1(c)]¹. Following the measurements of N_{CP_SD} , N_{CP_S} and N_{CP_D} , N_{inv} can be extracted using the relationship:

$$N_{inv} = N_{CP_S} + N_{CP_D} - N_{CP_SD} \quad (5.2)$$

¹Kerber *et al.* in [3] assumed device symmetry and used $N_{inv} = 2 \times N_{CP_S} - N_{CP}$. As we observed a slight difference between the measured N_{CP_S} and N_{CP_D} , which was attributed to our non self-aligned device fabrication process, we measured N_{CP_S} and N_{CP_D} and applied Equation 5.2 in order to obtain accurate N_{inv} .

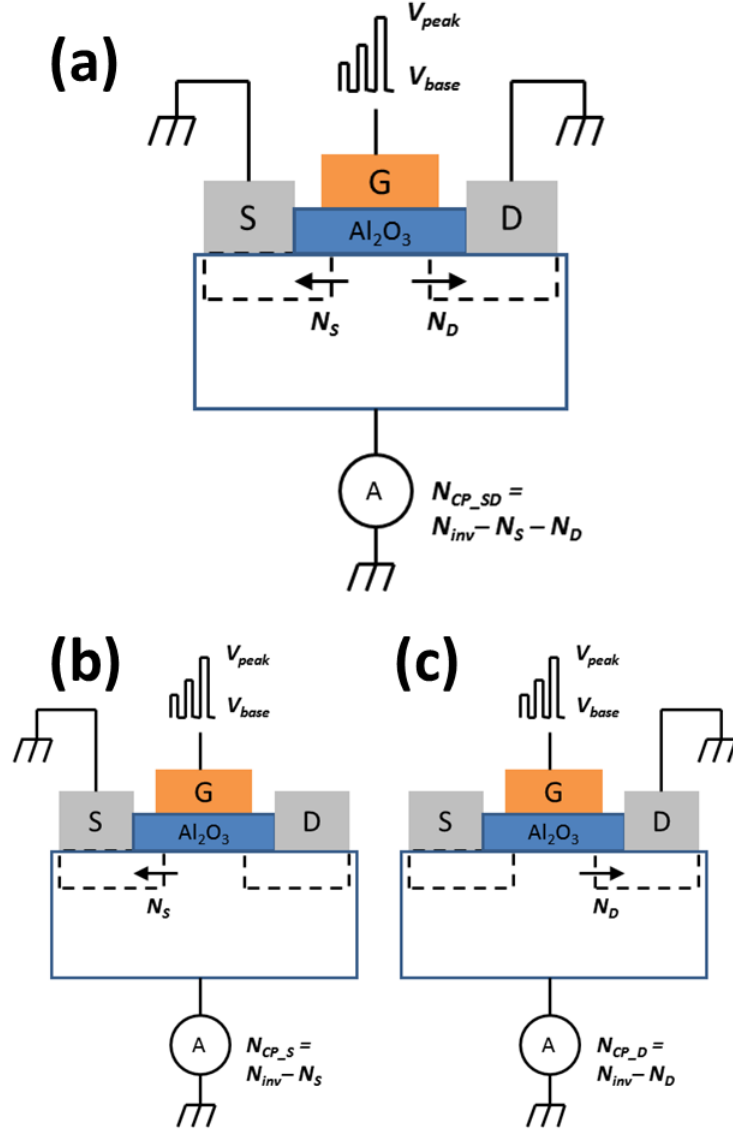


Figure 5.1: Schematics of the Inversion-Charge Pumping (ICP) setup used to extract the inversion charge density (N_{inv}) in long channel ($L > 20 \mu\text{m}$) $\text{Al}_2\text{O}_3/\text{In}_{0.53}\text{Ga}_{0.47}\text{As}$ MOSFETs through the measurements of (a) N_{CP_SD} , (b) N_{CP_S} and (c) N_{CP_D} . V_{base} , V_{peak} , N_S and N_D represent the base voltage, peak voltage, loss to the source and loss to the drain, respectively. N_{inv} is obtained using the relationship: $N_{inv} = N_{CP_S} + N_{CP_D} - N_{CP_SD}$.

In the case of devices featuring relatively high D_{it} and D_{bt} , such as high- k /InGaAs MOSFETs, the ICP measurement parameters need to be carefully selected in order to, not only maximize the geometrical component, but also minimize the trapped charge component.

5.3 Results and Discussion

5.3.1 Inversion-Charge Pumping Measurements

5.3.1.1 Reduction of the Interface Trap Contribution

5.3.1.1.1 Interface Trap Density Profile

Figure 5.2 shows the D_{it} vs V_g profile obtained on the $\text{Al}_2\text{O}_3/\text{In}_{0.53}\text{Ga}_{0.47}\text{As}$ MOSFETs using the high (1 MHz) - low (2 kHz) frequency method, [10], measured at a temperature (T) of 292 K along with the full-conductance method, [11], performed over a range of T going from 292 K to 78 K. An agreement was obtained between the two methods at 292 K. It is noted that the D_{it} is intentionally plotted against V_g (not against energy) in order to identify the different D_{it} contribution for varying V_{base} . The D_{it} vs V_g profile presents relatively high D_{it} levels ($D_{it} > C_{ox}/q = 4.75 \times 10^{12} / \text{cm}^2 \cdot \text{eV}$) going towards the middle of the $\text{In}_{0.53}\text{Ga}_{0.47}\text{As}$ bandgap for $V_g < -1$ V. D_{it} values of $\sim 2 \times 10^{12}$ to $\sim 5 \times 10^{12} / \text{cm}^2 \cdot \text{eV}$ are observed near the $\text{In}_{0.53}\text{Ga}_{0.47}\text{As}$ conduction band for V_g ranging from V_T to $V_T - 0.5$ V (i.e.: $V_g = -0.3$ V). These results are consistent with the analysis presented in Chapter 4 [(Figure 4.7(b), page 85)] and with the literature review shown for the $\text{Al}_2\text{O}_3/\text{In}_{0.53}\text{Ga}_{0.47}\text{As}$ system in Chapter 1 [Figure 1.8(b), page 11].

5.3.1.1.2 Impact of Base Voltage and Comparison with Split $C-V$ at Low Temperature

We found that the ICP measurement configuration where $V_{base} \approx V_{fb}$ [Figure 5.3(a)], initially developed by Kerber *et al.* [3] for the for the SiO_2/Si interface, featuring typical D_{it} values of $< 10^{11} / \text{cm}^2 \cdot \text{eV}$ [14, 15], was not suitable for the $\text{Al}_2\text{O}_3/\text{In}_{0.53}\text{Ga}_{0.47}\text{As}$ MOSFETs due to the large D_{it} level observed towards the middle of the $\text{In}_{0.53}\text{Ga}_{0.47}\text{As}$ bandgap (Figure 5.2 and Chapter 4). Indeed, in this configuration, any interface trap located within the semiconductor bandgap can contribute to N_{CP} and, therefore, lead to an overestimation of N_{inv} . In this work, our approach was to raise V_{base} , as depicted in Figure 5.3(b), in order to increase the amount of interface traps constantly occupied during the ICP measurement and, therefore, reduce the D_{it} contribution to N_{CP} . This is demonstrated in Figure 5.4(a) with N_{CP} measurements obtained for a range of V_{base} going from -0.9 V to -0.3 V and corrected for the loss to the S/D ($1-\alpha$) using Equation 5.2. Indeed, as V_{base} was gradually raised to -0.3 V, which corresponds to the region of the D_{it} vs V_g profile where the D_{it} is the lowest [Figure 5.2], the N_{CP} vs V_{peak} curves are progressively

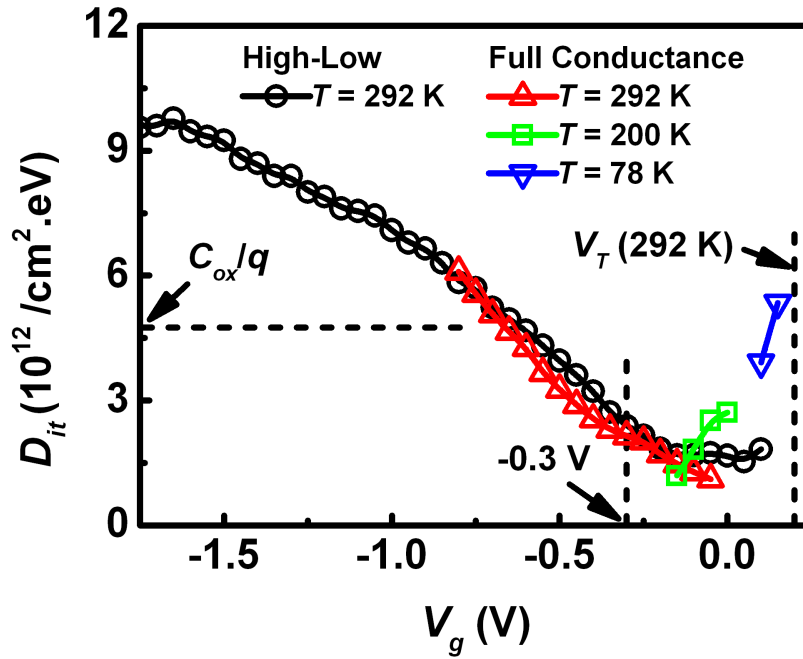


Figure 5.2: Density of interface traps (D_{it}) vs gate voltage (V_g) profile obtained using the high-low and full-conductance methods. The high-low was performed at a temperature (T) of 292 K while that of the full-conductance method was varied from 292 K to 78 K in order to access interface traps located in different parts of the $\text{In}_{0.53}\text{Ga}_{0.47}\text{As}$ bandgap [12]. The relatively large D_{it} values (greater than C_{ox}/q) obtained with the high-low method for $V_g < -0.75$ V preclude the use of a conductance-based method in that V_g range [13]. The threshold voltage (V_T) of 0.2 V, obtained at $T = 292$ K, is used to locate the $\text{In}_{0.53}\text{Ga}_{0.47}\text{As}$ conduction band edge.

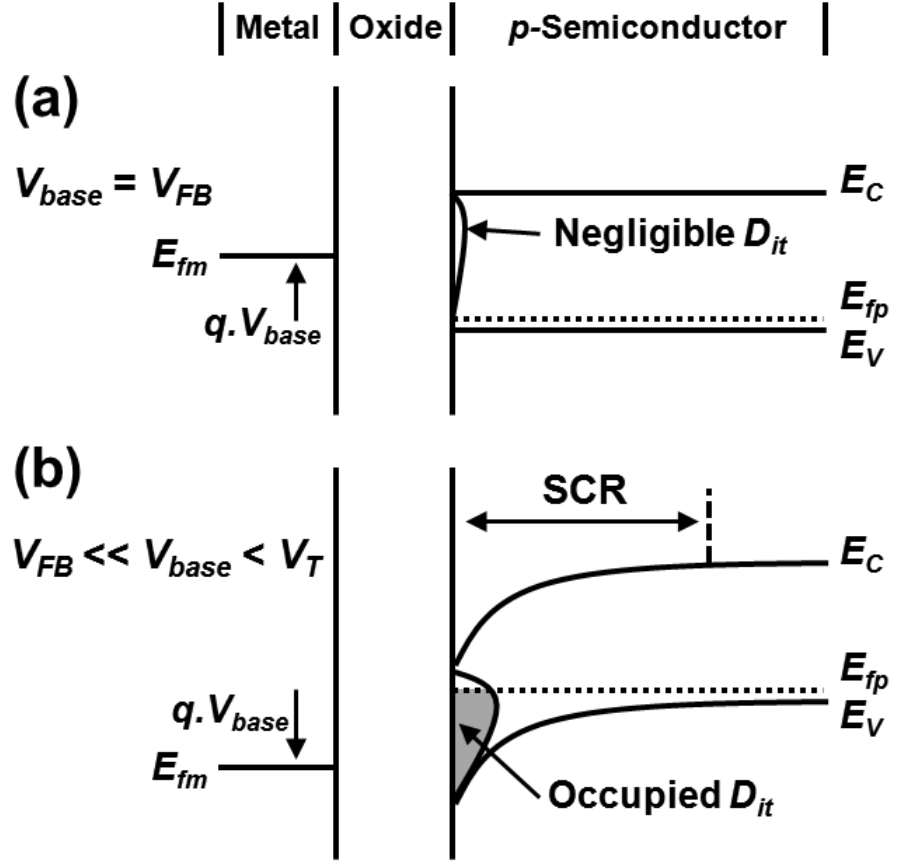


Figure 5.3: Energy band diagrams of a p -type metal-oxide-semiconductor (MOS) structure showing (a) the SiO₂/Si interface case, where the density of interface trap (D_{it}) distributed across the semiconductor bandgap is negligible ($< 10^{10}$ /cm².eV), allowing to perform the ICP measurement with $V_{base} = V_{fb}$, and (b) the high- k /In_{0.53}Ga_{0.47}As interface case, where the D_{it} is large, requiring $V_{fb} \ll V_{base} < V_T$ in order to maintain constant occupancy of most of the interface traps during the ICP measurement. It is noted that as V_{base} is raised from V_{fb} towards V_T , the structure is moved from a flat-band condition to a depletion condition, which involves the formation of a space charge region (SCR) energy barrier impeding the recombination of the inversion charge during the ICP measurement. In the diagrams, E_{fm} is the metal Fermi level while E_C , E_V and E_{fp} are the semiconductor conduction band edge, valence band edge and Fermi level, respectively.

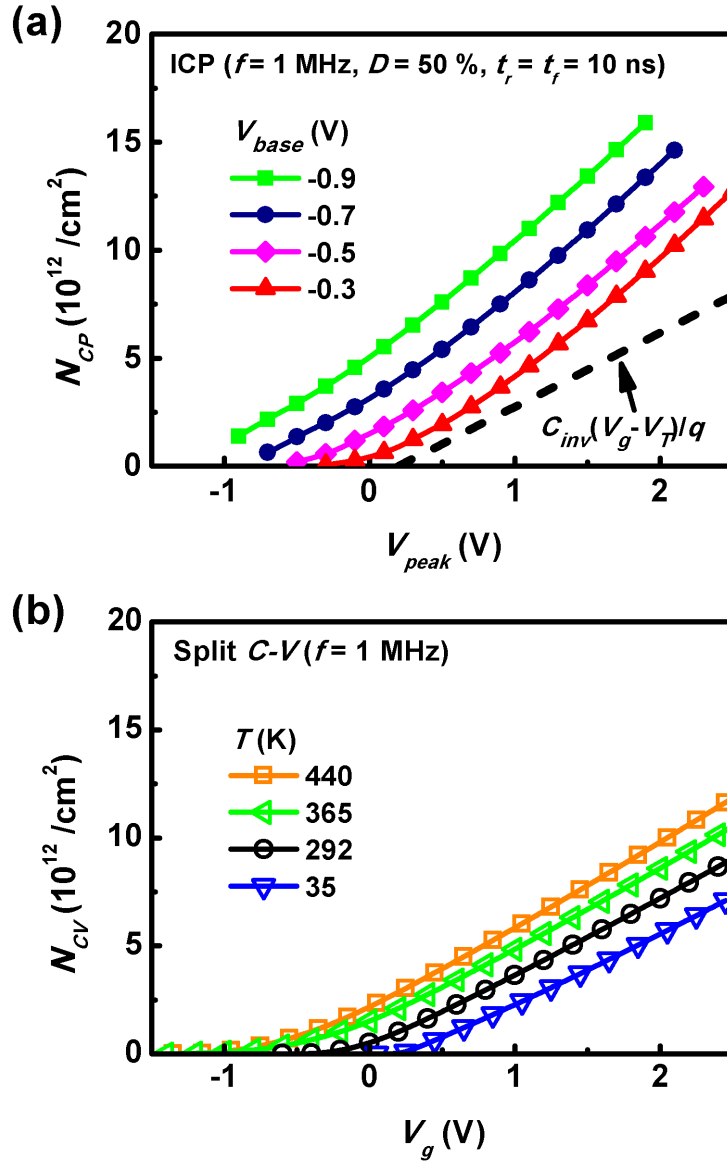


Figure 5.4: (a) Total pumped charge density (N_{CP}) vs peak voltage (V_{peak}) obtained for a base voltage (V_{base}) ranging from -0.3 V to -0.9 V. The ICP measurements were performed on a 40- μm -channel-length device with a frequency (f) of 1 MHz, a duty cycle (D) of 50 % and pulse rise time (t_r) and fall time (t_f) of 10 ns. The D_{it} contribution to N_{CP} reduces as V_{base} is raised from -0.9 V to -0.3 V. The experimental curves are non-linear and their slopes deviate from the theoretical $C_{inv} \cdot (V_g - V_T) / q$ curve, where C_{inv} is the capacitance in inversion measured by split C-V at a temperature (T) of 35 K and q is the charge of an electron. (b) Total charge density (N_{CV}) vs V_g obtained by split C-V at $f = 1$ MHz over a range of T going from 440 K to 35 K. The D_{it} contribution to N_{CV} reduces as T is reduced.

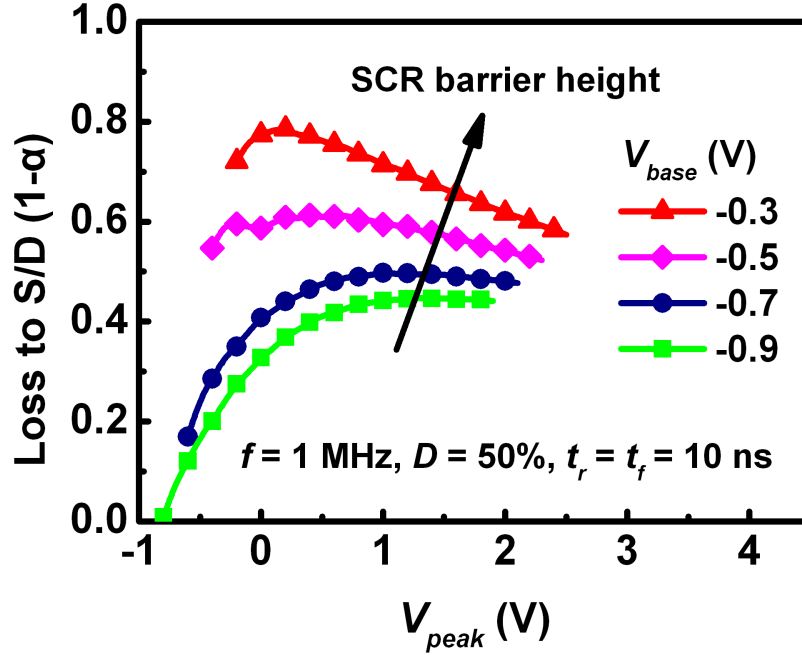


Figure 5.5: Loss to S/D ($1-\alpha$) vs peak voltage (V_{peak}) obtained for a base voltage (V_{base}) ranging from -0.3 V to -0.9 V. The space charge region (SCR) barrier height increases as V_{base} is raised from -0.9 V to -0.3 V.

shifted downwards in N_{CP} magnitude until a point where N_{CP} only starts rising at $V_{peak} \sim V_T$, suggesting that the response of the majority of the interface trap located within the $\text{In}_{0.53}\text{Ga}_{0.47}\text{As}$ bandgap is removed.

A similar approach was used in [16], where split C-V measurements were performed at a low T of 77 K in order to “freeze” the response of the interface traps located near the $\text{In}_{0.53}\text{Ga}_{0.47}\text{As}$ conduction band and extract a more accurate N_{inv} . We performed split C-V measurements over a wide range of T going from 440 K to 35 K Figure 5.4(b) in order to verify this concept and demonstrate that varying V_{base} in an ICP measurement performed at $T = 292$ K had the same impact as varying T in split C-V measurement. From Figure 5.4(b), where the N_{CV} , which is defined here as $N_{CV} = N_{inv} + (D_{it} + D_{bt}.t_{bt}).\Delta E$, is plotted against V_g , it is clear that the N_{CV} - V_g curves exhibit a progressive reduction in N_{CV} magnitude as T reduces from 440 K to 35 K. The similarity between the two trends observed in Figure 5.4(a) and (b) provides evidence to support the idea that raising V_{base} reduces the contribution of interface states, located in the upper part of the $\text{In}_{0.53}\text{Ga}_{0.47}\text{As}$ bandgap, to N_{CP} .

Having demonstrated the advantage of raising V_{base} , we now need to consider the issue associated with a higher V_{base} . Indeed, as V_{base} is raised towards V_T , the fraction ($1-\alpha$) of N_{inv} lost to

the S/D increases significantly (Figure 5.5) and the correction applied to N_{CP} using Equation 5.2 becomes larger. This is explained by the fact that as V_{base} increases, the barrier height of the space charge region (SCR) increases [Figure 5.3(b)], impeding the recombination of the inversion charge in the substrate but favoring its diffusion to the S/D, consistent with [9].

Referring back to Figure 5.4(a) and considering an inversion capacitance of 5.5×10^{-7} F/cm² extracted from the split C-V measurement at frequency (f) = 1 MHz and $T = 35$ K [Figure 5.4(b)], we can compare the measured N_{CP} - V_{peak} ($V_{base} = -0.3$ V) curve to a theoretical $C_{inv} \cdot (V_g - V_T) / q$ curve. It is evident that the N_{CP} - V_{peak} curve “curls up” and significantly deviates from $C_{inv} \cdot (V_g - V_T) / q$ as V_{peak} increases. If the only contribution to N_{CP} above V_T is N_{inv} , this relationship should be linear. We suggest that this deviation from linearity for $V_g > V_T$ is a consequence of a D_{bt} contribution. Moreover, the same D_{bt} affects the ICP and the split C-V measurement differently. This can be explained using the energy band diagram of a metal-oxide-semiconductor (MOS) structure assuming a simplified D_{bt} uniformly distributed across energy. In the case of the ICP measurement, the ΔE swept by the Fermi level going from V_{base} to V_{peak} increases with V_{peak} [Figure 5.6(a)]. As a result, the integrated border trap contribution $D_{bt} \cdot t_{bt} \cdot \Delta E$ to N_{CP} (Equation 5.1) also increases with V_{peak} , leading to the non-linearity observed on the N_{CP} - V_{peak} curves [Figure 5.4(a)]. In the case of a split C-V measurement, however, where the response to a small alternative current (ac) signal superposed to a slowly varying V_g is measured [Figure 5.6(b)], ΔE and, therefore, $D_{bt} \cdot t_{bt} \cdot \Delta E$ only depend on the amplitude of the ac signal (typically 25 mV) but remain independent of V_g . In the presence of a non-uniformly distributed D_{bt} across energy, $D_{bt} \cdot t_{bt} \cdot \Delta E$ will vary with V_g . However, this effect will not be as strong as in the case of the ICP.

5.3.1.2 Reduction of the Border Trap Contribution

5.3.1.2.1 Evidence of Border Trap Contribution

Recent studies have indicated the presence of border traps in high- k /InGaAs MOS structures using C-V [17, 18], charge pumping [19] and high-frequency transconductance [20] measurements. Evidence of the presence of border traps can also be observed in the I_d - V_g characteristic, where it is manifest as a hysteresis [21, 22]. Single pulse and DC I_d - V_g hysteresis, performed on a 1- μ m channel-length (L) device at a drain-to-source voltage (V_{ds}) of 50 mV, are shown in Figure 5.7. Going from a “slow” DC measurement to a “fast” single pulse measurement, the hysteresis increased from 70 mV to 195 mV, while the drain current at $V_g = 2.5$ V increased from 14.5 mA/mm to 16 mA/mm. This strongly suggests the presence of a charge trapping process involving border traps.

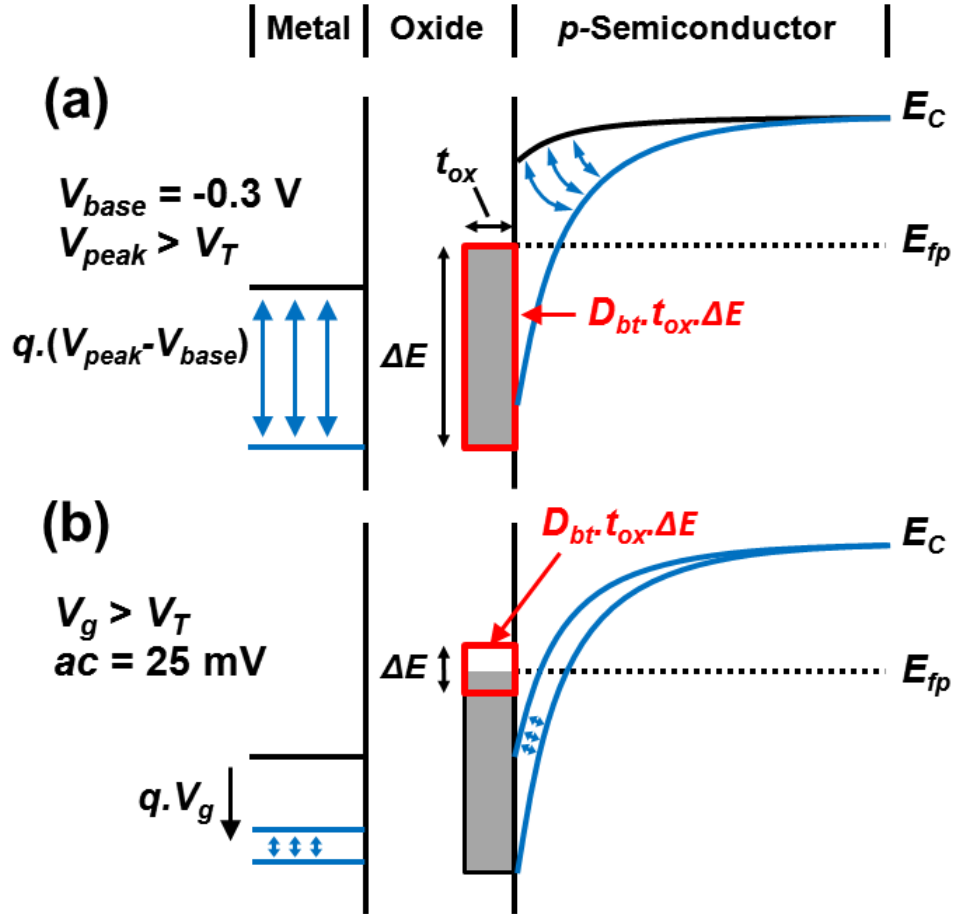


Figure 5.6: Example of energy band diagrams of a p -type metal-oxide-semiconductor (MOS) structure with a density of border traps (D_{bt}) assumed to be uniformly distributed across energy. (a) Case of an ICP measurement where the base voltage (V_{base}) is set to -0.3 V and the peak voltage (V_{peak}) is set to a value above the threshold voltage (V_T), respectively. (b) Case of a split $C-V$ measurement where the gate voltage (V_g) $> V_T$. In an ICP measurement, the energy range (ΔE) swept by the Fermi level increases with V_{peak} , while in a split $C-V$ measurement, ΔE depends on the amplitude of the AC signal (typically set to 25 mV) and not on V_g . Consequently, the $D_{bt} \cdot t_{ox} \cdot \Delta E$ contribution in an ICP measurement at large V_{peak} is much higher than that of a split $C-V$ measurement performed at a V_g matching V_{peak} . In the diagrams, E_C , and E_{fp} are the semiconductor conduction band edge, and Fermi level, respectively.

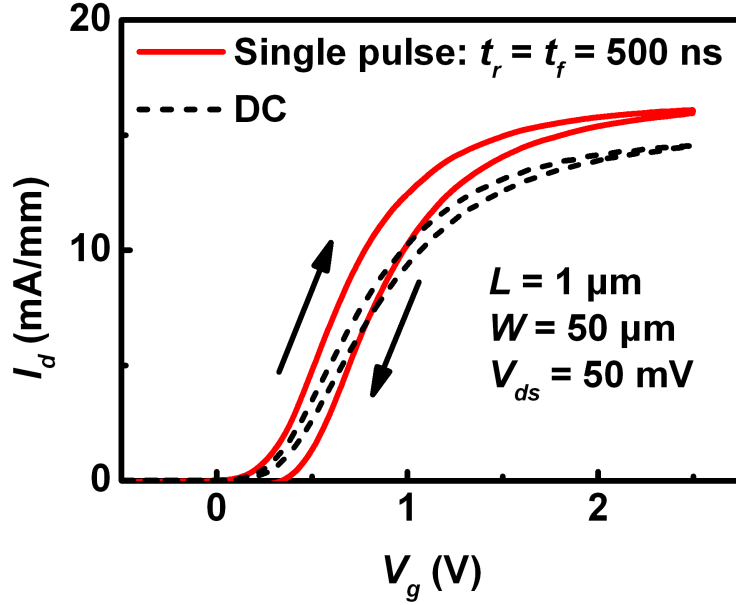


Figure 5.7: Single pulse and DC I_d - V_g hysteresis performed on a 1- μm -channel-length device at a drain-to-source voltage (V_{ds}) of 50 mV. The rise time (t_r) and fall time (t_f) of the single pulse measurement were set to 500 ns.

5.3.1.2.2 Impact of Duty Cycle

To minimize the D_{bt} contribution to N_{CP} , we propose to keep f constant but reduce the duty cycle (D) in order to reduce the transient charging time ($t_{charge} = D/f$) of the border traps. This approach is based on the premise that, since border traps capture charges from the inversion layer, the time to charge the border traps must be larger than the time required to form the inversion layer. The impact of D (t_{charge}) on N_{CP} is presented in Figure 5.8, where D (t_{charge}) is gradually reduced from 50% (500 ns) to 5% (50 ns) for $f = 1$ MHz. The “curling up” of the N_{CP} - V_{peak} curve, which was attributed to a D_{bt} contribution, gradually reduces as D reduces. At $D = 5\%$, the N_{CP} - V_{peak} curve nearly matches $C_{inv} \cdot (V_g - V_T)/q$ and the “curling up” almost disappears, suggesting a significant reduction in the D_{bt} contribution.

5.3.1.2.3 Multi-frequency Inversion-charge Pumping

In order to study the impact of f on the D_{bt} response, we performed ICP measurements over a range of f going from 10 kHz to 2 MHz for a fixed D of 50% and a V_{peak} going from 0 V to 2 V. In Figure 5.9, N_{CP} is plotted against f on the top x -axis and against t_{charge} on

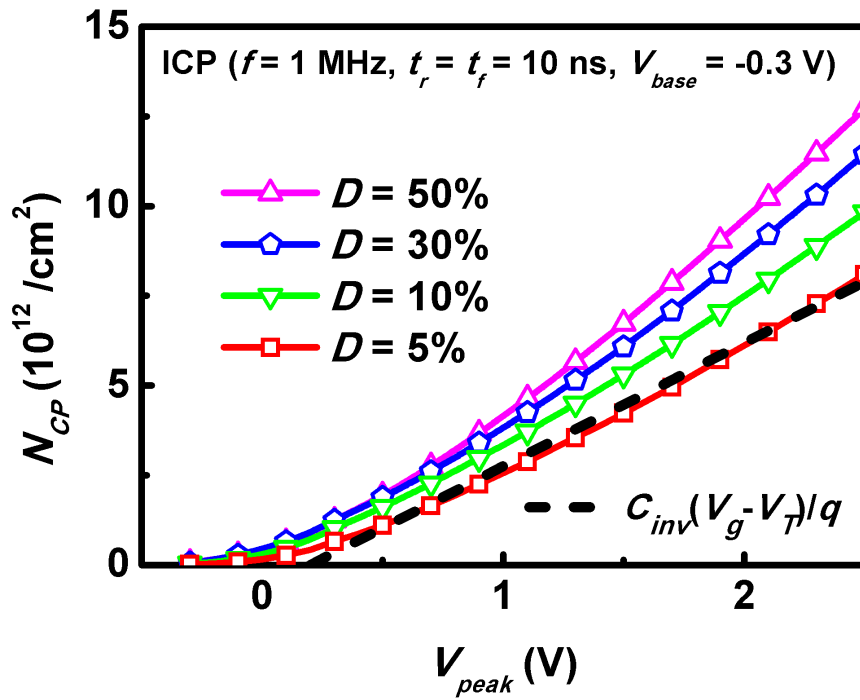


Figure 5.8: (a) Impact of duty cycle (D) on total pumped charge density (N_{CP}) obtained from ICP performed at a frequency (f) of 1 MHz and a rise time (t_r) and fall time (t_f) of 10 ns. The curve obtained at $D = 5\%$ nearly matches the theoretical $C_{inv} \cdot (V_g - V_T) / q$ curve, consistent with a reduction of the D_{bt} contribution to N_{CP} at low D .

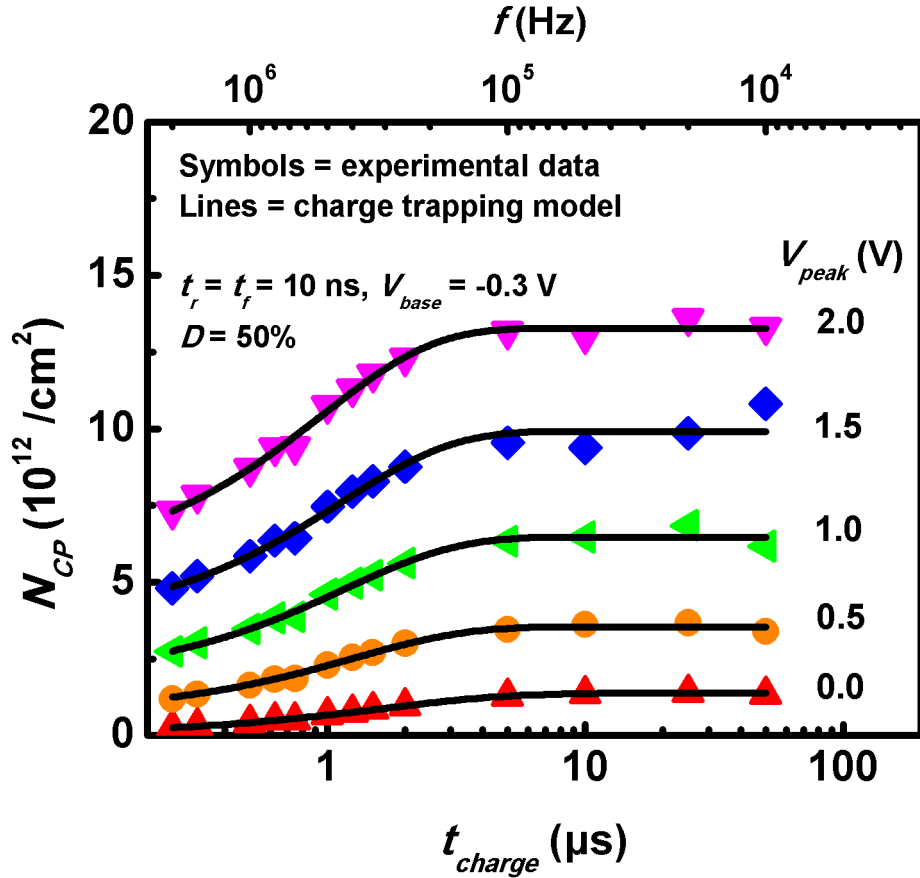


Figure 5.9: Total pumped charge density (N_{CP}) plotted against frequency (f) on the top x -axis and against charging time (t_{charge}), which is equal to $1/(2.f)$, on the bottom x -axis. The symbols show the experimental data obtained from the measurements performed on a $40\text{-}\mu\text{m}$ -channel-length device with the pulse rise time (t_r) and fall time (t_f) set to 10 ns, a base voltage (V_{base}) of -0.3 V and a duty cycle (D) of 50%. The peak voltage (V_{peak}) was varied from 0 V to 2 V. The lines represent the fitting of the data with the proposed charge trapping model.

Table 5.1: Model parameters fitted for a range of peak voltage (V_{peak}) values going from 0 V to 2 V. N_{bt}^0 is the border trap density in the Al_2O_3 integrated across energy and thickness, τ is the capture time constant, β is the distribution factor of capture time constant and N_{inv} is the inversion-charge density.

V_{peak} (V)	0	0.5	1	1.5	2
τ (μs)	1.7	1.2	1.2	1.1	1.0
β	1.0	1.0	1.0	1.0	1.0
N_{bt}^0 (10^{12} / cm^2)	1.4	2.9	4.6	6.3	7.8
N_{inv} (10^{12} / cm^2)	0.09	0.7	1.9	3.5	5.7
Adjusted R^2	0.997	0.991	0.984	0.964	0.991

the bottom x -axis [as $D = 50\%$, $t_{charge} = 0.5/f$]. N_{CP} increases as f reduces and a clear N_{cp} saturation is reached for $f < \sim 100$ kHz ($t_{charge} > \sim 5$ μs), suggesting a full D_{bt} response in that f range. In the high f region, however, no N_{CP} saturation is observed. This suggests that some border traps still respond at $f > 2$ MHz. This is in line with the work reported in [20], where evidence of “fast” border traps responding to $f > 1$ GHz is demonstrated. Unfortunately, the GHz frequency range is not accessible in our case. Indeed, considering the following equation for the recombination of the electrons of the inversion layer with the holes of the p -type substrate:

$$N_{inv}(t) = N_{inv}(0) \cdot \exp(-t/\tau_e) \quad (5.3)$$

and an electron lifetime (τ_e) of 30 ns for in p - $\text{In}_{0.53}\text{Ga}_{0.47}\text{As}$ doped to 4×10^{17} / cm^3 [23], we calculated that a channel with $N_{inv} = 10^{11}$ / cm^2 , 10^{12} / cm^2 and 10^{13} / cm^2 would be effectively depleted ($N_{inv} < 10^9$ / cm^2) in approximately 130 ns, 210 ns and 270 ns, respectively. This indicates that it is not possible to perform ICP measurements at $f > 2$ MHz and $D = 50\%$ as the transient discharge time [$t_{discharge} = (1-D)/f$] becomes too short to allow the full N_{inv} recombination, leading to an underestimation of N_{inv} . We propose to circumvent this issue by fitting the measured “multi-frequency ICP” data shown in Figure 5.9 using a charge trapping model, similar to that reported in [24–26], but including N_{inv} and assuming a negligible D_{it} contribution to N_{CP} (as $V_{base} = -0.3$ V):

$$N_{CP} = N_{bt}^0 \cdot [1 - \exp(-(t_{charge}/\tau)^\beta)] + N_{inv} \quad (5.4)$$

where τ is the capture time constant, β is the distribution factor of the capture cross section (σ) and N_{bt}^0 is the surface-equivalent density of border trap integrated across the energy range swept as V_g goes from V_{base} to V_{peak} . The τ , β , N_{bt}^0 and N_{inv} values obtained from the fitting of the multi-frequency N_{CP} data for V_{peak} ranging from 0 V to 2 V (Figure 5.9) are summarized in Table 5.1. Adjusted R^2 ranging from 0.964 to 0.997 were obtained, indicating a good fit of the

model to the experimental data.

As V_{peak} increased from 0 V to 2 V, a decrease in τ from 1.6 μ s to 1.0 μ s was observed. These τ values are consistent with the values reported in [27] for traps located at energy levels aligned with the $\text{In}_{0.53}\text{Ga}_{0.47}\text{As}$ conduction band. In the charge trapping model, the distribution factor β , which represents a measure of the width of the σ distribution of the traps, can range between a value of 1.0 and 0. A β value of 1.0 corresponds to a discrete σ , while values approaching 0 indicate very wide distributions of σ . The fact that our experimental data was best fitted with $\beta = 1.0$ indicates a discrete σ and suggests that the border traps could originate from a single type of physical defect. It is possible to estimate σ using:

$$\tau = (N \cdot \sigma \cdot v_{th})^{-1} \quad (5.5)$$

where N is the volume inversion density and v_{th} is the electron thermal velocity. Considering $\tau \sim 1 \mu$ s, $v_{th} = 5.5 \times 10^7$ cm/s [28] and $N = 4.1 \times 10^{18}$ /cm³,² we estimated that σ was $\sim 4.5 \times 10^{-21}$ cm². This rather small σ value is consistent with that of border traps [29], as σ values in the 10^{-13} to 10^{-17} range are generally considered for interface traps [12, 19, 30]. The distance (x) of the border traps from the semiconductor interface can be estimated using the relationship [31]:

$$x = \lambda \cdot \ln(t_t/\tau) \quad (5.6)$$

where t_t is the tunnelling time and λ is the attenuation coefficient. Considering that N_{CP} saturation is reached at $t \sim 5 \mu$ s (Figure 5.9) and $\lambda = 1.1 \times 10^{-8}$ cm [20], we calculated a distance x of $\sim 1.5 \text{ \AA}$ from the interface, consistent with the value reported in [20] for a $\text{HfO}_2/\text{Al}_2\text{O}_3/\text{In}_{0.53}\text{Ga}_{0.47}\text{As}$ system. The increase in N_{bt}^0 with V_{peak} is consistent with the presence of border traps located at energy levels aligned with the $\text{In}_{0.53}\text{Ga}_{0.47}\text{As}$ conduction band [17]. Moreover, assuming a $\sim 2\text{-\AA}$ -wide border trap distribution [20], consistent with a discrete σ , and considering that an energy range of 0.77 eV is swept when V_g goes from $V_{base} = -0.3$ V to $V_{peak} = 2$ V [obtained from the analysis of Chapter 4], a N_{bt}^0 of 7.8×10^{12} /cm² would equate to a D_{bt} of 5.1×10^{20} /cm³.eV, which is in reasonable agreement with the peak D_{bt} values of 1.05×10^{21} /cm³.eV and $\sim 1.6 \times 10^{21}$ /cm³.eV reported in [19] and [20], respectively. This analysis suggests the presence of border traps featuring a very small capture cross section and being located very close to the $\text{Al}_2\text{O}_3/\text{In}_{0.53}\text{Ga}_{0.47}\text{As}$ interface in a very narrow spatial distribution. We speculate that the presence of these border traps could be due to an ultra-thin interlayer of native oxide at the $\text{Al}_2\text{O}_3/\text{In}_{0.53}\text{Ga}_{0.47}\text{As}$ interface. This speculation warrants further investigation. It is noted that the fast trapping of electrons, in border-trap distributions presenting very similar

²Self-consistent Poisson Schrödinger calculations revealed an inversion layer thickness of 14 nm at $N_{inv} = 5.7 \times 10^{12}$ /cm², yielding $N = 4.1 \times 10^{18}$ /cm³.

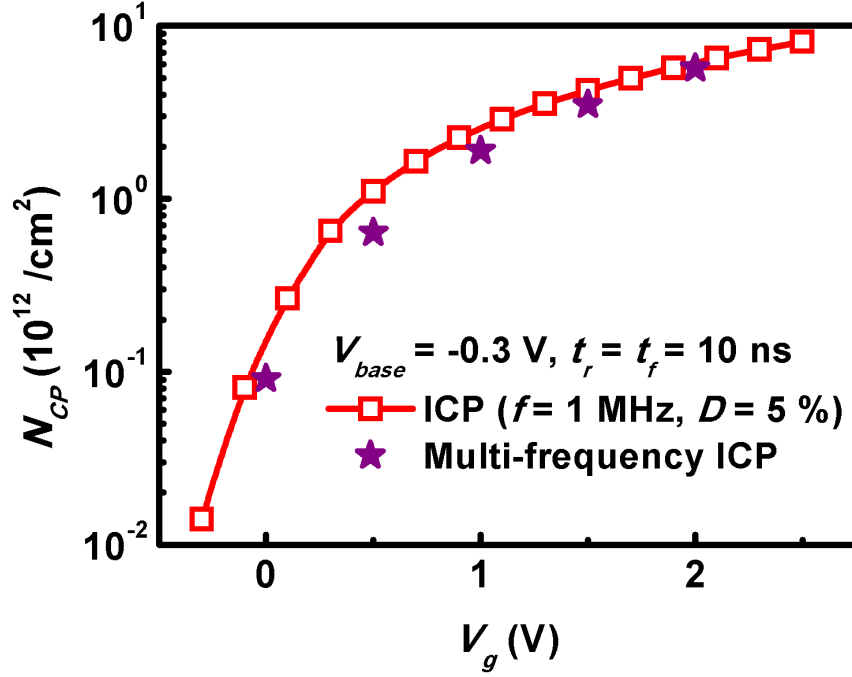


Figure 5.10: Comparison of the total pumped-charged density (N_{CP}) obtained from inversion-charge pumping (ICP) at a frequency (f) of 1 MHz and duty cycle (D) of 5%, and multi-frequency ICP. In both measurements the base voltage (V_{base}) was -0.3 V and the rise time (t_r) and fall time (t_f) were 10 ns.

features as that reported here, was attributed to a gap state injection process in a very recent report from Engstrom *et al.* [32].

The negligible N_{inv} value at $V_{peak} = 0$ V (Table 5.1) is consistent with a V_T of 0.2 V. As V_{peak} increases from 0.5 V to 2 V, N_{inv} increases from 7.0×10^{11} to 5.7×10^{12} /cm². Figure 5.10 compares the N_{CP} obtained from multi-frequency ICP to that obtained from ICP ($f = 1$ MHz and $D = 5\%$). The Multi-frequency ICP gives slightly lower N_{CP} values, confirming that some border traps can respond in less than 50 ns, consistent with [20].

Although the separation of the D_{bt} component of N_{CP} was successfully demonstrated through the fitting of the multi-frequency ICP data, it is important to note that a potential D_{it} component associated with interface traps located at energy levels aligned with the In_{0.53}Ga_{0.47}As conduction, [33], may still lead to an overestimation of N_{inv} . However, the integration of the total trap density *vs* energy profile obtained in Chapter 4 [Figure 4.6(b), page 83], across a ΔE corresponding to a V_g sweep going from 0.5 to 2 V, yielded a trap density of $\sim 4.4 \times 10^{12}$ /cm². This value is in close agreement with the value of 4.9×10^{12} /cm² obtained by subtracting the

N_{bt}^0 values obtained using the multi-frequency method for $V_{peak} = 2$ V and 0.5 V (Table 5.1). This provides a strong evidence that most of the traps located at energy levels aligned with the $\text{In}_{0.53}\text{Ga}_{0.47}\text{As}$ conduction could be border traps in these devices. It also suggests that the N_{inv} extracted by multi-frequency ICP represents a good estimate of the true N_{inv} .

The multi-frequency ICP technique was demonstrated to be an effective approach for the characterization of border traps and the extraction of N_{inv} . However, this approach suffers from one limitation: the very large number of measurements required to obtain a full N_{inv} vs V_g curve. For instance, obtaining the data shown in Figure 5.9 required the measurement of N_{CP_SD} , N_{CP_S} and N_{CP_D} (Figure 5.1) at 13 different f , representing a total of 39 measurements. Such a large number of measurements makes this approach difficult to implement without stressing the devices, especially when low f are required to investigate the full D_{bt} response.

5.3.2 I_d - V_g Measurements

5.3.2.1 Pulse I_d - V_g Measurements and Series Resistance Extraction

Figure 5.11 compares the pulsed and DC I_d - V_g measurements performed at a drain-to-source voltage (V_{ds}) of 50 mV on a device featuring a channel length (L) of 1 μm and a channel width (W) of 50 μm . The rise time (t_r) and fall time (t_f) of the pulsed I_d - V_g measurement were set to 10 ns. It is noted that the pulsed measurement resulted in a $\sim 10\%$ increase in the maximum drain current, consistent with a charge trapping process within the Al_2O_3 gate oxide. As the presence of “fast” border traps was demonstrated, we speculate that higher f or lower D may reveal an even higher maximum drain current. Unfortunately, our pulsed I - V setup does not allow such measurement conditions. Additional pulsed and DC I_d - V_g measurements were performed on devices with channel lengths of 2, 3, 5, 10 and 20 μm in order to extract S/D resistance (R_{SD}) values of 49 Ω and 59 Ω , respectively [inset Figure 5.11].

5.3.2.2 Low Temperature DC I_d - V_g Measurements and Series Resistance Extraction

The effect of reducing T in DC I_d - V_g measurements is illustrated in Figure 5.12. The V_T shifts towards more positive values as T reduces, consistent with Figure 5.4(b). A zero-temperature coefficient (ZTC) point at $V_g = 2.15$ V is observed. The inset of Figure 5.12 shows that R_{SD} increases when T is reduced. This is consistent with an incomplete ionization of the S/D dopant increasing as T reduces [34].

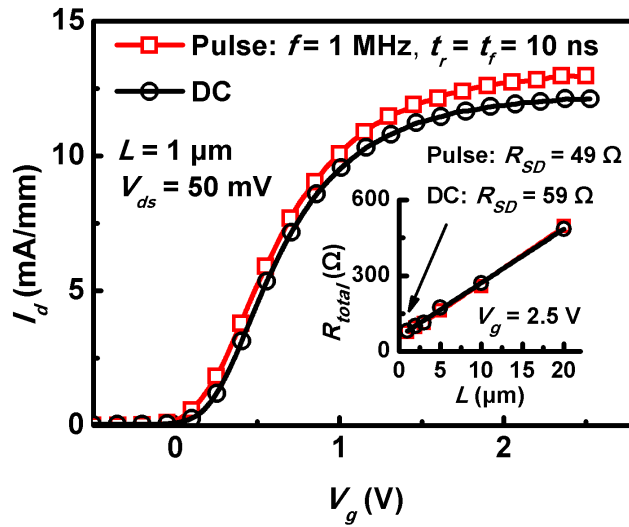


Figure 5.11: Comparison of the pulse and DC I_d - V_g characteristics performed on a $1\text{-}\mu\text{m}$ -channel-length device at a drain-to-source voltage (V_{ds}) of 50 mV . The rise time (t_r) and fall time (t_f) of the pulse measurement were set to 10 ns . Inset: R_{total} ($= V_{ds}/I_d$) vs channel length (L) at a gate voltage (V_g) of 2.5 V . The intercept on the y -axis yields the source and drain series resistance (R_{SD}).

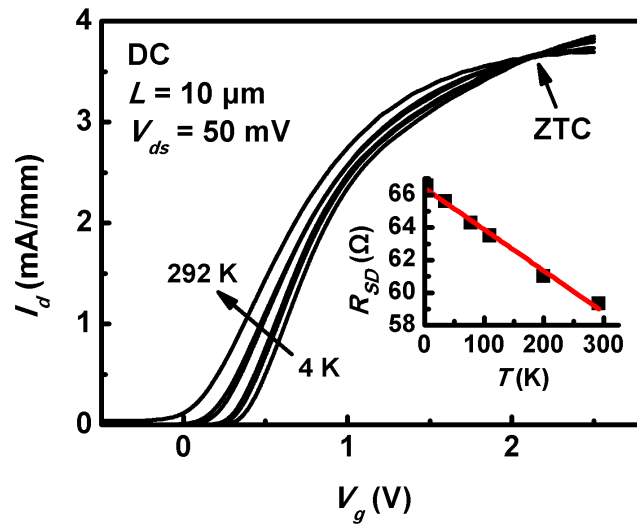


Figure 5.12: DC I_d - V_g characteristics measured over a range of temperature (T) going from 4 K to 292 K on a $10\text{-}\mu\text{m}$ -channel-length device at a drain-to-source voltage (V_{ds}) of 50 mV . A zero-temperature coefficient (ZTC) point is observed. Inset: Source and drain series resistance (R_{SD}) as a function of temperature (T).

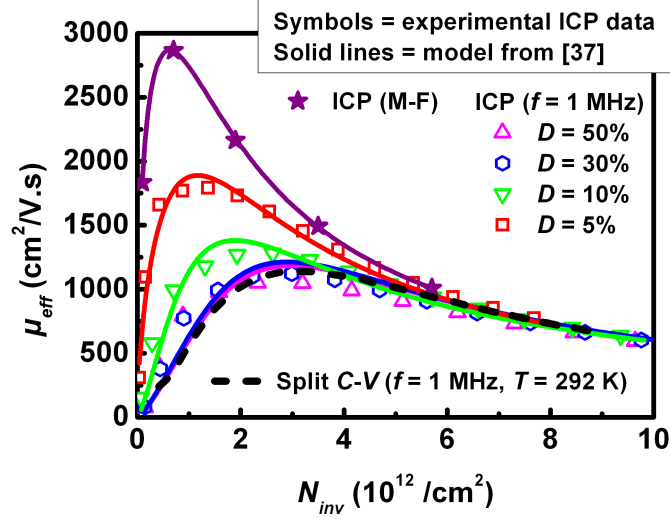


Figure 5.13: Effective mobility (μ_{eff}) vs inversion charge (N_{inv}) extracted using ICP at a frequency (f) of 1 MHz and a duty cycle (D) ranging from 50% to 5% and multi-frequency ICP. Excellent agreement is obtained between the μ_{eff} extracted from Split $C-V$ ($f = 1$ MHz, $T = 292$ K) and that extracted by ICP ($f = 1$ MHz, $D = 50\%$). The experimental μ_{eff} values (symbols) were fitted with the empirical model reported in [37].

5.3.3 Comparison of the Effective Mobility Extracted from the Inversion-Charge Pumping, Multi-frequency Inversion-Charge Pumping and Low Temperature Split $C-V$ Methods

Figure 5.13 compares the μ_{eff} extracted from ICP ($f = 1$ MHz, varied D), multi-frequency ICP and Split $C-V$ ($f = 1$ MHz, $T = 292$ K). Excellent agreement between the ICP at $D = 50\%$ and split $C-V$ was obtained. As the D_{bt} contribution to N_{CP} is reduced due to a reduction in D , μ_{eff} at low N_{inv} increases significantly. A peak μ_{eff} of $2850 \text{ cm}^2/\text{V.s}$ at a low N_{inv} of $7 \times 10^{11} \text{ cm}^2/\text{V.s}$ was obtained from multi-frequency ICP. However, a strong N_{inv} dependence is also observed as μ_{eff} rapidly drops down to $\sim 600 \text{ cm}^2/\text{V.s}$ at $N_{inv} = 1 \times 10^{13} / \text{cm}^2$. This strong N_{inv} dependence is consistent with a μ_{eff} dominated by surface roughness at high N_{inv} , in agreement with [16, 35, 36].

As the μ_{eff} degradation mechanism due to surface roughness is typically independent of T , we extracted μ_{eff} from Split $C-V$ ($f = 1$ MHz) measurements performed over a range of T going from 292 K to 35 K (Figure 5.14). While an increase in μ_{eff} is observed for $N_{inv} < 4 \times 10^{12} / \text{cm}^2$ as T reduces, consistent with the reduction of the D_{it} contribution to N_{inv} at lower T discussed in paragraph 5.3.1.1.2 and also reported in [16], it is very clear that μ_{eff} remains independent of T for $N_{inv} > 4 \times 10^{12} / \text{cm}^2$. This temperature independence and strong N_{inv} dependence

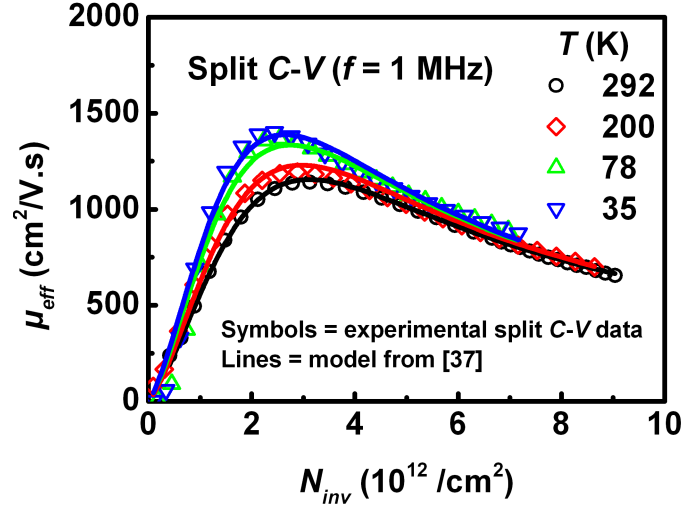


Figure 5.14: Effective mobility (μ_{eff}) vs inversion charge (N_{inv}) extracted using split C - V at a frequency (f) of 1 MHz for a range of temperature (T) going ranging from 292 K to 35 K. The experimental μ_{eff} values (symbols) were fitted with the empirical model reported in [37].

represent a strong evidence that μ_{eff} is dominated by surface roughness at high N_{inv} . However, the μ_{eff} extracted from split C - V at $T = 35$ K still remained lower than that extracted with the ICP ($D = 5\%$) and multi-frequency ICP methods.

5.3.4 Modeling of Effective Mobility

In order to gain further insight in the mechanisms involved in the μ_{eff} degradation, we fitted the extracted μ_{eff} using the empirical model reported in [37], where the phonon scattering mobility (μ_{ph}), the surface roughness scattering mobility (μ_{sr}), the Coulomb scattering mobility (μ_C) and the total mobility (μ_{tot}) are expressed in Equations 5.7, 5.8, 5.9, and 5.10, respectively:

$$\mu_{ph} = A.N_{inv}^{-0.3}.T^{-1.75} \quad (5.7)$$

$$\mu_{sr} = B.N_{inv}^{\beta} \quad (5.8)$$

$$\mu_C = C.N_{inv}^{\gamma} \quad (5.9)$$

$$1/\mu_{tot} = 1/\mu_{ph} + 1/\mu_{sr} + 1/\mu_C \quad (5.10)$$

The parameters A , B , β , C and γ were adjusted to fit the experimental μ_{eff} extracted from ICP ($f = 1$ MHz, varied D), multi-frequency ICP and split C - V ($f = 1$ MHz, varied T). As indicated by the $T^{-1.75}$ dependence of μ_{ph} , phonon scattering becomes negligible at low T .

Therefore, we first fitted the high N_{inv} part of the μ_{eff} curve extracted from split $C-V$ at $T = 35$ K in order to obtain the coefficients $B = 6.5 \times 10^{15}$ and $\beta = -1$ that define μ_{sr} . It is noted that, although surface roughness generally shows a N_{inv}^{-2} dependence, a $N_{inv}^{-0.7}$ dependence was reported in [36] for $\text{Al}_2\text{O}_3/\text{In}_x\text{Ga}_{1-x}\text{As}$ MOSFETs. We then obtained a γ of 1.3 for μ_C by fitting the low N_{inv} part of the curve. We then fitted μ_{eff} over a range of T going from 35 K to 292 K to obtain a coefficient A of $\sim 4 \times 10^{12}$ for μ_{ph} , which was found to be higher than $10^4 \text{ cm}^2/\text{V}\cdot\text{s}$ and have no significant impact on μ_{eff} , consistent with [35, 36]. The coefficient C of for μ_C was adjusted in order to account for the reduction of the D_{it} contribution to N_{CV} at lower T . The same model was also used to fit the ICP ($f = 1$ MHz, varied D) and multi-frequency ICP data, as shown in Figure 5.13. A simple adjustment of μ_C was found to be sufficient to obtain good fittings (Figure 5.15).

The approach presented in Chapter 4 was used in a parallel study to remove the contribution of traps aligned with the $\text{In}_{0.53}\text{Ga}_{0.47}\text{As}$ conduction band to a N_{CV} measured by split $C-V$ [35]. This enabled to extract N_{inv} and μ_{eff} and perform first-principles theoretical calculations [the calculations were performed by T. P. O'Regan (Tyndall)] in order to investigate the scattering mechanisms responsible for the μ_{eff} degradation. This analysis yielded results comparable to the results obtained with the multi-frequency ICP approach. Moreover, the theoretical calculations predicted a surface root mean square (RMS) roughness of 1.95 nm on the $\text{In}_{0.53}\text{Ga}_{0.47}\text{As}$ channel.

5.3.5 Analysis of the Surface Roughness of the Channel

RMS surface roughness measurements were obtained by atomic force microscopy (AFM) on a set of different samples in order to confirm the results obtained from the fitting of the electrical data and to identify the process step responsible for the high roughness of the $\text{In}_{0.53}\text{Ga}_{0.47}\text{As}$ surface. As listed in Table 5.2, the unpassivated sample [Figure 5.16(a)], the $(\text{NH}_4)_2\text{S}$ surface-passivated sample and the dilute-HF-dipped $p\text{-In}_{0.53}\text{Ga}_{0.47}\text{As}$ samples revealed low RMS surface roughness values of 0.21 ± 0.07 nm, 0.23 ± 0.04 nm and 0.21 ± 0.07 nm, respectively. However, a significantly high RMS surface roughness (1.95 ± 0.28 nm) was observed on the device sample, exposed to surface passivation, ALD of Al_2O_3 , activation anneal at 600°C for 15 sec and Al_2O_3 removal using dilute HF [Figure 5.16(b)]. This confirms the result obtained from the fitting of the μ_{eff} vs N_{inv} curves (Figure 5.13 and Figure 5.14) and suggests an RMS surface roughness increase following activation anneal at 600°C for 15 sec. We speculate that the As atoms desorbed from surface during the S/D activation anneal, leading to the formation of Ga aggregates [Figure 5.16]. The aggregates formation is very significant and the formation mechanisms warrant further investigation.

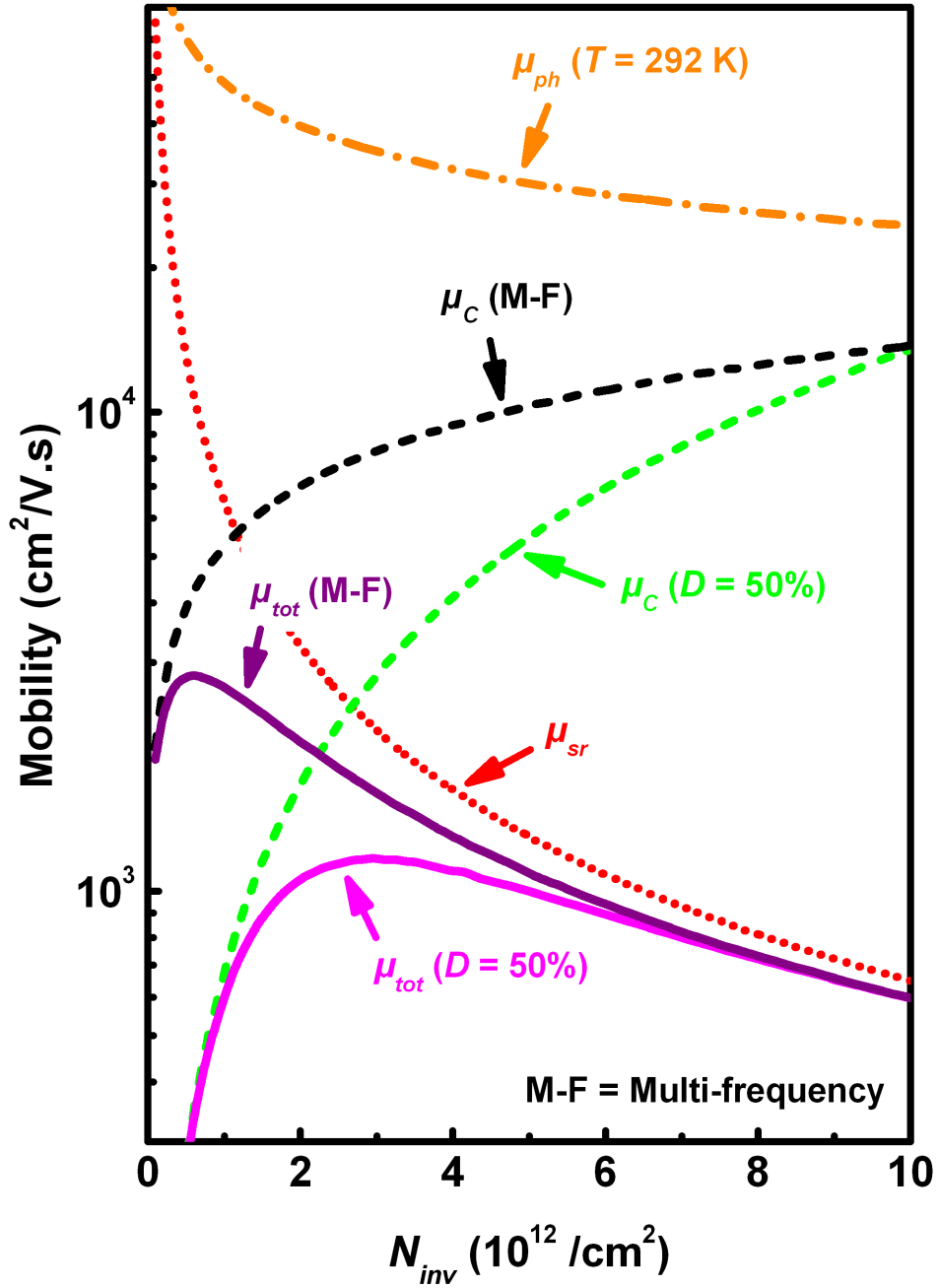


Figure 5.15: Scattering components obtained from the fitting of the effective mobility (μ_{eff}) vs inversion charge (N_{inv}) curves extracted from ICP ($f = 1$ MHz, $D = 50\%$) and multi-frequency (M-F) ICP. The phonon scattering mobility, the surface roughness scattering mobility, the Coulomb scattering mobility and the total mobility are noted μ_{ph} , μ_{sr} , μ_C , and μ_{tot} , respectively. While the same μ_{ph} and μ_{sr} were used to fit both curves, μ_C was adjusted to account for the removal of the border trap contribution to the total pumped-charged density (N_{CP}).

Table 5.2: RMS surface roughness extracted from AFM measurements. The quoted value represents the mean from at least three measurements at separate locations (each on a $1 \mu\text{m} \times 1 \mu\text{m}$ scan area) and the uncertainty is given by the standard deviation.

Sample	Treatment	RMS (nm)
1	Unpassivated	0.21 ± 0.07
2	10% $(\text{NH}_4)_2\text{S}$ (20 min)	0.23 ± 0.04
3	dilute HF (20 s)	0.21 ± 0.05
4	10% $(\text{NH}_4)_2\text{S}$ (20 min)/ALD Al_2O_3 /RTA (600°C , 15 s)/dilute HF (20 s)	1.95 ± 0.28

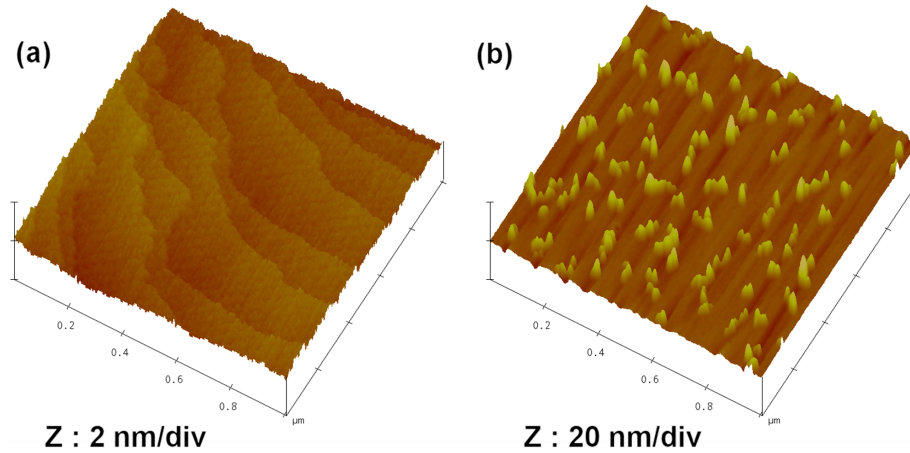


Figure 5.16: AFM topography data of (a) the unpassivated $p\text{-In}_{0.53}\text{Ga}_{0.47}\text{As}$ surface and (b) the $p\text{-In}_{0.53}\text{Ga}_{0.47}\text{As}$ surface after 10% $(\text{NH}_4)_2\text{S}$ pasivation for 20 min, 10 nm Al_2O_3 deposition by ALD, implant activation at 600°C for 15 s and finally Al_2O_3 etch using dilute HF. Both measurements were taken over a $1 \mu\text{m} \times 1 \mu\text{m}$ area. The AFM measurements were performed by M. Burke (Tyndall).

5.4 Conclusion

We applied the ICP method to extract the μ_{eff} of surface-channel $\text{Al}_2\text{O}_3/\text{In}_{0.53}\text{Ga}_{0.47}\text{As}$ MOSFETs. We adjusted the ICP measurement parameters in order to minimize the impact of D_{it} and D_{bt} on the measured N_{inv} . The V_{base} minimized the D_{it} response, while the duty cycle (D) was used to reduce the D_{bt} response. We proposed a multi-frequency ICP technique to investigate the D_{bt} response. The investigations suggested a discrete σ value of $\sim 4.5 \times 10^{-21} \text{ cm}^2$, consistent with a very narrow spatial distribution of border traps located very close ($\sim 1.5 \text{ \AA}$) to the $\text{Al}_2\text{O}_3/\text{In}_{0.53}\text{Ga}_{0.47}\text{As}$ interface. Although a peak μ_{eff} of $\sim 2850 \text{ cm}^2/\text{V.s}$ was extracted at a low N_{inv} of $7 \times 10^{11} / \text{cm}^2$ using the multi-frequency ICP technique, a sharp drop in μ_{eff} was observed at higher N_{inv} due to a dominant surface roughness scattering mechanism. This was confirmed by the lack of T dependence observed in the μ_{eff} at $N_{inv} > 4 \times 10^{12} / \text{cm}^2$ obtained by split C - V measurements performed over a range of T going from 292 K to 35 K along with the high RMS surface roughness of $1.95 \pm 0.28 \text{ nm}$ measured by AFM on the $\text{In}_{0.53}\text{Ga}_{0.47}\text{As}$ surface. Finally, the AFM measurements identify the S/D activation anneal process (600°C for 15 s) as being the cause of high $\text{In}_{0.53}\text{Ga}_{0.47}\text{As}$ surface roughness.

Bibliography

- [1] J. A. del Alamo, "Nanometre-scale electronics with III-V compound semiconductors," *Nature*, vol. 479, p. 317, Nov. 2011. [Online]. Available: <http://dx.doi.org/10.1038/nature10677>
- [2] K. Romanjek, F. Andrieu, T. Ernst, and G. Ghibaudo, "Improved split C-V method for effective mobility extraction in sub-0.1- μm Si MOSFETs," *Electron Device Letters, IEEE*, vol. 25, no. 8, p. 583, Aug. 2004. [Online]. Available: <http://dx.doi.org/10.1109/LED.2004.832786>
- [3] A. Kerber, E. Cartier, L.-A. Ragnarsson, M. Rosmeulen, L. Pantisano, R. Degraeve, Y. Kim, and G. Groeseneken, "Direct measurement of the inversion charge in MOSFETs: application to mobility extraction in alternative gate dielectrics," in *VLSI Technology, 2003. Digest of Technical Papers. 2003 Symposium on*, 2003, p. 159. [Online]. Available: <http://dx.doi.org/10.1109/VLSIT.2003.1221134>
- [4] É. O'Connor, B. Brennan, V. Djara, K. Cherkaoui, S. Monaghan, S. B. Newcomb, R. Contreras, M. Milojevic, G. Hughes, M. E. Pemble, R. M. Wallace, and P. K. Hurley, "A systematic study of $(\text{NH}_4)_2\text{S}$ passivation (22%, 10%, 5%, or 1%) on the interface properties of the $\text{Al}_2\text{O}_3/\text{In}_{0.53}\text{Ga}_{0.47}\text{As}/\text{InP}$ system for n -type and p -type $\text{In}_{0.53}\text{Ga}_{0.47}\text{As}$ epitaxial layers," *Journal of Applied Physics*, vol. 109, no. 2, p. 024101, Jan. 2011. [Online]. Available: <http://dx.doi.org/10.1063/1.3533959>
- [5] É. O'Connor, S. Monaghan, K. Cherkaoui, I. M. Povey, and P. K. Hurley, "Analysis of the minority carrier response of n -type and p -type $\text{Au}/\text{Ni}/\text{Al}_2\text{O}_3/\text{In}_{0.53}\text{Ga}_{0.47}\text{As}/\text{InP}$ capacitors following an optimized $(\text{NH}_4)_2\text{S}$ treatment," *Applied Physics Letters*, vol. 99, no. 21, p. 212901, Nov. 2011. [Online]. Available: <http://dx.doi.org/10.1063/1.3663535>
- [6] G. Groeseneken, H. Maes, N. Beltran, and R. De Keersmaecker, "A reliable approach to charge-pumping measurements in MOS transistors," *Electron Devices, IEEE Transactions on*, vol. 31, no. 1, p. 42, Jan. 1984. [Online]. Available: <http://dx.doi.org/10.1109/T-ED.1984.21472>
- [7] G. Groeseneken, "Introduction to charge pumping and its applications. Tutorial IEEE Semiconductor Interface Specialists Conference (SISC), San Diego, CA, Dec. 2008." [Online]. Available: <http://www.ieeesisc.org>
- [8] Y. Son, S. Park, T. Kang, B. Oh, and H. Shin, "Characterization of Border Trap Density With the Multifrequency Charge Pumping Technique in Dual-Layer Gate Oxide," *Electron*

-
- Devices, IEEE Transactions on*, vol. 58, no. 8, p. 2752, Aug. 2011. [Online]. Available: <http://dx.doi.org/10.1109/TED.2011.2157931>
- [9] G. Van den Bosch, G. Groeseneken, and H. Maes, "On the geometric component of charge-pumping current in MOSFETs," *Electron Device Letters, IEEE*, vol. 14, no. 3, p. 107, Mar. 1993. [Online]. Available: <http://dx.doi.org/10.1109/55.215126>
- [10] R. Castagné and A. Vapaille, "Description of the SiO₂/Si interface properties by means of very low frequency MOS capacitance measurements," *Surface Science*, vol. 28, no. 1, p. 157, Nov. 1971. [Online]. Available: [http://dx.doi.org/10.1016/0039-6028\(71\)90092-6](http://dx.doi.org/10.1016/0039-6028(71)90092-6)
- [11] K. Martens, C. O. Chui, G. Brammertz, B. De Jaeger, D. Kuzum, M. Meuris, M. M. Heyns, T. Krishnamohan, K. Saraswat, H. Maes, and G. Groeseneken, "On the Correct Extraction of Interface Trap Density of MOS Devices With High-Mobility Semiconductor Substrates," *Electron Devices, IEEE Transactions on*, vol. 55, no. 2, p. 547, Feb. 2008. [Online]. Available: <http://dx.doi.org/10.1109/TED.2007.912365>
- [12] G. Brammertz, K. Martens, S. Sioncke, A. Delabie, M. Caymax, M. Meuris, and M. Heyns, "Characteristic trapping lifetime and capacitance-voltage measurements of GaAs metal-oxide-semiconductor structures," *Applied Physics Letters*, vol. 91, no. 13, p. 133510, Sep. 2007. [Online]. Available: <http://dx.doi.org/10.1063/1.2790787>
- [13] R. Engel-Herbert, Y. Hwang, and S. Stemmer, "Comparison of methods to quantify interface trap densities at dielectric/III-V semiconductor interfaces," *Journal of Applied Physics*, vol. 108, no. 12, p. 124101, Dec. 2010. [Online]. Available: <http://dx.doi.org/10.1063/1.3520431>
- [14] A. Kerber, E. Cartier, L. Pantisano, R. Degraeve, T. Kauerauf, Y. Kim, A. Hou, G. Groeseneken, H. Maes, and U. Schwalke, "Origin of the threshold voltage instability in SiO₂/HfO₂ dual layer gate dielectrics," *Electron Device Letters, IEEE*, vol. 24, no. 2, p. 87, Feb. 2003. [Online]. Available: <http://dx.doi.org/10.1109/LED.2003.808844>
- [15] D. Bauza, "Electrical properties of Si-SiO₂ interface traps and evolution with oxide thickness in MOSFETs with oxides from 2.3 to 1.2 nm thick," *Solid-State Electronics*, vol. 47, no. 10, p. 1677, Oct. 2003. [Online]. Available: [http://dx.doi.org/10.1016/S0038-1101\(03\)00169-2](http://dx.doi.org/10.1016/S0038-1101(03)00169-2)
- [16] C. Hinkle, A. Sonnet, R. Chapman, and E. M. Vogel, "Extraction of the Effective Mobility of In_{0.53}Ga_{0.47}As MOSFETs," *Electron Device Letters, IEEE*, vol. 30, no. 4, p. 316, Apr. 2009. [Online]. Available: <http://dx.doi.org/10.1109/LED.2009.2012880>
- [17] G. Brammertz, A. Alian, D.-C. Lin, M. Meuris, M. Caymax, and W. E. Wang, "A Combined Interface and Border Trap Model for High-Mobility Substrate Metal-Oxide-Semiconductor Devices Applied to In_{0.53}Ga_{0.47}As and InP Capacitors," *Electron*

- Devices, IEEE Transactions on*, vol. 58, no. 11, p. 3890, Nov. 2011. [Online]. Available: <http://dx.doi.org/10.1109/TED.2011.2165725>
- [18] Y. Yuan, L. Wang, B. Yu, B. Shin, J. Ahn, P. C. McIntyre, P. Asbeck, M. J. W. Rodwell, and Y. Taur, "A Distributed Model for Border Traps in Al₂O₃-InGaAs MOS Devices," *Electron Device Letters, IEEE*, vol. 32, no. 4, p. 485, Apr. 2011. [Online]. Available: <http://dx.doi.org/10.1109/LED.2011.2105241>
- [19] M. E. Ramón, T. Akyol, D. Shahrjerdi, C. D. Young, J. Cheng, L. F. Register, and S. K. Banerjee, "Fast and slow transient charging in various III-V field-effect transistors with atomic-layer-deposited-Al₂O₃ gate dielectric," *Applied Physics Letters*, vol. 102, no. 2, p. 022104, Jan. 2013. [Online]. Available: <http://dx.doi.org/10.1063/1.4776678>
- [20] S. Johansson, M. Berg, K.-M. Persson, and E. Lind, "A High-Frequency Transconductance Method for Characterization of High-*K* Border Traps in III-V MOSFETs," *Electron Devices, IEEE Transactions on*, vol. 60, no. 2, p. 776, Feb. 2013. [Online]. Available: <http://dx.doi.org/10.1109/TED.2012.2231867>
- [21] R. Degraeve, A. Kerber, E. Cartier, L. Pantisano, and G. Groeseneken, "Characterization of charge trapping in SiO₂/HfO₂ dielectrics," in *Semiconductor Device Research Symposium, 2003 International*, 2003, p. 322. [Online]. Available: <http://dx.doi.org/10.1109/ISDRS.2003.1272115>
- [22] A. Kerber, E. Cartier, L. Pantisano, M. Rosmeulen, R. Degraeve, T. Kauerauf, G. Groeseneken, H. Maes, and U. Schwalke, "Characterization of the *V_T*-instability in SiO₂/HfO₂ gate dielectrics," in *Reliability Physics Symposium Proceedings, 2003. 41st Annual. 2003 IEEE International*, 2003, p. 41. [Online]. Available: <http://dx.doi.org/10.1109/RELPHY.2003.1197718>
- [23] R. K. Ahrenkiel, R. Ellingson, S. Johnston, and M. Wanlass, "Recombination lifetime of In_{0.53}Ga_{0.47}As as a function of doping density," *Applied Physics Letters*, vol. 72, no. 26, p. 3470, Jun. 1998. [Online]. Available: <http://dx.doi.org/10.1063/1.121669>
- [24] S. Zafar, A. Callegari, E. Gusev, and M. Fischetti, "Charge trapping in high-*k* gate dielectric stacks," in *Electron Devices Meeting, 2002. IEDM '02. International*, 2002, p. 517. [Online]. Available: <http://dx.doi.org/10.1109/IEDM.2002.1175893>
- [25] S. Zafar, A. Callegari, E. Gusev, and M. V. Fischetti, "Charge trapping related threshold voltage instabilities in high permittivity gate dielectric stacks," *Journal of Applied Physics*, vol. 93, no. 11, pp. 9298–9303, Jun. 2003. [Online]. Available: <http://dx.doi.org/10.1063/1.1570933>

- [26] W.-H. Wu, B.-Y. Tsui, M.-C. Chen, Y.-T. Hou, Y. Jin, H.-J. Tao, S.-C. Chen, and M.-S. Liang, "Transient Charging and Discharging Behaviors of Border Traps in the Dual-Layer HfO₂/SiO₂ High-*k* Gate Stack Observed by Using Low-Frequency Charge Pumping Method," *Electron Devices, IEEE Transactions on*, vol. 54, no. 6, p. 1330, Jun. 2007. [Online]. Available: <http://dx.doi.org/10.1109/TED.2007.895864>
- [27] A. Ali, H. Madan, S. Koveshnikov, S. Oktyabrsky, R. Kambhampati, T. Heeg, D. Schlom, and S. Datta, "Small-Signal Response of Inversion Layers in High-Mobility In_{0.53}Ga_{0.47}As MOSFETs Made With Thin High-*K* Dielectrics," *Electron Devices, IEEE Transactions on*, vol. 57, no. 4, p. 742, Apr. 2010. [Online]. Available: <http://dx.doi.org/10.1109/TED.2010.2041855>
- [28] [Online]. Available: <http://www.ioffe.rssi.ru/SVA/NSM/Semicond/GaInAs>
- [29] M. Passlack, "Interface state analysis on non-silicon semiconductors and the role of heterostructures. Tutorial IEEE Semiconductor Interface Specialists Conference (SISC), San Diego, CA, Dec. 2010." [Online]. Available: <http://www.ieeesisc.org>
- [30] W. Wang, J. Deng, J. C. M. Hwang, Y. Xuan, Y. Wu, and P. D. Ye, "Charge-pumping characterization of interface traps in Al₂O₃/In_{0.75}Ga_{0.25}As metal-oxide-semiconductor field-effect transistors," *Applied Physics Letters*, vol. 96, no. 7, p. 072102, Feb. 2010. [Online]. Available: <http://dx.doi.org/10.1063/1.3315870>
- [31] F. Heiman and G. Warfield, "The effects of oxide traps on the MOS capacitance," *Electron Devices, IEEE Transactions on*, vol. 12, no. 4, pp. 167–178, Apr. 1965. [Online]. Available: <http://dx.doi.org/10.1109/T-ED.1965.15475>
- [32] O. Engstrom, N. Sedghi, I. Z. Mitrovic, and S. Hall, "Analysis of electron capture at oxide traps by electric field injection," *Applied Physics Letters*, vol. 102, no. 21, p. 211604, May 2013. [Online]. Available: <http://dx.doi.org/10.1063/1.4807845>
- [33] N. Taoka, M. Yokoyama, S. Kim, R. Suzuki, R. Iida, S. Lee, T. Hoshii, W. Jevasuwan, T. Maeda, T. Yasuda, O. Ichikawa, N. Fukuhara, M. Hata, M. Takenaka, and S. Takagi, "Impact of Fermi level pinning inside conduction band on electron mobility of In_xGa_{1-x}As MOSFETs and mobility enhancement by pinning modulation," in *Electron Devices Meeting (IEDM), 2011 IEEE International*, 2011, p. 27.2.1. [Online]. Available: <http://dx.doi.org/10.1109/IEDM.2011.6131622>
- [34] A. Akturk, J. Allnut, Z. Dilli, N. Goldsman, and M. Peckerar, "Device Modeling at Cryogenic Temperatures: Effects of Incomplete Ionization," *Electron Devices*,

- IEEE Transactions on*, vol. 54, no. 11, p. 2984, Nov. 2007. [Online]. Available: <http://dx.doi.org/10.1109/TED.2007.906966>
- [35] M. Negara, V. Djara, T. O'Regan, K. Cherkaoui, M. Burke, Y. Gomeniuk, M. Schmidt, É. O'Connor, I. Povey, A. Quinn, and P. Hurley, "Investigation of electron mobility in surface-channel $\text{Al}_2\text{O}_3/\text{In}_{0.53}\text{Ga}_{0.47}\text{As}$ MOSFETs," *Solid-State Electronics*, vol. 88, p. 37, Oct. 2013. [Online]. Available: <http://dx.doi.org/10.1016/j.sse.2013.04.014>
- [36] W. Wang, J. Hwang, Y. Xuan, and P. Ye, "Analysis of Electron Mobility in $\text{Al}_2\text{O}_3/\text{In}_x\text{Ga}_{1-x}\text{As}$ Inversion-Mode MOSFETs," *Electron Devices, IEEE Transactions on*, vol. 58, no. 7, p. 1972, Jul. 2011. [Online]. Available: <http://dx.doi.org/10.1109/TED.2011.2146255>
- [37] S. Takagi, A. Toriumi, M. Iwase, and H. Tango, "On the universality of inversion layer mobility in Si MOSFET's: Part I-effects of substrate impurity concentration," *Electron Devices, IEEE Transactions on*, vol. 41, no. 12, p. 2357, Dec. 1994. [Online]. Available: <http://dx.doi.org/10.1109/16.337449>

Chapter 6

Impact of Channel Thickness on Junctionless MOSFET Performance

6.1 Introduction

The junctionless device concept for silicon on insulator (SOI) metal-oxide-semiconductor field-effect transistors (MOSFETs), first introduced by Colinge *et al.* in 2010 [1], has demonstrated considerable gains in terms of process simplicity when compared to conventional inversion-mode MOSFETs. While the original devices featured near-ideal subthreshold slope and extremely low OFF-state current, further work demonstrated an increase in ON-current through the use of strain-induced mobility enhancement techniques [2]. To extend on this work, we propose to apply the junctionless device concept to a III-V structure. *The following reasons suggest that the junctionless device concept could be particularly well suited to III-V structures:*

1. *The high donor doping concentration (N_d) required in the channel of a junctionless MOSFET is less problematic for $In_{0.53}Ga_{0.47}As$ than it is for Si. Indeed, the bulk electron mobility in Si is $100 \text{ cm}^2/\text{V}\cdot\text{s}$ at $N_d = 1 \times 10^{19} \text{ /cm}^3$ [3], while that in $In_{0.53}Ga_{0.47}As$ is $\sim 4000 \text{ cm}^2/\text{V}\cdot\text{s}$ at a similar N_d level [4].*
2. *The junctionless architecture circumvents the difficulties associated with the implantation [5, 6] or regrowth [7, 8] techniques generally used to form the source and drain (S/D) regions of III-V inversion-mode MOSFETs.*

The objective of this work is to implement the junctionless device concept in a planar III-V structure, where the SiO_2 of the SOI in [1] is replaced by a wide bandgap $p\text{-}In_{0.52}Al_{0.48}As$ barrier layer with a low acceptor doping concentration (N_a), in order to study the impact of the $In_{0.53}Ga_{0.47}As$ channel thickness (t_{InGaAs}) on the device performance.

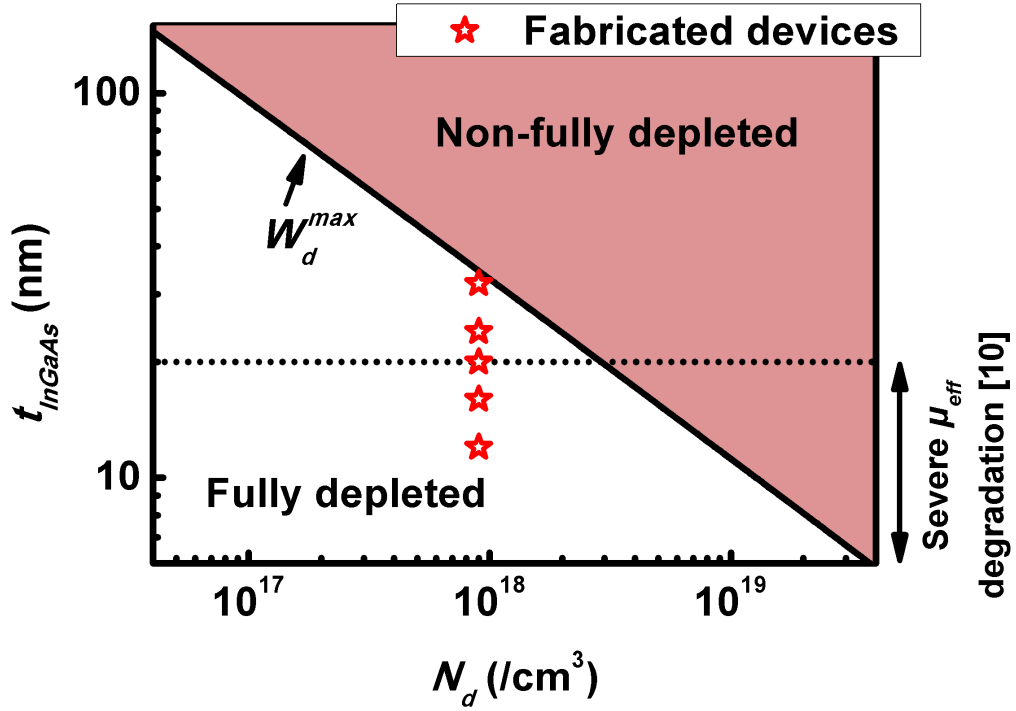


Figure 6.1: $\text{In}_{0.53}\text{Ga}_{0.47}\text{As}$ channel thickness (t_{InGaAs}) vs $\text{In}_{0.53}\text{Ga}_{0.47}\text{As}$ channel doping (N_d). The calculated maximum depletion width (W_d^{max}) yields the boundary between the fully depleted and non-fully depleted device structure. The 20 nm t_{InGaAs} limit, where severe effective electron mobility (μ_{eff}) degradation is reported [10], and the set of t_{InGaAs} (32, 24, 20, 16 and 12 nm) vs N_d ($9 \times 10^{17} / \text{cm}^3$) parameters corresponding to the fabricated devices are also indicated.

To obtain a planar junctionless $\text{In}_{0.53}\text{Ga}_{0.47}\text{As}$ MOSFET featuring a high ON-current (I_{ON}) and a low OFF-current (I_{OFF}), the $\text{In}_{0.53}\text{Ga}_{0.47}\text{As}$ channel N_d and t_{InGaAs} need to be carefully selected. Indeed, a high N_d is required to obtain a high I_{ON} and a good source and drain (S/D) contact resistance [9]. However, since the channel has to be fully depleted of carriers for the device to be switched off, a low I_{OFF} will only be achieved if the channel thickness is thinner than the maximum depletion width (W_d^{max}), which is given by:

$$W_d^{\text{max}} = 2 \cdot \sqrt{\frac{\epsilon_s \cdot k_B \cdot T \cdot \ln(N_d/n_i)}{q^2 \cdot N_d}} \quad (6.1)$$

where ϵ_s is the semiconductor dielectric constant, k_B is the Boltzmann constant, T is the temperature, n_i is the intrinsic carrier concentration and q is the charge of an electron. The W_d^{max} boundary between the fully depleted and non-fully depleted structures is shown in Figure 6.1. One additional parameter to take into account when designing planar junctionless III-V

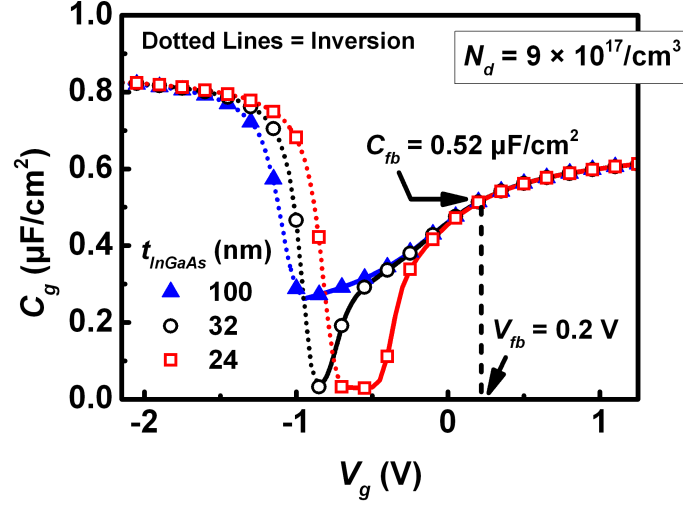


Figure 6.2: Quasi-static capacitance-voltage (C - V) characteristics obtained for Pd/Al₂O₃/ n -In_{0.53}Ga_{0.47}As/ p -In_{0.52}Al_{0.48}As/ p -InP structures using a self-consistent Poisson-Schrödinger solver. The structures featured In_{0.53}Ga_{0.47}As channel thicknesses (t_{InGaAs}) of 32, 24 and 16 nm and an In_{0.53}Ga_{0.47}As channel doping (N_d) of $9 \times 10^{17} /\text{cm}^3$. A flat-band capacitance (C_{fb}) of $0.52 \mu\text{F}/\text{cm}^2$ and flat-band voltage (V_{fb}) of 0.2 V were obtained. It is noted that the dotted line inversion response of the quasi-static C - V curves will not be typically observed experimentally in a multi-frequency C - V .

MOSFETs is the severe effective electron mobility (μ_{eff}) degradation observed in devices with sub-20 nm In_{0.53}Ga_{0.47}As channel thickness [10]. With this in mind, we varied t_{InGaAs} for a fixed N_d value in order to investigate the behavior of fully depleted devices.

To assist in the device analysis, self-consistent Poisson-Schrödinger calculations [11] were performed for ideal Pd/Al₂O₃/ n -In_{0.53}Ga_{0.47}As/ p -In_{0.52}Al_{0.48}As/ p^+ -InP device structures. In the calculations, the work function (W_f) of Pd on Al₂O₃, the Al₂O₃ film thickness (t_{ox}) and the Al₂O₃ k -value were set to 4.7 eV [12], 8.5 nm (see section 6.3) and 8.6 [6, 13, 14], respectively. The only parameter that was manually adjusted was the N_d in the In_{0.53}Ga_{0.47}As channel. The adjustment procedure, which yielded a N_d value of $9 \times 10^{17} /\text{cm}^3$ ($W_d^{max} \sim 34.5$ nm), will be presented in sub-section 6.4.3. It is noted that we could not extract N_d from the minimum capacitance (C_{min}) of the high-frequency capacitance-voltage (C - V) characteristic of the device metal-oxide-semiconductor (MOS) gate stack since $t_{InGaAs} < W_d^{max}$.

Figure 6.2 compares the quasi-static (Q-S) C - V characteristics calculated for t_{InGaAs} values of 100, 32 and 24 nm. The calculations revealed a flat-band capacitance (C_{fb}) of $0.52 \mu\text{F}/\text{cm}^2$ along with a flat-band voltage (V_{fb}) of 0.2 V. For $t_{InGaAs} = 100$ nm ($> W_d^{max}$) the quasi-static C - V characteristic presents the expected shape of an n -type MOS structure: a decreasing capacitance

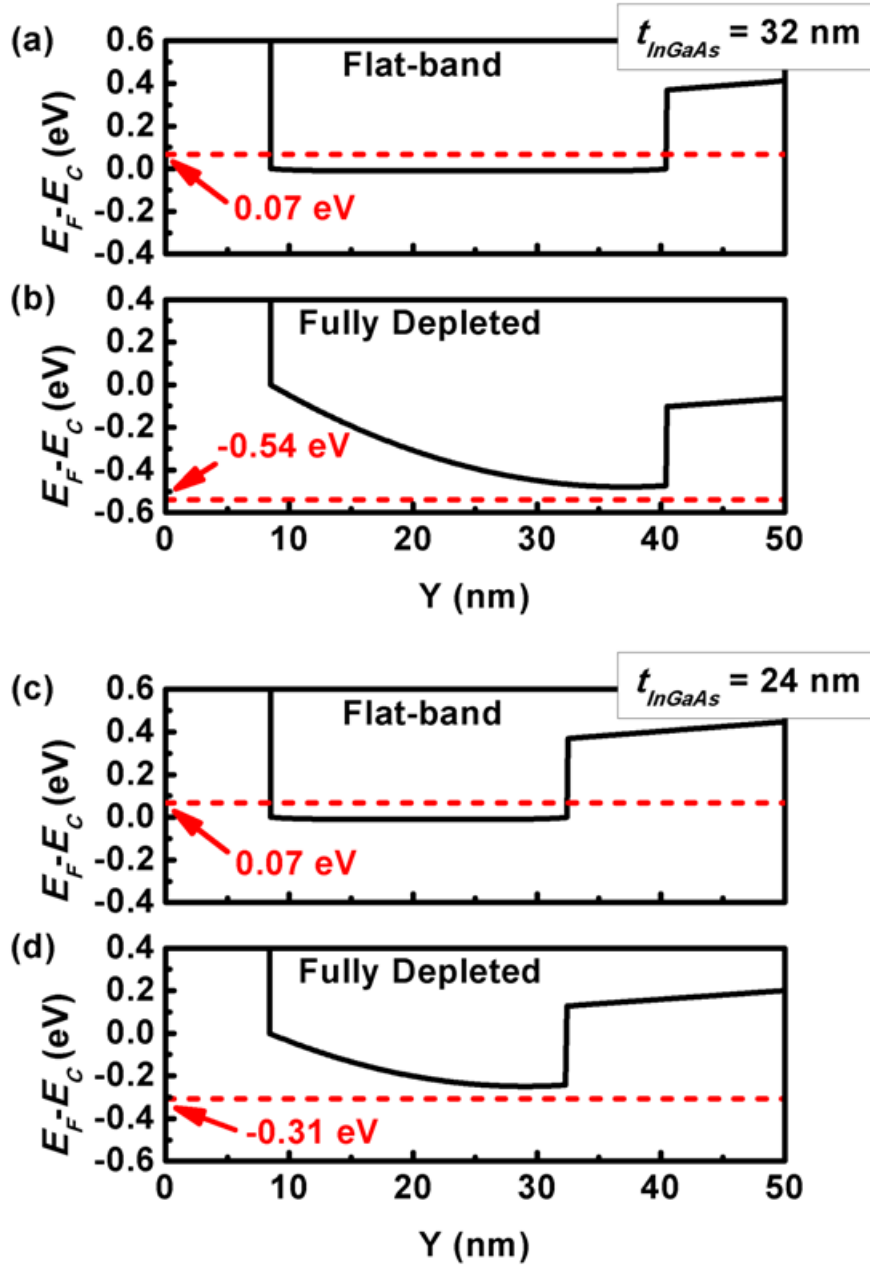


Figure 6.3: Conduction band diagrams of Pd/Al₂O₃/*n*-In_{0.53}Ga_{0.47}As/*p*-In_{0.52}Al_{0.48}As/*p*-InP structures obtained from self-consistent Poisson-Schrödinger calculations. Diagrams of a 32-nm-thick In_{0.53}Ga_{0.47}As channel device showing (a) the flat-band and (b) the fully depleted conditions. The Fermi level needs to move 0.07 eV above the conduction band edge (E_C) to reach flat-band and 0.54 eV below E_C to reach full depletion. Diagrams of a 24-nm-thick In_{0.53}Ga_{0.47}As channel device showing (c) the flat-band and (d) the fully depleted conditions. The Fermi level needs to move 0.07 eV above E_C to reach flat-band and 0.31 eV below E_C to reach full depletion.

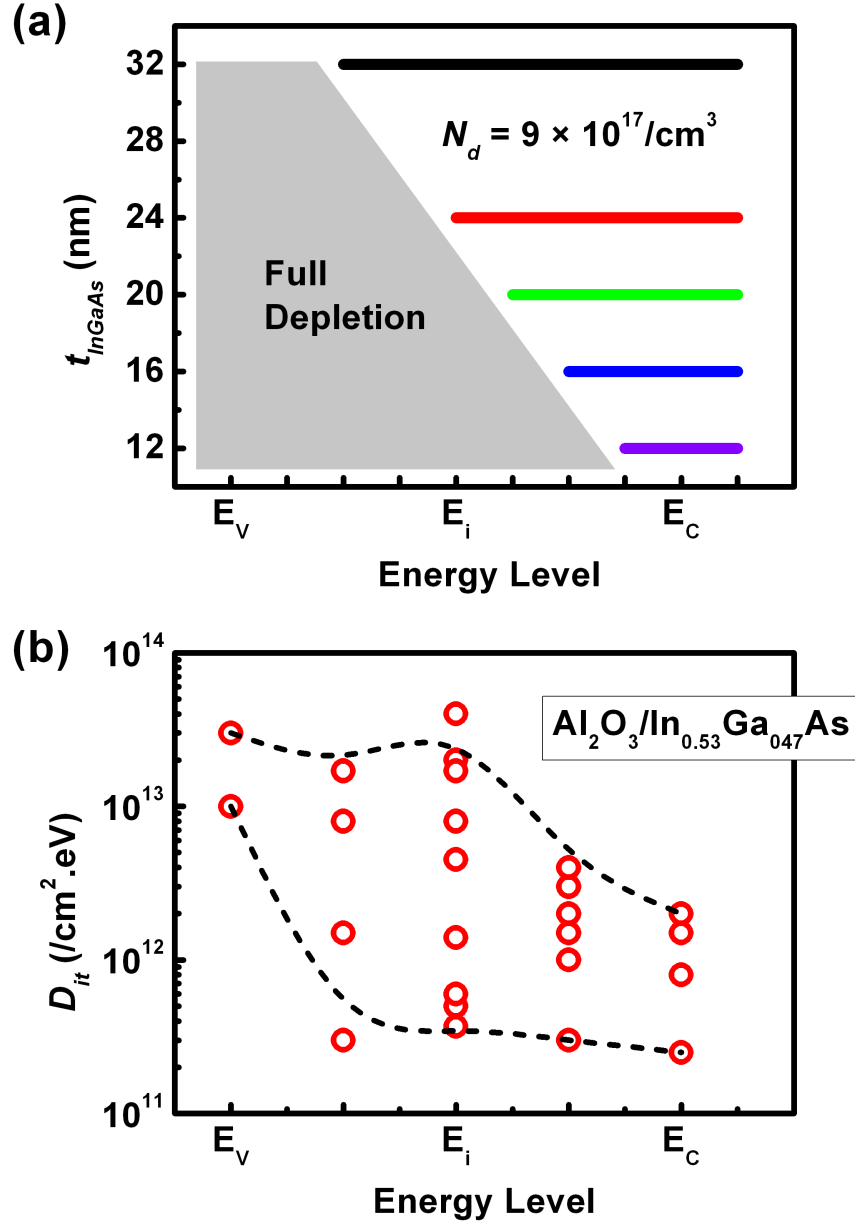


Figure 6.4: (a) Energy range required to move from flat-band to full depletion as a function of $In_{0.53}Ga_{0.47}As$ channel thickness (t_{InGaAs}). The values were obtained from self-consistent Poisson-Schrödinger calculations. (b) Comparison of the D_{it} values reported for $Al_2O_3/In_{0.53}Ga_{0.47}As$ MOS structures [15–26].

going from accumulation ($V_g > V_{fb}$) to depletion ($V_T < V_g < V_{fb}$), a C_{min} set by N_d and a sharp increase in capacitance going from depletion to inversion ($V_g < V_T$). However, for $t_{InGaAs} = 32$ and 24 nm ($< W_d^{max}$), the curves feature a C_{min} falling down to a negligible value of ~ 30 nF/cm², consistent with fully depleted structures. This comparison also highlights the fact that a thinner In_{0.53}Ga_{0.47}As channel requires a smaller V_g sweep to move from flat-band (ON-state) to fully depleted (OFF-state) and *vice versa*, which is highly desirable for low power device applications. A second advantage arising from the scaling of t_{InGaAs} can be observed on the band diagrams of the 32 and 24-nm-thick In_{0.53}Ga_{0.47}As channel devices shown in Figure 6.3. At flat-band [Figure 6.3(a) and (c)], the Fermi levels in both devices are located 0.07 eV above the conduction band. However, to reach full depletion in the 32-nm-thick In_{0.53}Ga_{0.47}As channel device, the Fermi level has to move 0.54 eV below the conduction band edge (E_C) [Figure 6.3(b)] while it only has to move 0.31 eV below E_C in the 24-nm-thick In_{0.53}Ga_{0.47}As channel device [Figure 6.3(d)]. From Figure 6.4(a), it is clear that the range of energy required to move from flat-band to fully depleted scales with t_{InGaAs} . The review of the D_{it} energy profile reported for Al₂O₃/In_{0.53}Ga_{0.47}As MOS structures [15–26] [Figure 6.4(b)] shows that this trend is particularly advantageous to Al₂O₃/In_{0.53}Ga_{0.47}As MOS devices. Indeed, while D_{it} values in the low-10¹¹ to mid-10¹² /cm².eV are generally reported for the upper part of the In_{0.53}Ga_{0.47}As bandgap, much higher D_{it} values in the 10¹³ /cm².eV range are observed in the lower part of the In_{0.53}Ga_{0.47}As bandgap¹. Consequently, we propose to scale t_{InGaAs} in order to avoid device operation in the lower part of the In_{0.53}Ga_{0.47}As bandgap and, therefore, achieve better switching performance.

6.2 Channel Thinning by Digital Etching

Figure 6.5 shows a diagram and a transmission electron microscopy (TEM) cross-section image of the n -In_{0.53}Ga_{0.47}As (32 nm)/ p -In_{0.52}Al_{0.48}As (500 nm) device structure grown by metal-organic vapor phase epitaxy (MOVPE) on p^+ -InP substrates. The nominal doping was 2×10^{18} /cm³ in the n -In_{0.53}Ga_{0.47}As and 8×10^{15} /cm³ in the p -In_{0.52}Al_{0.48}As. We used a 10% H₂O₂ / 10% HCl digital etch (DE) process [27] for the thinning of the n -In_{0.53}Ga_{0.47}As channel. The DE was characterized in terms of etch rate and surface roughness directly on the device structure.

Spectroscopic ellipsometry (SE) measurements were performed to monitor the In_{0.53}Ga_{0.47}As etch rate and thickness (Figure 6.6). SE enables direct extraction of film thicknesses of multi-layer structures through the fitting of the amplitude ratio and phase shift components measured upon reflection over a wide range of wavelength going from 245 nm to 1690 nm. The excellent agreement obtained between the TEM (Figure 6.5) and SE measurements performed before DE (Figure 6.6) validates the SE measurement technique. A DE rate of 0.8 nm/cycle was extracted

¹It is noted that a prominent peak located at around mid-gap can also be observed, depending on the In_{0.53}Ga_{0.47}As surface preparation and Al₂O₃ deposition techniques employed.

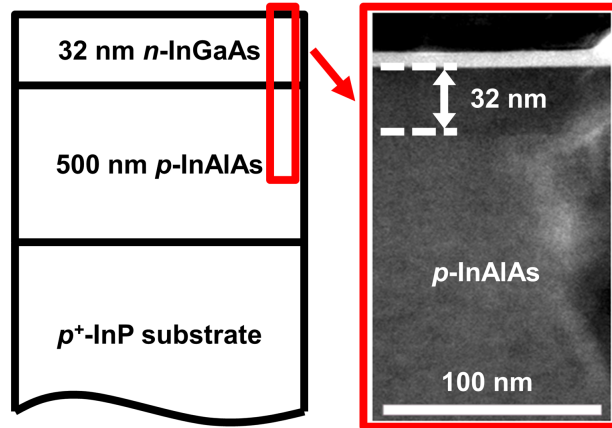


Figure 6.5: Diagram and cross-section transmission electron microscopy (TEM) image of the MOVPE grown $n\text{-In}_{0.53}\text{Ga}_{0.47}\text{As}$ (32 nm)/ $p\text{-In}_{0.52}\text{Al}_{0.48}\text{As}$ (500 nm)/ $p^+\text{-InP}$ wafer structure used for the digital etch (DE) process characterization and for the device fabrication.

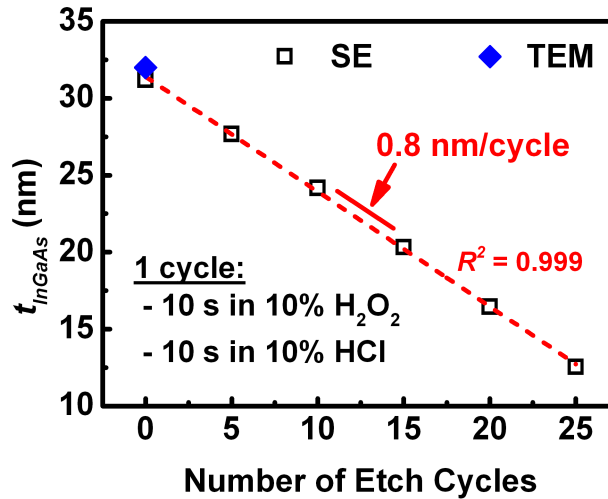


Figure 6.6: $\text{In}_{0.53}\text{Ga}_{0.47}\text{As}$ channel thinning using a $\text{H}_2\text{O}_2/\text{HCl}$ digital etch (DE) process [27]. Excellent agreement between spectroscopic ellipsometry (SE) and TEM (Figure 6.5) measurements was obtained prior to DE. An etch rate of 0.8 nm/cycle was extracted from the linear fit. The $R^2 = 0.999$ of the linear fit confirms the excellent control of the $\text{In}_{0.53}\text{Ga}_{0.47}\text{As}$ etch rate.

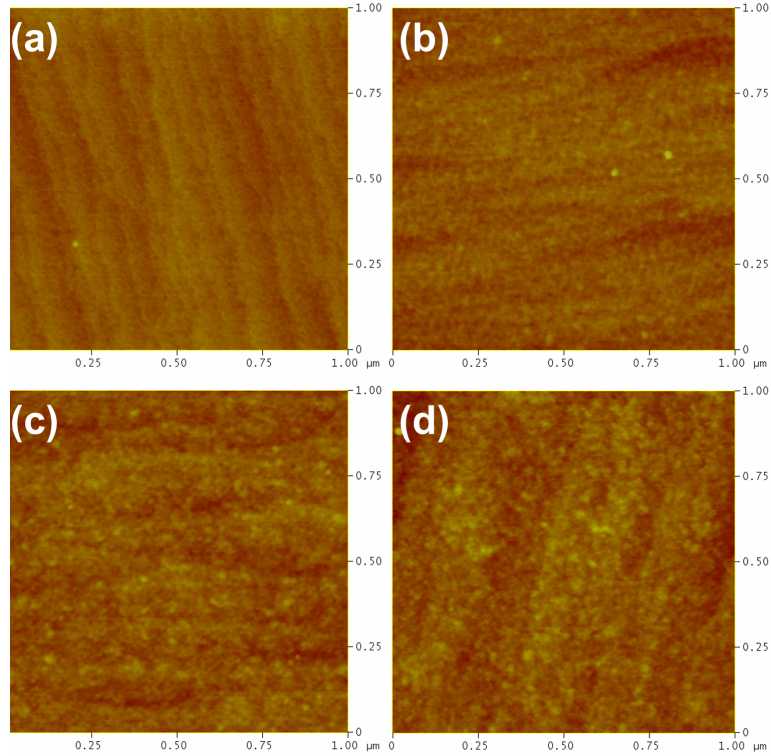


Figure 6.7: Atomic force microscopy (AFM) topography data of $n\text{-In}_{0.53}\text{Ga}_{0.47}\text{As}$ (a) before digital etch (DE) and after (b) a 10-cycle, (c) a 15-cycle and (d) a 20-cycle DE. The measurements were taken over $1\ \mu\text{m} \times 1\ \mu\text{m}$ scan areas. The AFM measurements were performed by M. Burke (Tyndall).

Table 6.1: Root mean square (RMS) surface roughness data from AFM measurements taken on $n\text{-In}_{0.53}\text{Ga}_{0.47}\text{As}$ before digital etch (DE) and after a 10-cycle, 15-cycle and 20-cycle (DE) (Figure 6.7). The quoted values represent the mean, maximum and minimum from four measurements at separate locations (each on a $1\ \mu\text{m} \times 1\ \mu\text{m}$ scan area). The uncertainties on the mean values are given by the standard deviation.

RMS	No Etch	DE Cycles		
		10	15	20
Mean (nm)	0.20 ± 0.01	0.21 ± 0.01	0.25 ± 0.01	0.28 ± 0.01
Max. (nm)	0.20	0.23	0.26	0.31
Min. (nm)	0.19	0.20	0.24	0.27

from the linear fit of the SE measurements *vs* number of etch cycles. The R^2 of 0.999 confirms the excellent control of the $\text{In}_{0.53}\text{Ga}_{0.47}\text{As}$ etch rate. It is noted that SE provides a more direct and more accurate alternative to the procedure reported in [28] for a similar process characterization. Atomic force microscopy (AFM) topography data were acquired before DE [Figure 6.7(a)] and after 10-cycle [Figure 6.7(b)], 15-cycle [Figure 6.7(c)] and 20-cycle [Figure 6.7(d)] DE in order to investigate the impact of DE on the $\text{In}_{0.53}\text{Ga}_{0.47}\text{As}$ surface roughness. The corresponding root mean square (RMS) surface roughness values are listed in Table 6.1 in terms of mean, maximum and minimum values, obtained from four measurements at separate locations. The mean RMS surface roughness gradually increases from 0.20 ± 0.01 nm before DE to 0.28 ± 0.01 nm after a 20-cycle DE, in line with [28].

6.3 Fabrication of Planar Gate-enclosed Junctionless MOSFETs

Five samples consisting of a 32-nm-thick $n\text{-In}_{0.53}\text{Ga}_{0.47}\text{As}$ on a 500-nm-thick $p\text{-In}_{0.52}\text{Al}_{0.48}\text{As}$ ($N_a = 8 \times 10^{15} / \text{cm}^3$) barrier grown by MOVPE on $p^+\text{-InP}$ substrates (Figure 6.5) were dedicated to the study of the impact of t_{InGaAs} on the performance of junctionless $\text{In}_{0.53}\text{Ga}_{0.47}\text{As}$ MOSFETs. Although a N_d of $2 \times 10^{18} / \text{cm}^3$ was targeted for the $\text{In}_{0.53}\text{Ga}_{0.47}\text{As}$ channel, our analysis revealed a N_d of $9 \times 10^{17} / \text{cm}^3$ (see sub-section 6.4.3). As already mentioned in section 6.1 (122), the N_d could not be measured experimentally. Moreover, no dopant calibration run was performed prior to the growth of the structure. While devices were fabricated directly on the first sample ($t_{\text{InGaAs}} = 32$ nm), additional DEs were performed on the 4 remaining samples to thin down the top $\text{In}_{0.53}\text{Ga}_{0.47}\text{As}$ layers prior to device fabrication. The numbers of etch cycles were adjusted in order to obtain $t_{\text{InGaAs}} = 24, 20, 16$ and 12 nm. A non-self-aligned gate-enclosed layout was employed to simplify the fabrication process flow of the planar junctionless MOSFETs. A surface passivation in 10% $(\text{NH}_4)_2\text{S}$ for 30 min [16, 21] was performed before atomic layer deposition (ALD) of an 8.5-nm-thick Al_2O_3 gate oxide film [Figure 6.8(a)]. It is noted that the t_{ox} of 8.5 nm was measured directly on the device samples by SE. A 200-nm-thick Pd gate was formed by e-beam evaporation and lift-off [Figure 6.8(b)]. The Al_2O_3 on the S/D contact areas was etched in dilute HF [Figure 6.8(c)]. A 20 sec surface treatment in 10% NH_4OH was performed prior to S/D contact formation by e-beam evaporation of a Au (14 nm)/Ge (14 nm)/Au (14 nm)/Ni (11 nm)/Au (200 nm) stack [29] and lift-off [Figure 6.8(d)].

The fabricated gate-enclosed junctionless $\text{In}_{0.53}\text{Ga}_{0.47}\text{As}$ MOSFETs featured a drain radius (r_d), a gate inner radius (r_g^{in}), a gate outer radius (r_g^{out}) and source radius (r_s) are 35, 45, 105 and 135 μm , respectively [Figure 6.8(e)].

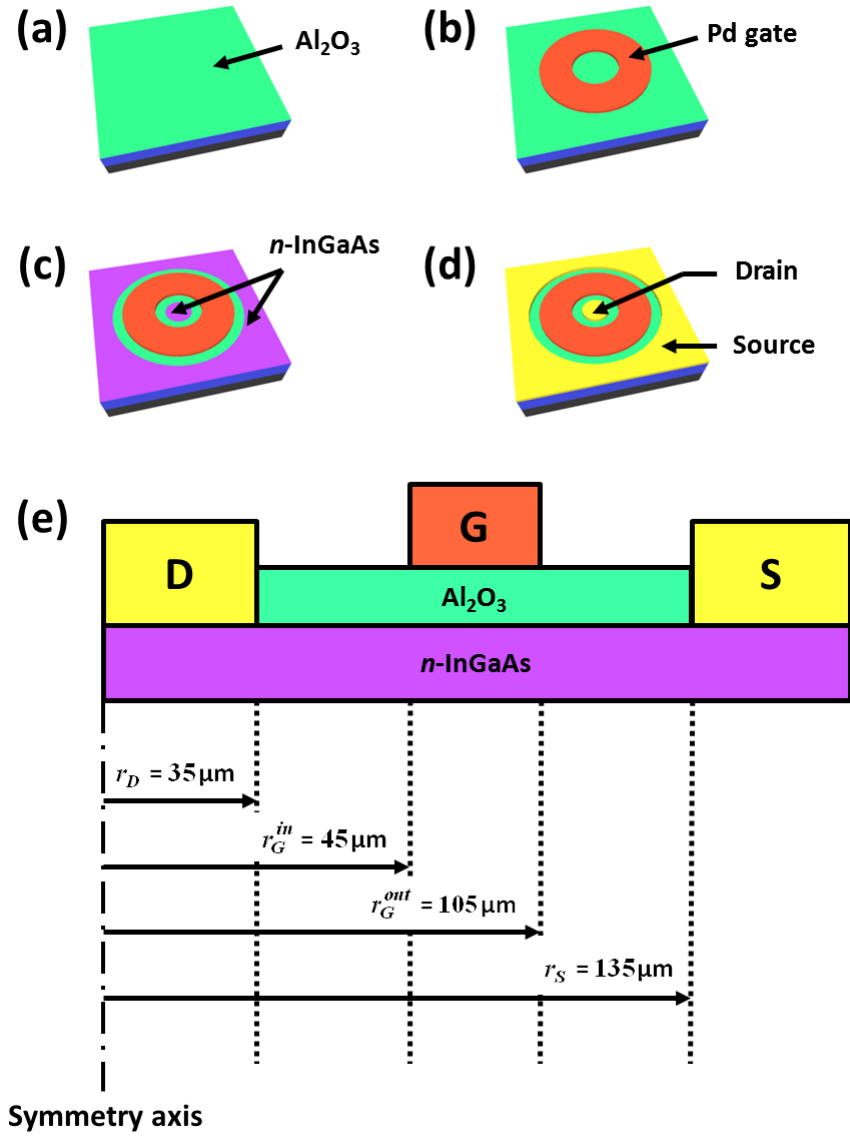


Figure 6.8: Fabrication process flow of planar Gate-enlosed Junctionless In_{0.53}Ga_{0.47}As MOSFETs including (a) 10% (NH₄)₂S for 30 min passivation [16, 21] prior to ALD Al₂O₃, (8.5 nm), (b) Pd (200 nm) gate lift-off, (c) Al₂O₃ etch in dilute HF for S/D contact opening and (d) 10% NH₄OH for 20 sec surface treatment followed by Au (14 nm)/Ge (14 nm)/Au (14 nm)/Ni (11 nm)/Au (200 nm) [29] S/D contact lift-off. (e) Cross-section diagram of a gate-enlosed junctionless MOSFET architecture. The drain radius (r_d), gate inner radius (r_g^{in}), gate outer radius (r_g^{out}) and source radius (r_s) are 35, 45, 105 and 135 μm , respectively.

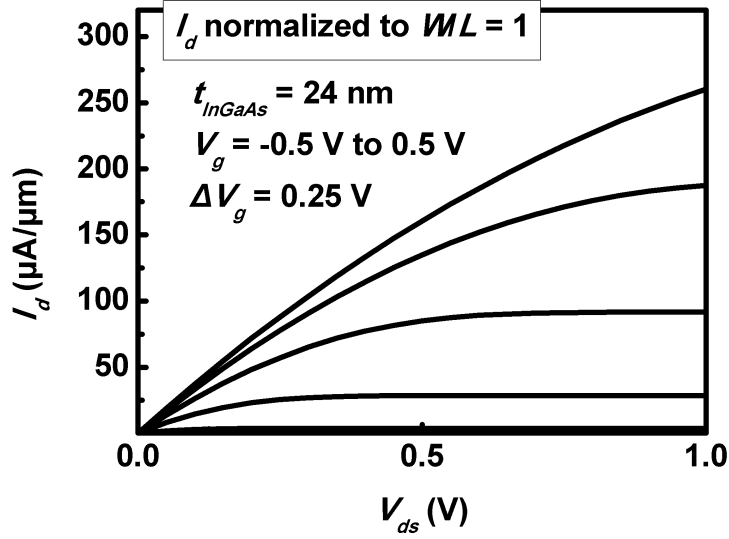


Figure 6.9: I_d - V_{ds} output characteristic of a planar gate-enclosed junctionless $\text{In}_{0.53}\text{Ga}_{0.47}\text{As}$ MOSFET featuring a 24-nm-thick $\text{In}_{0.53}\text{Ga}_{0.47}\text{As}$ channel. A $(W/L)_{eff}$ of 7.41 was used for the W/L normalization of I_d .

6.4 Analysis of Planar Gate-enclosed Junctionless MOSFETs

6.4.1 Impact of Channel Thickness on Device Performance

Figure 6.9 shows a well behaved I_d - V_{ds} output characteristic obtained for a planar gate-enclosed junctionless $\text{In}_{0.53}\text{Ga}_{0.47}\text{As}$ MOSFET featuring a 24-nm-thick $\text{In}_{0.53}\text{Ga}_{0.47}\text{As}$ channel. The output characteristic is normalized to $W/L = 1$ using [30]:

$$(W/L)_{eff} = 2\pi \cdot [\ln(r^{out}/r^{in})]^{-1} \quad (6.2)$$

A $(W/L)_{eff}$ of 7.41 was obtained based on the device dimensions shown in Figure 6.8(e). The normalized (measured) drive current at $V_g = 0.5$ V and $V_{ds} = 1$ V is $260 \mu\text{A}/\mu\text{m}$ (1.93 mA).

Figure 6.10 compares the I_d - V_g characteristics measured at a $V_{ds} = 50$ mV on devices featuring a t_{InGaAs} of 32, 24, 20, 16 and 12 nm. The I_d - V_g transfer characteristics are plotted in log scale to highlight the I_{ON}/I_{OFF}^2 and subthreshold swing (SS) of each device. The 20-nm-thick channel device exhibits the highest I_{ON}/I_{OFF} (1.5×10^5) [Figure 6.11]. It is interesting to note that for $t_{\text{InGaAs}} < 20$ nm the I_{ON}/I_{OFF} reduces due to a degradation of the I_{ON} , while for $t_{\text{InGaAs}} > 20$ nm the I_{ON}/I_{OFF} reduces due to an increase in I_{OFF} . Moreover, scaling t_{InGaAs} from 24 nm

² I_{ON}/I_{OFF} is defined here as the ratio between the maximum and minimum drain currents, irrespective of the gate voltage swing.

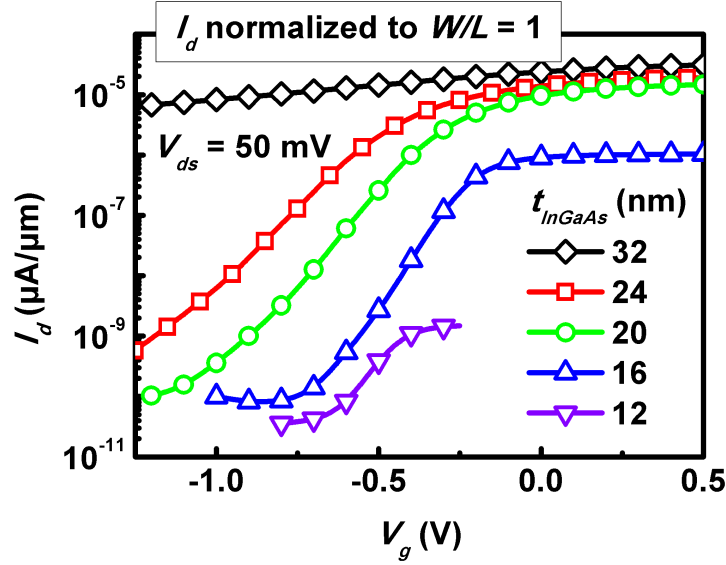


Figure 6.10: I_d - V_g transfer characteristics measured at $V_{ds} = 50$ mV on planar gate-enclosed junctionless $\text{In}_{0.53}\text{Ga}_{0.47}\text{As}$ MOSFETs with $t_{\text{InGaAs}} = 32, 24, 20, 16$ and 12 nm. A $(W/L)_{\text{eff}}$ of 7.41 was used for the W/L normalization of I_d .

to 16 nm reduces the SS from 178 mV/dec. to 115 mV/dec. [Figure 6.11]. We suggest that the severe degradation of the I_{ON} in the 12-nm-thick $\text{In}_{0.53}\text{Ga}_{0.47}\text{As}$ channel device is responsible for the change of trend of SS going from a t_{InGaAs} value of 16 nm to a value of 12 nm. It is noted that the SS of the 32-nm-thick $\text{In}_{0.53}\text{Ga}_{0.47}\text{As}$ channel device could not be extracted due to an excessive I_{OFF} .

The I - V characteristic of the n - $\text{In}_{0.53}\text{Ga}_{0.47}\text{As}/p$ - $\text{In}_{0.52}\text{Al}_{0.48}\text{As}$ heterojunction diode presented in Figure 6.12 indicates a forward to reverse bias current ratio of 4×10^7 . This suggests excellent junction isolation and, therefore, rules out the substrate leakage as the cause of high I_{OFF} in the 32-nm-thick $\text{In}_{0.53}\text{Ga}_{0.47}\text{As}$ channel device.

Figure 6.13(a) shows the C_{gc} - V_g characteristic³ of a 32-nm-thick $\text{In}_{0.53}\text{Ga}_{0.47}\text{As}$ -channel device measured at a frequency of 1 MHz. The measured capacitance of $\sim 0.2 \mu\text{F}/\text{cm}^2$ at $V_g = -2$ V indicates that the device is not fully depleted. We compared this capacitance value to the calculated theoretical C_{min} for a range of N_d values [inset Figure 6.13(a)]. The calculations revealed that a capacitance of $0.2 \mu\text{F}/\text{cm}^2$ can only be achieved for $N_d < 1.1 \times 10^{18} / \text{cm}^3$. This represents an important finding that gives further confidence in the N_d extraction that will be presented in sub-section 6.4.3. Figure 6.13(b) compares the evolution of the experimental

³The C_{gc} - V_g characteristic was obtained using a measurement configuration where the source and drain terminals are shorted and connected to the high of the impedance meter, the gate terminal is connected to the low and the substrate is left floating.

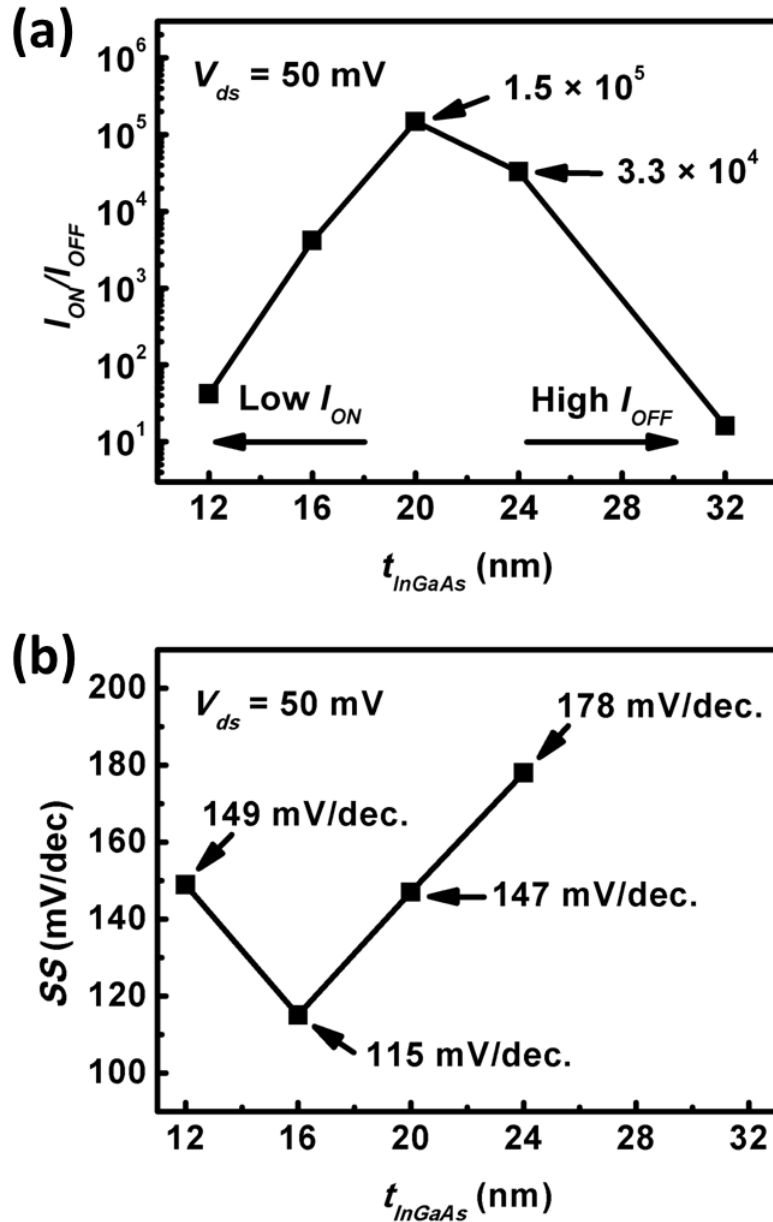


Figure 6.11: (a) I_{ON}/I_{OFF} vs t_{InGaAs} . The best I_{ON}/I_{OFF} value of 1.5×10^5 was obtained with $t_{InGaAs} = 20$ nm. For $t_{InGaAs} > 20$ nm, I_{ON}/I_{OFF} is degraded due to an increase in I_{OFF} . For $t_{InGaAs} < 20$ nm, the I_{ON}/I_{OFF} is degraded due to a decrease in I_{ON} . (b) Subthreshold swing (SS) vs t_{InGaAs} . SS scaling with t_{InGaAs} observed for t_{InGaAs} reducing from 24 nm to 16 nm. The lowest SS (115 mV/dec.) was obtained with $t_{InGaAs} = 16$ nm.

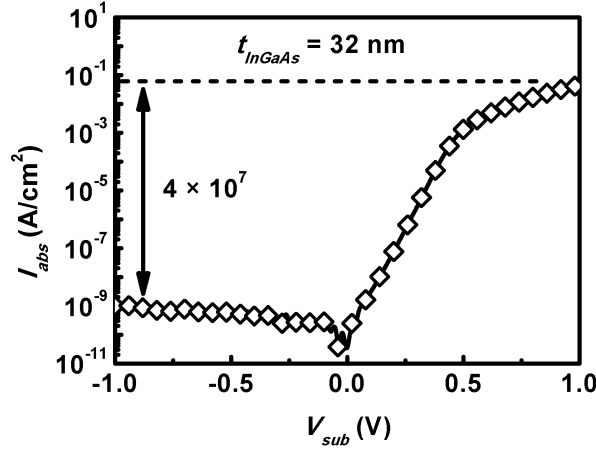


Figure 6.12: I - V characteristic of a n - $\text{In}_{0.53}\text{Ga}_{0.47}\text{As}/p$ - $\text{In}_{0.52}\text{Al}_{0.48}\text{As}$ heterojunction diode fabricated on the wafer structure shown in Figure 6.5. More than 7 orders of magnitude between the forward and reverse current is observed, indicating excellent junction isolation

and ideal E_F - E_C vs V_g curves, which suggest that the Fermi level is pinned ~ 0.45 eV below E_C . This is consistent with high D_{it} levels towards the lower part of $\text{In}_{0.53}\text{Ga}_{0.47}\text{As}$ bandgap [Figure 6.4(b)]. This Fermi level pinning prevents the 32-nm-thick $\text{In}_{0.53}\text{Ga}_{0.47}\text{As}$ -channel device from reaching full depletion, in agreement with the high I_{OFF} observed in the device I_d - V_g characteristic shown in Figure 6.10.

6.4.2 Density of Interface Traps

Figure 6.14(a) shows a multi-frequency C_{gc} - V_g characteristic of a device featuring a 24-nm-thick $\text{In}_{0.53}\text{Ga}_{0.47}\text{As}$ channel. The sharp drop of capacitance down to a C_{min} of ~ 40 nF/cm² confirms that the device is fully depleted at $V_g < -0.8$ V. In the V_g range going from -0.5 V to 0 V (towards accumulation), a very low frequency dispersion is observed, suggesting a low D_{it} in the upper part of the $\text{In}_{0.53}\text{Ga}_{0.47}\text{As}$ bandgap. A D_{it} profile [Figure 6.14(b)] was obtained from the conductance method [31] applied to the capacitance and conductance data shown in Figure 6.14(a) and for an oxide capacitance C_{ox} of 0.895 $\mu\text{F}/\text{cm}^2$. The inset of Figure 6.14(a) shows the evolution of the peak of conductance normalized to the angular frequency (G/ω) across the V_g range where the conductance method is applicable. As the frequency increases from 400 Hz to 100 kHz, the G/ω peak reduces and moves from -1.4 V to -0.8 V, consistent with a reducing D_{it} going from the middle of the $\text{In}_{0.53}\text{Ga}_{0.47}\text{As}$ bandgap towards conduction band edged. This trend was confirmed by the D_{it} profile obtained from the high-low method applied to the 100 kHz (high)⁴ and 100

⁴It is noted that a C_{gc} - V_g trace measured at a frequency of 1 MHz would have provided a better approximation of the true high-frequency response. Due to the large series resistance (R_{series}) arising from the use of a very thin

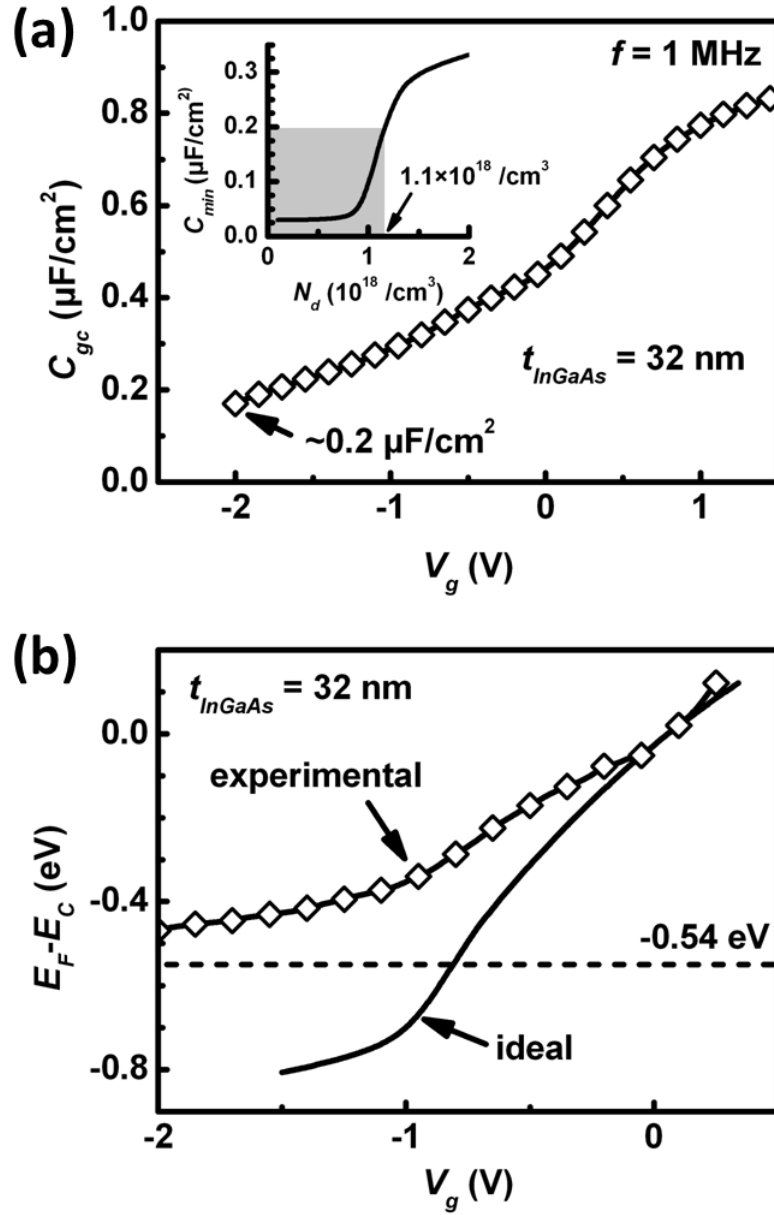


Figure 6.13: (a) C_{gc} - V_g characteristics measured at a frequency of 1 MHz on planar gate-enclosed junctionless $\text{In}_{0.53}\text{Ga}_{0.47}\text{As}$ MOSFETs with $t_{\text{InGaAs}} = 32 \text{ nm}$. Inset: Calculated minimum capacitance (C_{min}) vs $\text{In}_{0.53}\text{Ga}_{0.47}\text{As}$ doping (N_d). A measured C_{min} of $\sim 0.2 \mu\text{F}/\text{cm}^2$ at $V_g = -2 \text{ V}$ suggests a $N_d < 1.1 \times 10^{18}/\text{cm}^3$. (b) Fermi level position at the $\text{Al}_2\text{O}_3/\text{In}_{0.53}\text{Ga}_{0.47}\text{As}$ interface in an ideal and in the fabricated devices. In the fabricated device, the Fermi level is pinned above $E_F - E_C = -0.54 \text{ eV}$ [Figure 6.3(b)], preventing the full depletion of the 32-nm-thick $\text{In}_{0.53}\text{Ga}_{0.47}\text{As}$ channel.

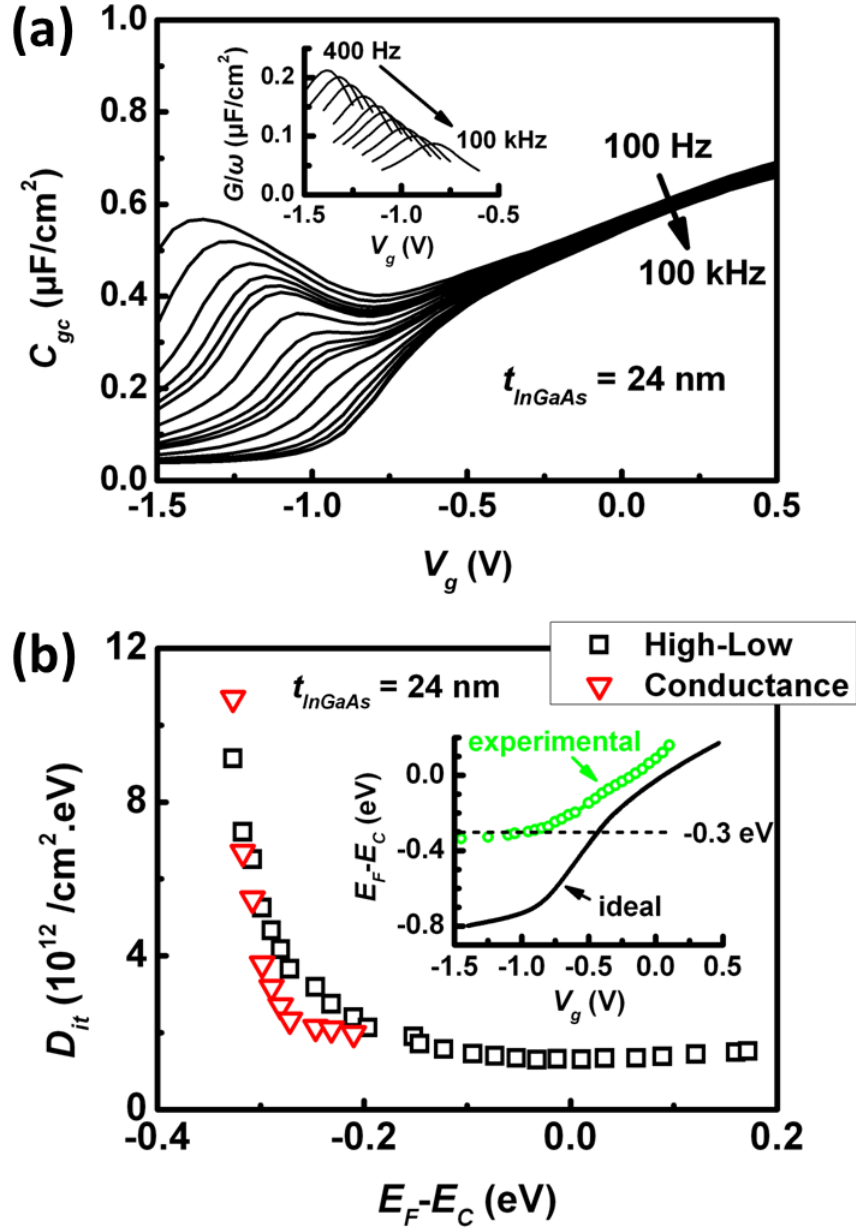


Figure 6.14: (a) Multi-frequency C_{gc} - V_g characteristic of a 24-nm-thick $\text{In}_{0.53}\text{Ga}_{0.47}\text{As}$ channel device showing low frequency dispersion near accumulation. The low C_{min} of ~ 40 nF/cm² suggests full depletion at $V_g < -1$ V. Inset: Evolution of the conductance peak normalized to angular frequency (G/ω). (b) Comparison of the conductance and high-low methods for the extraction of the density of interface traps (D_{it}). Inset: Fermi level position at the $\text{Al}_2\text{O}_3/\text{In}_{0.53}\text{Ga}_{0.47}\text{As}$ interface in an ideal and in the fabricated devices. In the fabricated device, the Fermi level reaches $E_F - E_C = -0.3$ eV at $V_g = -1$ V, demonstrating the full depletion of the 24-nm-thick $\text{In}_{0.53}\text{Ga}_{0.47}\text{As}$ channel.

Hz (low) capacitance traces shown in Figure 6.14(a). It is noted that the presence of a peak at ~ -1.4 V in the 100 Hz capacitance response suggests a D_{it} response rather than a minority carrier response, providing more confidence in the D_{it} extraction using the high-low method [16]. The inset of Figure 6.14(b) shows the Fermi level position at the $\text{Al}_2\text{O}_3/\text{In}_{0.53}\text{Ga}_{0.47}\text{As}$ interface as a function of V_g in an ideal and in the fabricated 24-nm-thick $\text{In}_{0.53}\text{Ga}_{0.47}\text{As}$ channel device. In contrast to the case of the 32-nm-thick $\text{In}_{0.53}\text{Ga}_{0.47}\text{As}$ channel device, the Fermi level in the 24-nm-thick $\text{In}_{0.53}\text{Ga}_{0.47}\text{As}$ channel device can be moved below the energy level required to reach full depletion (i.e.: $E_F - E_C = -0.31$ eV [Figure 6.3(d)]), in agreement with the good I_{ON}/I_{OFF} of 3.3×10^4 obtained with $t_{\text{InGaAs}} = 24$ nm [Figure 6.11(a)]. The reasonably low D_{it} values of 1.3×10^{12} to 5.2×10^{12} /cm².eV obtained within the 0.3 eV energy range below E_C suggest that the DE process does not significantly degrade the $\text{Al}_2\text{O}_3/\text{In}_{0.53}\text{Ga}_{0.47}\text{As}$ interface .

6.4.3 Surface Carrier Concentration, Substrate Doping and Dark Space

Figure 6.15(a) compares the 100-kHz $C_{gc}-V_g$ characteristics measured on the 24, 20 and 16-nm-thick $\text{In}_{0.53}\text{Ga}_{0.47}\text{As}$ channel devices. The theoretical C_{fb} obtained from the calculation was used in conjunction with the experimental $C_{gc}-V_g$ characteristics in order to extract a flat-band voltage of 0 V. The total surface charge density at flat-band (N_{tot}), including the surface carrier density at flat-band (N_s) along with a D_{it} contribution, was obtained by integrating the experimental C_{gc} curve across a V_g range where the device goes from full depletion to flat-band [Figure 6.15(b)]. Following the calculation of N_{tot} , we extracted the free charge density in the conduction band ($= N_s$) by subtracting to the integrated D_{it} integrated across the energy range of operation of the device from N_{tot} . This procedure was performed for $t_{\text{InGaAs}} = 24, 20$ and 16 nm [Figure 6.15(b)]. We also calculated the theoretical N_s at flat-band for a range of t_{InGaAs} and N_d [Figure 6.15(b)]. An excellent match was obtained between the experimental N_s and the theoretical N_s for $N_d = 9 \times 10^{17}$ /cm³.

We extrapolated the curves obtained from the calculations in order to show the x -intercepts, which represent the amount of surface depletion (dark space) arising from quantum-mechanical effects pushing the carriers away from the top and bottom interfaces. This effect is more significant in an $\text{Al}_2\text{O}_3/\text{In}_{0.53}\text{Ga}_{0.47}\text{As}/\text{In}_{0.52}\text{Al}_{0.48}\text{As}$ structure than in a SiO_2/SOI structure. Indeed, a total dark space thickness accounting for the top and bottom interfaces (t_{dark}) of 7.5 nm is extracted for the $\text{Al}_2\text{O}_3/\text{In}_{0.53}\text{Ga}_{0.47}\text{As}/\text{In}_{0.52}\text{Al}_{0.48}\text{As}$ structure with a channel N_d of 9×10^{17} /cm³, while a t_{dark} of only 1.8 nm is obtained for the SiO_2/SOI structure at the same channel N_d . We suggest that this issue could partly explain the severe I_{ON} degradation observed for $t_{\text{InGaAs}} = 16$ and 12 nm [Figure 6.10]. The calculations also indicate that t_{dark} could be reduced by increasing N_d , in agreement with the trend reported for high- k/Ge MOSFETs in [32].

(24 nm) $\text{In}_{0.53}\text{Ga}_{0.47}\text{As}$ channel, our measurements were limited to a maximum frequency of 100 kHz.

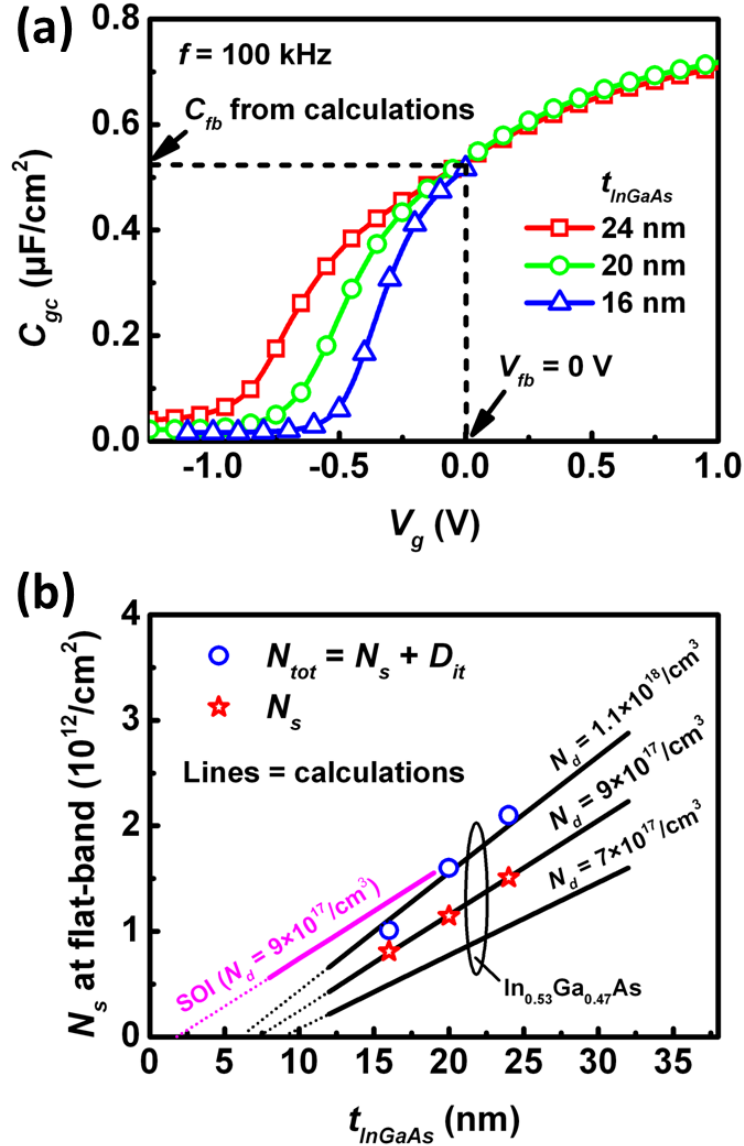


Figure 6.15: (a) 100-kHz C_{gc} - V_g characteristics measured on 24, 20 and 16-nm-thick $\text{In}_{0.53}\text{Ga}_{0.47}\text{As}$ -channel devices. The theoretical flat-band capacitance (C_{fb}) obtained from calculations is reported on the curves to extract a flat-band voltage (V_{fb}) of 0 V. (b) Plot of the surface carrier density (N_s) at flat-band vs t_{InGaAs} . The total charge density (N_{tot}) was obtained by integrating C_{gc} . N_s was obtained by correcting N_{tot} for the density of interface trap (D_{it}) integrated across the energy range of operation of the corresponding device. The N_s at flat-band vs t_{InGaAs} curves were calculated for ideal devices with $N_d = 1.1 \times 10^{18}$, 9×10^{17} and $7 \times 10^{17}/\text{cm}^3$. The x -intercepts obtained by extrapolation of the curves yielded the total dark space thickness values (accounting for the top and bottom interfaces). The case of a SiO_2/Si -on-insulator (SOI) structure with a channel N_d of $9 \times 10^{17}/\text{cm}^3$ is shown for comparison.

6.4.4 Series Resistance

Figure 6.16(a) represents the circuit equivalent model of a gate-enclosed junctionless device, where $R_{c,D}$ and $R_{c,S}$, are the contact resistances to the drain and source, respectively; R_D , R_S , R_{D-to-G} and R_{G-to-S} are the series resistances associated with the sheet resistance of the drain area, source area, non-gated drain-to-gate area and non-gated gate-to-source area, respectively; and R_{ch} is the channel resistance, which is controlled by the gate. In order to estimate the contribution of R_D , R_S , R_{D-to-G} , and R_{G-to-S} , we start with the expression of the resistance associated with the sheet resistance of a linear bar of semi-conductor:

$$R = R_{sheet} \cdot (W/L)^{-1} = [q \cdot \mu \cdot n \cdot t_{bar} \cdot (W/L)]^{-1} \quad (6.3)$$

where R_{sheet} is the sheet resistance of the semi-conductor material, q is the charge of an electron, μ is the carrier mobility, n is the carrier density, and t_{bar} , W and L are the thickness, length and width of the bar, respectively. To obtain the resistance of a ring structure with r^{in} and r^{out} as inner and outer radii, the W/L ratio in Equation 6.3 is replaced by the $(W/L)_{eff}$ of Equation 6.2, yielding:

$$R_{ring} = [q \cdot \mu \cdot n \cdot t \cdot (W/L)_{eff}]^{-1} = \ln(r^{out}/r^{in}) \cdot [2 \cdot \pi \cdot q \cdot \mu \cdot n \cdot t]^{-1} \quad (6.4)$$

Considering the dimensions of the planar gate-enclosed junctionless $\text{In}_{0.53}\text{Ga}_{0.47}\text{As}$ MOSFETs shown in Figure 6.8(e), and assuming conservative values of $5 \times 10^{-6} \Omega \cdot \text{cm}^2$ for the specific contact resistance, $0.5 \mu\text{m}$ for the transfer length and $2000 \text{ cm}^2/\text{V} \cdot \text{s}$ for the carrier mobility in $n\text{-In}_{0.53}\text{Ga}_{0.47}\text{As}$ along with the extracted $\text{In}_{0.53}\text{Ga}_{0.47}\text{As}$ N_d of $9 \times 10^{17} / \text{cm}^3$, we calculated each contribution to the total series resistance (R_{series}). The calculations revealed that the series resistance contribution associated with the sheet resistances of the non-gated areas (R_{D-to-G} and R_{G-to-S}), represented at least 91% of R_{series} (depending on t_{InGaAs}), suggesting that $R_{series} \approx (R_{D-to-G} + R_{G-to-S})$. As a result, the sheet resistances of the drain (R_D) and source (R_S) areas and contact resistances to the drain ($R_{c,D}$) and source ($R_{c,S}$) areas can be neglected and the circuit equivalent model for the series resistance shown in Figure 6.16(a) can be simplified to that shown in Figure 6.16(b). The total resistance (R_{tot}) is obtained from a device I_d-V_g characteristic:

$$R_{tot} = V_{ds}/I_d = R_{ch} + R_{series} \quad (6.5)$$

It is noted that the R_{sheet} of the semiconductor underneath the gate is controlled by V_g . In an ideal device, the R_{sheet} of the channel area is the same as that of the non-gated area when V_g is set to the flat-band voltage (V_{fb}). The presence of a fixed charge (Q_{fixed}) in the $\text{Al}_2\text{O}_3/\text{In}_{0.53}\text{Ga}_{0.47}\text{As}$ system was reported in [33, 34]. Q_{fixed} has two components: a fixed negative charge at the $\text{Al}_2\text{O}_3/\text{In}_{0.53}\text{Ga}_{0.47}\text{As}$ interface and a fixed positive charge distributed

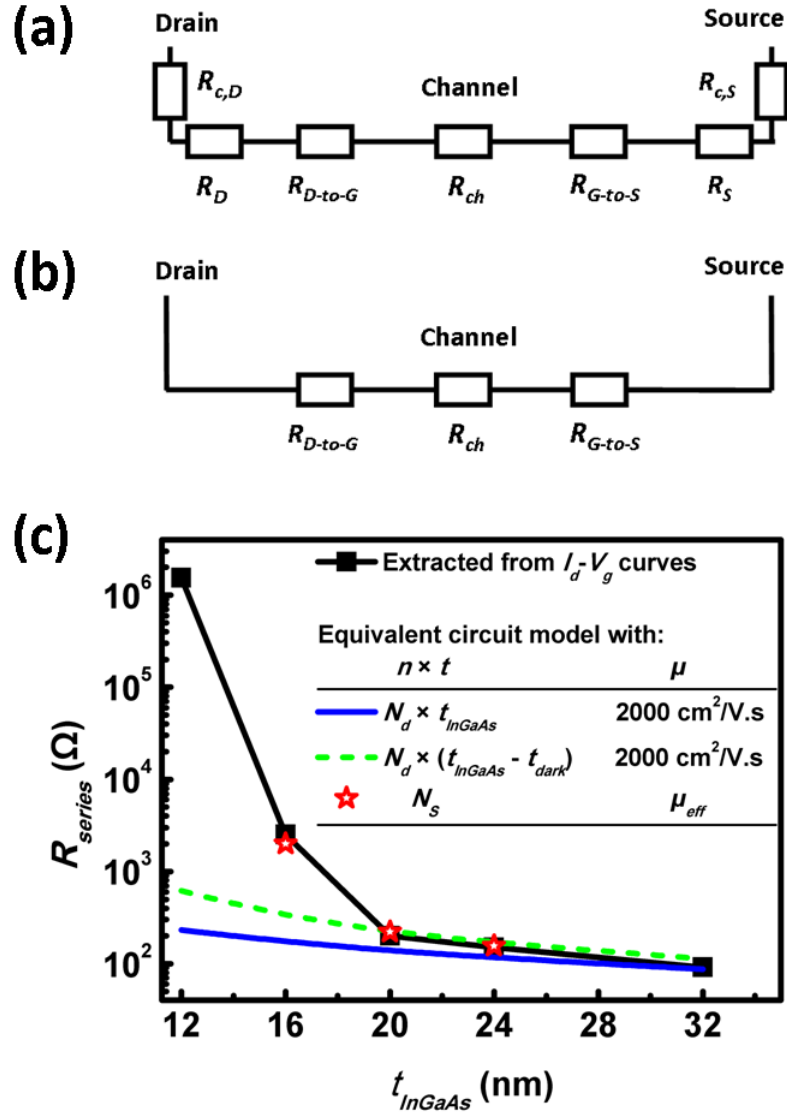


Figure 6.16: (a) Circuit equivalent model of the device. $R_{c,D}$ and $R_{c,S}$ are the resistances of the contacts to the drain and source areas, respectively. R_D , R_S , R_{D-to-G} and R_{G-to-S} are the resistances associated with the sheet resistance of the drain, source, drain-to-source and gate-to-source areas, respectively. R_{ch} is the resistance of the channel. (b) Simplified circuit equivalent model assuming a specific contact resistance (ρ_c) of $5 \times 10^{-6} \Omega \cdot \text{cm}^2$, a transfer length (L_t) of $0.5 \mu\text{m}$ and a mobility in the $n\text{-In}_{0.53}\text{Ga}_{0.47}\text{As}$ ($N_d = 9 \times 10^{17} / \text{cm}^3$) layer of $2000 \text{ cm}^2/\text{V}\cdot\text{s}$. (c) Comparison of the series resistance (R_{series}) vs t_{InGaAs} extracted from the I_d-V_g curves shown in Figure 6.10 and calculated from the simplified equivalent circuit model shown in (b) with estimated and/or extracted surface carrier density [noted $n \cdot t$ in Equation 6.4] and carrier mobility (μ) parameters.

throughout the bulk of the Al_2O_3 film. It is noted that Q_{fixed} plays an important role in the device operation, as it not only degrades μ_{eff} due to Coulomb scattering, but it also impacts R_{series} through R_{D-to-G} and R_{G-to-S} . Indeed, a negative (positive) fixed charge will deplete (accumulate) the non-gated n -type semiconductor, increasing (decreasing) the contribution of R_{D-to-G} and R_{G-to-S} to R_{series} .

A value of -0.2 V, corresponding to the flat-band voltage shift (ΔV_{fb}) induced by Q_{fixed} , was obtained by comparing the experimental V_{fb} of 0 V [Figure 6.15(a)] to the theoretical V_{fb} of 0.2 V (Figure 6.2)⁵. The negative ΔV_{fb} indicates a net positive surface-equivalent fixed charge in the Al_2O_3 , consistent with [34] for $t_{ox} = 8.5$ nm, suggesting that the non-gated areas are in slight accumulation. Therefore, applying $V_g = (V_{fb} - \Delta V_{fb})$ to the gate terminal enables to set the channel at the same accumulation level as that of the non-gated areas, leading to a uniform R_{sheet} between the source and drain terminals. Under this particular condition, the channel and non-gated areas can be considered as a single disk of uniform R_{sheet} , allowing the calculation of R_{tot} using Equation 6.5 and the extraction of R_{D-to-G} , R_{G-to-S} and R_{series} with Equation 6.4.

Figure 6.16(c) shows the R_{series} extracted for the 32, 24, 20, 16 and 12-nm-thick $\text{In}_{0.53}\text{Ga}_{0.47}\text{As}$ channel devices. A dramatic increase in R_{series} is observed for $t_{InGaAs} < 20$ nm. The calculated R_{series} curves, obtained using the simplified equivalent circuit model shown in Figure 6.16(b), Equation 6.4 and the estimated and/or extracted surface carrier density [noted n_t in Equation 6.4] and carrier mobility (μ) parameters, indicate that the dramatic increase in R_{series} is observed for $t_{InGaAs} < 20$ nm cannot be entirely explained by the reduction in surface carrier density arising from the scaling of t_{InGaAs} and the dark space phenomenon. This suggests that a μ degradation for $t_{InGaAs} < 20$ nm, consistent with [10].

6.4.5 Effective Mobility

The effect of t_{InGaAs} on the μ_{eff} of planar gate-enclosed junctionless $\text{In}_{0.53}\text{Ga}_{0.47}\text{As}$ MOSFETs is shown in Figure 6.17. It is noted that the μ_{eff} values are corrected for R_{series} and D_{it} . The 24 and 20-nm-thick $\text{In}_{0.53}\text{Ga}_{0.47}\text{As}$ channel devices feature a peak μ_{eff} at flat-band of 2130 and 1975 $\text{cm}^2/\text{V}\cdot\text{s}$, respectively. A marked drop in μ_{eff} is observed on the 16-nm-thick $\text{In}_{0.53}\text{Ga}_{0.47}\text{As}$ channel device. This agrees with [10] and is also consistent with the lower I_{ON} and higher R_{series} obtained in Sub-sections 6.4.1 and 6.4.4, respectively. We calculated the R_{series} using the simplified equivalent circuit model with the extracted N_s and μ_{eff} at flat-band (Figure 6.16). Excellent agreement was obtained with the R_{series} extracted from the I_d-V_g curves, confirming that the sharp increase in R_{series} for $t_{InGaAs} < 16$ nm is mainly due to a μ_{eff} degradation.

The μ_{eff} of an inversion-mode Pd/ Al_2O_3 / $\text{In}_{0.53}\text{Ga}_{0.47}\text{As}$ MOSFET measured at a temperature (T) of 35 K is also shown for comparison. Since the μ_{eff} values of the junctionless device

⁵The extraction of ΔV_{fb} is totally dependent on the value used for the W_f of Pd on Al_2O_3 in the calculations. A dedicated study would be required to correctly estimate the fixed oxide charge density in the Al_2O_3 film.

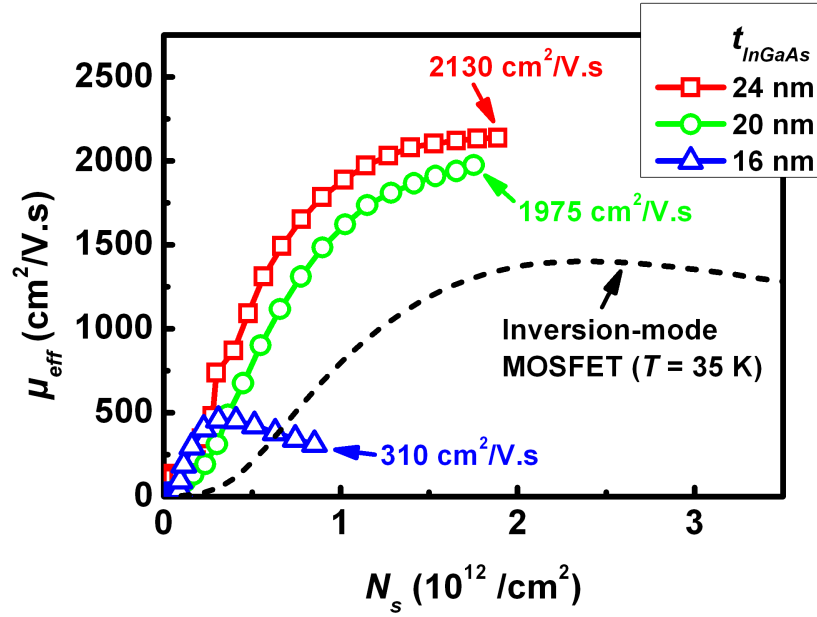


Figure 6.17: Effective electron mobility (μ_{eff}) vs N_s . Values of μ_{eff} at flat-band of 2130, 1975 and 310 $\text{cm}^2/\text{V.s}$ were obtained for planar gate-enclosed junctionless $\text{In}_{0.53}\text{Ga}_{0.47}\text{As}$ MOSFETs featuring t_{InGaAs} of 24, 20 and 16 nm, respectively. The abrupt drop in μ_{eff} observed for $t_{\text{InGaAs}} = 16$ nm is consistent with [10]. The μ_{eff} of an inversion-mode Pd/ Al_2O_3 / $\text{In}_{0.53}\text{Ga}_{0.47}\text{As}$ MOSFET with implanted S/D measured at a temperature (T) of 35 K (see 5) is shown for comparison. The μ_{eff} data of the junctionless devices are corrected for R_{series} and D_{it} . The μ_{eff} data of the inversion-mode device is only corrected for R_{series} but the reduced T acts as a D_{it} correction [35].

are corrected for D_{it} , we selected a T of 35 K for the μ_{eff} of the inversion-mode device in order to obtain a fair comparison between the two devices. Indeed, as reported in [35], low temperature measurements can be used to “freeze” the contribution of the D_{it} located near the conduction band and obtain a D_{it} correction. Moreover, we showed in Chapter 5 that the μ_{eff} of the inversion-mode device was dominated by surface roughness scattering and that phonon scattering had no significant impact at $T = 292$ K, indicating that the μ_{eff} at 35 K represents a good estimate of the μ_{eff} at 292 K corrected for D_{it} . The severe μ_{eff} degradation due to surface roughness scattering in the inversion-mode device arises from the use of a 600°C for 30 sec implant activation anneal process, which is required to form the S/D terminals of the device. The junctionless device concept obviates the need for such high temperature anneal processes. Moreover, since the AFM measurements taken on the $\text{In}_{0.53}\text{Ga}_{0.47}\text{As}$ channel after 10, 15 and 20 DE cycles only revealed a small increase in surface roughness with DE, we suggest that surface roughness scattering may not be responsible for the significant μ_{eff} degradation of the junctionless device at $t_{\text{InGaAs}} = 16$ nm. We speculate that the lower μ_{eff} at $t_{\text{InGaAs}} = 16$ nm could be due to quantum confinement effects. Rigorous calculations would be required to verify this point.

6.5 Conclusion

We applied the junctionless MOSFET concept to an $\text{Al}_2\text{O}_3/n\text{-In}_{0.53}\text{Ga}_{0.47}\text{As}/p\text{-In}_{0.52}\text{Al}_{0.48}\text{As}$ structure. The $n\text{-In}_{0.53}\text{Ga}_{0.47}\text{As}/p\text{-In}_{0.52}\text{Al}_{0.48}\text{As}$ heterojunction offered excellent device isolation. Moreover, we showed that thinning the $\text{In}_{0.53}\text{Ga}_{0.47}\text{As}$ channel using a DE process did not significantly degrade the $\text{Al}_2\text{O}_3/n\text{-In}_{0.53}\text{Ga}_{0.47}\text{As}$ interface properties in terms of D_{it} and surface roughness. Although a detailed analysis of the device operation and performance was presented, further investigations of the μ_{eff} degradation mechanisms involved in devices with sub-20-nm $\text{In}_{0.53}\text{Ga}_{0.47}\text{As}$ channel thickness are required.

Bibliography

- [1] J.-P. Colinge, C.-W. Lee, A. Afzalian, N. D. Akhavan, R. Yan, I. Ferain, P. Razavi, B. O'Neill, A. Blake, M. White, A.-M. Kelleher, B. McCarthy, and R. Murphy, "Nanowire transistors without junctions," *Nature Nano.*, vol. 5, p. 225, Feb. 2010. [Online]. Available: <http://dx.doi.org/10.1038/nnano.2010.15>
- [2] J.-P. Raskin, J.-P. Colinge, I. Ferain, A. Kranti, C. W. Lee, N. Dehdashti, R. Yan, P. Razavi, and R. Yu, "Mobility improvement in nanowire junctionless transistors by uniaxial strain," in *SOI Conference (SOI), 2010 IEEE International*, 2010, pp. 1–2. [Online]. Available: <http://dx.doi.org/10.1109/SOI.2010.5641390>
- [3] [Online]. Available: <http://www.ioffe.rssi.ru/SVA/NSM/Semicond/GaInAs>
- [4] R. J. Young, L. O. Mereni, N. Petkov, G. R. Knight, V. Dimastrodonato, P. K. Hurley, G. Hughes, and E. Pelucchi, "Low-angle misorientation dependence of the optical properties of InGaAs/AlInAs quantum wells," *J. Cryst. Growth*, vol. 312, no. 9, p. 1546, Apr. 2010. [Online]. Available: <http://dx.doi.org/10.1016/j.jcrysgro.2010.01.033>
- [5] V. Djara, K. Cherkaoui, S. B. Newcomb, K. Thomas, E. Pelucchi, D. O'Connell, L. Floyd, V. Dimastrodonato, L. O. Mereni, and P. K. Hurley, "On the activation of implanted silicon ions in p -In_{0.53}Ga_{0.47}As," *Semiconductor Science and Technology*, vol. 27, no. 8, p. 082001, Aug. 2012. [Online]. Available: <http://dx.doi.org/10.1088/0268-1242/27/8/082001>
- [6] M. Negara, V. Djara, T. O'Regan, K. Cherkaoui, M. Burke, Y. Gomeniuk, M. Schmidt, É. O'Connor, I. Povey, A. Quinn, and P. Hurley, "Investigation of electron mobility in surface-channel Al₂O₃/In_{0.53}Ga_{0.47}As MOSFETs," *Solid-State Electronics*, vol. 88, p. 37, Oct. 2013. [Online]. Available: <http://dx.doi.org/10.1016/j.sse.2013.04.014>
- [7] U. Singisetti, M. A. Wistey, G. Burek, A. Baraskar, B. J. Thibeault, A. Gossard, M. J. W. Rodwell, B. Shin, E. Kim, P. C. McIntyre, B. Yu, Y. Yuan, D. Wang, Y. Taur, P. Asbeck, and Y.-J. Lee, "In_{0.53}Ga_{0.47}As Channel MOSFETs With Self-Aligned InAs Source/Drain Formed by MEE Regrowth," *Electron Device Letters, IEEE*, vol. 30, no. 11, p. 1128, Nov. 2009. [Online]. Available: <http://dx.doi.org/10.1109/LED.2009.2031304>
- [8] U. Singisetti, M. Wistey, G. Burek, A. Baraskar, J. Cagnon, B. Thibeault, A. Gossard, S. Stemmer, M. Rodwell, E. Kim, B. Shin, P. McIntyre, and Y.-J. Lee, "Enhancement mode In_{0.53}Ga_{0.47}As MOSFET with self-aligned epitaxial source/drain regrowth," in *Indium Phosphide Related Materials, 2009. IPRM '09. IEEE International Conference on*, May 2009, p. 120. [Online]. Available: <http://dx.doi.org/10.1109/ICIPRM.2009.5012456>

-
- [9] S. Barraud, M. Berthome, R. Coquand, M. Casse, T. Ernst, M. P. Samson, P. Perreau, K. Bourdelle, O. Faynot, and T. Poiroux, "Scaling of Trigate Junctionless Nanowire MOSFET With Gate Length Down to 13 nm," *Electron Device Letters, IEEE*, vol. 33, no. 9, p. 1225, Sep. 2012. [Online]. Available: <http://dx.doi.org/10.1109/LED.2012.2203091>
- [10] M. Yokoyama, R. Iida, S. Kim, N. Taoka, Y. Urabe, T. Yasuda, H. Takagi, H. Yamada, N. Fukuhara, M. Hata, M. Sugiyama, Y. Nakano, M. Takenaka, and S. Takagi, "Extremely-thin-body InGaAs-on-insulator MOSFETs on Si fabricated by direct wafer bonding," in *Electron Devices Meeting (IEDM), 2010 IEEE International*, 2010, pp. 3.1.1–3.1.4. [Online]. Available: <http://dx.doi.org/10.1109/IEDM.2010.5703286>
- [11] [Online]. Available: <http://www.nd.edu/~gsnider/>
- [12] A. Diligenti and M. Stagi, "Tunnelling in aluminium/aluminium-oxide/palladium junctions: hydrogen-induced variations," *Electronics Letters*, vol. 19, no. 18, p. 717, Jul. 1983. [Online]. Available: <http://dx.doi.org/10.1049/el:19830488>
- [13] V. Djara, K. Cherkaoui, M. Schmidt, S. Monaghan, É. O'Connor, I. Povey, D. O'Connell, M. Pemble, and P. K. Hurley, "Impact of Forming Gas Annealing on the Performance of Surface-Channel In_{0.53}Ga_{0.47}As MOSFETs With an ALD Al₂O₃ Gate Dielectric," *Electron Devices, IEEE Transactions on*, vol. 59, no. 4, p. 1084, Apr. 2012. [Online]. Available: <http://dx.doi.org/10.1109/TED.2012.2185242>
- [14] V. Djara, T. P. O'Regan, K. Cherkaoui, M. Schmidt, S. Monaghan, É. O'Connor, I. M. Povey, D. O'Connell, M. E. Pemble, and P. K. Hurley, "Electrically active interface defects in the In_{0.53}Ga_{0.47}As MOS system," *Microelectronic Engineering*, vol. 109, no. 0, p. 182, Sep. 2013. [Online]. Available: <http://dx.doi.org/10.1016/j.mee.2013.03.026>
- [15] M. E. Ramón, T. Akyol, D. Shahrjerdi, C. D. Young, J. Cheng, L. F. Register, and S. K. Banerjee, "Fast and slow transient charging in various III-V field-effect transistors with atomic-layer-deposited-Al₂O₃ gate dielectric," *Applied Physics Letters*, vol. 102, no. 2, p. 022104, Jan. 2013. [Online]. Available: <http://dx.doi.org/10.1063/1.4776678>
- [16] É. O'Connor, B. Brennan, V. Djara, K. Cherkaoui, S. Monaghan, S. B. Newcomb, R. Contreras, M. Milojevic, G. Hughes, M. E. Pemble, R. M. Wallace, and P. K. Hurley, "A systematic study of (NH₄)₂S passivation (22%, 10%, 5%, or 1%) on the interface properties of the Al₂O₃/In_{0.53}Ga_{0.47}As/InP system for *n*-type and *p*-type In_{0.53}Ga_{0.47}As epitaxial layers," *Journal of Applied Physics*, vol. 109, no. 2, p. 024101, Jan. 2011. [Online]. Available: <http://dx.doi.org/10.1063/1.3533959>

- [17] R. Suzuki, N. Taoka, M. Yokoyama, S. Lee, S. H. Kim, T. Hoshii, T. Yasuda, W. Jevasuwan, T. Maeda, O. Ichikawa, N. Fukuhara, M. Hata, M. Takenaka, and S. Takagi, “1-nm-capacitance-equivalent-thickness $\text{HfO}_2/\text{Al}_2\text{O}_3/\text{InGaAs}$ metal-oxide-semiconductor structure with low interface trap density and low gate leakage current density,” *Applied Physics Letters*, vol. 100, no. 13, p. 132906, Mar. 2012. [Online]. Available: <http://dx.doi.org/10.1063/1.3698095>
- [18] H.-C. Lin, W.-E. Wang, G. Brammertz, M. Meuris, and M. Heyns, “Electrical study of sulfur passivated $\text{In}_{0.53}\text{Ga}_{0.47}\text{As}$ MOS capacitor and transistor with ALD Al_2O_3 as gate insulator,” *Microelectronic Engineering*, vol. 86, no. 7-9, p. 1554, Jul.-Sep. 2009. [Online]. Available: <http://dx.doi.org/10.1016/j.mee.2009.03.112>
- [19] G. Brammertz, H.-C. Lin, M. Caymax, M. Meuris, M. Heyns, and M. Passlack, “On the interface state density at $\text{In}_{0.53}\text{Ga}_{0.47}\text{As}/\text{oxide}$ interfaces,” *Applied Physics Letters*, vol. 95, no. 20, p. 202109, Nov. 2009. [Online]. Available: <http://dx.doi.org/10.1063/1.3267104>
- [20] H. D. Trinh, E. Y. Chang, P. W. Wu, Y. Y. Wong, C. T. Chang, Y. F. Hsieh, C. C. Yu, H. Q. Nguyen, Y. C. Lin, K. L. Lin, and M. K. Hudait, “The influences of surface treatment and gas annealing conditions on the inversion behaviors of the atomic-layer-deposition $\text{Al}_2\text{O}_3/\text{n-In}_{0.53}\text{Ga}_{0.47}\text{As}$ metal-oxide-semiconductor capacitor,” *Applied Physics Letters*, vol. 97, no. 4, p. 042903, Jul. 2010. [Online]. Available: <http://dx.doi.org/10.1063/1.3467813>
- [21] É. O’Connor, S. Monaghan, K. Cherkaoui, I. M. Povey, and P. K. Hurley, “Analysis of the minority carrier response of n-type and p-type $\text{Au}/\text{Ni}/\text{Al}_2\text{O}_3/\text{In}_{0.53}\text{Ga}_{0.47}\text{As}/\text{InP}$ capacitors following an optimized $(\text{NH}_4)_2\text{S}$ treatment,” *Applied Physics Letters*, vol. 99, no. 21, p. 212901, Nov. 2011. [Online]. Available: <http://dx.doi.org/10.1063/1.3663535>
- [22] Z. Liu, S. Cui, P. Shekhter, X. Sun, L. Kornblum, J. Yang, M. Eizenberg, K. S. Chang-Liao, and T. P. Ma, “Effect of H on interface properties of $\text{Al}_2\text{O}_3/\text{In}_{0.53}\text{Ga}_{0.47}\text{As}$,” *Applied Physics Letters*, vol. 99, no. 22, p. 222104, Nov. 2011. [Online]. Available: <http://dx.doi.org/10.1063/1.3665395>
- [23] T. Hoshii, S. Lee, R. Suzuki, N. Taoka, M. Yokoyama, H. Yamada, M. Hata, T. Yasuda, M. Takenaka, and S. Takagi, “Reduction in interface state density of $\text{Al}_2\text{O}_3/\text{InGaAs}$ metal-oxide-semiconductor interfaces by InGaAs surface nitridation,” *Journal of Applied Physics*, vol. 112, no. 7, p. 073702, Oct. 2012. [Online]. Available: <http://dx.doi.org/10.1063/1.4755804>
- [24] H. C. Chiu, L. T. Tung, Y. H. Chang, Y. J. Lee, C. C. Chang, J. Kwo, and M. Hong, “Achieving a low interfacial density of states in atomic layer deposited Al_2O_3 on

- In_{0.53}Ga_{0.47}As,” *Applied Physics Letters*, vol. 93, no. 20, p. 202903, Nov. 2008. [Online]. Available: <http://dx.doi.org/10.1063/1.3027476>
- [25] H.-P. Chen, Y. Yuan, B. Yu, J. Ahn, P. C. McIntyre, P. Asbeck, M. J. W. Rodwell, and Y. Taur, “Interface-State Modeling of Al₂O₃-InGaAs MOS From Depletion to Inversion,” *Electron Devices, IEEE Transactions on*, vol. 59, no. 9, p. 2383, Sep. 2012. [Online]. Available: <http://dx.doi.org/10.1109/TED.2012.2205255>
- [26] Y. Xuan, Y. Wu, H. Lin, T. Shen, and P. Ye, “Submicrometer Inversion-Type Enhancement-Mode InGaAs MOSFET With Atomic-Layer-Deposited Al₂O₃ as Gate Dielectric,” *Electron Device Letters, IEEE*, vol. 28, no. 11, p. 935, Nov. 2007. [Online]. Available: <http://dx.doi.org/10.1109/LED.2007.906436>
- [27] X. Cao and I. Thayne, “Novel high uniformity highly reproducible non-selective wet digital gate recess etch process for InP HEMTs,” *Microelectronic Engineering*, vol. 67-68, Jun. 2003. [Online]. Available: [http://dx.doi.org/10.1016/S0167-9317\(03\)00087-X](http://dx.doi.org/10.1016/S0167-9317(03)00087-X)
- [28] A. Alian, C. Merckling, G. Brammertz, M. Meuris, M. Heyns, and K. D. Meyer, “InGaAs MOS Transistors Fabricated through a Digital-Etch Gate-Recess Process and the Influence of Forming Gas Anneal on Their Electrical Behavior,” *ECS Journal of Solid State Science and Technology*, vol. 1, no. 6, p. P310, Oct. 2012. [Online]. Available: <http://dx.doi.org/10.1149/2.001301jss>
- [29] P. A. F. Herbert, L. P. Floyd, J. I. Braddell, E. M. Baldwin, and W. M. Kelly, “The application of ohmic contacts to nanometric structures,” *Microelectronic Engineering*, vol. 17, no. 1-4, p. 541, Mar. 1992. [Online]. Available: [http://dx.doi.org/10.1016/0167-9317\(92\)90111-4](http://dx.doi.org/10.1016/0167-9317(92)90111-4)
- [30] J. De Lima, S. Gimenez, and K. Cirne, “Modeling and Characterization of Overlapping Circular-Gate mosfet and Its Application to Power Devices,” *Power Electronics, IEEE Transactions on*, vol. 27, no. 3, Mar. 2012. [Online]. Available: <http://dx.doi.org/10.1109/TPEL.2011.2117443>
- [31] E. H. Nicollian and J. R. Brews, *MOS Physics and Technology*. New York: Wiley, 1982.
- [32] Y.-S. Wu and P. Su, “A Closed-Form Quantum “Dark Space” Model for Predicting the Electrostatic Integrity of Germanium MOSFETs With High-*k* Gate Dielectric,” *Electron Devices, IEEE Transactions on*, vol. 59, no. 3, pp. 530–535, Mar. 2012. [Online]. Available: <http://dx.doi.org/10.1109/TED.2011.2177091>
- [33] B. Shin, J. R. Weber, R. D. Long, P. K. Hurley, C. G. V. de Walle, and P. C. McIntyre, “Origin and passivation of fixed charge in atomic layer deposited aluminum oxide gate

- insulators on chemically treated InGaAs substrates,” *Applied Physics Letters*, vol. 96, no. 15, p. 152908, Apr. 2010. [Online]. Available: <http://dx.doi.org/10.1063/1.3399776>
- [34] R. D. Long, B. Shin, S. Monaghan, K. Cherkaoui, J. Cagnon, S. Stemmer, P. C. McIntyre, and P. K. Hurley, “Charged Defect Quantification in Pt/Al₂O₃/In_{0.53}Ga_{0.47}As/InP MOS Capacitors,” *Journal of The Electrochemical Society*, vol. 158, no. 5, p. G103, Mar. 2011. [Online]. Available: <http://dx.doi.org/10.1149/1.3545799>
- [35] C. Hinkle, A. Sonnet, R. Chapman, and E. M. Vogel, “Extraction of the Effective Mobility of In_{0.53}Ga_{0.47}As MOSFETs,” *Electron Device Letters, IEEE*, vol. 30, no. 4, p. 316, Apr. 2009. [Online]. Available: <http://dx.doi.org/10.1109/LED.2009.2012880>

Chapter 7

Conclusions and Suggestions for Further Research

7.1 Conclusions

The primary aim of this PhD was to develop $\text{In}_{0.53}\text{Ga}_{0.47}\text{As}$ metal-oxide-semiconductor field-effect transistors (MOSFETs) building on the knowledge of the high- $k/\text{In}_{0.53}\text{Ga}_{0.47}\text{As}$ metal-oxide-semiconductor (MOS) system developed at Tyndall since 2006. This involved both a conventional surface channel $\text{In}_{0.53}\text{Ga}_{0.47}\text{As}$ MOSFETs with Si implanted source and drain (S/D) regions and the development of the junctionless MOSFET concept with an $\text{In}_{0.53}\text{Ga}_{0.47}\text{As}$ channel. The main results are summarized below:

- The activation of Si implant in p -type $\text{In}_{0.53}\text{Ga}_{0.47}\text{As}$ was first investigated for the formation the source and drain terminals of an inversion-mode $\text{In}_{0.53}\text{Ga}_{0.47}\text{As}$ MOSFET. While a number of groups had already demonstrated the use of Si implantation and activation in the process flow of inversion-mode III-V MOSFETs, we could not find a systematic study of the impact of activation anneal temperature and anneal time on the sheet resistance (R_{sheet}) of the S/D areas. We, therefore, prepared implanted $\text{In}_{0.53}\text{Ga}_{0.47}\text{As}$ test structures based on the transfer length method (TLM) as part of a Doehlert design of experiment (DOE) to investigate a wide process window going from 625°C to 725°C for 15 s to 45 s. The analysis of the Doehlert DOE revealed an optimized process point at 715°C for 32 sec giving a low R_{sheet} of $195.6 \pm 3.4 \Omega/\square$. The impact of the activation anneal on the gate stack was then investigated through the use of pre-metal annealed metal-oxide-semiconductor capacitors (MOSCAPs). The analysis of the capacitance-voltage (C-V)/conductance-voltage (G-V) measurements performed on the MOSCAPs indicated a degradation of the high- $k/\text{In}_{0.53}\text{Ga}_{0.47}\text{As}$ interface with increasing anneal temperature. The density of interface traps (D_{it}) was found to increase by $\sim 16\%$ for every 25°C increase

within the studied temperature range of 675°C to 725°C. While the results obtained for the S/D implantation suggest that the 10^{19} - 10^{20} /cm³ doping levels required to achieve ultralow resistance ohmic contacts for logic devices, these results may still be relevant to other applications with less stringent requirements.

- A reduced thermal budget of 600°C for 30 s was, therefore, selected for the S/D activation of the inversion-mode Al₂O₃/In_{0.53}Ga_{0.47}As MOSFETs. The obtained devices were used as test vehicles to investigate the impact of a 300°C for 30 min forming gas (H₂/N₂) anneal (FGA) process on the gate stack. The FGA process was found to be efficient at removing or passivating fixed positive charges in the Al₂O₃, resulting in a shift of the threshold voltage from -0.63 V to 0.43 V and in an increase in the ON-state-to-OFF-state current ratio (I_{ON}/I_{OFF}) of three orders of magnitude. Following FGA, the devices exhibited a subthreshold swing (SS) of 150 mV/decade, and the transconductance, drive current and peak effective mobility (μ_{eff}) increased by 29%, 25% and 15%, respectively. The FGA significantly improved the source or drain-to-substrate junction isolation, with a reduction of two orders of magnitude in the reverse bias leakage exhibited by the Si-implanted In_{0.53}Ga_{0.47}As n^+/p junctions, which is consistent with a passivation of mid-gap defects in the In_{0.53}Ga_{0.47}As by the FGA process. After FGA, the devices featured sufficient performance to be used as test structures to perform detailed analysis of the gate stack defects and channel electron mobility.
- A “full-gate capacitance” method involving the fitting of the measured full-gate capacitance (C_g) vs gate voltage (V_g) characteristic and corresponding Maserjian Y-function using a self-consistent Poisson-Schrödinger solver was then developed to obtain the energy distribution of traps [$D_{trap}(E)$] across the In_{0.53}Ga_{0.47}As bandgap and extending into the In_{0.53}Ga_{0.47}As conduction band. The obtained $D_{trap}(E)$ featured a peak of donor-like interface traps with a density of 1.5×10^{13} /cm².eV located at ~ 0.36 eV above the In_{0.53}Ga_{0.47}As valence band edge (E_V) and a high density of donor-like traps increasing towards E_V . The analysis also indicated acceptor-like traps located in the In_{0.53}Ga_{0.47}As conduction band, with a density of $\sim 2.5 \times 10^{13}$ /cm².eV at 0.3 eV above the In_{0.53}Ga_{0.47}As conduction band edge (E_C). The proposed method provides a more complete information than the conventional methods (i.e.: High-Low, Terman and conductance). Moreover, the information obtained from this method can be combined with theoretical calculation models to gain further insight into the atomic origin of the traps observed in the high- k /In_{0.53}Ga_{0.47}As MOS system.
- A “multi-frequency” inversion-charge pumping (ICP) technique was developed to separate the contribution of traps aligned with the In_{0.53}Ga_{0.47}As conduction band from the inversion-charge density (N_{inv}). The analysis yielded (1) a very narrow spatial distribution of traps

located ~ 1.5 Å away from the $\text{Al}_2\text{O}_3/\text{In}_{0.53}\text{Ga}_{0.47}\text{As}$ interface, (2) a peak density of $\sim 5.7 \times 10^{20} / \text{cm}^3 \cdot \text{eV}$ and (3) a discrete capture cross section (σ) of $4.5 \times 10^{-21} \text{ cm}^2$. These results confirm the presence of border traps, consistent with the results obtained with the full-gate capacitance technique and with the results reported in the literature.

- The N_{inv} obtained from the multi-frequency ICP was combined with pulsed drain current (I_d) vs V_g measurements in an attempt to extract the “true” μ_{eff} . A μ_{eff} peaking at $\sim 2850 \text{ cm}^2/\text{V}\cdot\text{s}$ at a low N_{inv} of $7 \times 10^{11} \text{ cm}^2/\text{V}\cdot\text{s}$ and rapidly decreasing to $\sim 600 \text{ cm}^2/\text{V}\cdot\text{s}$ at $N_{inv} = 1 \times 10^{13} / \text{cm}^2$ was obtained. The analysis of μ_{eff} revealed that surface roughness scattering was the dominant μ_{eff} degradation mechanism. This result was confirmed by conventional split C-V measurements, performed over a wide range of temperature (T) going from 292 K to 35 K, as μ_{eff} was found to be independent of T for $N_{inv} > 4 \times 10^{12} / \text{cm}^2$. Physical evidence of a large root mean square (RMS) surface roughness of $1.95 \pm 0.28 \text{ nm}$ was obtained by atomic force microscopy (AFM). Further AFM analysis revealed that the activation anneal process at 600°C for 30 sec was responsible for the surface roughness degradation.
- To circumvent the problems associated with the activation anneal process, a planar junctionless $\text{Al}_2\text{O}_3/\text{In}_{0.53}\text{Ga}_{0.47}\text{As}$ MOSFET was developed. A digital etch (DE) process was also developed in order to study the impact of the $\text{In}_{0.53}\text{Ga}_{0.47}\text{As}$ channel thickness (t_{InGaAs}) on the device operation and performance. The DE process characterization revealed an etch rate per cycle of 0.8 nm/cycle along with an RMS surface roughness of 0.28 nm after 20 cycles. Scaling of the SS with t_{InGaAs} was observed for t_{InGaAs} going from 24 to 16 nm, yielding a minimum SS of 115 mV/dec. for $t_{InGaAs} = 16 \text{ nm}$. D_{it} values near the conduction band in the low- $10^{12} / \text{cm}^2 \cdot \text{eV}$ were also extracted, suggesting that the DE process can provide acceptable $\text{Al}_2\text{O}_3/\text{In}_{0.53}\text{Ga}_{0.47}\text{As}$ interface properties. Flat-band μ_{eff} values of 2130 and $1975 \text{ cm}^2/\text{V}\cdot\text{s}$ were extracted on devices with $t_{InGaAs} = 24$ and 20 nm , respectively.

7.2 Suggestions for Further Research

A range of fabrication process modules, characterization techniques and device architectures were developed and explored as part of this PhD. The list below gives one suggestion for further work in each of these areas:

- This work highlighted the difficulties associated with the formation of the S/D terminals of inversion-mode $\text{In}_{0.53}\text{Ga}_{0.47}\text{As}$ MOSFETs using implantation and activation. It was shown that the high thermal budget required to obtain maximum activation and low series

resistance (R_{series}) was responsible for the severe degradation of the high- k /In_{0.53}Ga_{0.47}As interface in terms of interface traps and surface roughness. It would be interesting to try to improve the protection of the In_{0.53}Ga_{0.47}As surface for the activation anneal. Varying capping materials and capping film thicknesses could have an impact on the In_{0.53}Ga_{0.47}As RMS surface roughness for a given thermal budget. It could also be interesting to try to activate the implant in an metal-organic vapor phase epitaxy (MOVPE) system under arsine ambient.

- An alternative method to extract the energy distribution of traps across the In_{0.53}Ga_{0.47}As bandgap and extending into the In_{0.53}Ga_{0.47}As conduction band was proposed. The method is based on the fitting of the measured C_g - V_g characteristic (and Maserjian Y -function) measured at a frequency (f) of 1 MHz and a T of -50°C. The method relied on the assumption that the measured characteristic was a good approximation of the true high-frequency (H-F) characteristic. It would be interesting to repeat this analysis using a better approximation of the H-F C_g - V_g characteristic obtained at a T of 77 K or lower.
- The study of the impact of t_{InGaAs} on the performance of planar junctionless In_{0.53}Ga_{0.47}As MOSFETs was presented. The study indicated a dramatic increase in R_{series} as t_{InGaAs} reduced. It would be interesting to fabricate and characterize devices with $t_{InGaAs} < 16$ nm with raised S/D terminals. This could be achieved by selectively etching the channel without etching the S/D area. This would only require a slight alteration of the fabrication process flow but no modification of the lithography mask. The fabrication process flow is given in Appendix C.

Appendix A

Doehlert Design of Experiment

A.1 Implementation

The Doehlert design of experiment (DOE) relies on the following second-order equation [1, 2]:

$$y = \beta_0 + \beta_1 x_1 + \beta_2 x_2 + \beta_{11} x_1^2 + \beta_{22} x_2^2 + \beta_{12} x_1 x_2 + e \quad (\text{A.1})$$

where y is the experimental response, x_1 and x_2 are the two distinct variables and e is the residual error. The obtained seven-equation system with six unknown β coefficients can be expressed by the matrix representations (A.2) and (A.3):

$$\begin{pmatrix} y_1 \\ y_2 \\ y_3 \\ y_4 \\ y_5 \\ y_6 \\ y_7 \end{pmatrix} = \begin{pmatrix} 1 & x_{1,1} & x_{1,2} & x_{1,1} \times x_{1,2} & x_{1,1}^2 & x_{1,2}^2 \\ 1 & x_{2,1} & x_{2,2} & x_{2,1} \times x_{2,2} & x_{2,1}^2 & x_{2,2}^2 \\ 1 & x_{3,1} & x_{3,2} & x_{3,1} \times x_{3,2} & x_{3,1}^2 & x_{3,2}^2 \\ 1 & x_{4,1} & x_{4,2} & x_{4,1} \times x_{4,2} & x_{4,1}^2 & x_{4,2}^2 \\ 1 & x_{5,1} & x_{5,2} & x_{5,1} \times x_{5,2} & x_{5,1}^2 & x_{5,2}^2 \\ 1 & x_{6,1} & x_{6,2} & x_{6,1} \times x_{6,2} & x_{6,1}^2 & x_{6,2}^2 \\ 1 & x_{7,1} & x_{7,2} & x_{7,1} \times x_{7,2} & x_{7,1}^2 & x_{7,2}^2 \end{pmatrix} \times \begin{pmatrix} \beta_0 \\ \beta_1 \\ \beta_2 \\ \beta_{12} \\ \beta_{11} \\ \beta_{22} \end{pmatrix} + \begin{pmatrix} e_1 \\ e_2 \\ e_3 \\ e_4 \\ e_5 \\ e_6 \\ e_7 \end{pmatrix} \quad (\text{A.2})$$

$$Y = X.B + E \quad (\text{A.3})$$

where Y , X , B and E are the experimental-response vector, the Doehlert matrix (A.4), the coefficient vector and the residual-error vector, respectively.

$$X = \begin{pmatrix} 1 & 0 & 0 & 0 & 0 & 0 \\ 1 & 1 & 0 & 0 & 1 & 0 \\ 1 & 1/2 & \sqrt{3}/2 & \sqrt{3}/4 & 1/4 & 3/4 \\ 1 & -1/2 & \sqrt{3}/2 & -\sqrt{3}/4 & 1/4 & 3/4 \\ 1 & -1 & 0 & 0 & 1 & 0 \\ 1 & -1/2 & -\sqrt{3}/2 & \sqrt{3}/4 & 1/4 & 3/4 \\ 1 & 1/2 & -\sqrt{3}/2 & -\sqrt{3}/4 & 1/4 & 3/4 \end{pmatrix} \quad (\text{A.4})$$

The Doehlert matrix (A.4) is based on a set of dimensionless normalized values $x_{i,j}$ attributed to the two variables of the model. The normalization allows comparison of experimental factors F_1 and F_2 having different dimensions (e.g.: temperature and time). The transformation of normalized values $x_{i,j}$ (where i is the run number and j the factor/variable number) into real factor levels $l_{i,j}$ is obtained according to the following relationship:

$$l_{i,j} = (x_{i,j} \times \delta l_j) + l_{1,j} \quad (\text{A.5})$$

where $l_{1,j}$ is a level of factor F_j at the center of the experimental domain and δl_j is the step variation between consecutive levels of F_j . The regression coefficients are obtained using the method of least squares, which enables to fit the experimental response with the lowest residual error possible. As a result, equation A.3 can be simplified into:

$$\hat{Y} = X \cdot \hat{B} \quad (\text{A.6})$$

where \hat{Y} is the estimated-response vector and \hat{B} is the regression-coefficient vector. Equation A.6 is rearranged and applied to the experimental-response vector Y in order to obtain vector \hat{B} :

$$\hat{B} = (X^T \cdot X)^{-1} \cdot X^T \cdot Y \quad (\text{A.7})$$

The center point of the Doehlert DOE (run 1) is repeated i times to allow estimation of the response standard error $\hat{\sigma}_e^2$.

$$\hat{\sigma}_e^2 = \frac{1}{i-1} \sum_i (\bar{y}_7 - y_{7,i})^2 \quad (\text{A.8})$$

The estimates of the standard error of each regression coefficient are:

$$\hat{\sigma}(\hat{B}_j) = \sqrt{C_{j,j} \times \hat{\sigma}_e^2} \quad (\text{A.9})$$

where $C_{j,j}$ are diagonal elements of matrix $(X^T \cdot X)^{-1}$.

A.2 Statistical Analysis

The statistical significance of each coefficient of the model is checked using a Student's t -test [3]. A coefficient is considered to be significant when its P -value is below α (here $\alpha = 0.05$). The test of the overall significance of the model is achieved by analysis of variance (ANOVA) (F -test) [2]. The model is considered to be significant when the P -value of the regression is below α and the P -value of the lack-of-fit above α . The determinant coefficient R^2 and the correlation coefficient R are used to assess the quality of the fit. The closer the R^2 and the R to 1, the better the fit.

A.3 Process Optimization

The process optimization is performed using the Lagrange criterion, which is based on the calculation of the Hessian determinant H of \hat{Y} [4]:

$$H = \begin{vmatrix} \frac{\partial^2 \hat{Y}}{\partial X_1^2} & \frac{\partial^2 \hat{Y}}{\partial X_1 \partial X_2} \\ \frac{\partial^2 \hat{Y}}{\partial X_2 \partial X_1} & \frac{\partial^2 \hat{Y}}{\partial X_2^2} \end{vmatrix} = \left(\frac{\partial^2 \hat{Y}}{\partial X_1^2} \right) \left(\frac{\partial^2 \hat{Y}}{\partial X_2^2} \right) - \left(\frac{\partial^2 \hat{Y}}{\partial X_2 \partial X_1} \right) \left(\frac{\partial^2 \hat{Y}}{\partial X_1 \partial X_2} \right) \quad (\text{A.10})$$

The following four possible situations enable to determine the nature of the critical point of the response function:

- $H > 0$ and $\frac{\partial^2 \hat{Y}}{\partial X_1^2} < 0$: the critical point is a maximum
- $H > 0$ and $\frac{\partial^2 \hat{Y}}{\partial X_1^2} > 0$: the critical point is a minimum
- $H < 0$: the critical point is a saddle point
- $H = 0$: no information

The coordinate of the critical point are obtained by solving the following system of two equations:

$$\frac{\partial \hat{Y}}{\partial X_1} = 0 \text{ and } \frac{\partial \hat{Y}}{\partial X_2} = 0 \quad (\text{A.11})$$

Bibliography

- [1] Y. Cheng, G. Xu, D. Zhu, W. Zhu, and L. Luo, "Thermal analysis for indirect liquid cooled multichip module using computational fluid dynamic simulation and response surface methodology," *Components and Packaging Technologies, IEEE Transactions on*, vol. 29, no. 1, p. 39, Mar. 2006. [Online]. Available: <http://dx.doi.org/10.1109/TCAPT.2006>
- [2] M. A. Bezerra, R. E. Santelli, E. P. Oliveira, L. S. Villar, and L. A. Escaleira, "Response surface methodology (RSM) as a tool for optimization in analytical chemistry," *Talanta*, vol. 76, no. 5, p. 965, Sep. 2008. [Online]. Available: <http://dx.doi.org/10.1016/j.talanta.2008.05.019>
- [3] B. Zhou, Y. Li, J. Gillespie, G.-Q. He, R. Horsley, and P. Schwarz, "Doehlert Matrix Design for Optimization of the Determination of Bound Deoxynivalenol in Barley Grain with Trifluoroacetic Acid (TFA)," *Journal of Agricultural and Food Chemistry*, vol. 55, no. 25, p. 10141, Nov. 2007. [Online]. Available: <http://dx.doi.org/10.1021/jf0722957>
- [4] S. L. Ferreira, W. N. dos Santos, C. M. Quintella, B. B. Neto, and J. M. Bosque-Sendra, "Doehlert matrix: a chemometric tool for analytical chemistry-review ," *Talanta*, vol. 63, no. 4, p. 1061, Jul. 2004. [Online]. Available: <http://dx.doi.org/10.1016/j.talanta.2004.01.015>

Appendix B

Masks

- **Linear TLM structures**

Mask name: FORME1-TLM

- **Layer 1:** etch of alignment marks
- **Layer 2:** implantation
- **Layer 3:** mesa etch
- **Layer 4:** metal contacts lift-off

- **Inversion-mode MOSFETs and circular TLM structures**

Mask name: FORME3 Mask1

- **Layer 1:** etch of alignment marks / isolation
- **Layer 2:** S/D implantation
- **Layer 3:** oxide etch for opening for S/D and body contacts
- **Layer 4:** oxide lift-off for gate pad

Mask name: FORME3 Mask2

- **Layer 5:** S/D contacts lift-off
- **Layer 6:** gate pad + body contact lift-off
- **Layer 7:** gate metal lift-off
- **Layer 8:** metal lift-off for circular TLM structures

Appendix C

Process Flow for Junctionless MOSFETs with Raised Source and Drain

Use mask: JLESS-INGAAS1(PO No 404-96284)

1. Litho level 0: ALIGN ETCH

- Standard S1813 process for wet etch
- Wet etch alignment marks InGaAs/InP (target depth \sim 200 - 300 nm) with $\text{H}_2\text{SO}_4:\text{H}_2\text{O}_2:\text{DI}$ (1:1:8) for \sim 20 s
- PR removal with hot 1165 only (no plasmod)

2. Litho level1: GATE LIFTOFF (**Note: This is for an etch**)

- Standard S1813 process for wet etch
- Digital wet etch of the InGaAs channel (16 - 20 nm deep) with cycles of dips in $\text{HCl}:\text{DI}$ 1:10 (10 s) and dilute $\text{H}_2\text{O}_2:\text{DI}$ 1:10 (10 s). Target: for 16 nm etch depth \rightarrow 20 cycles, for 20 nm etch depth \rightarrow 25 cycles. Ellipsometry model: "In53Ga47As on InP Vladimir".
- PR removal with hot 1165 only (no plasmod)

3. Optimized surface passivation in 10% $(\text{NH}_4)_2\text{S}$ for 30 min **immediately followed** by 8 nm ALD Al_2O_3

4. Litho level1: GATE LIFTOFF

-
- Standard LOR3A/S1805 process for liftoff
 - 200 nm Pd evap, pre-evap heat to 100°C for 30 min. Evap at 80°C, evap rate: 0.5 Å/s for first 50 nm then 1 Å/s.

5. Litho level2: OXIDE ETCH

- Standard S1813 process for wet etch
- BOE/DI (1/10) etch for 25 s to remove Al₂O₃
- PR removal with hot 1165 only (no plasmod)

6. Litho level3: S/D LIFTOFF

- Standard LOR3A/S1805 process for liftoff
- Pre-load heat 90°C.
- Pre-deposition dip in ammonia/DI (1:10) for 20 s before loading
- Deposit N-metal Au/Ge/Au/Ni/Au (14/14/14/11/200 nm)

Standard litho processes:

- S1813 for etch : HMDS 4000 rpm for 60 s, S1813 4000 rpm for 60 s , bake 115°C for 2 min, expose 7.5 s, develop MF319 for 45 s, oven bake 90°C for 30 min
- LOR3A/S1805 for liftoff : HMDS 3000 rpm for 50 s, LOR3A 3000 rpm for 50 s, bake 150°C for 3min, HMDS 3000 rpm for 50 s, S1805 3000 rpm for 50 s, bake 115°C for 2 min, expose 4.5 s, develop MF319 for 1 min 15 s, oven bake 90°C for 30 min

Appendix D

List of Achievements

• Filed Patent Application

1. P. K. Hurley, K. Cherkaoui, **V. Djara**, “ Junctionless Nanowire Transistors for 3D Monolithic Integration of CMOS Inverters,” European Patent Office, Application no. 13162474.4 - 1555, filed 05/04/13.

• Accepted Publications

1. **V. Djara**, K. Cherkaoui, M. Schmidt, S. Monaghan, É. O’Connor, I. M. Povey, D. O’Connell, M. E. Pemble, and P. K. Hurley, “Impact of Forming Gas Annealing on the Performance of Surface-Channel $\text{In}_{0.53}\text{Ga}_{0.47}\text{As}$ MOSFETs With an ALD Al_2O_3 Gate Dielectric,” *IEEE Trans. Electron Devices*, vol. 59, no. 4, p. 1084, 2012.
2. **V. Djara**, K. Cherkaoui, S. B. Newcomb, K. K. Thomas, E. Pelucchi, D. O’Connell, L. Floyd, V. Dimastrodonato, L. O. Mereni, and P. K. Hurley, “On the Activation of Implanted Silicon Ions in $p\text{-In}_{0.53}\text{Ga}_{0.47}\text{As}$,” *Semicond. Sci. Technol.*, vol. 27, no. 8, p. 082001, 2012.
3. **V. Djara**, T. P. O’Regan, K. Cherkaoui, M. Schmidt, S. Monaghan, É. O’Connor, I. M. Povey, D. O’Connell, M. E. Pemble, and P. K. Hurley, “Electrically Active Interface Defects in the $\text{In}_{0.53}\text{Ga}_{0.47}\text{As}$ MOS system,” *Microelectron. Eng.*, vol. 109, p. 182, 2013.
4. M. A. Negara, **V. Djara**, T. P. O’Regan, K. Cherkaoui, M. Burke, Y. Y. Gomeniuk, M. Schmidt, É. O’Connor, I. M. Povey, A. J. Quinn, and P. K. Hurley, “Investigation of Electron Mobility in Surface-Channel $\text{Al}_2\text{O}_3/\text{In}_{0.53}\text{Ga}_{0.47}\text{As}$ MOSFETs,” *Solid-State Electron.*, vol. 88, p. 37, 2013.
5. P. K. Hurley, É. O’Connor, **V. Djara**, S. Monaghan, I. M. Povey, R. D. Long, B. Sheehan, J. Lin, P. C. McIntyre, B. Brennan, R. M. Wallace, M. E. Pemble, and

-
- K. Cherkaoui, "The characterisation and passivation of fixed oxide charges and interface states in the Al₂O₃/InGaAs MOS system," *IEEE Trans. Device and Materials Reliability* (2013) - in press.
6. É. O'Connor, B. Brennan, **V. Djara**, K. Cherkaoui, S. Monaghan, S. B. Newcomb, R. Contreras, M. Milojevic, G. Hughes, M. E. Pemble, R. M. Wallace, and P. K. Hurley, "A Systematic Study of (NH₄)₂S Passivation (22%, 10%, 5%, or 1%) on the Interface Properties of the Al₂O₃/In_{0.53}Ga_{0.47}As/InP System for N-type and P-type In_{0.53}Ga_{0.47}As Epitaxial Layers," *J. Appl. Phys.*, vol. 109, no. 2, p. 024101-10, 2011 - *This paper is in the top 20 most cited J. Appl. Phys. papers in 2012.*
 7. K. Cherkaoui, **V. Djara**, É. O'Connor, J. Lin, M. A. Negara, I. M. Povey, S. Monaghan, and Paul K. Hurley, "Can Metal/Al₂O₃/In_{0.53}Ga_{0.47}As/InP MOSCAP Properties Translate to Metal/Al₂O₃/In_{0.53}Ga_{0.47}As/InP MOSFET Characteristics?," *ECS Transactions*, vol. 45, no. 3, p. 79, 2012.
 8. P. K. Hurley, R. D. Long, T. P. O'Regan, É. O'Connor, S. Monaghan, **V. Djara**, M. A. Negara, A. O'Mahony, I. M. Povey, A. Blake, R. Nagle, D. O'Connell, M. E. Pemble, and K. Cherkaoui, "Equivalent Oxide Thickness Correction in the High-*k*/In_{0.53}Ga_{0.47}As/InP System," *ECS Transactions*, vol. 33, no. 3, p. 433, 2010.
 9. A. O'Mahony, S. Monaghan, R. Chiodo, I. Povey, K. Cherkaoui, R. Nagle, É. O'Connor, R. Long, **V. Djara**, D. O'Connell, F. Crupi, M. E. Pemble, and P. K. Hurley, "Structural and Electrical Analysis of Thin Interface Control Layers of MgO or Al₂O₃ Deposited by Atomic Layer Deposition and Incorporated at the High-*k*/III-V Interface of MO₂/In_xGa_{1-x}As (M = Hf|Zr, x = 0|0.53) Gate Stacks," *ECS Transactions*, vol. 33, no. 2, p. 69, 2010.

• Oral Presentations at International Conferences

1. **V. Djara**, K. Cherkaoui, M. A. Negara, J. MacHale, M. Burke, É. O'Connor, I. M. Povey, D. O'Connell, M. E. Pemble, A. Quinn, and P. K. Hurley, "Inversion-Charge Pumping Method for Mobility Extraction in Surface-Channel Al₂O₃/In_{0.53}Ga_{0.47}As MOSFETs," *IEEE Semiconductor Interface Specialists Conference (SISC)*, San Diego - United States, 2012.
2. **V. Djara**, K. Cherkaoui, M. Schmidt, Y. Y. Gomeniuk, É. O'Connor, I. M. Povey, D. O'Connell, S. Monaghan, M. E. Pemble, and P. K. Hurley, "Study of Interface and Oxide Defects in High-*k*/In_{0.53}Ga_{0.47}As n-MOSFETs," *IEEE Ultimate Integration on Silicon (ULIS)*, Grenoble - France, 2012.
3. **V. Djara**, *et al.*, "Impact of Forming Gas Anneal on Performance of Surface-Channel

Pd/Al₂O₃/In_{0.53}Ga_{0.47}As MOSFETs,” *IEEE Semiconductor Interface Specialists Conference (SISC)*, Arlington - United States, 2011.

4. **V. Djara**, K. Cherkaoui, K. K. Thomas, E. Pelucchi, D. O’Connell, L. Floyd, and P. K. Hurley, “Annealing Investigations for High-*k* First N-channel In_{0.53}Ga_{0.47}As MOSFET Development,” *IEEE Ultimate Integration on Silicon (ULIS)*, Cork - Ireland, 2011.
5. **V. Djara**, K. Cherkaoui, K. K. Thomas, E. Pelucchi, D. O’Connell, L. Floyd, V. Dimastrodonato, L. O. Mereni, and P. K. Hurley, “Anneal Process Optimization for Silicon Dopant Activation in Indium Gallium Arsenide Using a Doehlert Design of Experiment,” *European Materials Research Society (E-MRS)*, Strasbourg - France, 2010.

• Poster Presentations at International Conferences

1. **V. Djara**, K. Cherkaoui, T. Lopez, É. O’Connor, I. M. Povey, K. K. Thomas, and P. K. Hurley, “Junctionless InGaAs MOSFETs with InAlAs Barrier Isolation and Channel Thinning by Digital Wet Etching,” *IEEE Device Research Conference (DRC)*, Notre Dame - United States, 2013.
2. **V. Djara**, T. P. O’Regan, M. A. Negara, K. Cherkaoui, M. Burke, Y. Y. Gomeniuk, M. Schmidt, É. O’Connor, I. M. Povey, A. J. Quinn, and P. K. Hurley, “Electron Mobility Degradation in Surface-Channel Al₂O₃/In_{0.53}Ga_{0.47}As MOSFETs,” *IEEE Semiconductor Interface Specialists Conference (SISC)*, San Diego - United States, 2012.

• Award

1. BOC Gases Ireland Postgraduate Bursary Award 2012 (runner up) for research accomplishments in the field of high-*k*/III-V metal-oxide-semiconductor field-effect transistors (MOSFETs).

• Publications in Preparation

1. **V. Djara**, K. Cherkaoui, M. A. Negara, M. Burke, J. MacHale, D. O’Connell, A. Quinn, and P. K. Hurley, “Investigation of Border Traps and Mobility in Al₂O₃/In_{0.53}Ga_{0.47}As MOSFETs Using Inversion-charge Pumping,” *IEEE Trans. Electron Devices*.
2. **V. Djara**, K. Cherkaoui, T. Lopez, M. Burke, É. O’Connor, I. M. Povey, K. K. Thomas, and P. K. Hurley, “Impact of Channel Thickness in Junctionless Al₂O₃/In_{0.53}Ga_{0.47}As MOSFETs,” *IEEE Trans. Electron Devices*.

• Accepted Publications (Not Related to the PhD)

1. A. Wiczorek, **V. Djara**, F. H. Peters, J. O'Callaghan, K. K. Thomas, and B. Corbett, "Inductively Coupled Plasma Deep Etching of InP/InGaAsP in Cl₂/CH₄/H₂ Based Chemistries With the Electrode at 20°C," *J. Vac. Sci. Technol. B*, vol. 30, no. 5, p. 051208, 2012.
2. É. O'Connor, **V. Djara**, S. Monaghan, P. K. Hurley, and K. Cherkaoui, "Capacitance-Voltage and Interface State Density Characteristics of GaAs and In_{0.53}Ga_{0.47}As MOS Capacitors Incorporating a PECVD Si₃N₄ Dielectric," *ECS Transactions*, vol. 35, no. 3, p. 415, 2011.
3. S. Monaghan, K. Cherkaoui, É. O'Connor, **V. Djara**, P. K. Hurley, L. Oberbeck, E. Tois, L. Wilde, and S. Teichert, "TiN/ZrO₂/Ti/Al Metal-Insulator-Metal Capacitors With Subnanometer CET Using ALD-Deposited ZrO₂ for DRAM Applications," *IEEE Electron Device Lett.*, vol. 30, no. 3, p. 219, 2009.
4. M. Shayesteh, K. Huet, I. Toque-Tresonne, R. Negru, C. L. M. Daunt, N. Kelly, D. O'Connell, R. Yu, **V. Djara**, P. Carolan, N. Petkov, and R. Duffy, "Atomically-Flat Low-Resistive Germanide Contacts Formed By Laser Thermal Anneal," *IEEE Trans. Electron Devices*, vol. 60, no. 7, p. 2178, 2013.
5. M. Shayesteh, C. L. M. Daunt, D. O'Connell, **V. Djara**, M. White, B. Long, and R. Duffy, "NiGe Contacts and Junction Architectures for P and As Doped Germanium Devices," *IEEE Trans. Electron Devices*, vol. 58, no. 11, p. 3801, 2011.
6. R. A. Farrell, N. Petkov, M. T. Shaw, **V. Djara**, J. D. Holmes, and M. A. Morris, "Monitoring PMMA Elimination by Reactive Ion Etching from a Lamellar PS-*b*-PMMA Thin Film by *ex-situ* TEM Methods," *Macromolecules*, vol. 43, no. 20, p. 8651, 2010.
7. B. Toomey, K. Cherkaoui, S. Monaghan, **V. Djara**, É. O'Connor, D. O'Connell, L. Oberbeck, E. Tois, T. Blomberg, S. B. Newcomb, and P. K. Hurley, "The Structural and Electrical Characterization of a HfErO_x Dielectric for MIM Capacitor DRAM Applications," *Microelectron. Eng.*, vol. 94, p. 7, 2012.
8. Y. M. Georgiev, N. Petkov, B. McCarthy, R. Yu, **V. Djara**, D. O'Connell, O. Lotty, A. M. Nightingale, N. Thamsumet, J. C. deMello, A. Blake, S. Das, and J. D. Holmes, "Fully CMOS-compatible top-down fabrication of sub-50 nm silicon nanowire sensing devices," *Microelectron. Eng.*, 2014 (*accepted*).
9. M. Shayesteh, R. Duffy, B. McCarthy, A. Blake, M. White, J. Scully, R. Yu, **V. Djara**, M. Schmidt, N. Petkov, and A.-M. Kelleher, "Germanium Fin Structure Optimization

- for Future MugFET and FinFET Applications,” *ECS Transactions*, vol. 35, no. 2, p. 27, 2011.
10. R. Farrell, N. Kinahan, S. Hansel, K. Stuen, N. Petkov, M. Shaw, L. West, **V. Djara**, R. Dunne, O. Varona, P. Gleeson, S.-J. Jung, H.-Y. Kim, M. Kolesnik, T. Lutz, C. Murray, J. D. Holmes, P. Nealey, G. Duesberg, V. Krstic, and M. A. Morris, “Large-Scale Parallel Arrays of Silicon Nanowires via Block Copolymer Directed Self-Assembly,” *Nanoscale*, vol. 4, no. 10, p. 3228, 2012.
 11. R. G. Hobbs, M. Schmidt, C. T. Bolger, Y. M. Georgiev, P. Fleming, M. A. Morris, N. Petkov, J. D. Holmes, F. Xiu, K. L. Wang, **V. Djara**, R. Yu, and J. P. Colinge, “Resist-substrate Interface Tailoring for Generating High Density Arrays of Ge and Bi₂Se₃ Nanowires by Electron Beam Lithography,” *J. Vac. Sci. Technol. B*, vol. 30, no. 4, p. 041602, 2012.